Mechanisms in Wing-In-Ground Effect Aerodynamics

Marvin Alan Jones

University College London

University of London

A thesis submitted for the degree of

Doctor of Philosophy

November 1999

ProQuest Number: U644143

ProQuest U644143

To my Parents

for giving me the opportunity to learn and to understand.

To my Teachers

for showing me how to write it down.

To my Sister

for being there every step of the way.

Acknowledgements

Abstract

An aircraft in low-level flight experiences a large increase in lift and a marked reduction in drag, compared with flight at altitude. This phenomenon is termed the 'wing-in-ground' effect. In these circumstances a region of high pressure is created beneath the aerofoil, and a pressure difference is set up between its upper and lower surfaces. A pressure difference is not permitted at the trailing edge and therefore a mechanism must exist which allows the pressures above and below to adjust themselves to produce a continuous pressure field in the wake. It is the study of this mechanism and its role in the aerodynamics of low-level flight that forms the basis of our investigation. We begin in Chapter 2 by considering the flow past a thin aerofoil moving at moderate distances from the ground, the typical ground clearance α being of order unity. The aforementioned mechanism is introduced and described in detail in the context of this inviscid problem. Chapter 3 considers the same flow for large and small ground clearances and in the later case shows that the flow solution beneath the aerofoil takes on a particularly simple form. In this case the lift is shown to increase as α^{-1}. In Chapter 4 we focus on the flow past the trailing edge of an aerofoil moving even nearer the ground, with the ground just outside the boundary layer. We show that in this case our asymptotic theory for small α is consistent with a 'triple-deck' approach to the problem which incorporates ground effects via a new pressure-displacement law. The triple-deck ground-interference problem is stated and solved. In Chapter 5 we investigate the case where the aerofoil is so near the ground that the ground is inside the boundary layer. Here the moving ground interacts with the aerofoil in a fully viscous way and the non-linear boundary layer equations hold along the entire length of the aerofoil. Again a pressure difference at the trailing edge is not permitted and this produces upstream adjustment back to the leading edge. Regions of reversed flow can occur and their effects, with regard to downforce production and racing car undertray design, are considered. In Chapter 6 we consider 'wing-in-tunnel' effects.

Contents

List of Figures

Chapter 1

Introduction

Is it a boat? Is it a plane? Is it a car? No, it's a WIG. This is the term given to wing-in-ground effect vehicles which are designed to exploit the aerodynamic efficiency gains associated with low level flight.

Ever since the beginning of manned flight, pilots have experienced something strange when landing aircraft. Just before touchdown it feels as if the aircraft doesn't want to land, as if it is floating on a cushion of air; this phenomenon is termed 'wing-in-ground effect' or simply, 'ground effect'.

Aerodynamically speaking, two things happen as an aircraft approaches the ground and these two phenomena are termed span-dominated and chord-dominated ground effect. The former results in a reduction in the induced drag, D, and the latter results in an increase in the lift, L, experienced by the aircraft.

The two main sources of drag experienced by aircraft in flight are referred to as the skin drag and the induced drag. As the name suggests the first is caused by friction of the air on the skin of the aircraft, whilst the second is produced as a direct result of the wing's ability to generate lift and is sometimes called the 'lift induced drag'. When a wing generates lift the high pressure air, created beneath the wing, leaks around the wing tip to meet the low pressure air on top of the wing and

causes a wing-tip vortex. These vortices are sometimes visible when water in the air condenses in the low pressure vortex core and appear as spiral lines extending backwards from the wing tips. The energy that is stored in these vortices is lost and is experienced by the aircraft as drag. Hence the term 'lift induced drag'.

When the aircraft approaches the ground these wing-tip vortices become weaker due to destructive interference between the vortices themselves and their counter-rotating image vortices beneath the ground. This leads to a corresponding reduction in the induced drag on the aircraft.

As mentioned earlier chord dominated ground effect increases lift. When in ground effect, the air passing beneath the wing is slowed down so that the pressure there rises causing a large increase in lift; this is sometimes referred to as 'ram effect'. In some circumstances the fluid beneath the aerofoil can be made to stagnate producing large pressures, leading to large lift.

The combined result of the two phenomena described above is to increase the ratio L/D, which is commonly used to measure the efficiency of aircraft since when in steady flight weight is equal to lift and thrust is equal to drag and so L/D is an expression of how much weight can be carried for a given amount of thrust. In fact, lift-to-drag ratios for wings in ground effect are roughly twice as good as those for wings in free flight, making wing-in-ground effect flight one of the most energy efficient methods of transportation available.

This thesis is concerned with identifying and understanding the underlying aerodynamic mechanisms which give rise to chord-dominated ground effects for the entire range of possible ground clearances from flight at altitude to surface skimming.

The phenomenon of wing-in-ground effect has been known since 1920, in fact the Wright Brothers unknowingly used ground effects in their first attempts to fly in the 1900's and the first theoretical investigation of ground effect was made by Wieselsberger (1922). In the Second World War pilots flying twin engined bombers were

well aware that if one of their engines was damaged, making sustained flight at altitude impossible, an alternative to ditching in the ocean was to descend almost to sea level and use wing-in-ground effect to get home on their one remaining engine. Large birds, such as the Albatross, are also known to utilise wing-in-ground effect to conserve energy on long flights.

In 1935 the Finnish engineer Kaario (1959a,b) was the first to build a vehicle specifically designed to take advantage of ground effects. However it wasn't until the 1960's that independent research in many countries including the USSR, USA, Japan, and Germany began to take off.

In the USSR the major developments took place at the Central Hydrofoil Design Bureau, led by Rotislav Alexiev. The need for faster transportation over water led Alexiev to consider wing-in-ground effect vehicles as an improvement upon his earlier invention, the hydrofoil. His work eventually led to the development of the 540 tonne KM Ekranoplan dubbed the 'Caspian Sea Monster' by American intelligence officers after they spotted its peculiar planform-shape in satellite images. The KM is characterised by its relatively short stubby wings and its huge Y-shaped tail, which operates out of ground effect and gives the craft stability. It was approximately 100 metres long and travelled at an altitude of 20 metres above the Caspian Sea at around 300 mph! See Figures 1.1 and 1.2.

Around the same time the German aerodynamiscist Lippisch (1964), inventor of the delta-wing, designed a revolutionary new WIG; the X-112. It had a reversed delta-wing planform with negative dihedral at the leading edge and a large T-shaped tail, again for stability. This configuration proved to be inherently stable in ground effect and many recent designs have been based on the original Lippisch concept. See Figures 1.3 and 1.4

More recently, further development in the USA, Japan, Germany, and Australia have lead to many weird and wonderful WIG designs. For example, the Amphistar designed by Dimitri Sinitsyn (Sinitsyn (1996), Sinitsyn and Maskalik (1996)) who

Figure 1.1: The KM Ekranoplan, designed by Rotislav Alexiev, with its relatively short stubby wings and Y-shaped tail.

Figure 1.2: The KM Ekranoplan as viewed from the side.

Figure 1.3: The X-112, designed by Alexander Lippisch, with its reverse delta-wing planform.
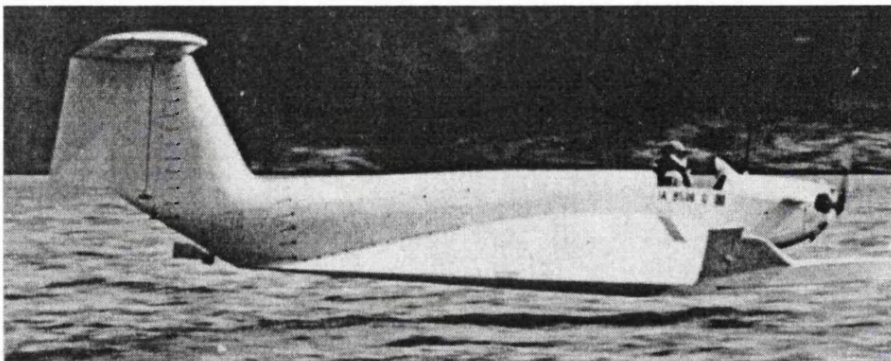
Figure 1.4: The X-112 as viewed from the side.

worked with Alexiev on the Caspian Sea Monster project; the Flairboat designed by Gunther Jorg (Jorg (1987, 1997)) with its tandem wing configuration; the Airfisch 3 designed by Hanno Fischer (Fischer (1989, 1988)), the most modern re-incarnation of the Lippisch; and the Hoverwing also designed by Hanno Fischer (Fischer and Matjasic (1996, 1997)), which combines catamaran and hovercraft technology to aid take off; this being important since initially getting free of the water, and into ground effect, efficiently is one of the major practical difficulties associated with wing-in-ground effect flight. See Figures 1.5, 1.6, 1.7, and 1.8.

It is our aim throughout this thesis to gain an understanding of the physical mechanisms involved in producing aerodynamic ground effects, these being the fluid dynamical phenomena that are introduced when one forces an aerofoil to perform in close proximity to the ground. In fact we will only consider the lift enhancing properties of wing-in-ground effect flight.

As mentioned earlier, in ground effect a region of high pressure is created beneath the aerofoil and a pressure difference is set up between its upper and lower surfaces; this pressure-difference is responsible for the increased lift experienced by aircraft when travelling near the ground. For thin two-dimensional aerofoils the lift, L, per unit length is given by

$$L = \int_0^1 (p_- (x) - p_+ (x)) \, dx + \cdots, \qquad (1.1)$$

to leading order, where the leading and trailing edges of the aerofoil are at $x = 0$ and 1 for convenience and the functions $p_+ (x)$ and $p_- (x)$ denote the pressures on the upper and lower surfaces of the aerofoil respectively. As one can clearly see it is the difference in the pressures $p_+ (x)$ and $p_- (x)$ that creates the lift.

However, a difference in pressure is not permitted at the trailing edge, due to the fact that the pressure may not vary across the aerofoil's thin viscous wake, and therefore a mechanism must exist which allows the pressures above and below the aerofoil

Figure 1.5: The Amphistar designed by Dimitri Sinitsyn. The modern incarnation of the KM ekranoplan.
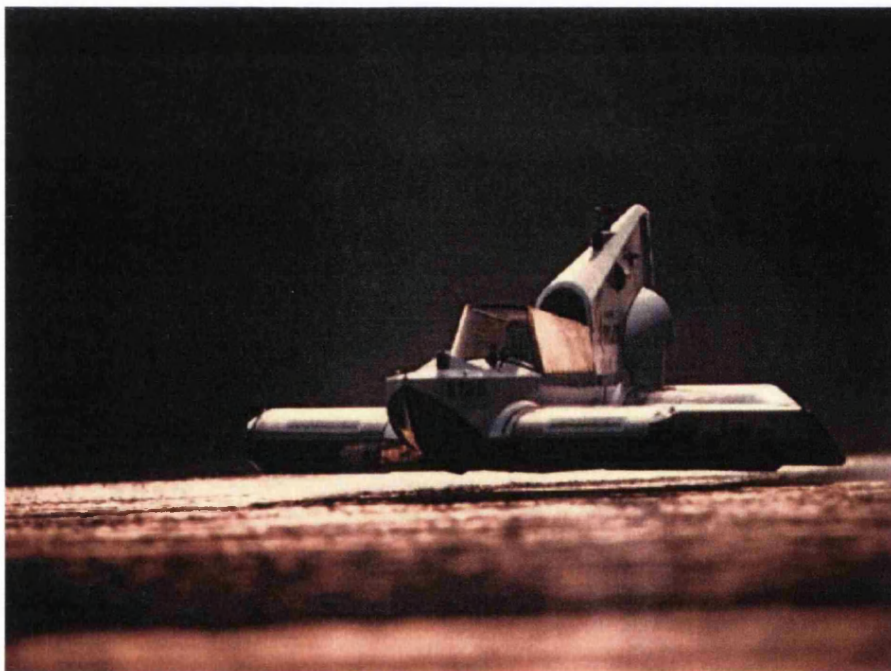
Figure 1.6: The Flairboat, desined by Gunther Jorg, with its tandem aerofoil configuration.

Figure 1.7: The Airfisch 3 designed by Hanno Fischer. The most modern incarnation of the Lippisch X-112.

Figure 1.8: The Hoverwing, also designed by Hanno Fischer, with its unique catamaran/hovercraft take-off system.

to 'feel'each other and adjust themselves accordingly so as to produce a continuous pressure field at the trailing edge and in the wake.

It is the study of this mechanism and its role in the aerodynamics of thin aerofoils travelling parallel with and close to the ground that forms the basis of the following investigation.

We begin, in Chapter 2, by considering the inviscid potential flow past a thin aerofoil flying at relatively large distances from the ground. The aforementioned mechanism is introduced and described in the context of this classical thin aerofoil problem (Sedov (1965)). A great deal of work has been focused on this and similar problems in two and three dimensions and at large and small ground clearances including significant contributions by Widnall and Barrows (1970), Tuck (1971), Kida and Miyai (1973), Tuck (1980), Plotkin and Kennell (1981), Newman (1982), Tan and Plotkin (1986), and Plotkin and Dodbele (1988).

However, in contrast to all of the above work we include the effects of viscosity by considering the influence of the attached Blasius boundary layers (Blasius (1908)) and the aerofoil's thin Goldstein wake (Goldstein (1930)) on the inviscid outer flow. This is achieved by effectively incorporating the displacement thicknesses of the thin viscous layers into the function which describes the aerofoil shape. The inclusion of these effects is essential since the singular nature of the Blasius and Goldstein displacement thicknesses greatly influence the lift on the aerofoil in ground-effect, especially when smaller values of the ground clearance parameter α are considered.

Having included these viscous effects the boundary condition on the ground is replaced by a symmetry condition, which leads to the introduction of an image aerofoil beneath the ground. The problem of finding the flow solution is then reduced, using complex analytical techniques (Carrier et al. (1966)) to that of solving a singular integral equation for the lift distribution on the aerofoil. The relevant solution is obtained analytically (Kondo (1991)) and is evaluated numerically for a range of ground clearances using the flat plate aerofoil as an example.

In Chapter 3 we examine the large and small ground clearance limits of the ground-interference problem introduced in Chapter 2. We begin with the integral equations derived in Chapter 2 and use Fourier integral transform techniques (Sneddon (1972)) to simplify the integral equations in each limit.

For large ground clearances we are able to show that the aerofoil does not feel the presence of the ground to leading order and at next order the effect of the ground's presence is to add a virtual angle of attack to the aerofoil.

For small ground clearances we show that the flow solution directly beneath the aerofoil takes a very simple form, which depends ultimately on the flow solution in two scaled regions around the leading and trailing edges. Two classes of edge-flow solutions are identified and application of the Kutta condition at the trailing edge allows a unique solution to be constructed in a logical way. The Wiener-Hopf technique (Noble (1958), Sparenberg (1956), and Sparenberg (1958)) is used to find one class of edge-flow solution whilst a conformal mapping technique (Churchill and Ward Brown (1990)) is employed to find the other. The lift on the aerofoil is crucially shown to <u>increase</u> as $\epsilon \alpha^{-1}$ for small ground clearances α, where $\epsilon = Re^{-1/2}$.

In Chapter 4 we focus in on the trailing edge region and consider this edge-flow when the aerofoil is even nearer the ground, with the ground just outside the classical boundary layer. In this case the inviscid asymptotic theory for small ground clearances, developed in Chapter 3, is entirely consistent with a 'triple deck' flow structure at the trailing edge (Stewartson (1969) and Messiter (1970)), which incorporates ground effects via a new pressure-displacement interaction law. This consistency is entirely due to the fact that viscous effects were included in the original inviscid problem and it is now clear why these effects must be included from the outset if one is to construct a sensible theory.

The triple deck ground-interference problem is stated and solved in part analytically and in part numerically using a Wiener-Hopf solution of the new pressure displacement law coupled with an iterative finite difference method based on the work of

Carter (1979). Solutions for the pressures and displacements are presented for a range of ground-clearances and shown to agree, for large ground-clearances, with the results of Jobe and Burggraf (1974) for flow past the trailing edge of a flat plate in the absence of the ground. The new pressure-displacement law for flows with ground interference takes on a particularly simple form for small ground clearances and the implications in terms of the solutions presented are discussed.

In chapter 5, we consider the flow past a thin aerofoil moving extremely close to the ground, with the ground <u>inside</u> the classical boundary layer. The governing equations inside and outside the gap are shown to be the boundary layer equations and the moving ground can now strongly influence the flow solution in a fully viscous way. In contrast with the work of Tuck and Bentwich (1983), Tichy and Chen (1985), Tichy (1986), Szeri (1987), and Wilson and Duffy (1998) we concentrate on the flow in a diverging channel where the minimum ground clearance is towards the front of the aerofoil. The diverging channel case typically produces negative lift or <u>downforce</u> and applications in Formula One racing car design are considered. The mechanisms encountered in the context of these flows include a viscous-inviscid interaction which fills the entire gap and is again associated with the requirement of pressure continuity at the trailing edge, the generation of strong upstream influence which forces a localised pressure jump at the leading edge, and importantly substantial flow separation and reversed flow at the trailing edge leading to certain wake effects. The governing equations are solved numerically and the solutions are shown to agree with the predictions of the inviscid asymptotic theory of Chapter 3 for larger gaps and those of lubrication theory (Batchelor (1967)) for smaller ones.

Finally, in Chapter 6 we consider the effects of adding a ceiling into the problems discussed in Chapters 2, 3, and 4, thus effectively considering wing-in-tunnel effects. We show that the results of Chapters 2, 3, and 4 can be generalised to include tunnel effects by simply replacing the algebraic kernels appearing in the integral equations in these chapters with similar exponential ones. Flow solutions for thin aerofoils

moving through tunnels can then be obtained in much the same way as for those of thin aerofoils in ground effect.

Therefore, in the investigation that follows we present a complete description of the phenomenon of two-dimensional chord-dominated "wing-in-ground" effect, as applied to thin aerofoils, spanning the entire range of ground clearances from those of flight at altitude to those of surface-skimming lubrication flows.

Chapter 2

Inviscid 'Wing-In-Ground' Effect

2.1 Introduction

As mentioned already an aircraft in low-level flight can experience a large increase in lift and a marked reduction in drag, compared with flight at altitude. This phenomenon is termed 'wing-in-ground' effect. In this chapter we consider the increase in lift produced by essentially inviscid fluid mechanics, on a thin aerofoil travelling near the ground . The inviscid assumption is valid for the case in which the ground does not directly interfere with the viscous boundary layers produced on the aerofoil surfaces.

One can consider this chapter as a preliminary study of 'wing-in-ground' effect, specifically a study of the phenomenon in its weakest form. The inclusion of this chapter allows us the opportunity to introduce some of the important physical ideas and mathematical techniques, which will be developed in the later chapters, in the familiar context of a potential flow problem. In fact the 'ground work' done in this chapter allows us to approach the problems of the later chapters more readily, in the knowledge that the assumptions made later are based on solid foundations.

Inviscid potential flow theory predicts the occurrence of a rapid variation in pressure

near the trailing edge of certain slender aerodynamic shapes, when placed in a uniform stream. It is the precise nature of this pressure variation which gives rise to the 'Triple-Deck' theory of trailing edge flow due to Stewartson (1969) and Messiter (1970). If we are to extend triple-deck theory to include the effects of ground-interference we must first understand the aforementioned pressure variation in the context of a thin aerofoil moving near the ground.

Therefore we begin our investigation by considering the flow past a thin aero-foil travelling at moderate distances from, and parallel to, the ground. We non-dimensionalise the lengths and velocities in the problem on L and U respectively where L is the aerofoil chord length and U is the aerofoil's speed relative to the ground. As a result the fluid pressure is non-dimensionalised based on the quantity ρU^2 where ρ is the fluid density. We will limit the discussion by considering only two-dimensional, incompressible, steady flows at high Reynolds number and will consequently take as our starting point the 2D steady Navier-Stokes equations in non-dimensional form as written below.

$$U\frac{\partial U}{\partial x} + V\frac{\partial U}{\partial y} = -\frac{\partial P}{\partial x} + \frac{1}{Re}\left(\frac{\partial^2 U}{\partial x^2} + \frac{\partial^2 U}{\partial y^2}\right), \tag{2.1}$$

$$U\frac{\partial V}{\partial x} + V\frac{\partial V}{\partial y} = -\frac{\partial P}{\partial y} + \frac{1}{Re}\left(\frac{\partial^2 V}{\partial x^2} + \frac{\partial^2 V}{\partial y^2}\right), \tag{2.2}$$

$$\frac{\partial U}{\partial x} + \frac{\partial V}{\partial y} = 0. \tag{2.3}$$

The streamwise and transverse components of the velocity vector field are denoted by $U(x,y)$ and $V(x,y)$ respectively and the scalar pressure field is denoted $P(x,y)$. The non-dimensional Reynolds number is defined to be $Re = \frac{UL}{\nu}$, where ν is the kinematic viscosity of the fluid. We will assume $Re \gg 1$.

In a frame moving with the aerofoil, our task becomes one of determining the flow around a thin body in a uniform stream, close to a plane boundary which is moving at the free stream velocity. See Figure 2.1.

We denote the typical non-dimensional distance between the ground and the aerofoil by α, which is assumed to be of order unity here. We are concerned with solving the

above inviscid ground-interference problem. However, we must include the effects of viscosity by incorporating boundary conditions into the problem which are consistent with the presence of thin boundary layers adjacent to the aerofoil, followed by a thin viscous wake. The inclusion of the wake, of unknown shape $s(x)$, allows the possibility of a discontinuous velocity field across the wake centerline whilst retaining the need for a continuous pressure field there. Also, by allowing this layer the freedom to adjust its shape, we introduce the mechanism by which the pressures above and below the plate, $p_+(x)$ and $p_-(x)$, may adjust themselves so as to meet the required pressure continuity condition at the trailing edge, $p_+(1) = p_-(1)$.

Finally we solve the governing potential flow equations, subject to the appropriate boundary conditions, using complex analytical techniques for a range of ground clearances. At the heart of the problem lies a singular integral equation which must be solved for the lift distribution on the aerofoil. Once this all-important lift distribution has been found the flow solution can be completed. The lift is qualitatively shown to increase as α^{-1} for decreasing ground clearance α and the rapid variation in pressure predicted at the trailing edge for flows without ground-interference is shown to persist in flows close to the ground.

2.2 Problem Formulation

We begin by studying the flow past a general thin aerofoil, with both camber and thickness, moving parallel with and close to the ground. Since we are dealing with a thin aerofoil we expect the flow to differ only slightly from that of an undisturbed uniform stream, almost everywhere, and therefore construct the solution in terms of the following perturbation expansions.

$$U(x,y) \;=\; 1 + \varepsilon u(x,y) + \cdots, \qquad (2.4)$$

$$V(x,y) \;=\; 0 + \varepsilon v(x,y) + \cdots, \qquad (2.5)$$

$$P(x,y) \;=\; p_\infty + \varepsilon p(x,y) + \cdots. \qquad (2.6)$$

The expansion parameter is the classical boundary layer thickness and typical aerofoil thickness, $\varepsilon = Re^{-1/2}$. The expansions above are expected to hold everywhere except in the boundary layers, the wake, the ground layer and near the leading and trailing edges. The flows in these regions are considered in Appendix A. The boundary layers and wake are of Blasius and Goldstein type respectively, the ground layer is a passive linear diffusion layer and the flow in the neighbourhood of the trailing edge is described by the triple-deck theory of Stewartson (1969) and Messiter (1970). The leading edge flow is not considered.

We substitute expansions (2.4)-(2.6) into the Navier-Stokes equations and obtain, at leading order, the inviscid equations of linearised potential flow.

$$\frac{\partial u}{\partial x}(x,y) = -\frac{\partial p}{\partial x}(x,y), \qquad (2.7)$$

$$\frac{\partial v}{\partial x}(x,y) = -\frac{\partial p}{\partial y}(x,y), \qquad (2.8)$$

$$\frac{\partial u}{\partial x}(x,y) + \frac{\partial v}{\partial y}(x,y) = 0. \qquad (2.9)$$

After the elimination of $u(x,y)$ these become the Cauchy-Riemann equations in the unknown perturbations $p(x,y)$ and $v(x,y)$,

$$\frac{\partial p}{\partial x}(x,y) = \frac{\partial v}{\partial y}(x,y), \qquad (2.10)$$

$$\frac{\partial p}{\partial y}(x,y) = -\frac{\partial v}{\partial x}(x,y). \qquad (2.11)$$

Our concern, then, is with finding the complex function $w(x+iy) = p(x,y) + iv(x,y)$, analytic in a slit upper half plane, bounded in the far field, and satisfying the boundary conditions,

$$w(x+0i) = p_+(x) + iv_+(x), \qquad (2.12)$$

$$w(x-0i) = p_-(x) + iv_-(x), \qquad (2.13)$$

$$w(x-i\alpha) = p_=(x) + 0i, \qquad (2.14)$$

$$p_+(x) = p_-(x) \quad \text{for} \quad x \notin [0,1], \qquad (2.15)$$

where $p_=(x)$ is ground pressure. Displacement effects produced by the aerofoil profile, the Blasius boundary layers on the aerofoil surfaces, and the Goldstein wake are included via the condition on $v_+(x)$ and $v_-(x)$ given below (see Appendix A).

$$
v_\pm(x) = \left\{ \begin{array}{ll}
s'(x) & \text{for} \quad x \in (-\infty, 0) \\
c'(x) \pm \frac{1}{2}t'(x) \pm \delta_b'(x) & \text{for} \quad x \in [0, 1] \\
s'(x) \pm \delta_g'(x) & \text{for} \quad x \in (1, +\infty)
\end{array} \right\}, \qquad (2.16)
$$

where the Blasius and Goldstein displacement thicknesses are denoted $\varepsilon\delta_b(x)$ and $\varepsilon\delta_g(x)$ respectively, the camber and thickness of the aerofoil are denoted $\varepsilon c(x)$ and $\varepsilon t(x)$ respectively, and the unknown shape of the dividing streamline upstream and the deflected wake downstream are denoted $\varepsilon s(x)$. We also define the total displacement thicknesses $\varepsilon\delta_\pm(x)$ by writing

$$
\delta_\pm(x) = \int_0^x v_\pm(\xi)\, d\xi. \qquad (2.17)
$$

2.3 Mathematical Methods

2.3.1 Symmetry Arguments

We simplify the problem slightly by eliminating $p_=(x)$. This is achieved by re-interpreting the no-penetration condition imposed at the plane boundary, $z = x - i\alpha$, as a symmetry condition. We are then faced with the problem of finding the complex function $w(x + iy) = p(x, y) + iv(x, y)$ which is analytic in a doubly slit plane, bounded in the far field, and satisfies the new boundary conditions,

$$
w(x + 0i) = p_+(x) + iv_+(x), \qquad (2.18)
$$

$$
w(x - 0i) = p_-(x) + iv_-(x), \qquad (2.19)
$$

$$
w(x - i\beta + 0i) = p_-(x) - iv_-(x), \qquad (2.20)
$$

$$
w(x - i\beta - 0i) = p_+(x) - iv_+(x), \qquad (2.21)
$$

$$
p_+(x) = p_-(x) \quad \text{for} \quad x \notin [0, 1], \qquad (2.22)
$$

where $\beta = 2\alpha$. Due to these symmetry arguments we have introduced an image aerofoil beneath the ground and are now essentially considering the flow past an unstaggered, non-lifting biplane with two thin viscous wakes. See Figure 2.2.

2.3.2 The Solution

We find a solution by applying Cauchy's integral formula for $w\left(z\right)$ three times, using the contours Γ_+, $\Gamma_=$, and Γ_- in the complex ζ plane defined in Figure 2.3.

Taking the limit as $\lim_{R \to \infty}$, summing the resulting balances, and imposing the boundary conditions (2.18)-(2.21) yields the solution

$$w\left(z\right) = \frac{1}{2\pi i}\int_{-\infty}^{+\infty}\frac{[p]\left(\xi\right)+i\left[v\right]\left(\xi\right)}{\left(\xi-z\right)}d\xi - \frac{1}{2\pi i}\int_{-\infty}^{+\infty}\frac{[p]\left(\xi\right)-i\left[v\right]\left(\xi\right)}{\left(\xi-i\beta-z\right)}d\xi, \quad (2.23)$$

where for convenience we have introduced the notation

$$[v]\left(x\right) = v_+\left(x\right)-v_-\left(x\right), \quad (2.24)$$

$$\langle v\rangle\left(x\right) = v_+\left(x\right)+v_-\left(x\right), \quad (2.25)$$

$$[p]\left(x\right) = p_+\left(x\right)-p_-\left(x\right), \quad (2.26)$$

$$\langle p\rangle\left(x\right) = p_+\left(x\right)+p_-\left(x\right), \quad (2.27)$$

for sums and differences. We can find the pressure and transverse velocity perturbations, $p\left(x,y\right)$ and $v\left(x,y\right)$, by taking real and imaginary parts of equation (2.23) to obtain

$$p\left(x,y\right) = \frac{1}{2\pi}\int_{-\infty}^{+\infty}\left(\frac{\left(\xi-x\right)}{\left(\xi-x\right)^2+y^2}+\frac{\left(\xi-x\right)}{\left(\xi-x\right)^2+\left(y+\beta\right)^2}\right)[v]\left(\xi\right)d\xi$$
$$+\frac{1}{2\pi}\int_{-\infty}^{+\infty}\left(\frac{y}{\left(\xi-x\right)^2+y^2}-\frac{\left(y+\beta\right)}{\left(\xi-x\right)^2+\left(y+\beta\right)^2}\right)[p]\left(\xi\right)d\xi,$$
$$\quad (2.28)$$

$$v\left(x,y\right) = \frac{1}{2\pi}\int_{-\infty}^{+\infty}\left(\frac{y}{\left(\xi-x\right)^2+y^2}+\frac{\left(y+\beta\right)}{\left(\xi-x\right)^2+\left(y+\beta\right)^2}\right)[v]\left(\xi\right)d\xi$$
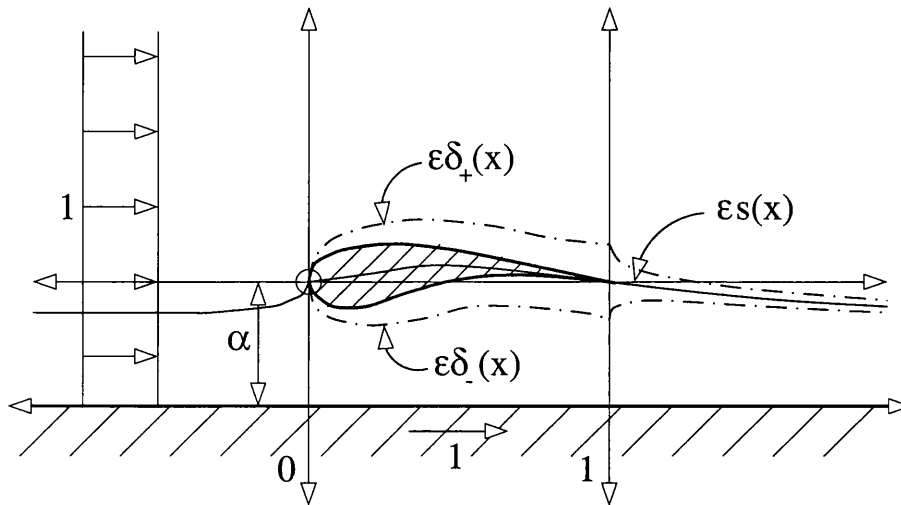
Figure 2.1: Cross-section of an aerofoil of thickness ε with two viscous boundary layers and a thin viscous wake flying at a ground clearance α
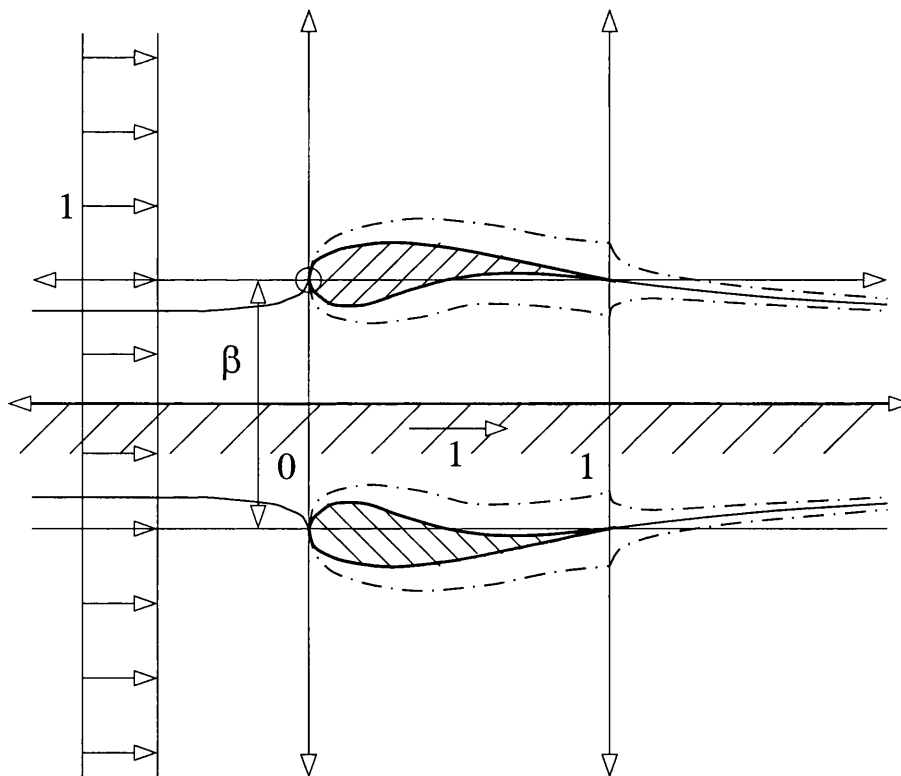
Figure 2.2: Symmetry arguments lead to the introduction of a virtual image aerofoil beneath the ground

$$-\frac{1}{2\pi}\int\limits_{-\infty}^{+\infty}\left(\frac{(\xi-x)}{(\xi-x)^2+y^2}-\frac{(\xi-x)}{(\xi-x)^2+(y+\beta)^2}\right)[p]\,(\xi)\,d\xi.$$

$$(2.29)$$

The streamwise velocity perturbation $u\,(x,y)$ is then found via the simple relation

$$u\,(x,y)=-p\,(x,y).$$

$$(2.30)$$

The solution is therefore determined in terms of the differences $[v]\,(x)$ and $[p]\,(x)$.

However, although we know the function $[v]\,(x)$ everywhere and the pressure continuity condition (2.22) informs us that $[p]\,(x)\,=\,0$ outside the interval $x\,\in\,[0,1]$, $[p]\,(x)$ is unknown <u>inside</u> this interval. The function $[p]\,(x)$ in the interval $x\,\in\,[0,1]$ describes the lift distribution on the aerofoil and is therefore of primary importance. It must be found before the solution is complete.

2.3.3 Completing the Boundary Conditions

We now turn to the task of completing the boundary conditions by finding the pressure difference $[p]\,(x)$ in the interval $x\,\in\,[0,1]$. Using Cauchy's integral formula once again, we consider the solution at a point on the aerofoil surface. We redefine the contours Γ_+ and $\Gamma_=$ slightly by adding a small circumnavigation of the pole which is now encountered in the integrand at this point. See Figure 2.4 .

Having done this we continue as before by applying Cauchy's integral formula three times using the new contours Γ_+ and $\Gamma_=$ for $w\,(x+0i)$ and $w\,(x-0i)$ respectively. Taking the limit $\lim\limits_{R\to\infty}\lim\limits_{\epsilon\to 0}$ and summing the three resulting balances gives

$$\omega\,(x+0i)+\omega\,(x-0i)\;=\;\frac{1}{\pi i}\fint\limits_{-\infty}^{+\infty}\frac{\omega\,(\xi+0i)-\omega\,(\xi-0i)}{(\xi-x)}d\xi$$

$$+\frac{1}{\pi i}\int\limits_{-\infty}^{+\infty}\frac{\omega\,(\xi-i\beta+0i)-\omega\,(\xi-i\beta-0i)}{(\xi-x)-i\beta}d\xi.$$

$$(2.31)$$
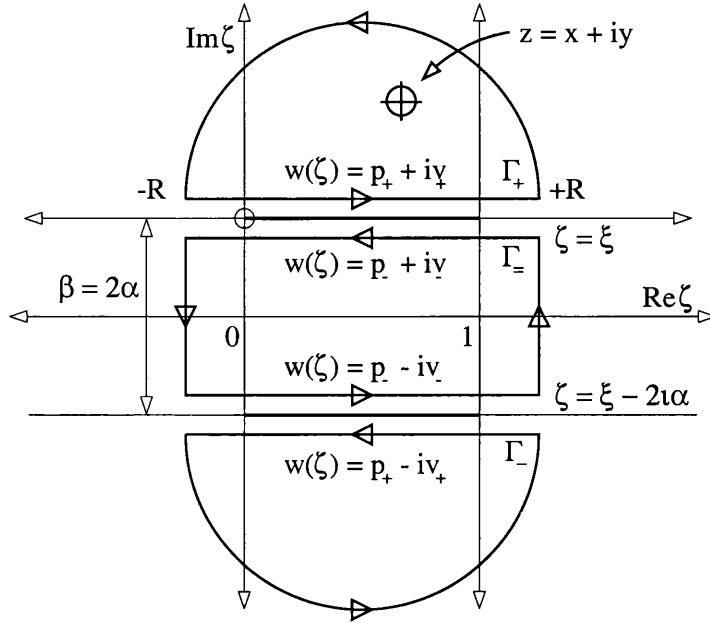
Figure 2.3: The integration contours Γ_+, $\Gamma_=$, and Γ_- are defined in the complex ζ plane as above
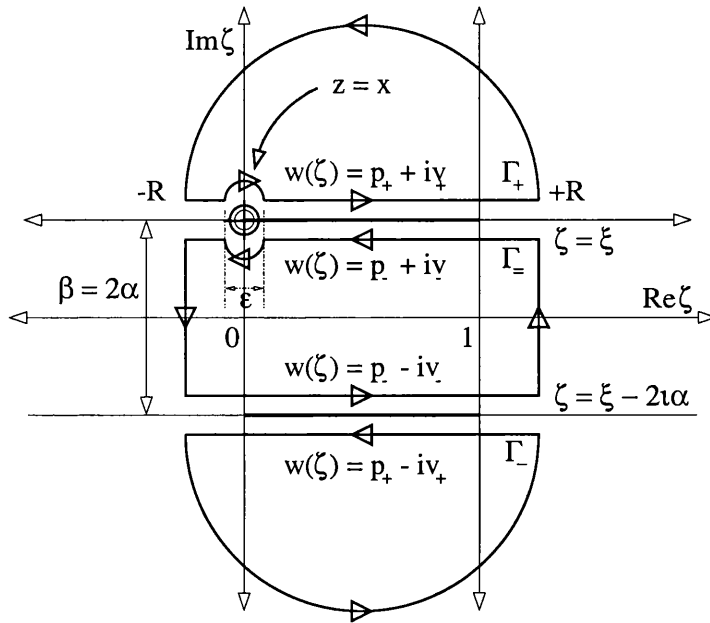
Figure 2.4: The pole in the integrand must be circumnavigated when z is on the surface of the aerofoil

Applying the boundary conditions (2.18)-(2.21) and using the shorthand notation for sums and differences we arrive at the expression

$$\langle p \rangle (x) + i \langle v \rangle (x) \;=\; \frac{1}{\pi i} \int\limits_{-\infty}^{+\infty} \frac{[p](\xi) + i[v](\xi)}{(\xi - x)} d\xi$$

$$-\frac{1}{\pi i} \int\limits_{-\infty}^{+\infty} \frac{([p](\xi) - i[v](\xi))((\xi - x) + i\beta)}{(\xi - x)^2 + \beta^2} d\xi.$$

(2.32)

If we take imaginary and real parts of this expression we obtain a pair of coupled integral equations involving the sums and differences, $[v](x)$, $\langle v \rangle (x)$, $[p](x)$, and $\langle p \rangle (x)$, namely

$$\langle v \rangle (x) \;=\; \frac{1}{\pi} \int\limits_{-\infty}^{\infty} l(\xi - x)[v](\xi) d\xi - \frac{1}{\pi} \int\limits_{-\infty}^{\infty} \left(\frac{1}{(\xi - x)} - m(\xi - x) \right) [p](\xi) d\xi,$$

(2.33)

$$\langle p \rangle (x) \;=\; \frac{1}{\pi} \int\limits_{-\infty}^{\infty} \left(\frac{1}{(\xi - x)} + m(\xi - x) \right) [v](\xi) d\xi - \int\limits_{-\infty}^{\infty} l(\xi - x)[p](\xi) d\xi,$$

(2.34)

$$\text{where} \quad l(x) = \frac{\beta}{x^2 + \beta^2} \quad \text{and} \quad m(x) = \frac{x}{x^2 + \beta^2}.$$

In the above equations $\beta = 2\alpha$ where α is the non-dimensional ground-clearance parameter. For convenience we will now adopt β as our parameter of choice. It is important since it is the distance between the aerofoil and its virtual partner beneath the ground. See Figure 2.2

The two integral equations must be solved subject to the mixed displacement and pressure-continuity boundary conditions,

$$[v](x) \;=\; \left\{ \begin{array}{ll} 0 & \text{for} \quad x \in (-\infty, 0) \\ t'(x) + 2\delta_b'(x) & \text{for} \quad x \in [0, 1] \\ 2\delta_g'(x) & \text{for} \quad x \in (1, +\infty) \end{array} \right\}, \qquad (2.35)$$

$$\langle v \rangle (x) \;=\; \left\{ \begin{array}{ll} 2c'(x) & \text{for} \quad x \in [0, 1] \\ ? & \text{for} \quad x \notin [0, 1] \end{array} \right\}, \qquad (2.36)$$

$$[p]\,(x) \;=\; \left\{ \begin{array}{lll} ? & \text{for} & x \in [0,1] \\[2mm] 0 & \text{for} & x \notin [0,1] \end{array} \right\}, \tag{2.37}$$

$$\langle p \rangle\,(x) \;=\; \left\{ \begin{array}{lll} ? & \text{for} & x \in [0,1] \\[2mm] ? & \text{for} & x \notin [0,1] \end{array} \right\}, \tag{2.38}$$

where ? is used to highlight the fact that the functions in question are unknown in the corresponding intervals shown above.

The Solution of the Integral Equations

It is clear from an examination of the integral equations and boundary conditions above that we must use our knowledge of $\langle v \rangle\,(x)$ in the interval $x \in [0,1]$ to find $[p]\,(x)$ in the interval $x \in [0,1]$. We can accomplish this by considering integral equation (2.33) for $x \in [0,1]$. We apply the pressure-continuity condition $[p]\,(x) = 0$ for $x \notin [0,1]$ and, after a minor rearrangement, equation (2.33) becomes the integral equation

$$\frac{1}{\pi} \fint_0^1 \left(\frac{1}{(\xi - x)} - m\,(\xi - x) \right) [p]\,(\xi)\,d\xi \;=\; \frac{1}{\pi} \int_{-\infty}^{\infty} l\,(\xi - x)\,[v]\,(\xi)\,d\xi - \langle v \rangle\,(x), \tag{2.39}$$

valid for $x \in [0,1]$. This is a singular Fredholm integral equation of the first kind for the pressure difference, $[p]\,(x)$, in the interval $x \in [0,1]$. The right hand side of the equation is known. The equation has a Cauchy type kernel and we refer to Muskhelishvili (1946) for advice on its solution.

In order to solve the equation we must first reduce it into an integral equation of the second kind which is easier to solve. This reduction involves finding the solution of the related 'dominant' equation. The dominant integral equation admits more than one solution and we must choose the one that is consistent with the physically relevant constraint of zero pressure difference at the trailing edge. The appropriate solution is identified and the subsequent reduction is performed. Finally,

the resulting Fredholm equation of the second kind is solved for $[p](x)$ in the interval $x \in [0, 1]$.

Once $[p](x)$ is determined we can explicitly determine $\langle v \rangle (x)$ and $\langle p \rangle (x)$ everywhere using the integral expressions (2.33) and (2.34) respectively. Furthermore once the sums and differences, $[p](x)$, $\langle p \rangle (x)$, $[v](x)$, and $\langle v \rangle (x)$ are all completely determined, we may calculate $p_\pm (x)$ and $v_\pm (x)$ from the simple relations

$$p_\pm (x) \;=\; \frac{1}{2} \left(\langle p \rangle (x) \pm [p](x) \right), \tag{2.40}$$

$$v_\pm (x) \;=\; \frac{1}{2} \left(\langle v \rangle (x) \pm [v](x) \right). \tag{2.41}$$

The Singular Integral Equation of the First Kind

We have reduced the problem under consideration to that of finding the solution of an integral equation subject to the additional constraint that the solution must be zero at $x = 1$. The integral equation (2.39) can be written as

$$\frac{1}{\pi} \fint_0^1 \left(\frac{1}{(\xi - x)} - m(\xi - x) \right) [p](\xi)\, d\xi = f(x), \tag{2.42}$$

for $x \in [0, 1]$ where

$$f(x) \equiv \frac{1}{\pi} \int_{-\infty}^{\infty} l(\xi - x) [v](\xi)\, d\xi - \langle v \rangle (x), \tag{2.43}$$

is a known function of x in the interval $x \in [0, 1]$.

The kernel of equation (2.42) is split into a singular part and a regular part. We recognise the singular part as the Cauchy-Hilbert kernel, and refer to it as the dominant part of the kernel. We rewrite (2.42) as

$$\frac{1}{\pi} \fint_0^1 \frac{[p](\xi)}{(\xi - x)}\, d\xi = f(x) + \frac{1}{\pi} \int_0^1 m(\xi - x) [p](\xi)\, d\xi, \tag{2.44}$$

for $x \in [0, 1]$ by taking the regular part of the kernel onto the right-hand side. We then proceed by seeking the solution of this dominant equation as if the right-hand side were a known function of x, say $g(x)$.

The Solution of the Dominant Equation

The solution of the dominant equation

$$\frac{1}{\pi} \int_0^1 \frac{[p]\,(\xi)}{(\xi - x)} d\xi = g\,(x) \tag{2.45}$$

is now considered. It is not uniquely defined by equation (2.45) and we must identify the appropriate solution by imposing the constraint of zero pressure difference at the trailing edge, $[p]\,(1) = 0$. The solution we require is written below for $x \in [0, 1]$. For the details of its derivation see Muskhelishvili (1946, section 113).

$$[p]\,(x) = -\frac{1}{\pi} \sqrt{\frac{1 - x}{x}} \int_0^1 \sqrt{\frac{\xi}{1 - \xi}} \frac{g\,(\xi)}{(\xi - x)} d\xi \tag{2.46}$$

We now use the above solution to reduce the original singular Fredholm integral equation of the first kind into a non-singular integral equation of the second kind.

The Reduction of the Integral Equation

We apply the integral operator defined by equation (2.46) to both sides of the dominant equation (2.44) to obtain

$$[p]\,(x) = \sqrt{\frac{1 - x}{x}} \left[h\,(x) + \frac{1}{\pi} \int_0^1 M\,(x, \xi)\,[p]\,(x)\, d\xi \right] \tag{2.47}$$

for $x \in [0, 1]$ where

$$h\,(x) \equiv -\frac{1}{\pi} \int_0^1 \sqrt{\frac{\xi}{1 - \xi}} \frac{f\,(\xi)}{(\xi - x)} d\xi \tag{2.48}$$

and

$$M\,(x, \xi) \equiv -\frac{1}{\pi} \int_0^1 \sqrt{\frac{\xi_1}{1 - \xi_1}} \frac{m\,(\xi_1 - \xi)}{(\xi_1 - x)} d\xi_1. \tag{2.49}$$

In short, we have undone the effects of the Cauchy-Hilbert operator on the left of equation (2.44) by finding and applying a suitable inverse integral operator.

Equation (2.47) is nothing more than a Fredholm integral equation of the *second* kind for the pressure difference $[p](x)$ in the interval $x \in [0, 1]$. Before we consider the solution of (2.47) we make a minor alteration with regard to the square root singularities appearing in equations (2.47)-(2.49). If it is our intention to evaluate the solution numerically then these square root singularities could cause problems. Therefore we factor the square root out of equation (2.47) and thereby make sure that any such singularities appear under an integral sign, where their contributions remain finite. We do this by introducing the function

$$\psi(x) = \sqrt{\frac{x}{1-x}} [p](x), \qquad (2.50)$$

which leads to the following non-singular Fredholm integral equation of the second kind for the function $\psi(x)$ in the interval $x \in [0, 1]$,

$$\psi(x) = h(x) + \frac{1}{\pi} \int_0^1 \sqrt{\frac{1-\xi}{\xi}} M(x, \xi) \psi(\xi) \, d\xi. \qquad (2.51)$$

The Solution of the Integral Equation of the Second Kind

We must now solve the equation (2.51) for $\psi(x)$ in the interval $x \in [0, 1]$. We begin by writing (2.51) as

$$\psi(x) = h(x) + \frac{1}{\pi} \int_0^1 N(x, \xi) \psi(\xi) \, d\xi, \qquad (2.52)$$

where

$$N(x, \xi) = \sqrt{\frac{1-\xi}{\xi}} M(x, \xi). \qquad (2.53)$$

The solution of (2.52) can be found using the method of successive substitution. See Kondo (1991, page 43) . We substitute for $\psi(\xi)$ on the right-hand side of (2.52) using the expression (2.52) itself with x replaced by ξ and ξ replaced by ξ_1 to obtain

$$\psi(x) = h(x) + \frac{1}{\pi} \int_0^1 N(x, \xi) \left[h(\xi) + \frac{1}{\pi} \int_0^1 N(\xi, \xi_1) \psi(\xi_1) \, d\xi_1 \right] d\xi$$

$$= h(x) + \frac{1}{\pi} \int_0^1 N(x,\xi) h(\xi) d\xi + \frac{1}{\pi^2} \int_0^1 \int_0^1 N(x,\xi_1) N(\xi_1,\xi) \psi(\xi) d\xi_1 d\xi.$$

$$(2.54)$$

Substituting successively for $\psi(\xi)$ in a similar manner $(n-1)$ times gives

$$\psi(x) = h(x) + \frac{1}{\pi} \int_0^1 N(x,\xi) h(\xi) d\xi$$

$$+ \frac{1}{\pi^2} \int_0^1 \int_0^1 N(x,\xi_1) N(\xi_1,\xi) h(\xi) d\xi_1 d\xi$$

$$+ \frac{1}{\pi^3} \int_0^1 \int_0^1 \int_0^1 N(x,\xi_1) N(\xi_1,\xi_2) N(\xi_2,\xi) h(\xi) d\xi_1 d\xi_2 d\xi$$

$$+ \cdots + \frac{1}{\pi^n} \int_0^1 \int_0^1 \cdots \int_0^1 N(x,\xi_1) \cdots N(\xi_{n-1},\xi) \psi(\xi) d\xi_1 \cdots d\xi_{n-1} d\xi.$$

$$(2.55)$$

Assuming the above partial sum tends to a well defined limit as $n \to \infty$ we obtain the solution

$$\psi(x) = h(x) + \frac{1}{\pi} \int_0^1 N(x,\xi) h(\xi) d\xi$$

$$+ \frac{1}{\pi^2} \int_0^1 \int_0^1 N(x,\xi_1) N(\xi_1,\xi) h(\xi) d\xi_1 d\xi$$

$$+ \frac{1}{\pi^3} \int_0^1 \int_0^1 \int_0^1 N(x,\xi_1) N(\xi_1,\xi_2) N(\xi_2,\xi) h(\xi) d\xi_1 d\xi_2 d\xi$$

$$+ \cdots + \frac{1}{\pi^n} \int_0^1 \int_0^1 \cdots \int_0^1 N(x,\xi_1) \cdots N(\xi_{n-1},\xi) h(\xi) d\xi_1 \cdots d\xi_{n-1} d\xi$$

$$+ \cdots$$

$$(2.56)$$

in the form of a convergent infinite series.

2.3.4 The Pressure Difference Solution

We are finally in a position to write down the solution for $[p](x)$. In the interval $x \in [0,1]$ the pressure difference takes the form

$$[p](x) = \sqrt{\frac{1-x}{x}}\psi(x) \tag{2.57}$$

where

$$\psi(x) = h(x) + \frac{1}{\pi}\int_0^1 N(x,\xi)h(\xi)d\xi$$

$$+ \frac{1}{\pi^2}\int_0^1\int_0^1 N(x,\xi_1)N(\xi_1,\xi)h(\xi)d\xi_1 d\xi + \cdots$$

$$+ \frac{1}{\pi^n}\int_0^1\int_0^1\cdots\int_0^1 N(x,\xi_1)\cdots N(\xi_{n-1},\xi)h(\xi)d\xi_1\cdots d\xi_{n-1}d\xi + \cdots. \tag{2.58}$$

In the above equation $h(x)$ and $N(x,\xi)$ are defined to be

$$h(x) \equiv -\frac{1}{\pi}\fint_0^1\sqrt{\frac{\xi}{1-\xi}}\frac{f(\xi)}{(\xi-x)}d\xi \tag{2.59}$$

and

$$N(x,\xi) \equiv -\frac{1}{\pi}\sqrt{\frac{1-\xi}{\xi}}\fint_0^1\sqrt{\frac{\xi_1}{1-\xi_1}}\frac{m(\xi_1-\xi)}{(\xi_1-x)}d\xi_1. \tag{2.60}$$

To complete the solution $f(x)$ is given by

$$f(x) \equiv \frac{1}{\pi}\int_{-\infty}^{\infty} l(\xi-x)[v](\xi)d\xi - \langle v\rangle(x) \tag{2.61}$$

where

$$l(x) \equiv \frac{\beta}{x^2+\beta^2} \quad \text{and} \quad m(x) \equiv \frac{x}{x^2+\beta^2}. \tag{2.62}$$

Outside the interval $x \in [0,1]$ the pressure difference is of course equal to zero.

2.4 Numerical Methods

2.4.1 The Evaluation of the Pressure Difference $[p](x)$

The solution as derived in the previous section is far from simple in form and its evaluation is not a straight-forward matter. The structure of the solution is such that we must consider its evaluation in stages. To start with we must determine the function $f(x)$ in the interval $x \in [0,1]$ using equation (2.61). We then go on to evaluate the expressions (2.59) and (2.60) for $h(x)$ and the kernel $N(x,\xi)$ respectively. Finally, $\psi(x)$ is calculated using the infinite sum (2.58). This completes the solution in the form (2.57)

Each of these stages presents its own difficulties, associated with the accurate evaluation of a singular integral or an infinite sum, and we shall address each one in turn. We will begin with the last stage first, by considering an efficient way to calculate the infinite sum appearing in equation (2.58).

2.4.2 The Evaluation of $\psi(x)$

We are faced with the task of evaluating $\psi(x)$ in the form of the infinite sum (2.58) which is the solution to the integral equation (2.52). The task is completed by using the method of successive approximations. We use the form of (2.52) to define a sequence of approximations to $\psi(x)$ which are calculated in an iterative manner.

The iteration is defined on the interval $x \in [0,1]$ by

$$\psi_0(x) = 0, \tag{2.63}$$

$$\psi_n(x) = h(x) + \frac{1}{\pi}\int_0^1 N(x,\xi)\,\psi_{n-1}(\xi)\,d\xi, \tag{2.64}$$

where $\psi_n(x)$ is the nth approximation to $\psi(x)$.

We must now show that this process does indeed yield a useful approximation to the solution $\psi(x)$. We do this in a similar way to section (2.3.3), by substituting for $\psi_{n-1}(\xi)$ above using equation (2.64) itself with x replaced by ξ, ξ replaced by ξ_1, and n replaced by $n-1$.

$$
\begin{aligned}
\psi_n(x) &= h(x) + \frac{1}{\pi}\int_0^1 N(x,\xi)\left[h(\xi) + \frac{1}{\pi}\int_0^1 N(\xi,\xi_1)\psi_{n-2}(\xi_1)\,d\xi_1\right]d\xi \\
&= h(x) + \frac{1}{\pi}\int_0^1 N(x,\xi)\,h(\xi)\,d\xi + \frac{1}{\pi^2}\int_0^1\int_0^1 N(x,\xi_1)N(\xi_1,\xi)\psi_{n-2}(\xi)\,d\xi_1 d\xi
\end{aligned}
$$

$$(2.65)$$

By successively back-substituting in this way n times we obtain the following expression for the nth approximation to $\psi(x)$, $\psi_n(x)$, in terms of the initial approximation, $\psi_0(x)$.

$$
\begin{aligned}
\psi_n(x) = h(x) \;&+\; \frac{1}{\pi}\int_0^1 N(x,\xi)\,h(\xi)\,d\xi \\
&+\; \frac{1}{\pi^2}\int_0^1\int_0^1 N(x,\xi_1)N(\xi_1,\xi)\,h(\xi)\,d\xi_1 d\xi \\
&+\; \frac{1}{\pi^3}\int_0^1\int_0^1\int_0^1 N(x,\xi_1)N(\xi_1,\xi_2)N(\xi_2,\xi)\,h(\xi)\,d\xi_1 d\xi_2 d\xi \\
&+\; \cdots + \frac{1}{\pi^n}\int_0^1\int_0^1\cdots\int_0^1 N(x,\xi_1)\cdots N(\xi_{n-1},\xi)\,\psi_0(\xi)\,d\xi_1\cdots d\xi_{n-1}d\xi
\end{aligned}
$$

$$(2.66)$$

In our case $\psi_0(x) = 0$ and so the last term disappears and we obtain

$$
\begin{aligned}
\psi_n(x) = h(x) \;&+\; \frac{1}{\pi}\int_0^1 N(x,\xi)\,h(\xi)\,d\xi \\
&+\; \frac{1}{\pi^2}\int_0^1\int_0^1 N(x,\xi_1)N(\xi_1,\xi)\,h(\xi)\,d\xi_1 d\xi + \cdots \\
&+\; \frac{1}{\pi^{n-1}}\int_0^1\int_0^1\cdots\int_0^1 N(x,\xi_1)\cdots N(\xi_{n-2},\xi)\,h(\xi)\,d\xi_1\cdots d\xi_{n-2}d\xi.
\end{aligned}
$$

$$(2.67)$$

By comparison with the solution (2.58) we see that by carrying out the iterative procedure n times we obtain the first n terms of the solution. Hence $\psi_n(x)$ is a useful approximation to $\psi(x)$ for large enough n. If the series solution is convergent then the iteration defines a way of finding the solution to arbitrary accuracy.

Before implementing the iteration we make a minor adjustment regarding the square root singularity appearing in equation (2.60) for $N(x,\xi)$ at $\xi = 0$. We make the change of variable $\xi = \sin^2\theta$ in equation (2.64) and obtain the new iterative step

$$\psi_n\left(\sin^2\phi\right) = h\left(\sin^2\phi\right) + \frac{2}{\pi}\int_0^{\pi/2}\cos^2\theta M\left(\sin^2\phi,\sin^2\theta\right)\psi_{n-1}\left(\sin^2\theta\right)d\theta,$$

(2.68)

where $M(x,\xi)$ is defined in equation (2.49) and where the substitution $x = \sin^2\phi$ has also been made for convenience.

2.4.3 The Evaluation of $h(x)$ and $M(x,\xi)$

Next we consider the evaluation of the function $h(x)$ and the kernel $M(x,\xi)$. The expressions for both these functions are essentially the same. They both contain a Cauchy principle value integral which is complicated by the presence of a square root end-point singularity. For $h(x)$ we have

$$h(x) \equiv -\frac{1}{\pi}\int_0^1\sqrt{\frac{\xi}{1-\xi}}\frac{f(\xi)}{(\xi-x)}d\xi.$$

(2.69)

Again we remove the square root end point singularity by making the appropriate substitution to obtain

$$h\left(\sin^2\phi\right) \equiv -\frac{2}{\pi}\int_0^{\pi/2}\frac{\sin^2\theta}{\left(\sin^2\theta-\sin^2\phi\right)}f\left(\sin^2\theta\right)d\theta.$$

(2.70)

We multiply the top and bottom of the integrand by $(\theta - \phi)$ and make use of the identity $\sin^2\theta - \sin^2\phi = \sin(\theta+\phi)\sin(\theta-\phi)$ to obtain the ordinary Cauchy prin-

ciple value integral

$$h\left(\sin^2\phi\right) \equiv -\frac{2}{\pi}\int_0^{\pi/2}\frac{(\theta-\phi)\sin^2\theta}{\sin(\theta+\phi)\sin(\theta-\phi)}\frac{f\left(\sin^2\theta\right)}{(\theta-\phi)}d\theta. \tag{2.71}$$

The non-Cauchy part of the integrand in the above integral is regular at the point $\theta=\phi$ since it has a *removable* singularity there and at this point takes the value

$$\lim_{\theta\to\phi}\left[\frac{(\theta-\phi)\sin^2\theta}{\sin(\theta+\phi)\sin(\theta-\phi)}\right]f\left(\sin^2\phi\right) = \frac{1}{2}\tan\phi f\left(\sin^2\phi\right). \tag{2.72}$$

All arguments extend to the evaluation of $M(x,\xi)$ and we obtain the following expression $M\left(\sin^2\phi,\sin^2\theta\right)$ where the non-Cauchy part of the integrand is again regular at $\theta=\phi$.

$$M\left(\sin^2\phi,\sin^2\theta\right) = -\frac{2}{\pi}\int_0^{\pi/2}\frac{(\theta_1-\phi)\sin^2\theta_1}{\sin(\theta_1+\phi)\sin(\theta_1-\phi)}\frac{m\left(\sin^2\theta_1-\sin^2\theta\right)}{(\theta_1-\phi)}d\theta_1,$$

$$\tag{2.73}$$

The Fortran NAG library routine D01AQF is then used to accurately evaluate the Cauchy principle value integrals appearing above. The routine works by pairing integrand values on either side of the singular point which, due to the nature of the Cauchy kernel, almost cancel with each other thus making it possible to obtain an accurate approximation to the integrals in question.

2.4.4   The Evaluation of $f(x)$

Now we turn to the evaluation of the function

$$f(x) \equiv \frac{1}{\pi}\int_{-\infty}^{\infty}l(\xi-x)[v](\xi)d\xi - \langle v\rangle(x). \tag{2.74}$$

for $x\in[0,1]$. Since $f(x)$ contains the transverse velocity boundary conditions in the form of $[v](x)$ and $\langle v\rangle(x)$ we will consider its evaluation in the context of a specific example, the case of an horizontal flat plate aerofoil travelling parallel with and near

the ground. We consider this case not only because it is the simplest realistic case but also since this particular aerofoil produces no lift when flying at altitude. This ensures that any lift produced in the current context must be attributed solely to ground proximity.

The aerofoil in question has no thickness ($t(x) \equiv 0$), no camber, and no angle of attack ($c(x) \equiv 0$). However the aerofoil does produce thin Blasius boundary layers on its upper and lower surfaces and a thin Goldstein wake downstream of its trailing edge. This translates into the following boundary conditions for $[v](x)$ and $\langle v \rangle (x)$.

$$
[v](x) = \begin{cases} 0 & \text{for} \quad x \in (-\infty, 0) \\ c_1 x^{-\frac{1}{2}} & \text{for} \quad x \in [0, 1] \\ -\frac{2}{3} c_2 (x-1)^{-\frac{2}{3}} (1 + c_3 (x-1))^{-\frac{4}{3}} & \text{for} \quad x \in (1, +\infty) \end{cases} \tag{2.75}
$$

$$
\langle v \rangle (x) = \begin{cases} 0 & \text{for} \quad x \in [0, 1] \\ ? & \text{for} \quad x \notin [0, 1] \end{cases}, \tag{2.76}
$$

where c_1, c_2, and c_3 are known constants. For details of the derivation of these boundary conditions see equations (2.35), (2.36), and Appendix A. The introduction of these boundary conditions into the equation for $f(x)$ yields

$$
f(x) \equiv \frac{c_1}{\pi} \int_0^1 l(\xi - x) \xi^{-\frac{1}{2}} d\xi - \frac{2c_2}{3\pi} \int_1^{+\infty} l(\xi - x)(\xi - 1)^{-\frac{2}{3}} (1 + c_3(\xi - 1))^{-\frac{4}{3}} d\xi. \tag{2.77}
$$

The first integrand is singular at $\xi = 0$ and the second is singular at $\xi = 1$. We can remove these singularities by making the change of variable $s = \xi^{1/2}$ in the first integral and $s = c_3^{1/3} (\xi - 1)^{1/3} (1 + c_3(\xi - 1))^{-1/3}$ in the second. We obtain the regular expression

$$
f(x) \equiv \frac{2c_1}{\pi} \int_0^1 l(s^2 - x) \, ds - \frac{2c_2}{\pi c_3^{1/3}} \int_0^1 l \left(\frac{s^3}{c_3(1 - s^3)} + 1 - x \right) ds, \tag{2.78}
$$

which can be easily evaluated numerically. Examples of the functions $f(x)$, $h(x)$,

$M(x, \xi)$, and $\psi(x)$ are shown in Figure 2.5 for the case where the ground clearance parameter α equals 0.5.

We are now in a position to calculate the pressure difference solution $[p](x)$ in the interval $x \in [0, 1]$ as described in section 2.3.4 for the case of a flat plate aerofoil travelling parallel with and near to the ground.

2.4.5 The Evaluation of $\langle p \rangle (x)$ and $\langle v \rangle (x)$

Since the differences $[p](x)$ *and* $[v](x)$ are now completely determined we may complete the boundary conditions by using equations (2.33) and (2.34) to calculate $\langle v \rangle (x)$ and $\langle p \rangle (x)$ respectively. Upon substitution of the known functions $[v](x)$ and $[p](x)$ on the right hand side of these equations we obtain the singular expressions

$$
\begin{aligned}
\langle v \rangle (x) \;=\; & \frac{c_1}{\pi} \int_0^1 l\,(\xi - x)\,\xi^{-1/2}\,d\xi \\
& - \frac{2c_2}{3\pi} \int_1^\infty l\,(\xi - x)\,(\xi - 1)^{-2/3}\,(1 + c_3\,(\xi - 1))^{-4/3}\,d\xi \\
& - \frac{1}{\pi} \fint_0^1 \sqrt{\frac{1-\xi}{\xi}} \left(\frac{1}{(\xi - x)} - m\,(\xi - x) \right) \psi(\xi)\,d\xi, & (2.79)
\end{aligned}
$$

$$
\begin{aligned}
\langle p \rangle (x) \;=\; & \frac{c_1}{\pi} \int_0^1 \left(\frac{1}{(\xi - x)} + m\,(\xi - x) \right) \xi^{-1/2}\,d\xi \\
& - \frac{2c_2}{3\pi} \fint_0^1 \left(\frac{1}{(\xi - x)} + m\,(\xi - x) \right) (\xi - 1)^{-2/3}\,(1 + c_3\,(\xi - 1))^{-4/3}\,d\xi \\
& - \frac{1}{\pi} \int_0^1 \sqrt{\frac{1-\xi}{\xi}}\,l\,(\xi - x)\,\psi(\xi)\,d\xi. & (2.80)
\end{aligned}
$$

As before we make the changes of variable $s = \xi^{1/2}$ in the first integral on the right hand sides above, $s = c^{1/3}\,(\xi - 1)^{1/3}\,(1 + c_3\,(\xi - 1))^{-1/3}$ in the second, and $\xi = \sin^2 \theta$

in the third giving

$$
\langle v \rangle (x) = \frac{2c_1}{\pi} \int_0^1 l \left(s^2 - x \right) ds
$$

$$
- \frac{2c_2}{\pi c_3^{1/3}} \int_0^1 l \left(\frac{s^3}{c_3 \left(1 - s^3 \right)} + 1 - x \right) ds
$$

$$
- \frac{2}{\pi} \fint_0^{\pi/2} \cos^2 \theta \left(\frac{1}{\left(\sin^2 \theta - x \right)} - m \left(\sin^2 \theta - x \right) \right) \psi \left(\sin^2 \theta \right) d\theta,
$$

(2.81)

$$
\langle p \rangle (x) = \frac{2c_1}{\pi} \int_0^1 \left(\frac{1}{\left(s^2 - x \right)} + m \left(s^2 - x \right) \right) ds
$$

$$
- \frac{2c_2}{\pi c_3^{1/3}} \fint_1^{\infty} \left(\frac{1}{\left(s^3 \left(c_3 \left(1 - s^3 \right) \right)^{-1} + 1 - x \right)} + m \left(\frac{s^3}{c_3 \left(1 - s^3 \right)} + 1 - x \right) \right) ds
$$

$$
- \frac{2}{\pi} \int_0^{\pi/2} \cos^2 \theta l \left(\sin^2 \theta - x \right) \psi \left(\sin^2 \theta \right) d\theta.
$$

(2.82)

This has the effect of making sure all the integrands are finite apart from inside the Cauchy principle value integrals, which are manipulated in a similar way to equation (2.70) before being evaluated using the Fortran NAG library routine D01AQF. Examples of the sums and differences $[p] (x)$, $\langle p \rangle (x)$, $[v] (x)$, and $\langle v \rangle (x)$ are shown in Figure 2.6 for $\alpha = 0.5$

Once $\langle p \rangle (x)$ and $\langle v \rangle (x)$ are determined it only remains to calculate $p_{\pm} (x)$ and $v_{\pm} (x)$ from the simple relations (2.40) and (2.41) respectively. See Figure 2.7 for the results of this calculation, again for $\alpha = 0.5$.

Finally, the pressure $p (x, y)$, transverse velocity $v (x, y)$, and streamwise velocity $u (x, y)$ perturbations can be evaluated in a similar way to $\langle p \rangle (x)$ and $\langle v \rangle (x)$ using equations (2.28), (2.29), and (2.30) respectively. The solutions for $p (x, y)$, $v (x, y)$, and $u (x, y)$ are shown as surface plots against x and y in Figures 2.8, 2.9, and 2.10 respectively for $\alpha = 0.5$.
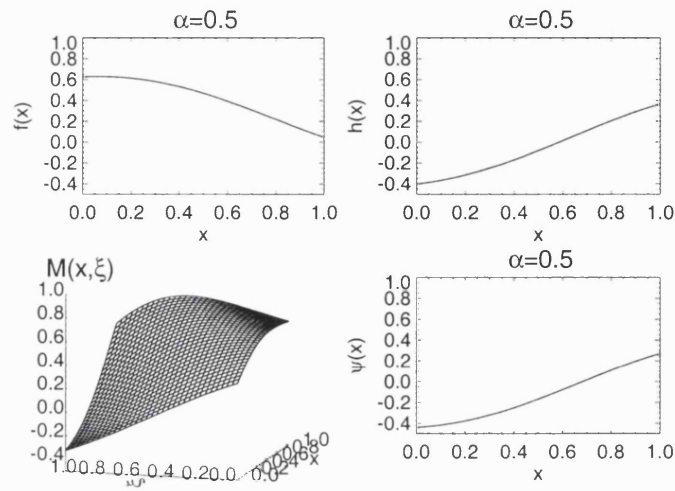
Figure 2.5: The functions $f(x)$, $h(x)$, $M(x,\xi)$, and $\psi(x)$ for $\alpha = 0.5$.
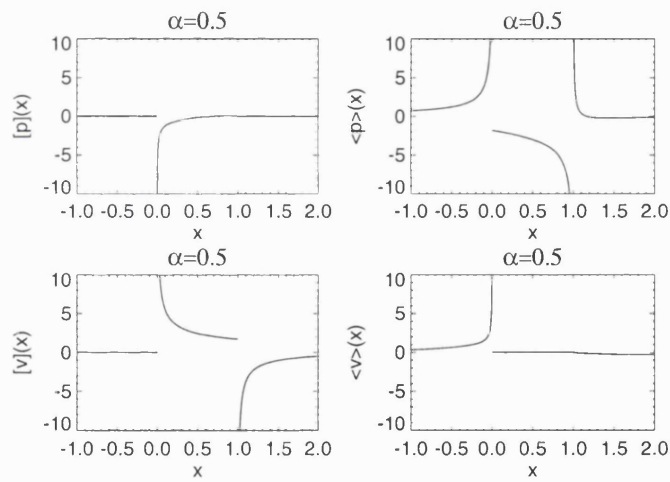
Figure 2.6: The sums and differences $[p](x)$, $\langle p \rangle (x)$, $[v](x)$, and $\langle v \rangle (x)$ for $\alpha = 0.5$.
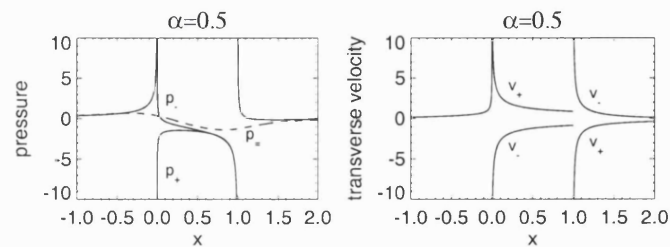
Figure 2.7: The pressures and velocities $p_{\pm}(x)$ and $v_{\pm}(x)$ for $\alpha = 0.5$.
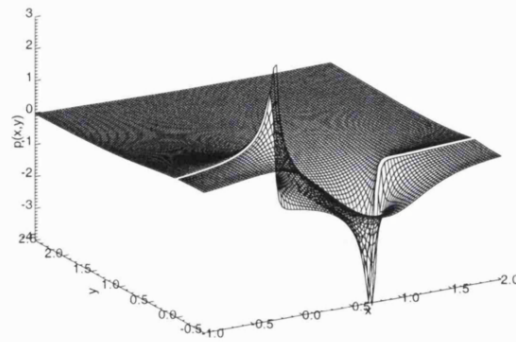
Figure 2.8: The pressure perturbation $p(x, y)$ for $\alpha = 0.5$.
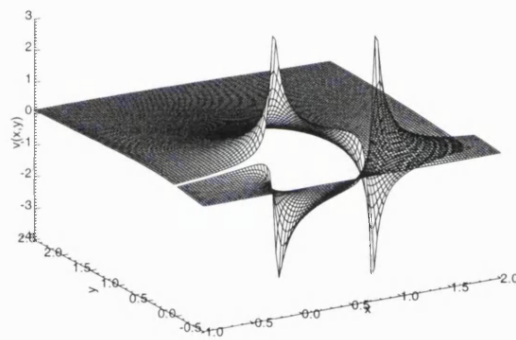
Figure 2.9: The transverse velocity perturbation $v(x, y)$ for $\alpha = 0.5$.
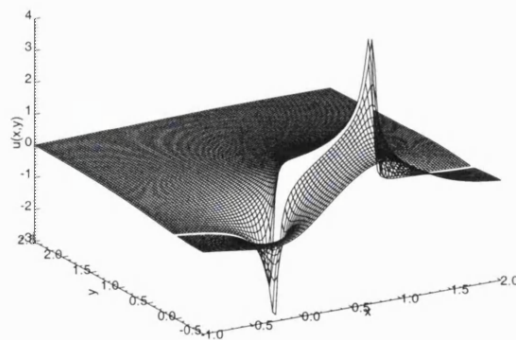
Figure 2.10: The streamwise velocity perturbation $u(x, y)$ for $\alpha = 0.5$.

2.5 Flow Properties

Figures 2.11 and 2.12 show the displacement thicknesses $\delta_\pm(x)$ and the pressures $p_\pm(x)$ on a horizontal flat plate aerofoil in ground effect, for a range of ground clearances from $\alpha = 16$ to $\alpha = \frac{1}{16}$.

Wing-in-ground effects are known, from a practical standpoint, to significantly effect aerofoil performance for ground clearances less than half the aerofoil chord-length. The results in Figures 2.11 and 2.12 confirm this rule of thumb, as for $\alpha > \frac{1}{2}$ the pressures on the aerofoil are virtually identical. The first ground effects do indeed appear at $\alpha = \frac{1}{2}$ and the solutions then change dramatically as α is reduced further.

To begin with, we note that the pressure is singular at both the leading and trailing edges for all α. This is due to the singular nature of the displacement gradients, $\delta'_\pm(x)$, at $x = 0$ and $x = 1$ respectively and is not attributable to ground proximity.

The most significant change introduced into the solution by decreasing α is the rapid growth in magnitude of the pressure beneath the aerofoil, $p_-(x)$. This effect together with the fact that the pressure above the aerofoil remains relatively unchanged leads to a corresponding large increase in lift as expected. Closer examination of the bottom three graphs in Figure 2.12 suggests that the magnitude of $p_-(x)$ in fact increases as α^{-1} for small α and this trend is explored in detail in the next chapter. This relationship explains the stability associated with wing-in-ground effect flight;as the vehicle comes closer to the ground the lift goes up and as a result the vehicle returns to its previous altitude. If the vehicle is designed correctly a stable equilibrium height can be achieved. Certain vehicles are so stable that they have been flown in ground effect for up to 45 minutes without the pilot needing to touch the controls! The shape of $p_-(x)$ directly beneath the plate also takes a particularly simple form for small α which seems to reflect the shape of the displacement thickness $\delta_-(x)$ there.

Another feature of the small α solutions is the flatness of the lower displacement
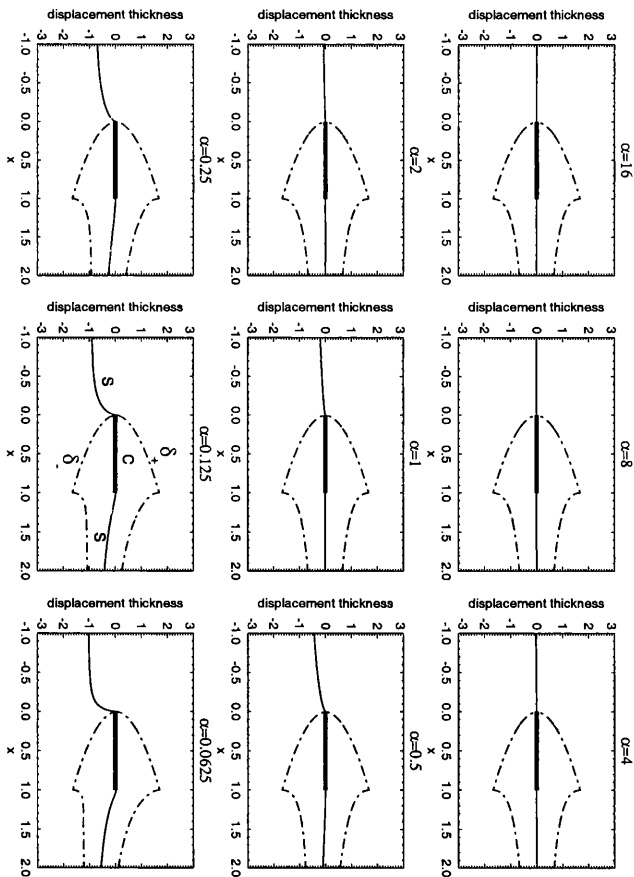
Figure 2.11: The total displacement thicknesses $\delta_\pm(x)$ of a horizontal flat plate aerofoil in ground effect for $\alpha = 16$ to $\frac{1}{16}$.
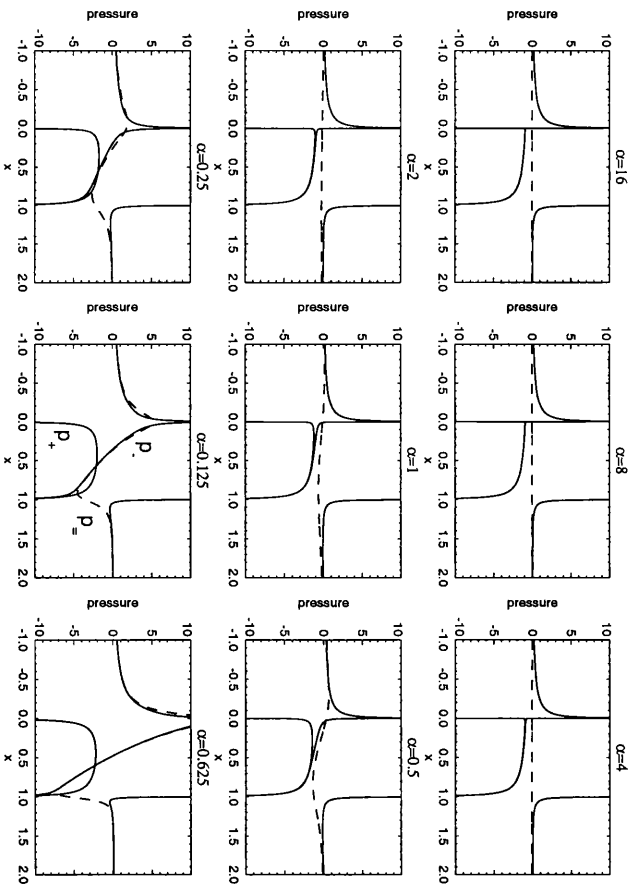
Figure 2.12: The pressures $p_\pm(x)$ on a horizontal flat plate aerofoil in ground effect for $\alpha = 16$ to $\frac{1}{16}$.

function $\delta_-(x)$ in the wake of the aerofoil. This flat shape is induced by the physical need for pressure continuity across the wake and ultimately causes the downward deflection of the centerline $s(x)$. Physically speaking, this flat shape indicates that little fluid is drawn into the thin Goldstein wake from below, in contrast with the large α case where equal amounts of fluid are entrained from both above and below.

In addition to those already mentioned there are several, more subtle effects taking place as α becomes small. However the discussion of these effects is left until the next chapter.

Figures 2.13 and 2.14 show a similar set of results for a flat plate aerofoil at positive angle of attack and Figures 2.15 and 2.16 show the results for a flat plate aerofoil at negative angle of attack. The trends described for the horizontal flat plate case are all present in these two sets of results and wing-in-ground effect is shown to enhance the pre-existing lift or downforce in each case respectively.

To recap then, in this chapter we have introduced the wing-in-ground effect phenomenon through an inviscid study of the fluid dynamical mechanisms which are introduced when an aerofoil is forced to perform in close proximity to the ground. We have identified the physical necessity for pressure continuity upstream, at the trailing edge, and in the wake of the aerofoil and have introduced the mechanism by which this condition is achieved, that being a deflection of the wake centre-line. We have given this mechanism a mathematical form in terms of the two coupled integral equations (2.33) and (2.34) and have solved these equations to obtain flow solutions for a range of ground clearances α. The resulting pressure solutions show the predicted large increase in lift associated with ground proximity and the effect is shown to become significant at ground clearances less then half the aerofoil chordlength. We note that for small α the pressure directly beneath the aerofoil scales like α^{-1} and takes a particularly simple form. The small α regime is now examined in detail.
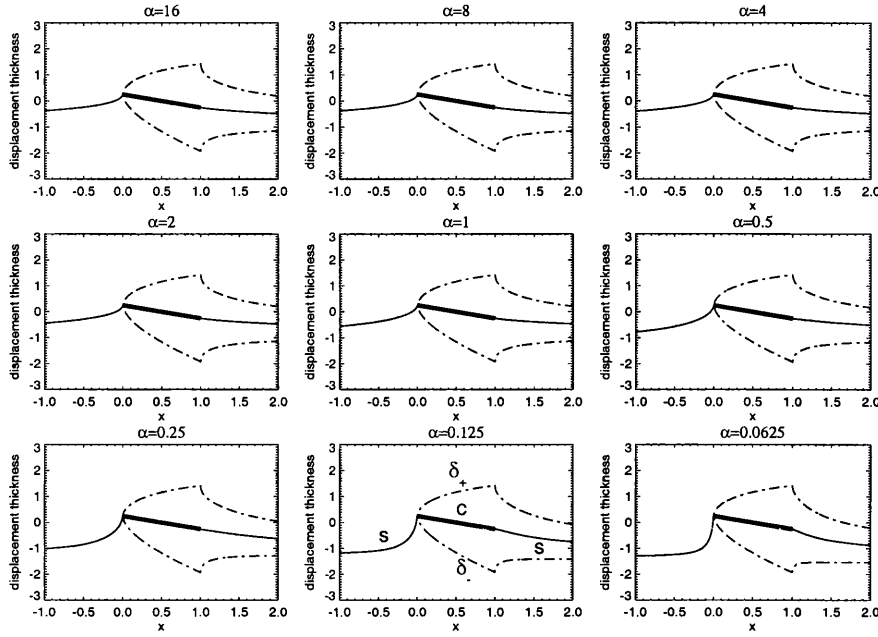
Figure 2.13: The displacements $\delta_\pm (x)$ of a flat plate aerofoil in ground effect at positive angle of attack for $\alpha = 16$ to $\frac{1}{16}$.
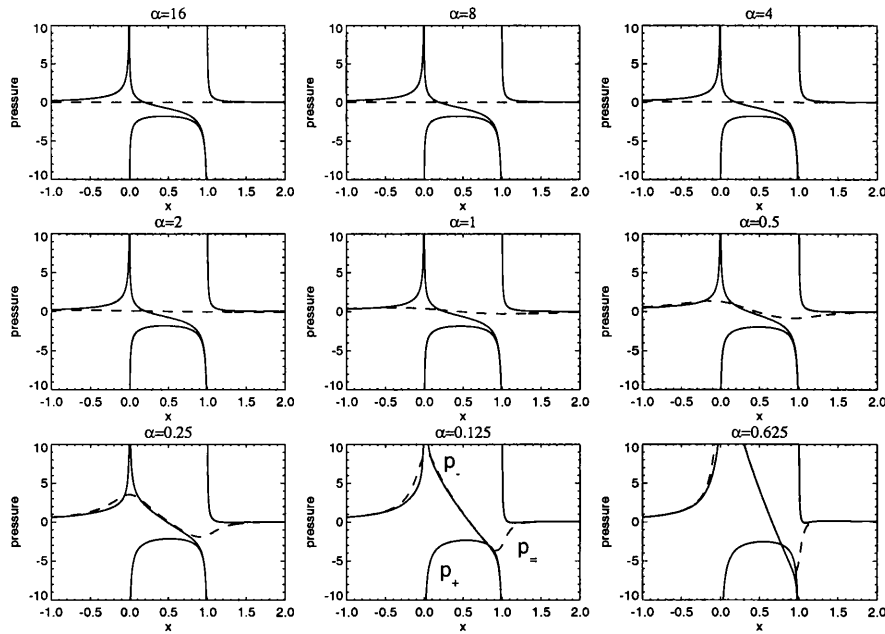
Figure 2.14: The pressures $p_\pm (x)$ on a flat plate aerofoil in ground effect at positive angle of attack for $\alpha = 16$ to $\frac{1}{16}$.
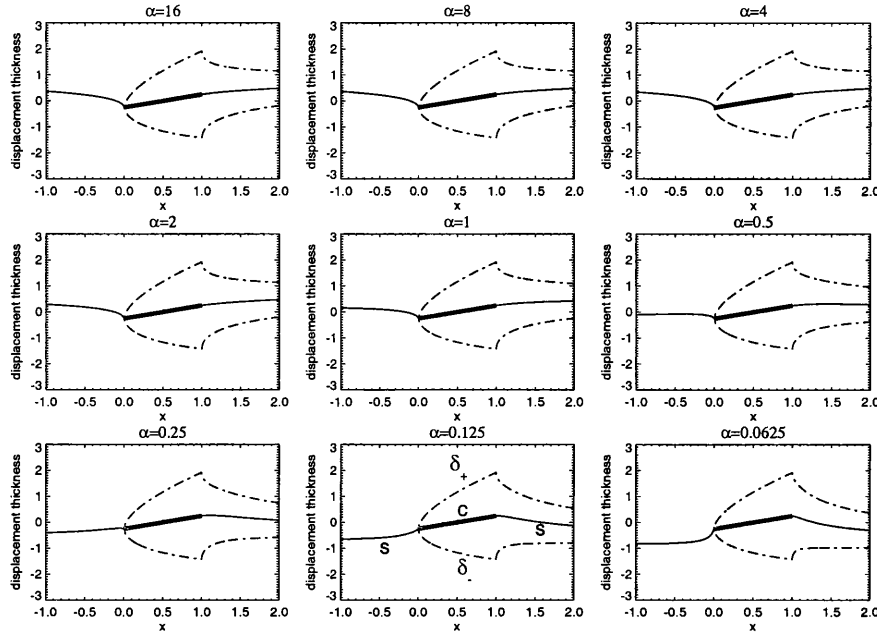
Figure 2.15: The displacements $\delta_\pm (x)$ of a flat plate aerofoil in ground effect at negative angle of attack for $\alpha = 16$ to $\frac{1}{16}$.
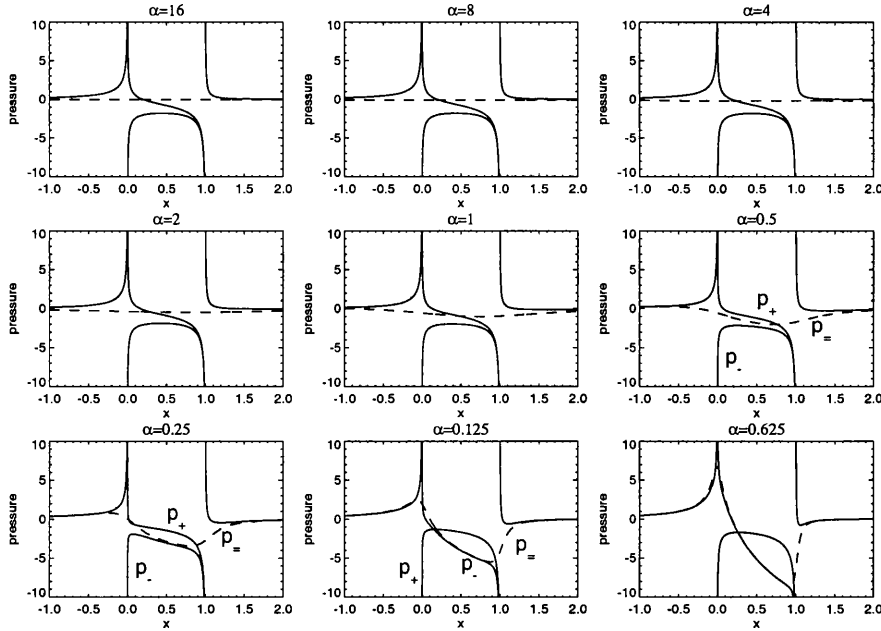
Figure 2.16: The pressures $p_\pm (x)$ on a flat plate aerofoil in ground effect at negative angle of attack for $\alpha = 16$ to $\frac{1}{16}$.

Chapter 3

Inviscid Solutions for $\beta \gg 1$ and $\beta \ll 1$

3.1 Introduction

The results presented in the previous chapter show that the solution of the ground-interference problem under consideration takes on a relatively simple form for large or small values of the parameter β. In this chapter we try to quantify this statement for each of these asymptotic regimes in turn.

We begin by considering the case when the aerofoil is flying at large distances from the ground and is only weakly influenced by its presence. In this case $\beta \gg 1$ and we might expect the leading order solution to be that for flow past a thin aerofoil in the absence of the ground. This is shown to be the case. The next order correction to this basic solution is considered and constitutes the leading order ground effect for large β.

Afterwards we consider the opposite limit in which the aerofoil is flying at very low altitude and $\beta \ll 1$. In this regime the aerofoil is said to be 'in-ground-effect', or indeed well within it, and is strongly influenced by the proximity of the ground.

Again the leading order solution has a simple form and most importantly the lift is shown to increase as β^{-1}.

For small β the large pressures created beneath the aerofoil (which produce the large increase in lift associated with wing-in-ground effect flight in practice) must be smoothly joined with the much smaller pressures in the bulk of the fluid outside the gap. This is accomplished in small scaled regions around the leading and trailing edges (Regions II and III) where local coordinates, scaled on β, are introduced. See Figure 3.1.

Two distinct types of edge flow solution exist: an eigensolution, which satisfies homogeneous transverse velocity boundary conditions and physically represents an 'around-the-edge' flow, and a non-eigensolution which is driven by non-zero transverse velocity boundary conditions and physically represents a streamlined edge flow. See Figure 3.2.

The Kutta condition for small β permits only the streamlined non-eigensolutions at the trailing edge and therefore forces the eigensolutions to appear only at the leading edge. The 'strengths' of the eigensolutions are unknown and the mechanism by which the strengths are set is one of the most interesting features of the small β solution.

First the non-eigensolution is completely determined from the boundary conditions and sets the pressure beneath the aerofoil just upstream of the trailing edge. This in turn determines the solution along the entire length of the underside of the aerofoil and the corresponding unknown eigensolution strength is then set by smoothly joining the gap solution to the solution in the bulk of the fluid at the leading edge. This mechanism allows large upstream influence in the flow and furthermore identifies the local trailing edge region as the dominant region in the flow field, the solution there effecting the properties of the flow everywhere else.
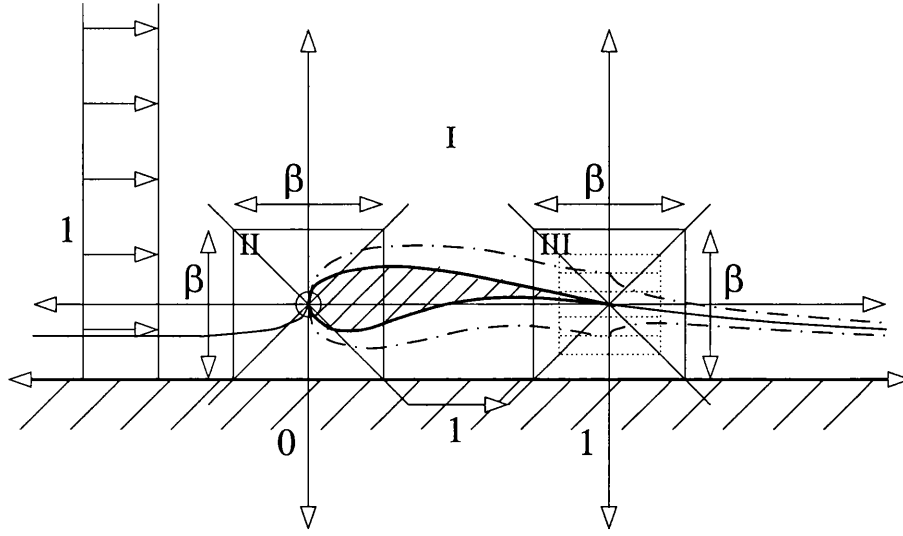
Figure 3.1: The flow structure for $\beta \ll 1$. Note the square β by β local leading and trailing edge regions and that the triple-deck structure, shown in dotted lines, lies within the local trailing edge region.
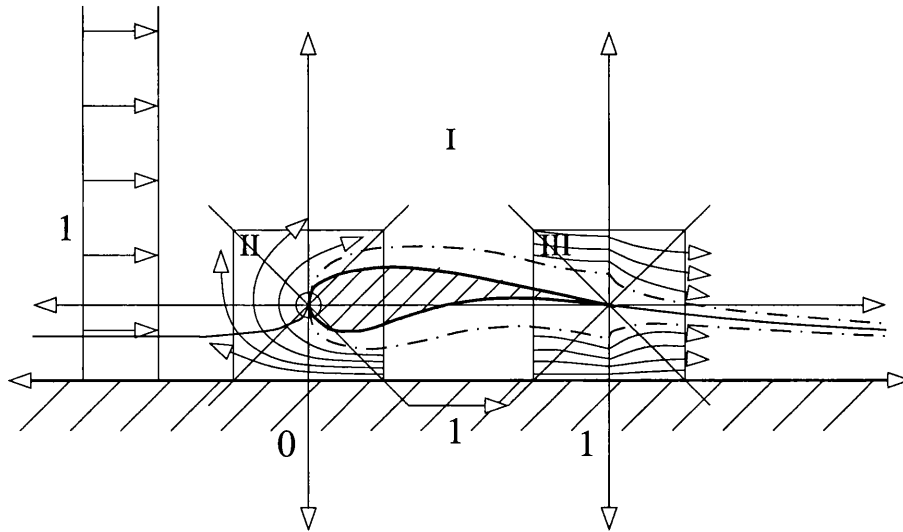
Figure 3.2: The 'around-the-edge' eigensolution which is permitted only at the leading edge (II) and the streamlined non-eigensolution which may occur at either the trailing edge (III) or the leading edge.

3.2   Problem Formulation

The earlier analysis of section 2.3 is valid for all $\beta > 0$ and so there is no need to return to the original governing (Cauchy-Riemann) partial differential equations. Instead we may take the coupled integral equations (2.33) and (2.34) as our starting point. As before these integral equations must be solved in order to complete the boundary conditions before the perturbations $p(x, y)$, $v(x, y)$, and $u(x, y)$ can be evaluated using equations (2.28), (2.29), and (2.30) respectively. This must be done for both large and small β. The complete flow solution can then be obtained to first order using the perturbation expansions (2.4), (2.5), and (2.6).

3.3   Mathematical Methods

The method used to develop these asymptotic solutions is outlined below. The integral equations are of convolution type and are therefore easily Fourier transformed using the convolution theorem. The transformed kernels, which contain β explicitly, are then expanded for large or small β and the transforms $\widehat{\langle v \rangle}(k)$, $\widehat{[v]}(k)$, $\widehat{\langle p \rangle}(k)$, and $\widehat{[p]}(k)$ are replaced by their asymptotic expansions in the relevant limit. Equations at each order are then separated out and inverse Fourier transformed. The proper boundary conditions are then imposed in real-space and the simplified set of equations is solved subject to them.

This method works well but relies on the fact that no non-trivial manipulations are carried out in Fourier space. A non-trivial manipulation in Fourier space would constitute the inversion or introduction of an integral operator in real space.

3.3.1   Fourier Transforming the Integral Equations

We begin with the coupled system of integral equations (2.33) and (2.34) derived earlier, in Chapter 2. At this stage no boundary conditions have been imposed and

the above equations are valid for all $\beta > 0$. We notice that the integrals appearing in equations (2.33) and (2.34) are of convolution type and can be Fourier transformed easily using the convolution theorem. We define the Fourier transform $\widehat{f}(k)$ of a function $f(x)$ to be

$$\widehat{f}(k) \;=\; \int\limits_{-\infty}^{\infty} f(x)\, e^{+ikx} dx, \tag{3.1}$$

and remind ourselves of the convolution theorem in the form

$$\int\limits_{-\infty}^{\infty} e^{+ikx} \left(\int\limits_{-\infty}^{+\infty} f(x - \xi)\, g(\xi)\, d\xi \right) dx \;=\; \widehat{f}(k)\,\widehat{g}(k). \tag{3.2}$$

The transforms are performed and the integral equations (2.33) and (2.34) become

$$\widehat{\langle v \rangle}(k) \;=\; e^{-\beta|k|}\,\widehat{[v]}(k) + i\,\mathrm{sgn}(k)\left(1 - e^{-\beta|k|}\right) \widehat{[p]}(k), \tag{3.3}$$

$$\widehat{\langle p \rangle}(k) \;=\; -i\,\mathrm{sgn}(k)\left(1 + e^{-\beta|k|}\right) \widehat{[v]}(k) - e^{-\beta|k|}\,\widehat{[p]}(k), \tag{3.4}$$

respectively, in Fourier space, where we have made use of the integral identities

$$\frac{1}{\pi} \int\limits_{-\infty}^{+\infty} \frac{e^{+ikx}}{x}\, dx \;=\; i\,\mathrm{sgn}(k), \tag{3.5}$$

$$\frac{1}{\pi} \int\limits_{-\infty}^{+\infty} \frac{x}{x^2 + \beta^2}\, e^{+ikx} dx \;=\; i\,\mathrm{sgn}(k)\, e^{-\beta|k|}, \tag{3.6}$$

$$\frac{1}{\pi} \int\limits_{-\infty}^{+\infty} \frac{\beta}{x^2 + \beta^2}\, e^{+ikx} dx \;=\; e^{-\beta|k|}, \tag{3.7}$$

when transforming the kernels.

Upon examination of equations (3.3) and (3.4) we notice that the terms involving β explicitly are relatively easy to understand for large and small values of the ground-clearance parameter β and therefore these equations can be used to develop asymptotic solutions for $\beta \gg 1$ and $\beta \ll 1$.

3.4 Flying High $(\beta \gg 1)$

For $\beta \gg 1$ we seek a solution in Fourier space of the form

$$\widehat{[v]}(k) = \widehat{[v]}_0(k) + \beta^{-1}\widehat{[v]}_1(k) + \cdots, \tag{3.8}$$

$$\widehat{\langle v \rangle}(k) = \widehat{\langle v \rangle}_0(k) + \beta^{-1}\widehat{\langle v \rangle}_1(k) + \cdots, \tag{3.9}$$

$$\widehat{[p]}(k) = \widehat{[p]}_0(k) + \beta^{-1}\widehat{[p]}_1(k) + \cdots, \tag{3.10}$$

$$\widehat{\langle p \rangle}(k) = \widehat{\langle p \rangle}_0(k) + \beta^{-1}\widehat{\langle p \rangle}_1(k) + \cdots, \tag{3.11}$$

for no other reason than we expect β^{-1} to be small compared with unity for $\beta \gg 1$.

The kernels in equations (3.3) and (3.4) are expanded as follows

$$e^{-\beta|k|} = 2\beta^{-1}\delta(k) + \cdots, \tag{3.12}$$

$$\left(1 + e^{-\beta|k|}\right) = 1 + 2\beta^{-1}\delta(k) + \cdots, \tag{3.13}$$

$$\left(1 - e^{-\beta|k|}\right) = 1 - 2\beta^{-1}\delta(k) + \cdots, \tag{3.14}$$

since we can define the Dirac delta function $\delta(k)$ as the limiting form of the function $\frac{\beta}{2}e^{-\beta|k|}$ as $\beta \to \infty$.

Upon substitution of these asymptotic expansions into equations (3.3) and (3.4) we obtain at leading order

$$\widehat{\langle v \rangle}_0(k) = i sgn(k)\,\widehat{[p]}_0(k), \tag{3.15}$$

$$\widehat{\langle p \rangle}_0(k) = -i sgn(k)\,\widehat{[v]}_0(k), \tag{3.16}$$

and at next order

$$\widehat{\langle v \rangle}_1(k) = 2\delta(k)\left(\widehat{[v]}_0(k) - \widehat{\langle v \rangle}_0(k)\right) + i sgn(k)\,\widehat{[p]}_1(k), \tag{3.17}$$

$$\widehat{\langle p \rangle}_1(k) = 2\delta(k)\left(\widehat{\langle p \rangle}_0(k) - \widehat{[p]}_0(k)\right) - i sgn(k)\,\widehat{[v]}_1(k). \tag{3.18}$$

Having simplified the problem in Fourier space we now inverse Fourier transform these equations so that we can impose the relevant boundary conditions in real

space. This yields at leading order

$$\langle v \rangle_0 (x) = -\frac{1}{\pi} \fint_0^1 \frac{[p]_0 (\xi)}{(\xi - x)} d\xi, \tag{3.19}$$

$$\langle p \rangle_0 (x) = \frac{1}{\pi} \fint_{-\infty}^{+\infty} \frac{[v]_0 (\xi)}{(\xi - x)} d\xi, \tag{3.20}$$

and at next order

$$\langle v \rangle_1 (x) = A - \frac{1}{\pi} \fint_0^1 \frac{[p]_1 (\xi)}{(\xi - x)} d\xi, \tag{3.21}$$

$$\langle p \rangle_1 (x) = B + \frac{1}{\pi} \fint_{-\infty}^{+\infty} \frac{[v]_1 (\xi)}{(\xi - x)} d\xi, \tag{3.22}$$

where

$$A = \frac{1}{\pi} \int_{-\infty}^{+\infty} \left([v]_0 (x) - \langle v \rangle_0 (x) \right) dx, \tag{3.23}$$

$$B = \frac{1}{\pi} \int_{-\infty}^{+\infty} \left(\langle p \rangle_0 (x) - [p]_0 (x) \right) dx, \tag{3.24}$$

and the pressure continuity condition $[p]_i (x) = 0$ for $x \notin [0, 1]$ has been imposed at each order.

3.4.1 The Leading Order Solution for $\beta \gg 1$

The leading order integral equations (3.19) and (3.20) are now solved. We must first obtain the pressure difference across the aerofoil $[p]_0 (x)$ in the interval $x \in [0, 1]$. In order to do this we consider the first integral equation (3.19) for $x \in [0, 1]$ and invert it subject to the constraint $[p]_0 (1) = 0$.

We have already encountered and solved this problem in subsection 2.3.3 and using the result stated there we may write down the following expression for the leading order pressure difference $[p]_0 (x)$ in the interval $x \in [0, 1]$.

$$[p]_0 (x) = \frac{1}{\pi} \sqrt{\frac{1 - x}{x}} \fint_0^1 \sqrt{\frac{\xi}{1 - \xi}} \frac{\langle v \rangle_0 (\xi)}{(\xi - x)} d\xi. \tag{3.25}$$

As the differences $[v]_0 (x)$ and $[p]_0 (x)$ are now determined for all x we can obtain the sums $\langle v \rangle_0 (x)$ and $\langle p \rangle_0 (x)$ explicitly by using equations (3.19) and (3.20) respectively. The leading order boundary conditions are then complete and take the form

$$[v]_0 (x) = \begin{cases} 0 & \text{for} \quad x \in (-\infty, 0) \\ t'(x) + 2\delta_b'(x) & \text{for} \quad x \in [0, 1] \\ 2\delta_g'(x) & \text{for} \quad x \in (1, +\infty) \end{cases}, \tag{3.26}$$

$$\langle v \rangle_0 (x) = \begin{cases} 2c'(x) & \text{for} \quad x \in [0, 1] \\ -\frac{1}{\pi} \fint_0^1 \frac{[p]_0(\xi)}{(\xi - x)} d\xi & \text{for} \quad x \notin [0, 1] \end{cases}, \tag{3.27}$$

$$[p]_0 (x) = \begin{cases} \frac{1}{\pi} \sqrt{\frac{1-x}{x}} \fint_0^1 \sqrt{\frac{\xi}{1-\xi}} \frac{\langle v \rangle_0(\xi)}{(\xi - x)} d\xi & \text{for} \quad x \in [0, 1] \\ 0 & \text{for} \quad x \notin [0, 1] \end{cases}, \tag{3.28}$$

$$\langle p \rangle_0 (x) = \begin{cases} \frac{1}{\pi} \fint_{-\infty}^{+\infty} \frac{[v]_0(\xi)}{(\xi - x)} d\xi & \text{for} \quad x \in [0, 1] \\ \frac{1}{\pi} \fint_{-\infty}^{+\infty} \frac{[v]_0(\xi)}{(\xi - x)} d\xi & \text{for} \quad x \notin [0, 1] \end{cases}, \tag{3.29}$$

The above boundary conditions are exactly those we would obtain if we were to the consider the flow past a thin aerofoil in the absence of the ground. Therefore at leading order the aerofoil does not feel the presence of the ground at all.

We can see this fact more clearly if we remove all non-symmetry from the aerofoil shape and consider an aerofoil with no camber at zero angle of attack. For such an aerofoil $c(x) \equiv 0$ and as a result equations (3.27) and (3.28) tell us that $\langle v \rangle_0 (x) = 0$ and $[p]_0 (x) = 0$ for all x. This simplifies matters considerably and we are left with the relations

$$v_{0\pm} (x) = \begin{cases} \pm\frac{1}{2} t'(x) \pm \delta_b'(x) & \text{for} \quad x \in [0, 1] \\ \pm\delta_g'(x) & \text{for} \quad x \notin [0, 1] \end{cases}, \tag{3.30}$$

$$p_{0\pm} (x) = \pm\frac{1}{\pi} \fint_{-\infty}^{+\infty} \frac{v_{0\pm}(\xi)}{(\xi - x)} d\xi \quad \text{for all } x \quad, \tag{3.31}$$

in terms of the transverse velocity and pressure boundary conditions above and below the aerofoil. These relations are clearly recognisable as those which we would

obtain if we were to consider the flow past a symmetric aerofoil at zero angle of attack in the absence of the ground. See Sedov (1965).

3.4.2 The Next Order Correction for $\beta \gg 1$

The integral equations encountered at next order are very similar to those encountered at leading order and we can calculate the corrections to the boundary conditions using the same method as was used at leading order. We obtain the corrections in the form

$$[v]_1(x) = \begin{cases} 0 & \text{for} \quad x \in [0,1] \\ 0 & \text{for} \quad x \notin [0,1] \end{cases}, \tag{3.32}$$

$$\langle v \rangle_1(x) = \begin{cases} 0 & \text{for} \quad x \in [0,1] \\ A - \frac{1}{\pi} \int_0^1 \frac{[p]_1(\xi)}{(\xi-x)} d\xi & \text{for} \quad x \notin [0,1] \end{cases}, \tag{3.33}$$

$$[p]_1(x) = \begin{cases} -\frac{A}{\pi}\sqrt{\frac{1-x}{x}} \int_0^1 \sqrt{\frac{\xi}{1-\xi}} \frac{d\xi}{(\xi-x)} & \text{for} \quad x \in [0,1] \\ 0 & \text{for} \quad x \notin [0,1] \end{cases}, \tag{3.34}$$

$$\langle p \rangle_1(x) = \begin{cases} B & \text{for} \quad x \in [0,1] \\ B & \text{for} \quad x \notin [0,1] \end{cases}. \tag{3.35}$$

The displacement effects which drive the flow at leading order are no longer present at next order; however the leading order boundary conditions appear via the constants A and B and drive the flow correction in this way. The effect of the constant term A is to add a virtual angle of attack to the aerofoil, giving rise to non-symmetric boundary conditions even when symmetric aerofoils at zero angle of attack are considered. Because of this, the flow correction at order β^{-1} represents the leading order ground effect for $\beta \gg 1$.

3.5 Flying Low $(\beta \ll 1)$

Here we examine the character and structure of the solution for $\beta \ll 1$, that being the case where the aerofoil is travelling just above the ground well within 'ground-effect'. The solution is first considered on the global, order one, length scale and the approach adopted in the large β case is used once again to complete the boundary conditions at each order. However in this case we are forced to introduce arbitrary constants into the boundary conditions at each order and so the boundary conditions remain incomplete.

In order to determine these constants the solution in scaled regions around the leading and trailing edges must be considered. Two types of edge flow are identified, as described earlier, and the issue of which type is required at the leading and trailing edges is discussed in detail at each order.

Once again we take as our starting point the Fourier transformed versions of the integral equations (2.33) and (2.34), namely (3.3) and (3.4). The next stage, as before, is to develop asymptotic expansions for the kernels, which contain β explicitly, and the unknown transforms $\widehat{[v]}\,(k)$, $\widehat{\langle v \rangle}\,(k)$, $\widehat{[p]}\,(k)$, and $\widehat{\langle p \rangle}\,(k)$. The kernels are expanded as

$$e^{-\beta|k|} \;=\; 1 - \beta\,|k| + \frac{1}{2}\beta^2\,|k|^2 - \cdots + \cdots, \tag{3.36}$$

$$\left(1 + e^{-\beta|k|}\right) \;=\; 2 - \beta\,|k| + \frac{1}{2}\beta^2\,|k|^2 - \cdots + \cdots, \tag{3.37}$$

$$\left(1 - e^{-\beta|k|}\right) \;=\; \beta\,|k| - \frac{1}{2}\beta^2\,|k|^2 + \cdots - \cdots, \tag{3.38}$$

these expansions being valid for $\beta \ll 1$ and for moderate wave number k.

The important feature to notice in the above expansions is the fact that the leading order term in the last expansion appearing immediately above is of order β. Therefore in order for the product $\left(1 - e^{-\beta|k|}\right)\widehat{[p]}\,(k)$ in equation (3.3) to remain of order one, and produce a non-trivial balance, the Fourier transform of the pressure difference, $\widehat{[p]}\,(k)$, must scale like β^{-1}. Since it is this pressure difference which gives

rise to the lift on the aerofoil this scaling argument explains how the large increase in lift, associated with wing-in-ground effect flight, is produced and quantifies the trend observed in the small β solutions presented in section 2.5. With this scaling argument in mind the following asymptotic expansions for $\widehat{[v]}(k)$, $\widehat{\langle v \rangle}(k)$, $\widehat{[p]}(k)$, and $\widehat{\langle p \rangle}(k)$ were written down.

$$\widehat{[v]}(k) = \widehat{[v]}_0(k) + \beta^f \widehat{[v]}_f(k) + \beta \widehat{[v]}_1(k) + \cdots, \tag{3.39}$$

$$\widehat{\langle v \rangle}(k) = \widehat{\langle v \rangle}_0(k) + \beta^f \widehat{\langle v \rangle}_f(k) + \beta \widehat{\langle v \rangle}_1(k) + \cdots, \tag{3.40}$$

$$\widehat{[p]}(k) = \beta^{-1} \widehat{[p]}_0(k) + \beta^{f-1} \widehat{[p]}_f(k) + \widehat{[p]}_1(k) + \cdots, \tag{3.41}$$

$$\widehat{\langle p \rangle}(k) = \beta^{-1} \widehat{\langle p \rangle}_0(k) + \beta^{f-1} \widehat{\langle p \rangle}_f(k) + \widehat{\langle p \rangle}_1(k) + \cdots, \tag{3.42}$$

where $f \in (0, 1)$ is an unknown fraction which must be determined as part of the solution.

The 'in-between' terms in the above expansions involving f are included since it is foreseen that non-integer powers of β will be forced to appear in the asymptotic expansions. It turns out that, in the example we consider, two such in-between terms are needed but since these terms do not interfere with each other or with the other terms in the expansions the inclusion of only the one generic term is sufficient.

The asymptotic expansions (3.36)-(3.42) are introduced into the Fourier transformed integral equations (3.3) and (3.4) and equations at each order are separated out. After some simplification we obtain at leading order

$$\widehat{\langle v \rangle}_0(k) = \widehat{[v]}_0(k) + ik \widehat{[p]}_0(k), \tag{3.43}$$

$$\widehat{\langle p \rangle}_0(k) = -\widehat{[p]}_0(k), \tag{3.44}$$

at in-between order

$$\widehat{\langle v \rangle}_f(k) = \widehat{[v]}_f(k) + ik \widehat{[p]}_f(k), \tag{3.45}$$

$$\widehat{\langle p \rangle}_f(k) = -\widehat{[p]}_f(k), \tag{3.46}$$

and at next order

$$\widehat{\langle v \rangle}_1 (k) = -\frac{|k|}{2} \left(\widehat{\langle v \rangle}_0 (k) + \widehat{[v]}_0 (k) \right) + \widehat{[v]}_1 (k) + ik \widehat{[p]}_1 (k), \qquad (3.47)$$

$$\widehat{\langle p \rangle}_1 (k) = -isgn(k) \left(\widehat{\langle v \rangle}_0 (k) + \widehat{[v]}_0 (k) \right) - \widehat{[p]}_1 (k). \qquad (3.48)$$

Notice that at the in-between order the equations are completely un-coupled from the equations at the other orders. The simplified equations (3.43)-(3.48) are now inverse Fourier transformed in order that the proper boundary conditions may be imposed in real-space.

We obtain at leading order

$$\langle v \rangle_0 (x) = [v]_0 (x) - [p]_0' (x), \qquad (3.49)$$

$$\langle p \rangle_0 (x) = - [p]_0 (x), \qquad (3.50)$$

at in-between order

$$\langle v \rangle_f (x) = [v]_f (x) - [p]_f' (x), \qquad (3.51)$$

$$\langle p \rangle_f (x) = - [p]_f (x), \qquad (3.52)$$

and at next order

$$\langle v \rangle_1 (x) = [v]_1 (x) - [p]_1' (x) + \frac{1}{2} A' (x), \qquad (3.53)$$

$$\langle p \rangle_1 (x) = - [p]_1 (x) + A (x), \qquad (3.54)$$

where in the above $A(x)$ is defined as

$$A (x) = \frac{1}{\pi} \int_{-\infty}^{+\infty} \frac{\langle v \rangle_0 (\xi) + [v]_0 (\xi)}{(\xi - x)} d\xi = \frac{2}{\pi} \int_{-\infty}^{+\infty} \frac{v_{0+} (\xi)}{(\xi - x)} d\xi, \qquad (3.55)$$

and prime denotes differentiation with respect to argument. These equations are now solved at each order in turn.

3.5.1 The Leading Order Solution for $\beta \ll 1$

The leading order boundary conditions are completed by solving the coupled system of equations (3.49) and (3.50) subject to the boundary conditions (2.35)–(2.38) given

in section 2.3.3. The leading order pressure difference across the aerofoil $[p]_0(x)$ in the interval $x \in [0,1]$ is obtained first by simply integrating and rearranging equation (3.49) to give

$$[p]_0(x) = [p]_0(0) - \int_0^x (\langle v \rangle_0(\xi) - [v]_0(\xi))\, d\xi, \qquad (3.56)$$

where $[p]_0(0)$ is a constant of integration and is unknown at this stage.

The other unknowns, $\langle v \rangle_0(x)$ and $\langle p \rangle_0(x)$, are then obtained from equations (3.49) and (3.50) directly. The completed leading order boundary conditions in terms of the sums and differences $\langle v \rangle_0(x)$, $[v]_0(x)$, $\langle p \rangle_0(x)$, and $[p]_0(x)$ are

$$[v]_0(x) = \begin{cases} 0 & \text{for } x \in (-\infty, 0) \\ t'(x) + 2\delta_b'(x) & \text{for } x \in [0,1] \\ 2\delta_g'(x) & \text{for } x \in (1, +\infty) \end{cases}, \qquad (3.57)$$

$$\langle v \rangle_0(x) = \begin{cases} 2c'(x) & \text{for } x \in [0,1] \\ [v]_0(x) & \text{for } x \notin [0,1] \end{cases}, \qquad (3.58)$$

$$[p]_0(x) = \begin{cases} [p]_0(0) - \int_0^x (\langle v \rangle_0(\xi) - [v]_0(\xi))\, d\xi & \text{for } x \in [0,1] \\ 0 & \text{for } x \notin [0,1] \end{cases}, \qquad (3.59)$$

$$\langle p \rangle_0(x) = \begin{cases} -[p]_0(x) & \text{for } x \in [0,1] \\ 0 & \text{for } x \notin [0,1] \end{cases}, \qquad (3.60)$$

Using equations (2.40) and (2.41) we can write the above result in the more familiar terms of the leading order transverse velocity boundary values $v_{0\pm}(x)$ and pressure boundary values $p_{0\pm}(x)$. We obtain

$$v_{0+}(x) = \begin{cases} 0 & \text{for } x \in (-\infty, 0) \\ c'(x) + \frac{1}{2}t'(x) + \delta_b'(x) & \text{for } x \in [0,1] \\ 2\delta_g'(x) & \text{for } x \in (1, +\infty) \end{cases}, \qquad (3.61)$$

$$v_{0-}(x) = \begin{cases} c'(x) - \frac{1}{2}t'(x) - \delta_b'(x) & \text{for } x \in [0,1] \\ 0 & \text{for } x \notin [0,1] \end{cases}, \qquad (3.62)$$

$$p_{0+}(x) = \left\{ \begin{array}{ll} 0 & \text{for} \quad x \in [0,1] \\ 0 & \text{for} \quad x \notin [0,1] \end{array} \right\}, \tag{3.63}$$

$$p_{0-}(x) = \left\{ \begin{array}{ll} p_{0-}(0) + 2\delta_-(x) & \text{for} \quad x \in [0,1] \\ 0 & \text{for} \quad x \notin [0,1] \end{array} \right\}, \tag{3.64}$$

where $+$ and $-$ denote quantities above and below the aerofoil respectively and $\delta_-(x)$ is defined in equation (2.17).

It is now possible to identify the major features of the flow solution, as highlighted in section (2.5). Since $v_{0-}(x) = 0$ outside the interval $x \in [0,1]$ no fluid is drawn into the thin wake from below at leading order and this gives rise to the flat shape of $\delta_-(x)$ in the wake as seen, for small α, in Figure 2.11. Also, the pressure at the underside of the aerofoil is the only non-zero pressure at leading order and takes a simple form which directly reflects the underside-shape of the aerofoil including its boundary layer displacement thickness. This pressure solution still contains an unknown constant $p_{0-}(0)$ whose value has the potential to greatly influence the lift.

3.5.2 The In-Between Order Solution for $\beta \ll 1$

The governing equations at in-between order are (3.51) and (3.52) and are identical to those at leading order, however, the displacement effects which drive the solution at leading order are no longer present and we obtain the very simple solution

$$[v]_f(x) = \left\{ \begin{array}{ll} 0 & \text{for} \quad x \in [0,1] \\ 0 & \text{for} \quad x \notin [0,1] \end{array} \right\}, \tag{3.65}$$

$$\langle v \rangle_f(x) = \left\{ \begin{array}{ll} 0 & \text{for} \quad x \in [0,1] \\ 0 & \text{for} \quad x \notin [0,1] \end{array} \right\}, \tag{3.66}$$

$$[p]_f(x) = \left\{ \begin{array}{ll} [p]_f(0) & \text{for} \quad x \in [0,1] \\ 0 & \text{for} \quad x \notin [0,1] \end{array} \right\}, \tag{3.67}$$

$$\langle p \rangle_f(x) = \left\{ \begin{array}{ll} -[p]_f(0) & \text{for} \quad x \in [0,1] \\ 0 & \text{for} \quad x \notin [0,1] \end{array} \right\}, \tag{3.68}$$

which leaves $p_{f-}(x)$ as the only non-zero quantity, namely

$$p_{f-}(x) = \left\{ \begin{array}{ll} p_{f-}(0) & \text{for } x \in [0,1] \\ 0 & \text{for } x \notin [0,1] \end{array} \right\}. \tag{3.69}$$

Again $p_{f-}(0)$ is an unknown constant. Thus the leading order pressure solution beneath the aerofoil may be translated upwards or downwards an 'in-between' order amount depending on the sign of $p_{f-}(0)$. This may have a significant effect on the lift produced.

3.5.3   The Next Order Correction for $\beta \ll 1$

The governing equations at next order, (3.53) and (3.54), are again very similar to those at leading order except for the inclusion of the function $A(x)$ defined in equation (3.55). The displacement effects are again absent at this order however the leading order displacements appear through $A(x)$ and thus drive the first non-zero pressure response on top of the aerofoil and in the bulk of the fluid. The completed boundary conditions take the form

$$[v]_1(x) = \left\{ \begin{array}{ll} 0 & \text{for } x \in [0,1] \\ 0 & \text{for } x \notin [0,1] \end{array} \right\}, \tag{3.70}$$

$$\langle v \rangle_1(x) = \left\{ \begin{array}{ll} 0 & \text{for } x \in [0,1] \\ \frac{1}{2}A'(x) & \text{for } x \notin [0,1] \end{array} \right\}, \tag{3.71}$$

$$[p]_1(x) = \left\{ \begin{array}{ll} [p]_1(0) + \frac{1}{2}(A(x) - A(0)) & \text{for } x \in [0,1] \\ 0 & \text{for } x \notin [0,1] \end{array} \right\}, \tag{3.72}$$

$$\langle p \rangle_1(x) = \left\{ \begin{array}{ll} -[p]_1(0) + \frac{1}{2}(A(x) + A(0)) & \text{for } x \in [0,1] \\ A(x) & \text{for } x \notin [0,1] \end{array} \right\}. \tag{3.73}$$

In terms of quantities above and below the aerofoil the above results become

$$v_{1+}(x) = \left\{ \begin{array}{ll} 0 & \text{for } x \in [0,1] \\ \frac{1}{4}A'(x) & \text{for } x \notin [0,1] \end{array} \right\}, \tag{3.74}$$

$$v_{1-}(x) = \left\{ \begin{array}{ll} 0 & \text{for } x \in [0,1] \\ \frac{1}{4}A'(x) & \text{for } x \notin [0,1] \end{array} \right\}, \qquad (3.75)$$

$$p_{1+}(x) = \left\{ \begin{array}{ll} \frac{1}{2}A(x) & \text{for } x \in [0,1] \\ \frac{1}{2}A(x) & \text{for } x \notin [0,1] \end{array} \right\}, \qquad (3.76)$$

$$p_{1-}(x) = \left\{ \begin{array}{ll} p_{1-}(0) & \text{for } x \in [0,1] \\ \frac{1}{2}A(x) & \text{for } x \notin [0,1] \end{array} \right\}, \qquad (3.77)$$

where $+$ and $-$ denote quantities above and below the aerofoil respectively. Again the pressure beneath the aerofoil is an unknown constant $p_{1-}(0)$.

3.6 Edge Flows

To set the unknown constants $p_{0-}(0)$, $p_{f-}(0)$, $p_{1-}(0)$, and indeed the index f itself in the global solutions just presented we must consider the flow solution within small scaled regions around the leading and trailing edges. The edge solutions fall into two distinct categories. The forced non-eigensolutions which are induced by displacement effects associated with the presence of the aerofoil and its boundary layers and the unforced eigensolutions which satisfy homogeneous transverse velocity boundary conditions. The non-eigensolutions represent 'streamlined' edge flows, whereas the eigensolutions do not and are therefore not permitted at the trailing edge according to the Kutta condition.

These two very different types of solution share one important property, the fact that they can support a large, non-zero pressure beneath the aerofoil and smoothly join this pressure with the smaller pressures in the bulk of the fluid. We will begin by considering the general eigen and non-eigen solutions in isolation before discussing in detail where these solutions occur and how their presence determines the unknown constants $p_{0-}(0)$, $p_{f-}(0)$, and $p_{1-}(0)$ in the global solution.

3.6.1   The Trailing Edge Non-Eigensolution

The non-eigensolution is usually encountered at the trailing edge and so we will construct our solution around a trailing edge geometry. We begin by introducing the local coordinate $X = (x - 1)/\beta$, the scaled wavenumber $K = \beta k$, and the local unknown sums and differences

$$\widehat{[V]}(K) = \widehat{[v]}(k), \tag{3.78}$$

$$\widehat{\langle V\rangle}(K) = \widehat{\langle v\rangle}(k), \tag{3.79}$$

$$\widehat{[P]}(K) = \widehat{[p]}(k), \tag{3.80}$$

$$\widehat{\langle P\rangle}(K) = \widehat{\langle p\rangle}(k), \tag{3.81}$$

where capitals letters are used to denote local quantities. Again taking the Fourier transformed integral equations (3.3) and (3.4) as our starting point we write these in terms of the local quantities above to give

$$\widehat{\langle V\rangle}(K) = e^{-|K|}\widehat{[V]}(K) + i sgn(K)\left(1 - e^{-|K|}\right)\widehat{[P]}(K), \tag{3.82}$$

$$\widehat{\langle P\rangle}(K) = -i sgn(K)\left(1 + e^{-|K|}\right)\widehat{[V]}(K) - e^{-|K|}\widehat{[P]}(K). \tag{3.83}$$

We notice that β is explicitly absent from these equations and no simplification can be made for $\beta \ll 1$. Also, equation (3.82) forces the velocity sum and difference transforms, $\widehat{\langle V\rangle}(K)$ and $\widehat{[V]}(K)$, to balance the pressure difference transform, $\widehat{[P]}(K)$ which is of order β^{-1} at leading order. With this in mind we write down the asymptotic expansions

$$\widehat{[V]}(K) = \beta^{-1}\widehat{[V]}_0(K) + \beta^{f-1}\widehat{[V]}_f(K) + \widehat{[V]}_1(K) + \cdots, \tag{3.84}$$

$$\widehat{\langle V\rangle}(K) = \beta^{-1}\widehat{\langle V\rangle}_0(K) + \beta^{f-1}\widehat{\langle V\rangle}_f(K) + \widehat{\langle V\rangle}_1(K) + \cdots, \tag{3.85}$$

$$\widehat{[P]}(K) = \beta^{-1}\widehat{[P]}_0(K) + \beta^{f-1}\widehat{[P]}_f(K) + \widehat{[P]}_1(K) + \cdots, \tag{3.86}$$

$$\widehat{\langle P\rangle}(K) = \beta^{-1}\widehat{\langle P\rangle}_0(K) + \beta^{f-1}\widehat{\langle P\rangle}_f(K) + \widehat{\langle P\rangle}_1(K) + \cdots, \tag{3.87}$$

to ensure that this balance is possible at every order. As expected substitution of these expansions into (3.82) and (3.83) yields the same equations at every order and

inverse Fourier transforming gives, as we might expect, the integral equations

$$\langle V \rangle (X) = \frac{1}{\pi} \int_{-\infty}^{+\infty} L(\xi - X) [V](\xi) d\xi - \frac{1}{\pi} \fint_{-\infty}^{+\infty} \left(\frac{1}{(\xi - X)} - M(\xi - X) \right) [P](\xi) d\xi,$$

(3.88)

$$\langle P \rangle (X) = \frac{1}{\pi} \fint_{-\infty}^{+\infty} \left(\frac{1}{(\xi - X)} + M(\xi - X) \right) [V](\xi) d\xi - \frac{1}{\pi} \int_{-\infty}^{+\infty} L(\xi - X) [P](\xi) d\xi,$$

(3.89)

$$\text{where} \quad L(X) = \frac{1}{X^2 + 1} \quad \text{and} \quad M(X) = \frac{X}{X^2 + 1},$$

which must be solved subject to mixed boundary conditions of the form

$$[V](X) = \left\{ \begin{array}{ll} [V](X) & \text{for} \quad X \in (-\infty, 0] \\ [V](X) & \text{for} \quad X \in (0, +\infty) \end{array} \right\},$$

(3.90)

$$\langle V \rangle (X) = \left\{ \begin{array}{ll} \langle V \rangle (X) & \text{for} \quad X \in (-\infty, 0] \\ ? & \text{for} \quad X \in (0, +\infty) \end{array} \right\},$$

(3.91)

$$[P](X) = \left\{ \begin{array}{ll} ? & \text{for} \quad X \in (-\infty, 0] \\ 0 & \text{for} \quad X \in (0, +\infty) \end{array} \right\},$$

(3.92)

$$\langle p \rangle (X) = \left\{ \begin{array}{ll} ? & \text{for} \quad X \in (-\infty, 0] \\ ? & \text{for} \quad X \in (0, +\infty) \end{array} \right\},$$

(3.93)

where subscripts have been dropped on the understanding that this general edge problem must be solved at every order.

It seems as if we are back where we started! On the other hand, β is now absent from the integral equations (3.88) and (3.89) and the *half range* boundary conditions (3.90)-(3.93) are easier to deal with than those encountered in the global problem. The Wiener-Hopf technique is now employed to solve the general edge flow problem above. The technique makes extensive use of half-range Fourier transforms and we will first derive some basic results regarding these before completing the task of finding the solution.

Half-Range Functions

The boundary condition (3.92) for the pressure difference $[P](X)$ suggests that half-range functions, which are zero on a given half-line and non-zero on the other half-line, will form a fundamental part of the solution. Such functions will be termed '+' functions if they are non-zero on the positive half-line, '−' functions if they are non-zero on the negative half-line, and as such will be denoted $F(X)_+$ and $F(X)_-$ respectively.

As an example, the simplest + and − functions are the unit step functions

$$S(X)_+ = \left\{ \begin{array}{ll} 0 & \text{for} \quad X \in (-\infty, 0] \\ 1 & \text{for} \quad X \in (0, +\infty) \end{array} \right\}, \tag{3.94}$$

$$S(X)_- = \left\{ \begin{array}{ll} 1 & \text{for} \quad X \in (-\infty, 0] \\ 0 & \text{for} \quad X \in (0, +\infty) \end{array} \right\}. \tag{3.95}$$

Given a function $F(X)$ defined on the real line we can construct the functions $F(X)_\pm$ using the step functions $S(X)_\pm$ to obtain

$$F(X)_+ = \left(F(X) S(X)_+ \right)_+, \tag{3.96}$$

$$F(X)_- = \left(F(X) S(X)_- \right)_-. \tag{3.97}$$

These + and − functions also satisfy the additional relation

$$F(X) = F(X)_+ + F(X)_-. \tag{3.98}$$

The pressure difference $[P](X)$ is of course a − function and as such will be denoted $[P](X)_-$ from now on.

Half-Range Fourier Transforms

As the Wiener-Hopf technique relies heavily on the use of Fourier transforms it is essential to be able to Fourier transform these + and − functions. We therefore

introduce the half-range Fourier transforms

$$\widehat{F}(K)_+ = \int\limits_{-\infty}^{+\infty} F(X)_+ e^{+iKX} dX = \int\limits_{0}^{+\infty} F(X) e^{+iKX} dX, \qquad (3.99)$$

$$\widehat{F}(K)_- = \int\limits_{-\infty}^{+\infty} F(X)_- e^{+iKX} dX = \int\limits_{-\infty}^{0} F(X) e^{+iKX} dX. \qquad (3.100)$$

It should be pointed out that $\widehat{F}(K)_+$ is not a $+$ function itself, but is the Fourier transform of a $+$ function and as such is labelled with a plus sign. The functions $\widehat{F}(K)_\pm$ do have certain analyticity properties when viewed as functions of a complex variable and the reader is referred to Noble (1958) for a detailed account.

These half-range transforms also satisfy the additional relation

$$\widehat{F}(K) = \widehat{F}(K)_+ + \widehat{F}(K)_-, \qquad (3.101)$$

where $\widehat{F}(K)$ is the full-range Fourier transform of $F(X)$ defined by equation (3.1). Decompositions of this sort are fundamental to the Wiener-Hopf technique and we will now investigate how they are constructed in general.

Sum Decompositions

As we have seen it is trivial to perform sum decompositions of the type $F(X) = F(X)_+ + F(X)_-$ in real space. In Fourier space it is not so easy to see what the decomposition should be. We can however transform equations (3.96) and (3.97) directly, using the convolution theorem in reverse, to obtain the corresponding sum decomposition formulae in Fourier space, namely

$$\widehat{F}(K)_+ = \frac{1}{2}\left[\widehat{F}(K) + \frac{1}{\pi i}\int\limits_{-\infty}^{+\infty} \frac{\widehat{F}(\kappa)}{(\kappa - K)} d\kappa\right], \qquad (3.102)$$

$$\widehat{F}(K)_- = \frac{1}{2}\left[\widehat{F}(K) - \frac{1}{\pi i}\int\limits_{-\infty}^{+\infty} \frac{\widehat{F}(\kappa)}{(\kappa - K)} d\kappa\right], \qquad (3.103)$$

where we have used the identities

$$\int\limits_{-\infty}^{+\infty} S(X)_\pm e^{+iKX} dX = \pi\delta(K) \pm \frac{i}{K}, \qquad (3.104)$$

when transforming the step functions.

Equations (3.102) and (3.103) are the Plemelj formulae, from the theory of complex functions, and they describe the limiting value of a sectionally holomorphic function as approached from either side of a given contour, in this case the real line. They allow us to write any Fourier transform $\widehat{F}(K)$ as a sum of $+$ and $-$ transforms

$$\widehat{F}(K) = \widehat{F}(K)_+ + \widehat{F}(K)_-, \tag{3.105}$$

without reference to functions in real space.

Product Decompositions

In certain circumstances we will also require a Fourier transform $\widehat{F}(K)$ to be decomposed into a product of $+$ and $-$ transforms, namely

$$\widehat{F}(K) = \widehat{F}(K)_+ \widehat{F}(K)_-. \tag{3.106}$$

As it stands we cannot perform this decomposition directly, however if we take the logarithm of the equation immediately above we obtain

$$\ln\left(\widehat{F}(K)\right) = \ln\left(\widehat{F}(K)_+\right)_+ + \ln\left(\widehat{F}(K)_-\right)_-, \tag{3.107}$$

which is a sum decomposition and can be performed using the Plemelj formulae, (3.102) and (3.103), applied to the function $\ln\left(\widehat{F}(K)\right)$. We obtain the result

$$\ln\left(\widehat{F}(K)_+\right)_+ = \frac{1}{2}\left[\ln\left(\widehat{F}(K)\right) + \frac{1}{\pi i}\int\limits_{-\infty}^{+\infty}\frac{\ln \widehat{F}(\kappa)}{(\kappa - K)}d\kappa\right], \tag{3.108}$$

$$\ln\left(\widehat{F}(K)_-\right)_- = \frac{1}{2}\left[\ln\left(\widehat{F}(K)\right) - \frac{1}{\pi i}\int\limits_{-\infty}^{+\infty}\frac{\ln \widehat{F}(\kappa)}{(\kappa - K)}d\kappa\right]. \tag{3.109}$$

Applying the exponential function to either side of the above equations yields the product decomposition formulae, namely

$$\widehat{F}(K)_+ = \widehat{F}(K)^{1/2}\exp\left\{+\frac{1}{2\pi i}\int\limits_{-\infty}^{+\infty}\frac{\ln \widehat{F}(\kappa)}{(\kappa - K)}d\kappa\right\}, \tag{3.110}$$

$$\widehat{F}(K)_- = \widehat{F}(K)^{1/2}\exp\left\{-\frac{1}{2\pi i}\int\limits_{-\infty}^{+\infty}\frac{\ln \widehat{F}(\kappa)}{(\kappa - K)}d\kappa\right\}. \tag{3.111}$$

There are restrictions on the use of the product decomposition formulae (3.110) and (3.111). They can only be used when the transform $\widehat{F}(K)$ has no zeros and tends to 1 as $K \to \pm\infty$. This ensures that $\ln \widehat{F}(K)$ is finite everywhere and tends to zero as $K \to \pm\infty$ thus keeping the above integrand well behaved.

The Wiener-Hopf Solution

Having dealt with the preliminary definitions we now have the tools we need to solve the integral equations (3.88) and (3.89). However before we begin we need to consider the behaviour of the pressure difference $[P](X)$ and the pressure sum $\langle P \rangle (X)$ more carefully. Since the trailing edge region exists in order to smoothly join the large pressures created beneath the aerofoil with the smaller pressures in the bulk of the fluid we expect the upstream pressure difference $[P](-\infty)$ and upstream pressure sum $\langle P \rangle (-\infty)$ to be non-zero constants $[P]_\infty$ and $\langle P \rangle_\infty$ respectively. This means that the pressure sum and difference do not satisfy the usual conditions required of functions which are to be Fourier transformed and special care must be taken when taking their transforms. To accommodate the unusual upstream behaviour we write $[P](X)_-$ and $\langle P \rangle (X)$ in the form

$$[P](X)_- = [P]^*(X)_- + [P]_\infty S(X)_-, \qquad (3.112)$$

$$\langle P \rangle (X) = \langle P \rangle^*(X) + \langle P \rangle_\infty S(X)_-, \qquad (3.113)$$

where $[P]^*(X)_-$ and $\langle P \rangle^*(X)$ tend to zero as $X \to \pm\infty$ and can therefore be Fourier transformed in the usual way. The function $S(X)_-$ appearing above is the unit step function as defined in equation (3.95). We are now free to Fourier transform the pressure sum and difference to obtain the results

$$\widehat{[P]}(K)_- = \widehat{[P]}^*(K)_- + [P]_\infty \left(\pi\delta(K) - \frac{i}{K} \right)_-, \qquad (3.114)$$

$$\widehat{\langle P \rangle}(K) = \widehat{\langle P \rangle}^*(K) + \langle P \rangle_\infty \left(\pi\delta(K) - \frac{i}{K} \right)_-, \qquad (3.115)$$

where we have used equation (3.104) to transform $S(X)_-$.

Bearing the above comments in mind we begin to construct a solution by considering the first integral equation, (3.88), in isolation. We wish to separate out the parts of the equation which we know and don't know and so we write the equation as

$$\langle V \rangle (X)_+ + \langle V \rangle (X)_- = \frac{1}{\pi} \int\limits_{-\infty}^{+\infty} L(\xi - X) [V](\xi) \, d\xi$$

$$- \frac{1}{\pi} \fint\limits_{-\infty}^{+\infty} \left(\frac{1}{(\xi - X)} - M(\xi - X) \right) [P](\xi)_- \, d\xi,$$

$$(3.116)$$

where $\langle V \rangle (X)_+$ and $[P](X)_-$ are unknown. We then Fourier transform this equation, via the convolution theorem, to obtain

$$\widehat{\langle V \rangle} (K)_+ + \widehat{\langle V \rangle} (K)_- = e^{-|K|} \widehat{[V]}(K) + i\,sgn(K) \left(1 - e^{-|K|} \right) \widehat{[P]}(K)_-,$$

$$(3.117)$$

remembering that we must take care when transforming the pressure difference and that $\widehat{[P]}(K)_-$ is actually given by equation (3.114).

The Wiener-Hopf technique then insists that all 'mixed' functions be decomposed into their $+$ and $-$ components. All $+$ components are then collected onto the left hand side and all $-$ components onto the right hand side. Upon examination of equation (3.117) we can see that in order to do this we must first decompose the kernel $sgn(K) \left(1 - e^{-|K|} \right)$ into a product of $+$ and $-$ functions by writing

$$Q(K) \equiv sgn(K) \left(1 - e^{-|K|} \right) = Q(K)_+ Q(K)_-.\qquad(3.118)$$

Since $Q(K)$ has a zero at $K = 0$ we may not use the product decomposition formulae (3.110) and (3.111) directly. Instead we must consider the product decomposition of the related function

$$R(K) \equiv \frac{sgn(K) \left(1 - e^{-|K|} \right) (K^2 + \gamma^2)^{1/2}}{K} = R(K)_+ R(K)_-,\quad(3.119)$$

where γ is an arbitrary real constant. This function has the desired properties outlined in subsection 3.6.1 and can therefore be decomposed as a product using equations (3.110) and (3.111) to give $R\left(K\right)_{\pm}$ in the form

$$R\left(K\right)_{+} = R\left(K\right)^{1/2} \exp\left\{ +\frac{1}{2\pi i} \int_{-\infty}^{+\infty} \frac{\ln R\left(\kappa\right)}{\left(\kappa - K\right)} d\kappa \right\}, \qquad (3.120)$$

$$R\left(K\right)_{-} = R\left(K\right)^{1/2} \exp\left\{ -\frac{1}{2\pi i} \int_{-\infty}^{+\infty} \frac{\ln R\left(\kappa\right)}{\left(\kappa - K\right)} d\kappa \right\}. \qquad (3.121)$$

Performing the product decomposition of $R\left(K\right)$ allows us to write $Q\left(K\right)_{\pm}$ as

$$Q\left(K\right)_{+} = \frac{R\left(K\right)_{+}}{\left(K + i\gamma\right)^{1/2}_{+}} \quad \text{and} \quad Q\left(K\right)_{-} = \frac{KR\left(K\right)_{-}}{\left(K - i\gamma\right)^{1/2}_{-}} \qquad (3.122)$$

where the function $\left(K^2 + \gamma^2\right)^{1/2}$ has been decomposed as a product of $+$ and $-$ functions in the form $\left(K + i\gamma\right)^{1/2}_{+} \left(K - i\gamma\right)^{1/2}_{-}$.

Next, we must decompose $e^{-|K|}\widehat{[V]}\left(K\right)$ as a sum of $+$ and $-$ functions by writing

$$N\left(K\right) \equiv e^{-|K|}\widehat{[V]}\left(K\right) = N\left(K\right)_{+} + N\left(K\right)_{-}. \qquad (3.123)$$

This is done using the Plemelj formulae (3.102) and (3.103) applied to the function $e^{-|K|}\widehat{[V]}\left(K\right)$ and we obtain $N\left(K\right)_{\pm}$ in the form

$$N\left(K\right)_{+} = \frac{1}{2}\left[N\left(K\right) + \frac{1}{\pi i}\int_{-\infty}^{+\infty} \frac{N\left(K\right)}{\left(\kappa - K\right)} d\kappa \right], \qquad (3.124)$$

$$N\left(K\right)_{-} = \frac{1}{2}\left[N\left(K\right) - \frac{1}{\pi i}\int_{-\infty}^{+\infty} \frac{N\left(K\right)}{\left(\kappa - K\right)} d\kappa \right]. \qquad (3.125)$$

We now introduce these decompositions into equation (3.117) and obtain after some minor rearrangements

$$\frac{\left(K + i\gamma\right)^{1/2}_{+}}{R\left(K\right)_{+}} \left[\widehat{\langle V\rangle}\left(K\right)_{+} - N\left(K\right)_{+}\right] = \frac{\left(K + i\gamma\right)^{1/2}_{+}}{R\left(K\right)_{+}} \left[N\left(K\right)_{-} - \widehat{\langle V\rangle}\left(K\right)_{-}\right]$$
$$+ \frac{iKR\left(K\right)_{-}}{\left(K - i\gamma\right)^{1/2}_{-}}\widehat{[P]}\left(K\right)_{-}.$$

$$(3.126)$$

The only mixed function left is the first term on the right hand side which must be decomposed as a sum of + and − functions and written in the form

$$T(K) \equiv \frac{(K+i\gamma)_+^{1/2}}{R(K)_+} \left[N(K)_- - \widehat{\langle V \rangle}(K)_- \right] = T(K)_+ + T(K)_- . \quad (3.127)$$

Again the desired decomposition can be done using the Plemelj formulae (3.102) and (3.103) and we obtain

$$T(K)_+ = \frac{1}{2} \left[T(K) + \frac{1}{\pi i} \int_{-\infty}^{+\infty} \frac{T(K)}{(\kappa - K)} d\kappa \right], \quad (3.128)$$

$$T(K)_- = \frac{1}{2} \left[T(K) - \frac{1}{\pi i} \int_{-\infty}^{+\infty} \frac{T(K)}{(\kappa - K)} d\kappa \right]. \quad (3.129)$$

Finally, we *are* able to separate all + functions onto the left hand side and all − functions onto the right hand side to give

$$\frac{(K+i\gamma)_+^{1/2}}{R(K)_+} \left[\widehat{\langle V \rangle}(K)_+ - N(K)_+ \right] - T(K)_+ = T(K)_- + \frac{iKR(K)_-}{(K-i\gamma)_-^{1/2}} \widehat{[P]}(K)_- .$$

$$(3.130)$$

This completes the decomposition process.

We are left with an equation describing a function which is the transform of both a + function and a − function at the same time. There is only one such function and it is the the transform of the zero function, namely the zero function. As a result we may equate each side of the equation to zero and solve the two resulting equations separately for the unknowns $\widehat{\langle V \rangle}(K)_+$ and $\widehat{[P]}(K)_-$ respectively. If we do this we obtain the solutions in Fourier space

$$\widehat{\langle V \rangle}(K)_+ = \frac{R(K)_+ T(K)_+}{(K+i\gamma)_+^{1/2}} + N(K)_+ , \quad (3.131)$$

$$\widehat{[P]}(K)_- = \frac{i(K-i\gamma)_-^{1/2} T(K)_-}{KR(K)_-} . \quad (3.132)$$

Now that $\widehat{[P]}(K)_-$ is determined the Fourier transform of the pressure sum $\widehat{\langle P \rangle}(K)$ can be obtained directly from equation (3.83). For completeness

$$\widehat{\langle P \rangle}(K) = -isgn(K)\left(1+e^{-|K|}\right)\widehat{[V]}(K) - e^{-|K|}\widehat{[P]}(K)_- . \quad (3.133)$$

The boundary conditions are now complete in Fourier space and may be obtained in real-space by inverse Fourier transforming the three expressions immediately above.

Setting the Upstream Pressure Difference and Sum $[P]_\infty$ and $\langle P \rangle_\infty$

The boundary conditions are however not yet fully determined. We have still to set the upstream pressures by determining the constants $[P]_\infty$ and $\langle P \rangle_\infty$. We can do this by using the correct expressions (3.114) and (3.115) for the transforms $\widehat{[P]}\,(K)_-$ and $\widehat{\langle P \rangle}\,(K)$ respectively. If we substitute these expressions into the solutions (3.132) and (3.133) and rearrange the resulting equations for $\widehat{[P]}^*(K)_-$ and $\widehat{\langle P \rangle}^*(K)$ respectively we obtain

$$\widehat{[P]}^*(K)_- = \frac{i\,(K - i\gamma)_-^{1/2}\,T\,(K)_-}{K\,R\,(K)_-} - [P]_\infty \left(\pi\delta\,(K) - \frac{i}{K} \right)_- ,$$

$$(3.134)$$

$$\begin{aligned}
\widehat{\langle P \rangle}^*(K) = & -i\,sgn\,(K) \left(1 + e^{-|K|} \right) \widehat{[V]}\,(K) \\
& - e^{-|K|} \left(\widehat{[P]}^*(K)_- + [P]_\infty \left(\pi\delta\,(K) - \frac{i}{K} \right)_- \right) \\
& - \langle P \rangle_\infty \left(\pi\delta\,(K) - \frac{i}{K} \right)_- .
\end{aligned}$$

$$(3.135)$$

Since $\widehat{[P]}^*(K)_-$ and $\widehat{\langle P \rangle}^*(K)$ are both Fourier transforms in the usual sense they may contain no poles. We must therefore choose the constants $[P]_\infty$ and $\langle P \rangle_\infty$ so that the coefficients of K^{-1} in the above expressions are zero at $K = 0$. If we do this we obtain

$$[P]_\infty = -(-i\gamma)^{1/2} \frac{T\,(0)_-}{R\,(0)_-}, \qquad (3.136)$$

$$\langle P \rangle_\infty = -[P]_\infty . \qquad (3.137)$$

In terms of the upstream pressures above and below the aerofoil this becomes

$$P_+ \,(-\infty) = 0, \qquad (3.138)$$

$$P_- \,(-\infty) = (-i\gamma)^{1/2} \frac{T\,(0)_-}{R\,(0)_-}. \qquad (3.139)$$

As it stands this result means very little in terms of the complicated constants $T(0)_-$ and $R(0)_-$. However after some manipulation we can obtain the physically more relevant, equivalent result

$$P_-(-\infty) \;=\; -2 \int\limits_{-\infty}^{+\infty} V_-(X)\,dX. \qquad (3.140)$$

Since the governing equations are those of linearised potential flow the above equation represents a simple mass flux constraint applied to the flow confined first beneath the aerofoil and then beneath the wake.

3.6.2   The Leading Edge Eigensolution

As mentioned earlier the Kutta condition forbids the existence of an eigensolution at the trailing edge as the solution must separate there in a streamlined fashion. We therefore need only consider the eigensolution in the context of a leading edge geometry. Since the eigensolution by definition satisfies homogeneous transverse velocity boundary conditions any attempt to find this solution using the Wiener-Hopf technique of the previous section produces only the trivial zero solution. A non-trivial eigensolution does exist however and can be found using a conformal mapping approach.

Since the integral equations (2.33) and (2.34) are of no practical use here we take a step backwards and start with the Cauchy-Riemann equations (2.10) and (2.11) in the unknown perturbations $p(x, y)$ and $v(x, y)$. We begin by introducing the local leading edge coordinates $X = x/\beta$, $Y = y/\beta + 1/2$, and the local unknowns

$$P(X, Y) \;=\; p(x, y), \qquad (3.141)$$

$$V(X, Y) \;=\; v(x, y), \qquad (3.142)$$

where capitals again denote local quantities. Writing the governing Cauchy-Riemann equations in terms of local leading edge quantities we have

$$\frac{\partial P}{\partial X}(X, Y) \;=\; \frac{\partial V}{\partial Y}(X, Y), \qquad (3.143)$$

$$\frac{\partial P}{\partial Y}(X,Y) = -\frac{\partial V}{\partial X}(X,Y). \tag{3.144}$$

The local pressure perturbation $P(X,Y)$ is of order β^{-1} at leading order and again we write down the asymptotic expansions

$$P(X,Y) = \beta^{-1}P_0(X,Y) + \beta^{f-1}P_f(X,Y) + P_1(X,Y) + \cdots, \tag{3.145}$$

$$V(X,Y) = \beta^{-1}V_0(X,Y) + \beta^{f-1}V_f(X,Y) + V_1(X,Y) + \cdots, \tag{3.146}$$

to ensure the Cauchy-Riemann balances hold at every order. At each order we are therefore faced with the task of finding a complex function, $W(X+iY) = P(X,Y)+iV(X,Y)$ which is analytic in the leading edge geometry, bounded in the far field, and satisfies homogeneous transverse velocity boundary conditions.

The Conformal Mapping Solution

We find such a function by introducing the complex variables $Z = X + iY$ and $\zeta = \xi + i\eta$ and by using a conformal mapping technique. To obtain the desired eigensolution in the Z-plane we map a uniform channel flow in the ζ-plane, for which the complex velocity potential is given by $-P\zeta$, back onto the leading edge geometry (Z-plane) using the conformal mapping

$$Z = \zeta - \frac{1}{2\pi}\left(1 + e^{-2\pi\zeta}\right), \tag{3.147}$$

as used in Widnall and Barrows (1970). This conformal mapping is non-invertible and therefore we may only determine the solution implicitly using ζ. For a given ζ we have

$$W(Z(\zeta)) = \frac{P}{1 + e^{-2\pi\zeta}}, \tag{3.148}$$

We then find $P(X,Y)$ and $V(X,Y)$, the pressure and transverse velocity perturbations, by taking real and imaginary parts of this expression to give

$$P(X,Y) = \frac{P\left(1 + e^{-2\pi\xi}\cos 2\pi\eta\right)}{\left(1 + 2e^{-2\pi\xi}\cos 2\pi\eta + e^{-4\pi\xi}\right)}, \tag{3.149}$$

$$V(X,Y) = \frac{-Pe^{-2\pi\xi}\sin 2\pi\eta}{\left(1 + 2e^{-2\pi\xi}\cos 2\pi\eta + e^{-4\pi\xi}\right)}, \tag{3.150}$$

where

$$X = \xi - \frac{1}{2\pi} \left(1 + e^{-2\pi\xi} \cos 2\pi\eta \right), \qquad (3.151)$$

$$Y = \eta + \frac{1}{2\pi} e^{-2\pi\xi} \sin 2\pi\eta. \qquad (3.152)$$

The 'strength' of the eigensolution, P, is an arbitrary constant and is set by smoothly joining the eigensolution with the global solution beneath the aerofoil. To do this we need to know how the eigensolution behaves beneath the aerofoil as $X \to +\infty$. The corresponding limit in the ζ-plane is $\xi \to +\infty$ and in this limit the solution takes the simple asymptotic form

$$P(X,Y) \to P, \qquad (3.153)$$

$$V(X,Y) \to 0. \qquad (3.154)$$

For completeness we need also to consider the asymptotic form of the eigensolution downstream, above the aerofoil, in the limit $X \to +\infty$ and upstream, on the ground, as $X \to -\infty$. In each of these limits the solution takes the form

$$P(X,Y) \sim -\frac{P}{2\pi X}, \qquad (3.155)$$

$$V(X,Y) \to 0. \qquad (3.156)$$

3.6.3 Setting the Constants $p_{0-}(0)$, $p_{f-}(0)$, and $p_{1-}(0)$

Now that the possible edge flow solutions have been found in the general cases it is only left to discuss the details of where these edge solutions are required, in order to set the unknown constants $p_{0-}(0)$, $p_{f-}(0)$, and $p_{1-}(0)$ in the global solution.

In general we begin by determining the trailing edge non-eigensolution which sets the pressure beneath the aerofoil just upstream of the trailing edge. This solution then determines the value of, say $p_{0-}(1)$, which in turn sets the solution beneath the aerofoil and in particular the corresponding unknown constant $p_{0-}(0)$. An

eigensolution of strength $p_{0-}(0)$ is then introduced at the leading edge to smoothly join the solution beneath the aerofoil with that in the bulk of the fluid.

In the case where a non-eigensolution is induced at the leading edge an additional eigensolution of opposite strength must be introduced at the leading edge in order to cancel out the non-eigensolution's downstream behaviour at source and therefore avoid a pressure mismatch just downstream of the leading edge.

The process is best illustrated in the context of a specific example and we will again consider the flow past a flat plate aerofoil travelling parallel with and very close to the ground at zero angle of attack.

Our first task is to determine the value of f in the asymptotic expansions. We do this by considering the boundary conditions as they appear in the scaled regions around the leading and trailing edges. On the order one length scale the boundary conditions are those given in equations (2.35)-(2.38) and since we have used this aerofoil as an example before $[v](x)$ and $\langle v \rangle (x)$ take the specific forms given in equations (2.75) and (2.76).

In terms of the local leading edge coordinate $X = x/\beta$ the boundary conditions can be written

$$[V](X) = \left\{ \begin{array}{ll} 0 & \text{for} \quad X \in (-\infty, 0] \\ c_1 \beta^{-\frac{1}{2}} X^{-\frac{1}{2}} & \text{for} \quad X \in (0, +\infty) \end{array} \right\}, \tag{3.157}$$

$$\langle V \rangle (X) = \left\{ \begin{array}{ll} ? & \text{for} \quad X \in (-\infty, 0] \\ 0 & \text{for} \quad X \in (0, +\infty) \end{array} \right\}, \tag{3.158}$$

$$[P](X) = \left\{ \begin{array}{ll} 0 & \text{for} \quad X \in (-\infty, 0] \\ ? & \text{for} \quad X \in (0, +\infty) \end{array} \right\}, \tag{3.159}$$

$$\langle P \rangle (X) = \left\{ \begin{array}{ll} ? & \text{for} \quad X \in (-\infty, 0] \\ ? & \text{for} \quad X \in (0, +\infty) \end{array} \right\}, \tag{3.160}$$

and in terms of the local trailing edge coordinate $X = (x-1)/\beta$ the boundary

conditions are

$$[V](X) = \begin{cases} c_1 - \frac{1}{2}c_1\beta X + \cdots & \text{for} \quad X \in (-\infty, 0] \\ -\frac{2}{3}c_2\beta^{-2/3}X^{-2/3} - \cdots & \text{for} \quad X \in (0, +\infty) \end{cases}, \qquad (3.161)$$

$$\langle V \rangle (X) = \begin{cases} 0 & \text{for} \quad X \in (-\infty, 0] \\ ? & \text{for} \quad X \in (0, +\infty) \end{cases}, \qquad (3.162)$$

$$[P](X) = \begin{cases} ? & \text{for} \quad X \in (-\infty, 0] \\ 0 & \text{for} \quad X \in (0, +\infty) \end{cases}, \qquad (3.163)$$

$$\langle P \rangle (X) = \begin{cases} ? & \text{for} \quad X \in (-\infty, 0] \\ ? & \text{for} \quad X \in (0, +\infty) \end{cases}. \qquad (3.164)$$

As a result we are forced to update all our small β expansions by including two 'in-between terms', one with $f = \frac{1}{3}$ and one with $f = \frac{1}{2}$. This means we are now required to find the four constants $p_{0-}(0)$, $p_{\frac{1}{3}-}(0)$, $p_{\frac{1}{2}-}(0)$, and $p_{1-}(0)$ if we are to specify the solution to order unity. We do this by employing the strategy outlined at the beginning of this section, that is first determining the non-eigensolutions at the leading and trailing edges and then adding in a the correct strength eigensolution at the leading edge to ensure a smooth match with the flow outside the gap. We obtain the values of the constants

$$p_{0-}(0) = 2c_1, \qquad (3.165)$$

$$p_{\frac{1}{3}-}(0) = \lambda, \qquad (3.166)$$

$$p_{\frac{1}{2}-}(0) = 0, \qquad (3.167)$$

$$p_{1-}(0) = \nu. \qquad (3.168)$$

In total we are forced to add in an eigensolution at the leading edge of strength

$$P = 2c_1\beta^{-1} + \lambda\beta^{-2/3} - \mu\beta^{-1/2} + \nu + \cdots, \qquad (3.169)$$

where in the above c_1 is the coefficient appearing in the Blasius displacement thickness $\delta_b(x)$ and λ, μ, and ν are constants which are to be determined by performing

Wiener-Hopf calculations of the form given in section 3.6.1, at the $\beta^{-2/3}$, $\beta^{-1/2}$, and order unity orders respectively. These calculations are given in Appendix B.

This completes the global solution to order unity and all higher order terms tend to zero as β tends to zero. Similar arguments to those presented here can be applied at higher orders and the global solution can be calculated to arbitrary accuracy in principle.

3.7 The Global Solution for $\beta \ll 1$

For completeness we now write down the complete global solution for small β, up to and including order unity, for a flat plate aerofoil flying near the ground at zero angle of attack. We have

$$v_+(x) = \begin{cases} \frac{1}{2}\beta B'(x) + \cdots & \text{for} \quad x \in (-\infty, 0) \\ \delta_b'(x) & \text{for} \quad x \in [0,1] \\ 2\delta_g'(x) + \frac{1}{2}\beta B'(x) + \cdots & \text{for} \quad x \in (1, +\infty) \end{cases}, \qquad (3.170)$$

$$v_-(x) = \begin{cases} -\delta_b'(x) & \text{for} \quad x \in [0,1] \\ \frac{1}{2}\beta B'(x) + \cdots & \text{for} \quad x \notin [0,1] \end{cases}, \qquad (3.171)$$

$$p_+(x) = \begin{cases} B(x) + \cdots & \text{for} \quad x \in [0,1] \\ B(x) + \cdots & \text{for} \quad x \notin [0,1] \end{cases}, \qquad (3.172)$$

$$p_-(x) = \begin{cases} 2\beta^{-1}(c_1 - \delta_b(x)) + \lambda\beta^{-2/3} + \nu + \cdots & \text{for} \quad x \in [0,1] \\ B(x) + \cdots & \text{for} \quad x \notin [0,1] \end{cases}, \qquad (3.173)$$

where in the above

$$B(x) = \frac{1}{\pi}\int_0^1 \frac{\delta_b'(\xi)}{(\xi - x)}d\xi + \frac{2}{\pi}\int_1^{+\infty} \frac{\delta_g'(\xi)}{(\xi - x)}d\xi, \qquad (3.174)$$

$\delta_b(x)$ and $\delta_g(x)$ are the Blasius and Goldstein displacement thicknesses and

$$P = 2c_1\beta^{-1} + \lambda\beta^{-2/3} - \mu\beta^{-1/2} + \nu + \cdots. \qquad (3.175)$$

The unknown constants λ, γ, and μ are calculated in Appendix B to be

$$\lambda = -1.9105\cdots, \tag{3.176}$$

$$\mu = 1.33348\cdots, \tag{3.177}$$

$$\nu = \frac{c_1}{2\pi} = 0.27386\cdots. \tag{3.178}$$

3.8   Flow Properties

What follows is a comparison between the solutions for $p_+(x)$ and $p_-(x)$ as computed firstly using the technique developed in Chapter 2 and secondly using the small β asymptotic solution developed in this chapter. The comparison is made using the horizontal flat plate aerofoil as an example with $\alpha = \frac{1}{32}$. Figure 3.3 shows the Chapter 2 solution and Figure 3.4 shows the small β asymptotic one.

In Figure 3.4 the leading edge eigensolution (3.155) has been added to the global pressure solutions given in equations (3.172) and (3.173). The non-eigensolutions which appear both at the leading and trailing edges at the $\beta^{-2/3}$, $\beta^{-1/2}$, and order unity order are not included due to difficulties regarding their evaluation. See Section 3.6.1 and Appendix B.

By comparing the two plots one can see that there is very good agreement between the solutions except at the trailing edge where we expect that the inclusion of the non-eigensolution at the $\beta^{-2/3}$ order would add in the necessary adjustments. The two main small β flow features are now obvious. Most clear is the simple form of the pressure directly beneath the aerofoil, which reflects, in this example, the shape of the Blasius displacement thickness and secondly the large upstream influence caused by the x^{-1} behaviour of the pressure eigensolution at the leading edge, which is ultimately produced by the Kutta condition applied at the trailing edge.

The method developed in Chapter 2 was only able to accurately provide solutions for $\alpha \geq \frac{1}{32}$, the asymptotic small β solution is used for values smaller than this.
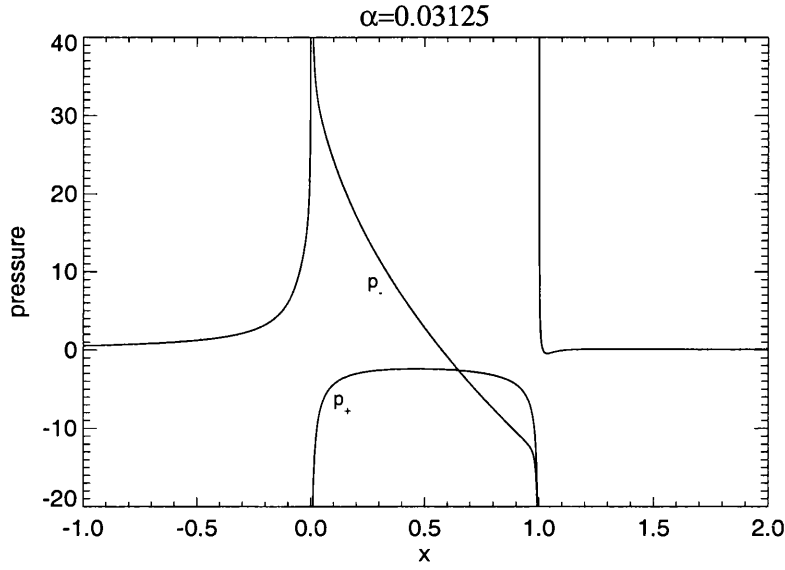
Figure 3.3: Numerical solutions for the pressures p_+ (x) and p_- (x) for $\alpha = \frac{1}{32}$ as computed using the method developed in Chapter 2.
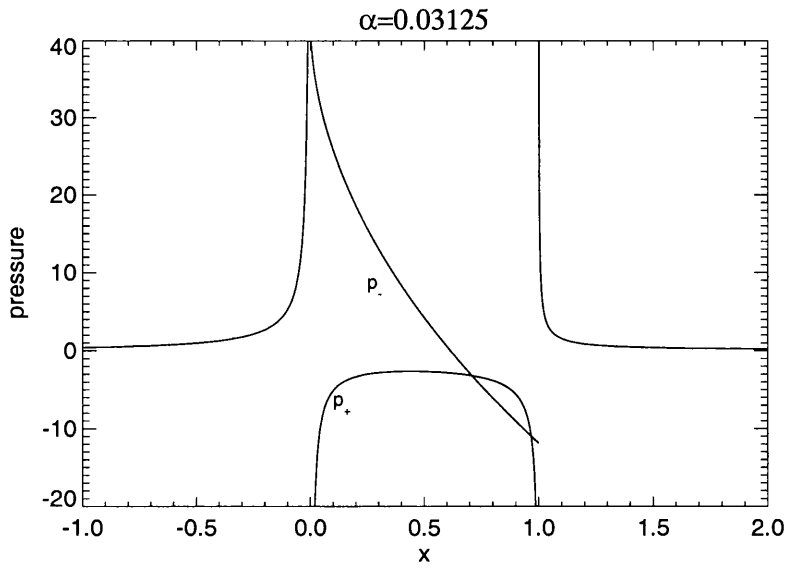
Figure 3.4: Analytic global solutions for the pressures p_+ (x) and p_- (x) for $\alpha = \frac{1}{32}$ as calculated using the small β theory developed in this chapter. The leading edge eigensolution has been added to the global solution of section 3.7, however the non-eigensolutions have not.

Chapter 4

Viscous-Inviscid 'Wing-In-Ground' Effect

4.1 Introduction

In this chapter we focus our attention further by considering the flow past the trailing edge of an aerofoil moving very near the ground. In chapter 2 we mentioned that the flow near the trailing edge of a thin aerofoil is described by the triple-deck theory of Stewartson (1969) and Messiter (1970), and in the previous chapter we have seen that for small non-dimensional ground clearances, $\alpha = \beta/2$, the triple-deck structure is embedded within a larger β by β region around the trailing edge. See Figure 3.1. We now consider the case in which the upper deck, of the triple-deck structure, and the local β by β region coincide.

This occurs when β is of the order $Re^{-3/8}$, the triple-deck length scale (see Appendix A). In this limit the asymptotic expansions in the β by β region at the trailing edge become identical with those of the upper deck in triple-deck theory. See Figure 4.1.

The ground is now just outside the classical boundary layer (Region II) but <u>inside</u> the upper deck (Region III) and can therefore influence the boundary layer flow, in

a viscous sub-layer, through a viscous-inviscid interaction at the trailing edge. This effect, which is studied in the present chapter, constitutes the first viscous response to the presence of the ground, as at larger ground clearances the flows in the thin boundary layers and the wake remain essentially unchanged from those of flight in the absence of the ground. See Figure 4.2

We therefore conclude that when β is of the order $Re^{-3/8}$ the local trailing edge flow is described by an interactive triple-deck theory which includes the effects of ground-interference. For convenience we introduce a scaled ground clearance parameter $\bar{\beta}$, of order unity here, by writing β as $\bar{\beta}Re^{-3/8}$.

In order to accommodate the non-symmetric nature of the problem it is necessary to modify standard triple-deck theory in two ways. To begin with we must introduce a diffusion layer (Region IV) adjacent to the ground, of thickness $Re^{-11/16}$ obtained from an order of magnitude estimate, in which the highest order normal derivatives in the governing equations are reinstated to allow the solution to meet the required no-slip condition on the ground. A similar layer is studied in Appendix A, section (A.3). An important feature of this layer is that it produces no displacement effect in the outer flow at leading order and this property is used to derive the second modification to the theory, that being a new pressure-displacement interaction law for flows with ground-interference. The new interaction law directly replaces the Cauchy-Hilbert integral relation in the standard theory and it is by making this simple change that ground effects are included.

Complications which occur due to the non-symmetric nature of the problem include the need for two different lower decks (Regions I$_\pm$) above and below the aerofoil which join at the trailing edge to form the beginnings of a viscous wake, the inclusion of the corresponding main decks (Regions II$_\pm$), the introduction of the two unknown pressures $P_\pm(X)$ and the two unknown displacements $A_\pm(X)$, and difficulties related to the actual implementation of the new pressure-displacement interaction law. Subscripts $+$ and $-$ are used to denote quantities above and below the
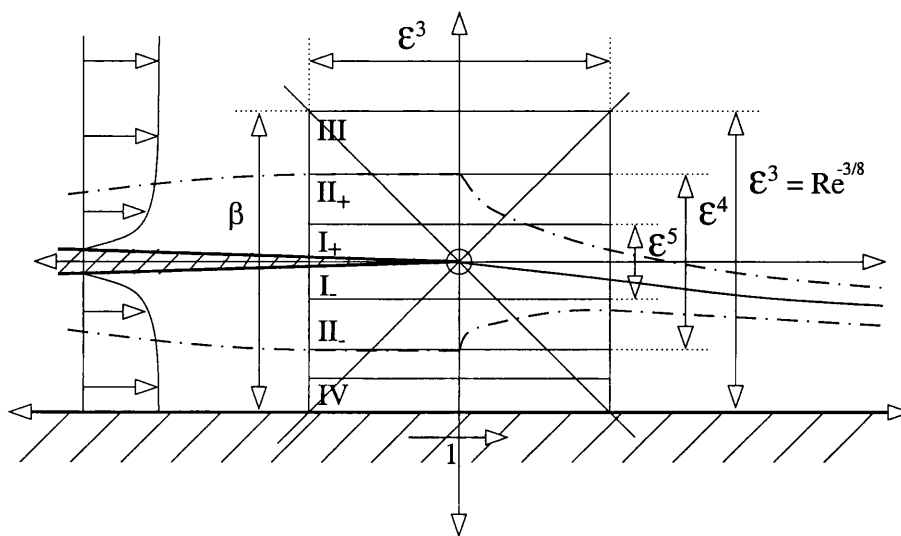
Figure 4.1: The triple deck flow structure at the trailing edge of an aerofoil in ground effect. Shows the lower decks ($I_\pm$), the main decks ($II_\pm$), the upper deck (III), and the ground diffusion layer (IV)
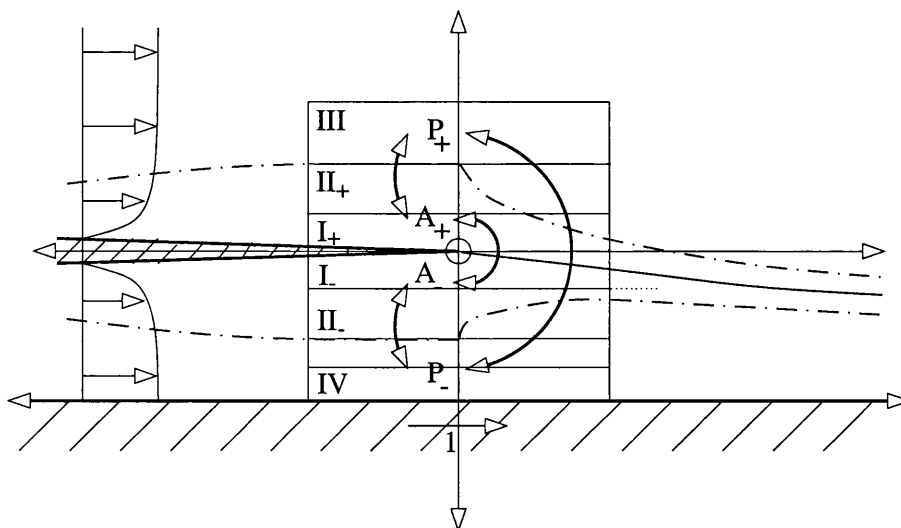
Figure 4.2: The interactive ground effect mechanism. Pressure continuity, in the wake, drives a displacement effect which in turn drives a pressure correction and so on.

aerofoil respectively.

4.2 Problem Formulation

As in the standard triple-deck theory of Stewartson (1969) and Messiter (1970) we introduce a local streamwise trailing edge coordinate X scaled on the triple deck length scale ε^3, where

$$\varepsilon = Re^{-1/8}, \tag{4.1}$$

and write down the following asymptotic expansions for the streamwise and transverse components of the velocity field and for the scalar pressure field in each of the decks. In the lower decks (Region $I_\pm$), where $y = \varepsilon^5 \underline{Y}$, we seek a solution of the form

$$U_\pm(X, \underline{Y}) = \varepsilon \underline{U}_\pm(X, \underline{Y}) + \cdots, \tag{4.2}$$

$$V_\pm(X, \underline{Y}) = \varepsilon^3 \underline{V}_\pm(X, \underline{Y}) + \cdots, \tag{4.3}$$

$$P_\pm(X, \underline{Y}) = \varepsilon^2 \underline{P}_\pm(X) + \cdots. \tag{4.4}$$

In the main decks (Region $II_\pm$), where $y = \varepsilon^4 Y$, the solution takes the linearised form

$$U_\pm(X, Y) = U_b(|Y|) + \varepsilon A_\pm(X) U_b'(|Y|) + \cdots, \tag{4.5}$$

$$V_\pm(X, Y) = -\varepsilon^2 A_\pm'(X) U_b(|Y|) + \cdots, \tag{4.6}$$

$$P_\pm(X, Y) = \varepsilon^2 P_\pm(X) + \cdots, \tag{4.7}$$

where $A_\pm(X)$ are arbitrary functions of X and $U_b(|Y|)$ is the Blasius boundary layer velocity profile at the trailing edge. Finally in the upper deck (Region III), where $y = \varepsilon^3 \overline{Y}$, we have

$$U\left(X, \overline{Y}\right) = 1 + \varepsilon^2 \overline{U}\left(X, \overline{Y}\right) + \cdots, \tag{4.8}$$

$$V\left(X, \overline{Y}\right) = \varepsilon^2 \overline{V}\left(X, \overline{Y}\right) + \cdots, \tag{4.9}$$

$$P\left(X, \overline{Y}\right) = \varepsilon^2 \overline{P}\left(X, \overline{Y}\right) + \cdots, \tag{4.10}$$

to ensure the governing equations are those of linearised potential flow. In the upper deck we do not need to distinguish between the flow above and below the aerofoil as the solution in this region is permitted a discontinuity along the line $\overline{Y} = 0$. This is due to the fact that the main and the lower decks, which lie well within the upper deck and for large enough Reynolds number appear as the line $\overline{Y} = 0$, can smooth out any discontinuous velocity profiles which may occur between the upper and lower portions of the upper deck.

After making the changes outlined in the introduction our task, as in standard triple-deck theory, eventually becomes one of solving the governing boundary layer equations

$$\underline{U}_{\pm}\frac{\partial \underline{U}_{\pm}}{\partial X} + \underline{V}_{\pm}\frac{\partial \underline{U}_{\pm}}{\partial \underline{Y}} \;=\; -P'_{\pm}(X) + \frac{\partial^2 \underline{U}_{\pm}}{\partial \underline{Y}^2}, \tag{4.11}$$

$$\frac{\partial \underline{U}_{\pm}}{\partial X} + \frac{\partial \underline{V}_{\pm}}{\partial \underline{Y}} \;=\; 0, \tag{4.12}$$

in each of the two lower decks which join smoothly at the trailing edge to form the beginnings of a thin Goldstein wake. We will consider the case of a horizontal flat plate aerofoil and in this case the boundary layer equations (4.11) and (4.12) must be solved subject to the no slip conditions

$$\underline{U}_{\pm}(X, 0_{\pm}) \;=\; 0 \quad \text{for} \quad X < 0, \tag{4.13}$$

$$\underline{V}_{\pm}(X, 0_{\pm}) \;=\; 0 \quad \text{for} \quad X < 0, \tag{4.14}$$

on the upper and lower surfaces of the aerofoil, the main deck matching conditions

$$\underline{U}_{\pm}(X, Y) \;\sim\; \lambda |Y| \pm \lambda A_{\pm}(X), \tag{4.15}$$

for all X as $|Y| \to \infty$ above and below, and the upstream matching condition,

$$\underline{U}_{\pm}(X, Y) \;\sim\; \lambda |Y|. \tag{4.16}$$

for all Y as $X \to -\infty$, where λ is the Blasius skin friction coefficient. An additional constraint in the form of a pressure displacement interaction law is required to complete the boundary conditions and for flows with ground interference we have

$$\langle A' \rangle (X) = \frac{1}{\pi} \int\limits_{-\infty}^{+\infty} L(\xi - X) [A'](\xi) d\xi + \frac{1}{\pi} \int\limits_{-\infty}^{+\infty} \left(\frac{1}{(\xi - X)} - M(\xi - X) \right) [P](\xi) d\xi,$$

$$(4.17)$$

$$\langle P \rangle (X) = -\frac{1}{\pi} \int\limits_{-\infty}^{+\infty} \left(\frac{1}{(\xi - X)} + M(\xi - X) \right) [A'](\xi) d\xi - \frac{1}{\pi} \int\limits_{-\infty}^{+\infty} L(\xi - X) [P](\xi) d\xi,$$

$$(4.18)$$

$$\text{where} \quad L(X) = \frac{\overline{\beta}}{X^2 + \overline{\beta}^2} \quad \text{and} \quad M(X) = \frac{X}{X^2 + \overline{\beta}^2},$$

and where sums and differences are denoted by

$$[A'](X) = A'_+(X) - A'_-(X), \tag{4.19}$$

$$\langle A' \rangle (X) = A'_+(X) + A'_-(X), \tag{4.20}$$

$$[P](X) = P_+(X) - P_-(X), \tag{4.21}$$

$$\langle P \rangle (X) = P_+(X) + P_-(X). \tag{4.22}$$

The above interaction law must be implemented subject to conditions of the form

$$[A'](X) = \left\{ \begin{array}{ll} [A'](X) & \text{for} \quad X < 0 \\ [A'](X) & \text{for} \quad X > 0 \end{array} \right\}, \tag{4.23}$$

$$\langle A' \rangle (X) = \left\{ \begin{array}{ll} \langle A' \rangle (X) & \text{for} \quad X < 0 \\ ? & \text{for} \quad X > 0 \end{array} \right\}, \tag{4.24}$$

$$[P](X) = \left\{ \begin{array}{ll} ? & \text{for} \quad X < 0 \\ 0 & \text{for} \quad X > 0 \end{array} \right\}, \tag{4.25}$$

$$\langle P \rangle (X) = \left\{ \begin{array}{ll} ? & \text{for} \quad X < 0 \\ ? & \text{for} \quad X > 0 \end{array} \right\}. \tag{4.26}$$

By solving the above system of equations and boundary conditions we can (perhaps uniquely) determine the unknown pressures $P_\pm(X)$ and displacements $A_\pm(X)$, and therefore complete the trailing edge solution in all decks.

It is useful to note here that the interaction law may be stated in a more familiar form. The functions $P'_+ (X)$ and $A''_+ (X)$ taken over all X are in fact related by the Cauchy-Hilbert integral pair

$$P'_+ (X) = -\frac{1}{\pi} \int\limits_{-\infty}^{+\infty} \frac{A''_+ (\xi)}{(\xi - X)} d\xi, \tag{4.27}$$

$$A''_+ (X) = \frac{1}{\pi} \int\limits_{-\infty}^{+\infty} \frac{P'_+ (\xi)}{(\xi - X)} d\xi, \tag{4.28}$$

as in standard triple-deck theory whilst $P'_- (X)$ and $A''_- (X)$ are related by a similar singular integral pair, namely

$$P'_- (X) = \frac{1}{\beta} \int\limits_{-\infty}^{+\infty} \frac{A''_- (\xi)}{\tanh \frac{\pi}{\beta} (\xi - X)} d\xi, \tag{4.29}$$

$$A''_- (X) = -\frac{1}{\beta} \int\limits_{-\infty}^{+\infty} \frac{P'_- (\xi)}{\sinh \frac{\pi}{\beta} (\xi - X)} d\xi. \tag{4.30}$$

Together equations (4.27)-(4.30) are equivalent to equations (4.17) and (4.18). However in the form given immediately above it is not clear how to impose the pressure continuity condition (4.25) and so the interaction law in the form (4.17) and (4.18) is preferred. The relations (4.27)-(4.30) are equally valid if $P'_\pm (X)$ and $A''_- (X)$ are replaced by $P_\pm (X)$ and $A'_- (X)$ respectively.

4.3 Mathematical Methods

Stable numerical integration of the boundary layer equations (4.11) and (4.12) requires, in many applications, that the displacement functions $A_\pm (X)$, in boundary condition (4.15), be specified rather than the pressure gradients $P'_\pm (X)$ in equation (4.11). However, the question mark in equation (4.24) implies that we cannot independently specify $A_\pm (X)$ in the wake until we have imposed the pressure continuity condition (4.25) by solving the integral equations (4.17) and (4.18).

4.3.1 The Solution of the Interaction Law Equations

Our first aim then is to solve the integral equations (4.17) and (4.18) subject to the conditions (4.24)-(4.26), given that we know $[A']\,(X)$ for all X and $\langle A'\rangle\,(X)$ for $X<0$, in order to find $\langle A'\rangle\,(X)$ in the wake. If we can do this we are then able to specify $A_\pm\,(X)$ for all X, confident in the knowledge that pressure continuity in the wake is guaranteed.

We have encountered a similar problem before, in Chapter 3. We notice that the interaction law is identical to the integral equations (3.88) and (3.89), which govern the inviscid flow in the β by β scaled region at the trailing edge, except for the fact that the ground clearance parameter has been reinstated in the form of $\bar{\beta}$ and $V_\pm\,(X)$ have been replaced by $-A'_\pm\,(X)$. This is in fact no coincidence as the upper deck is the β by β region in the regime we are considering, as mentioned at the beginning of this chapter, and therefore it exhibits the same physics as that region, described by the same integral equations. As a result we can use the Wiener-Hopf solution, presented in section (3.6.1), here to solve the integral equations and hence find the correct $\langle A'\rangle\,(X)$ for $X>0$.

Reinstating the ground clearance parameter $\bar{\beta}$, and replacing $V_\pm\,(X)$ with $-A'_\pm\,(X)$ in the Wiener-Hopf solution, results in the definitions for $R\,(K)$, $N\,(K)$, and $T\,(K)$, in equations (3.119), (3.123), and (3.127) respectively, changing slightly to become

$$R\,(K) \;\equiv\; \frac{sgn\,(K)\left(1-e^{-\bar{\beta}|K|}\right)\left(K^2+\gamma^2\right)^{1/2}}{K},$$

(4.31)

$$N\,(K) \;\equiv\; -e^{-\bar{\beta}|K|}\widehat{[A']}\,(K),$$

(4.32)

$$T\,(K) \;\equiv\; \frac{(K+i\gamma)_+^{1/2}}{R\,(K)_+}\left[N\,(K)_- + \widehat{\langle A'\rangle}_-\,(K)\right].$$

(4.33)

The solutions in Fourier-space for $\widehat{\langle A' \rangle}(K)_+$, $\widehat{[P]}(K)_-$, and $\widehat{\langle P \rangle}(K)$, in equations (3.131), (3.132), and (3.133) respectively, also change slightly to become

$$\widehat{\langle A' \rangle}(K)_+ \;=\; -\frac{R(K)_+ \, T(K)_+}{(K+i\gamma)_+^{1/2}} - N(K)_+ ,$$

(4.34)

$$\widehat{[P]}(K)_- \;=\; \frac{i\,(K-i\gamma)_-^{1/2}\,T(K)_-}{K R(K)_-} ,$$

(4.35)

$$\widehat{\langle P \rangle}(K) \;=\; isgn(K)\left(1 + e^{-\tilde{\beta}|K|}\right)\widehat{[A']}(K) - e^{-\tilde{\beta}|K|}\widehat{[P]}(K)_- .$$

(4.36)

Finally the last result in the section, equation (3.140), becomes

$$P_-(-\infty) \;=\; \frac{2}{\tilde{\beta}} \int\limits_{-\infty}^{+\infty} A'_-(X)\,dX.$$

(4.37)

Now that the required changes have been made in the Wiener-Hopf solution we can see that the Fourier transform of the very function we are seeking, $\widehat{\langle A' \rangle}(K)_+$, is given in equation (4.34). On the other hand this solution is in fact very complicated in nature.

In order to calculate $\langle A' \rangle(X)_+$, from the given functions $[A'](X)$ and $\langle A' \rangle(X)_-$, we would need to perform two Fourier transforms to find $\widehat{[A']}(K)$ and $\widehat{\langle A' \rangle}(K)_-$, followed by three Hilbert transforms to decompose $R(K)$, $N(K)$, and $T(K)$ into $R_\pm(K)$, $N_\pm(K)$, and $T_\pm(K)$ respectively, and then finally to perform the inverse Fourier transform of $\widehat{\langle A' \rangle}(K)_+$. To do this numerically using the integral definitions of the Fourier and Hilbert transforms would be prohibitively expensive in terms of the computer time needed and so in the actual implementation we opt to replace all Fourier and Hilbert integral transforms by their discrete transform counterparts.

These discrete transforms possess properties parallel to the continuous ones and so can be used in a similar way. The benefits of using them are mainly due to the

fact that they can be performed using the Fast Fourier Transform algorithm (FFT) (Press et al. (1995)) and so can be computed extremely efficiently. The details of how we use these discrete transforms to approximate the corresponding integral transforms are given in section (4.4.2). However, it is sufficient to state here that in principle we can define an algorithm which, given $[A']\,(X)$ for all X and $\langle A' \rangle\,(X)$ for $X < 0$, calculates that $\langle A' \rangle\,(X)$ for $X > 0$ which satisfies the interaction law equations (4.17) and (4.18) and the pressure continuity condition (4.25).

Now that we know $[A']\,(X)$ and $\langle A' \rangle\,(X)$ for all X, in principle, we may calculate $A'_{\pm}\,(X)$ using the simple formula

$$A'_{\pm}\,(X) \;=\; \frac{1}{2}\left(\langle A' \rangle\,(X) \pm [A']\,(X)\right), \tag{4.38}$$

and find $A_{\pm}\,(X)$ by integrating the above expression using the upstream boundary conditions (4.15) and (4.16) to deduce that $A_{\pm}\,(-\infty) = 0$. Likewise the functions $A''_{\pm}\,(X)$ and $A'''_{\pm}\,(X)$ can be found by differentiating equation (4.38).

4.3.2   The Evaluation of the Familiar Interaction Laws

We are now free to use the more familiar form for the interaction law, equations (4.27)-(4.30), to find the unknown pressure gradients $P'_{\pm}\,(X)$. However in their current form they are difficult to evaluate since the integrals appearing there are Cauchy principle value integrals. We must first consider a way of rewriting these expressions in a form that contains only ordinary integrals, i.e. no Cauchy principle values. We will demonstrate this procedure using the interaction law (4.27) as an example.

The correct way to write equation (4.27) is as the limit

$$P'_{+}\,(X) \;=\; -\frac{1}{\pi} \lim_{\delta \to 0} \left[\int_{-\infty}^{X-\delta} \frac{A''_{+}\,(\xi)}{(\xi - X)}d\xi + \int_{X+\delta}^{+\infty} \frac{A''_{+}\,(\xi)}{(\xi - X)}d\xi \right]. \tag{4.39}$$

We can then integrate the expression immediately above by parts, treating each of the two integrals separately, to obtain

$$P'_+(X) = -\frac{1}{\pi} \lim_{\delta \to 0} \left[\int_{-\infty}^{X-\delta} \frac{A'_+(\xi) - A'_+(X)}{(\xi - X)^2} d\xi + \int_{X+\delta}^{+\infty} \frac{A'_+(\xi) - A'_+(X)}{(\xi - X)^2} d\xi \right]$$

$$+ \frac{1}{\pi} \lim_{\delta \to 0} \left[\frac{A'_+(X-\delta) - 2A'_+(X) + A'_+(X+\delta)}{\delta} \right].$$

$$(4.40)$$

We recognise the last term in equation (4.40) as $A'''_+(X) \lim_{\delta \to 0} \delta$, and since this limit is obviously zero we are left with the expression

$$P'_+(X) = -\frac{1}{\pi} \int_{-\infty}^{+\infty} \frac{A'_+(\xi) - A'_+(X)}{(\xi - X)^2} d\xi, \qquad (4.41)$$

which still contains a Cauchy principle value integral. However, we may now add a term which is trivially equal to zero to both sides of equation (4.41) to obtain the final expression

$$P'_+(X) = -\frac{1}{\pi} \int_{-\infty}^{+\infty} \frac{A'_+(\xi) - A'_+(X) - (\xi - X)A''_+(X)}{(\xi - X)^2} d\xi, \qquad (4.42)$$

which is no longer a Cauchy principle value integral since the above integrand has a <u>removable</u> singularity at the point $\xi = X$ where it takes the finite value $A'''_+(X)/2$. This ordinary integral can be approximated numerically using Simpson's rule for example. Exactly similar manipulations can be made to equation (4.29) and we can derive the similar expression

$$P'_-(X) = \frac{1}{\pi} \int_{-\infty}^{+\infty} \frac{A'_-(\xi) - A'_-(X) - (\xi - X)A''_-(X)}{\left(\frac{\bar{\beta}}{\pi} \sinh \frac{\pi}{\beta}(\xi - X)\right)^2} d\xi - \frac{2}{\bar{\beta}} A'_-(X), \quad (4.43)$$

for $P'_-(X)$. The integrand above again has a removable singularity at the point $\xi = X$ and again takes the value $A'''_-(X)/2$ there. The additional term on the far right of equation (4.43) comes about due to the behaviour of the hyperbolic tangent function appearing in equation (4.29) at $\pm\infty$.

4.3.3 The Streamfunction-Vorticity Formulation

Backtracking slightly, knowing $A_{\pm}(X)$ for all X also allows us to perform a stable numerical integration of the boundary layer equations (4.11) and (4.12), subject to the boundary conditions (4.13)-(4.16), in order to find the unknown pressure gradients $P'_{\pm}(X)$.

We first renormalise, where m equals one quarter, $\left(U_{\pm}, V_{\pm}, P_{\pm}, A_{\pm}, X, \underline{Y}, \bar{\beta}\right)$ on $(\lambda^m, \lambda^{3m}, \lambda^{2m}, \lambda^{-3m}, \lambda^{-5m}, \lambda^{-3m}, \lambda^{-5m})$ which effectively allows us to set the constant λ equal to unity without loss of generality. We also drop the underline on the $\underline{Y}$ in the interests of clarity. Next, in order to satisfy the continuity equation (4.12), we introduce the streamfunctions $\psi_{\pm}(X, Y)$ such that

$$\underline{U}_{\pm}(X, Y) = \frac{\partial \psi_{\pm}}{\partial Y}, \tag{4.44}$$

$$\underline{V}_{\pm}(X, Y) = -\frac{\partial \psi_{\pm}}{\partial X}. \tag{4.45}$$

Differentiation of equation (4.11) with respect to Y then eliminates the pressure gradient term and, together with the introduction of the negative vorticities, $\Omega_{\pm}(X, Y)$, leads to the governing streamfunction-vorticity boundary layer equations

$$\frac{\partial^2 \Omega_{\pm}}{\partial Y^2} = \frac{\partial \psi_{\pm}}{\partial Y} \frac{\partial \Omega_{\pm}}{\partial X} - \frac{\partial \psi_{\pm}}{\partial X} \frac{\partial \Omega_{\pm}}{\partial Y}, \tag{4.46}$$

$$\frac{\partial^2 \psi_{\pm}}{\partial Y^2} = \Omega_{\pm}, \tag{4.47}$$

which must be solved subject to the no slip conditions

$$\psi_{\pm}(X, 0_{\pm}) = 0 \quad \text{for} \quad X < 0, \tag{4.48}$$

$$\frac{\partial \psi_{\pm}}{\partial Y}(X, 0_{\pm}) = 0 \quad \text{for} \quad X < 0, \tag{4.49}$$

on the upper and lower surfaces of the aerofoil, the main deck matching conditions

$$\frac{\partial \psi_{\pm}}{\partial Y}(X, Y) \sim |Y| \pm A_{\pm}(X), \tag{4.50}$$

$$\Omega_{\pm}(X, Y) \sim \pm 1, \tag{4.51}$$

valid for all X as $|Y| \to \infty$ above and below, and the upstream matching conditions,

$$\psi_\pm(X,Y) \sim \pm\frac{1}{2}Y^2, \tag{4.52}$$

$$\Omega_\pm(X,Y) \sim \pm 1, \tag{4.53}$$

valid for all Y as $X \to -\infty$.

The symmetries in equations (4.47) and (4.46) lead upon discretisation to simple difference equations which can be solved extremely efficiently at each streamwise location given the required upstream information. This makes for a fast numerical solution algorithm which once coded is relatively easy to debug. It is for these reasons that we have chosen to adopt a streamfunction-vorticity formulation instead of a primitive variable approach or a compact differenced box-scheme for example.

Once the solutions for $\psi_\pm(X,Y)$ and $\Omega_\pm(X,Y)$ have been obtained numerically the unknown pressure gradients may be retrieved by rearranging equation (4.11) for $P'_\pm(X)$. The resulting equation is easiest to evaluate either on a boundary, where the no slip condition holds, or in the farfield, where $\underline{U}_\pm(X,Y)$ and $\underline{V}_\pm(X,Y)$ take simple forms, and as a result we obtain the equations

$$P'_\pm(X) = \frac{\partial \Omega_\pm}{\partial Y}(X,0_\pm) \quad \text{for} \quad X < 0, \tag{4.54}$$

valid on the upper and lower surfaces of the aerofoil and

$$P'_\pm(X) = -A_\pm(X)A'_\pm(X) \mp B_\pm(X), \tag{4.55}$$

valid in the farfield as $|Y| \to \infty$ above and below. In the equation above

$$B_\pm(X) = \lim_{Y \to \pm\infty}\left[\underline{V}_\pm(X,Y) + |Y|A'_\pm(X)\right]. \tag{4.56}$$

We see then, that evaluation of the interaction laws (4.27) and (4.29) and numerical integration of the boundary layer equations (4.11) and (4.12) define two independent ways of finding the unknown pressure gradients $P'_\pm(X)$ from the displacement gradients $A'_\pm(X)$. To be consistent these two different methods of finding $P'_\pm(X)$

must ultimately lead to the same result and it is this idea which forms the basis of the numerical algorithm which we will use to solve the system of equations (4.11)-(4.26). In order to distinguish between these viscous and inviscid results we label the pressure gradients which we obtain from the <u>inviscid</u> interaction laws and the <u>viscous</u> boundary layer equations $P'_{I\pm}(X)$ and $P'_{V\pm}(X)$ respectively.

4.4 Numerical Methods

We solve the system of equations (4.11)-(4.26) by using an iterative method similar to that used by Carter (1979) to solve a more standard triple-deck problem. We are first required to make a guess for $[A'](X)$ for all X and $\langle A' \rangle (X)$ for $X < 0$. We then use a discretised version of the Wiener-Hopf solution given in section 4.3.1 to find that $\langle A' \rangle (X)$ for $X > 0$ which satisfies the interaction integral equations (4.17) and (4.18) *and* the pressure continuity condition (4.25). This then allows us to calculate $A_\pm(X)$ and its derivatives for all X.

The non-singular interaction laws, (4.42) and (4.43), are then used to find the inviscid pressure gradients $P'_{I\pm}(X)$ and a numerical integration of the streamfunction-vorticity boundary layer equations, (4.47) and (4.46), is performed to find the viscous pressure gradients $P'_{V\pm}(X)$.

The difference between these two pressure gradients is then used to find new guesses for the displacement gradients, $A'_\pm(X)$, according to the relaxation formulae

$$A'_+(X)_{i+1} = A'_+(X)_i + \omega(X)\left(P'_{I+}(X)_i - P'_{V+}(X)_i\right), \qquad (4.57)$$

$$A'_-(X)_{i+1} = A'_-(X)_i - \omega(X)\left(P'_{I-}(X)_i - P'_{V-}(X)_i\right). \qquad (4.58)$$

In turn new guesses for $[A'](X)$ for all X and $\langle A' \rangle (X)$ for $X < 0$ can be calculated using equations (4.19) and (4.20) respectively.

The procedure outlined above is repeated until the viscous and inviscid pressures

gradients, $P'_{V\pm}(X)$ and $P'_{I\pm}(X)$, are equal to within a given tolerance at which point the solution satisfies all of the required constraints and is therefore complete.

The amplitude of the relaxation function $\omega(X)$, appearing in equations (4.57) and (4.58), is chosen by trial and error to ensure the convergence of the scheme and its spatial distribution is chosen to damp any troublesome end effect errors which may creep into the calculation.

Our final task then, is to produce a numerical code which can accurately implement both the inviscid and viscous sides of the algorithm described above, combine their output, and iteratively repeat this procedure until a converged solution is obtained.

4.4.1 The Basic Discretisation

We begin by discretising the solution domain using an equi-spaced Cartesian grid with grid-spacings ΔX and ΔY in the streamwise and transverse directions respectively. The $(\ell, m)^{th}$ grid-point then has co-ordinates $(X_\ell, Y_m) = (\ell \Delta X, m \Delta Y)$, where the indices ℓ and m are integers and run between $\pm L$ and $\pm M$ respectively.

At the $(\ell, m)^{th}$ grid-point the value of the streamfunctions $\psi_\pm$, the streamwise and transverse components of velocity $U_\pm$ and $V_\pm$, and the vorticities $\Omega_\pm$ are denoted by ψ_m^ℓ, U_m^ℓ, V_m^ℓ, and Ω_m^ℓ respectively. Subscripts $+$ and $-$ are now dropped as both $\psi_\pm(X, Y)$ can be denoted using ψ_m^ℓ for example since the subscript m takes both positive and negative values.

At the ℓth streamwise station the values of the displacements $A_\pm$, the inviscid pressures $P_{I\pm}$, the viscous pressures $P_{V\pm}$ and their first derivatives are denoted by $A_{\ell\pm}$, $P_{\ell I\pm}$, $P_{\ell V\pm}$, $A'_{\ell\pm}$, $P'_{\ell I\pm}$, and $P'_{\ell V\pm}$ respectively. Since the skin friction can take different values on the upper and lower surfaces of the aerofoil these are denoted $\Omega_{\ell\pm}$ respectively.

4.4.2 The Discretised Wiener-Hopf Solution Algorithm

As mentioned towards the end of section (4.3.1) it is not practical to perform a straightforward evaluation of the solution for $\langle A' \rangle (X)_+$ given in equation (4.34) as the direct computation of the Fourier and Hilbert transforms in the solution would prove to be prohibitively expensive. This is especially relevant since such a calculation may need to be repeated many times as part of a larger iterative process. We must instead construct a discretised Wiener-Hopf solution which employs discrete transform methods and can therefore be evaluated efficiently using using the FFT algorithm.

There are two ways of constructing such a solution. The first is to return to the interaction law integral equations (4.17) and (4.18), discretise them by approximating the infinite range convolution integrals therein using finite sum convolutions, and then try to find a solution to the resulting discrete equations using discrete transform methods. The second is to use the continuous solution for $\langle A' \rangle (X)_+$, which we have already derived, and evaluate it approximately by replacing all the integral transforms with their discrete counterparts, calculating these efficiently using the FFT. We decide to use the later approach, as it is more in-keeping with the work already presented.

Leaving aside the basic algebraic manipulations required to calculate $\langle A' \rangle (X)_+$ we must find a way to approximate both Fourier and Hilbert integral transforms of discrete data, using the FFT algorithm.

Approximating the Fourier Integral Transform

We begin by defining the discrete Fourier transform of a list of Q complex function values f_q for $q = 0, 1, \cdots, Q - 1$ to be

$$\widehat{f}_p = \sum_{q=0}^{Q-1} f_q e^{2\pi i p q / Q}, \tag{4.59}$$

for $p = 0, 1, \cdots, Q - 1$. The discrete inverse Fourier transform, which recovers the f_q's from the $\widehat{f}_p$'s exactly, is calculated according to the formula

$$f_q = \frac{1}{Q} \sum_{p=0}^{Q-1} \widehat{f}_q e^{-2\pi i p q/Q}, \tag{4.60}$$

for $q = 0, 1, \cdots, Q - 1$. We now attempt to find a way of approximating the Fourier integral transform (3.1) using the discrete transform definitions above.

Ideally we would like to find approximations for the Fourier integral transform at the discrete wavenumbers $K_m = 2\pi m/2L\Delta X$ for $m = -L, -L+1, \cdots, L-1$ given the $2L$ function values f_ℓ at the discrete positions $X_\ell = \ell\Delta X$ for $\ell = -L, -L+1, \cdots, L-1$. A natural way to find such a approximation using the discrete Fourier transform would be to write

$$\widehat{f}(K_m) = \int_{-\infty}^{\infty} f(X) e^{+iK_m X} dX \approx \Delta X \sum_{\ell=-L}^{L-1} f_\ell e^{2\pi i m \ell/2L}. \tag{4.61}$$

However, the limits in the sum immediately above are different from those appearing in equation (4.59) with $Q = 2L$. We can get around this problem by noting that equations (4.59) and (4.60) are periodic in p and q respectively with period Q. As a result we can reorder the f_ℓ's and define them, over the required range, to be

$$f_\ell = \left\{ \begin{array}{ll} f_\ell & \text{for} \quad 0 \leq \ell \leq L - 1 \\ f_{\ell - 2L} & \text{for} \quad L \leq \ell \leq 2L - 1 \end{array} \right\}, \tag{4.62}$$

for $\ell = 0, 1, \cdots, 2L - 1$.

This allows us to approximate the Fourier integral transform using the formula

$$\widehat{f}(K_m) \approx \left\{ \begin{array}{ll} \Delta X \widehat{f}_{m+2L} & \text{for} \quad -L \leq m \leq -1 \\ \Delta X \widehat{f}_m & \text{for} \quad 0 \leq m \leq L - 1 \end{array} \right\}, \tag{4.63}$$

valid for $m = -L, -L + 1, \cdots, L - 1$. In the above formula the $\widehat{f}_m$'s have been calculated from the reordered f_ℓ's according to the definition (4.59) with p replaced by m, q by ℓ, and Q by $2L$. Since the discrete Fourier transform defined in equation (4.59) can be performed extremely efficiently using the FFT algorithm this gives us

a computationally efficient way of approximating Fourier integral transforms. The Inverse Fourier transform can be approximated in a similar way.

The method above is only useful if the functions which we are attempting to Fourier transform or inverse Fourier transform are in some way localised and fall off towards zero quickly as $X \to \pm\infty$. If this is not the case end effect errors are introduced due to the approximate nature of equation (4.61). In order to combat this problem the Wiener-Hopf portion of the calculation is carried out on an extended domain, usually four times as large in X as that on which the boundary layer solution is calculated. The end effects errors then occur outside the normal solution domain and are discarded, leaving only the un-tainted central portion of the solution for $\langle A' \rangle (X)_+$ to be used as part of our solution algorithm.

Approximating the Hilbert Integral Transform

We define the Hilbert integral transform of $f(X)$ to be

$$f^*(\xi) = -\frac{1}{\pi i} \int_{-\infty}^{+\infty} \frac{f(X)}{(X - \xi)} dX. \qquad (4.64)$$

Since the above integral is of convolution type it may be calculated by first Fourier transforming $f(X)$ to give $\hat{f}(K)$, then multiplying this transform by the Fourier transformed Hilbert kernel $sgn(K)$ in wavenumber space, and then finally inverse Fourier transforming the resulting product $sgn(K)\hat{f}(K)$ to obtain $f^*(X)$. In this way we may calculate the Hilbert integral transform $f^*(\xi)$ using the Fourier transform $\hat{f}(K)$ which may be approximated efficiently using the discrete methods already discussed.

We have shown then that it is possible to construct a discrete Wiener-Hopf solution for $\langle A' \rangle (X)_+$ which can be efficiently evaluated using the FFT.

4.4.3 The Discretised Interaction Laws

The non-singular forms of the interaction laws (4.42) and (4.43) are discretised using central difference formulae to approximate the derivatives therein and Simpson's rule to approximate the integrals themselves. We define the approximations to the second and third derivatives of $A_\pm(X)$ at the ℓth streamwise station to be

$$A''_{\ell\pm} = \frac{A'_{(\ell+1)\pm} - A'_{(\ell-1)\pm}}{2\Delta X}, \tag{4.65}$$

$$A'''_{\ell\pm} = \frac{A'_{(\ell+1)\pm} - 2A'_{\ell\pm} + A'_{(\ell-1)\pm}}{(\Delta X)^2}, \tag{4.66}$$

respectively for $\ell = -L+1, \cdots, L-1$, the end point values $A''_{\pm L\pm}$ and $A'''_{\pm L\pm}$ being calculated using linear interpolation.

Using equation (4.42) as an example we then define the value of the integrand at the point $X = X_\ell$, $\xi = X_j$ to be

$$G^\ell_{j+} = \left\{ \begin{array}{ll} \frac{A'_{j+} - A'_{\ell+} - \Delta X(j-\ell)A''_{\ell+}}{(\Delta X)^2(j-\ell)^2} & for \quad j \neq \ell \\ \frac{1}{2}A'''_{\ell+} & for \quad j = \ell \end{array} \right\}. \tag{4.67}$$

The inviscid pressure gradient at the ℓth streamwise station $P'_{\ell I+}$ is then calculated, from equation (4.27), using Simpson's rule according to the formula

$$P'_{\ell I+} = -\frac{\Delta X}{3\pi} \left[G^\ell_{-L} + 4\sum_{j=1}^{L} G^\ell_{2j-L-1} + 2\sum_{j=1}^{L-1} G^\ell_{2j-1} + G^\ell_L \right]. \tag{4.68}$$

The approximation for $P'_{\ell I-}$ is calculated in a similar way using equation (4.43).

In the method outlined above we have ignored the tails of the integrals appearing in equations (4.42) and (4.43). This results in errors being introduced predominantly near the ends of the solution domain. The influence of these end effect errors over many global iterations can lead to spurious results and so they must be locally damped. This is accomplished by choosing an appropriate form for $\omega(X)$ in the relaxation equations (4.57) and (4.58), which falls away to zero near the ends of the solution domain.

4.4.4 The Solution of the Boundary Layer Equations

We discretise the governing boundary layer equations (4.46) and (4.47) and boundary conditions (4.48)-(4.53) using a second order accurate finite difference scheme. The resulting difference equations are then solved using a downstream line marching approach which, for given ℓ, solves the difference equations for all m simultaneously before moving on to repeat the procedure at the next streamwise station, $\ell + 1$, and so on. The marching process begins at the most negative streamwise station with the given upstream profiles and marches downstream, step by step, finding the solution profiles for ψ and Ω at each streamwise station until the entire solution domain has been covered. In fact due to the geometry of the problem the regions above, below, and in the wake of the aerofoil must be considered separately and in turn, however the principle remains the same.

For given ℓ the difference equations over m can together be written in the form of a non-linear matrix equation which is then solved numerically for ψ_m^ℓ and Ω_m^ℓ for all m using Newton's method. If no flow reversal is encountered only one downstream march is needed, if flow reversal does occur then multiple downstream marches using upwind differencing are required. The difference equations are derived in the next section before the solution of the resulting non-linear matrix equation, at given ℓ, is discussed in the section after that.

The Difference Equations

At the $(\ell, m)^{th}$ grid-point we use 3-point upwind and backward difference formulae to approximate the X-derivatives in the first and second terms on the right hand side of equation (4.46) respectively, and use 3-point central difference formulae to approximate all other Y-derivatives in the governing equations. We also include a FLARE switch θ which may be used to set the up-winded terms in the difference equations to zero in the case where no upwind information is currently available.

At the $(\ell, m)^{th}$ grid-point we obtain the discretised versions of equations (4.46) and (4.47) in the form of the non-linear difference equations

$$\alpha_m^\ell - r\left(\beta_m^\ell\left(b_m\gamma_m^\ell - \theta f_m\lambda_m^\ell\right) - \mu_m^\ell\nu_m^\ell\right) = 0, \qquad (4.69)$$

$$\rho_m^\ell - t\Omega_m^\ell = 0, \qquad (4.70)$$

where in the above

$$\alpha_m^\ell = \Omega_{m+1}^\ell - 2\Omega_m^\ell + \Omega_{m-1}^\ell, \qquad (4.71)$$

$$\beta_m^\ell = \psi_{m+1}^\ell - \psi_{m+1}^\ell, \qquad (4.72)$$

$$\gamma_m^\ell = 3\Omega_m^\ell - 4\Omega_m^{\ell-1} + \Omega_m^{\ell-2}, \qquad (4.73)$$

$$\lambda_m^\ell = 3\Omega_m^\ell - 4\Omega_m^{\ell+1} + \Omega_m^{\ell+2}, \qquad (4.74)$$

$$\mu_m^\ell = 3\psi_m^\ell - 4\psi_m^{\ell-1} + \psi_m^{\ell-2}, \qquad (4.75)$$

$$\nu_m^\ell = \Omega_{m+1}^\ell - \Omega_{m-1}^\ell, \qquad (4.76)$$

$$\rho_m^\ell = \psi_{m+1}^\ell - 2\psi_m^\ell + \psi_{m-1}^\ell, \qquad (4.77)$$

and the backward and forward differencing switches b_m and f_m take the values

$$b_m = \left\{\begin{array}{lll} 1 & \text{if} & \psi_{m+1}^{\ell-1} \geq \psi_{m-1}^{\ell-1} \\ 0 & \text{if} & \psi_{m+1}^{\ell-1} < \psi_{m-1}^{\ell-1} \end{array}\right\}, \qquad (4.78)$$

$$f_m = \left\{\begin{array}{lll} 0 & \text{if} & \psi_{m+1}^{\ell-1} \geq \psi_{m-1}^{\ell-1} \\ 1 & \text{if} & \psi_{m+1}^{\ell-1} < \psi_{m-1}^{\ell-1} \end{array}\right\}. \qquad (4.79)$$

The FLARE switch θ takes the value 1 if upwind differencing is to be used and the value 0 if the FLARE approximation is to be used. The constants r and t are related to grid-spacings ΔX and ΔY by the formulae

$$r = \frac{\Delta Y}{4\Delta X} \quad \text{and} \quad t = \Delta Y^2. \qquad (4.80)$$

The boundary conditions (4.48)-(4.53) are discretised using 3-point central difference formulae to approximate the Y-derivatives therein, using equation (4.70) on the

boundary to eliminate all references to quantities outside the solution domain. We obtain the discretised no slip conditions

$$\psi_0^\ell = 0, \tag{4.81}$$

$$\pm 2 \left(\psi_{\pm 1}^\ell - \psi_0^\ell \right) \mp t\Omega_0^\ell = 0, \tag{4.82}$$

valid for $-L \leq \ell \leq 0$ on the upper and lower surfaces of the aerofoil, and the discretised main deck matching conditions

$$\pm 2 \left(\psi_{\pm M}^\ell - \psi_{\pm M \mp 1}^\ell \right) \pm t\Omega_{\pm M}^\ell - 2\Delta Y \left(|Y_{\pm M}| \pm A_{\ell \pm} \right) = 0, \tag{4.83}$$

$$\Omega_{\pm M}^\ell \mp 1 = 0, \tag{4.84}$$

valid for $-L \leq \ell \leq L$, which are applied at the outermost grid-points in Y, $m = \pm M$. The discretised upstream boundary conditions are

$$\psi_m^{-L} = \left\{ \begin{array}{ll} +\frac{1}{2} |Y_m|^2 & \text{for} \quad m > 0 \\ -\frac{1}{2} |Y_m|^2 & \text{for} \quad m < 0 \end{array} \right\}, \tag{4.85}$$

$$\Omega_m^{-L} = \left\{ \begin{array}{ll} +1 & \text{for} \quad m > 0 \\ -1 & \text{for} \quad m < 0 \end{array} \right\}, \tag{4.86}$$

where the true boundary conditions (4.52) and (4.53) have been approximated by imposing them at the most negative streamwise station in the discretised solution domain, $\ell = -L$.

The Iterative Matrix Solution at Each Step

As an example we will consider the solution of the difference equations above the aerofoil and up to the trailing edge in the region where $-L \leq \ell \leq 0$ and $0 \leq m \leq M$. At the ℓth streamwise station all upwind information is assumed known and equations (4.69) and (4.70) with $m = 1, 2, \cdots, M - 1$ supplemented with the relevant no slip conditions (4.81) and (4.82) and main deck matching conditions (4.83) and (4.84) constitute $2(M + 1)$ equations in the $2(M + 1)$ unknowns ψ_m^ℓ

and Ω_m^ℓ for $m = 0, 1, \cdots, M$. It is therefore possible to find the solution to these difference equations using Newton's method for nonlinear matrix equations. See Golub and Van Loan (1996).

Newton's method requires that we make initial guesses for the solution profiles $\psi_m^{\ell(0)}$ and $\Omega_m^{\ell(0)}$ for $m = 0, 1, \cdots, M$. It then updates these guesses according to the formulae

$$\psi_m^{\ell(i+1)} = \psi_m^{\ell(i)} - \Delta\psi_m^{\ell(i)}, \tag{4.87}$$

$$\Omega_m^{\ell(i+1)} = \Omega_m^{\ell(i)} - \Delta\Omega_m^{\ell(i)}, \tag{4.88}$$

by solving a linearised matrix equation for the small changes $\Delta\psi_m^{\ell(0)}$ and $\Delta\Omega_m^{\ell(0)}$ for $m = 0, 1, \cdots, M$, where i refers to the current Newton iteration number. The process is repeated until the maximum absolute value of the small changes $\Delta\psi_m^{\ell(i)}$ and $\Delta\Omega_m^{\ell(i)}$ is less than some specified tolerance.

The linearised matrix equation for the small changes, $\Delta\psi_m^{\ell(i)}$ and $\Delta\Omega_m^{\ell(0)}$, takes the following block tri-diagonal form

$$\begin{bmatrix} B_0 & C_0 & 0 & \cdots & \cdots & \cdots & 0 \\ A_1 & B_1 & C_1 & & & & \vdots \\ 0 & \ddots & \ddots & \ddots & & & \vdots \\ \vdots & & A_m & B_m & C_m & & \vdots \\ \vdots & & & \ddots & \ddots & \ddots & 0 \\ \vdots & & & & A_{M-1} & B_{M-1} & C_{M-1} \\ 0 & \cdots & \cdots & \cdots & 0 & A_M & B_M \end{bmatrix} \begin{bmatrix} \Delta_0 \\ \Delta_1 \\ \vdots \\ \Delta_m \\ \vdots \\ \Delta_{M-1} \\ \Delta_M \end{bmatrix} = \begin{bmatrix} D_0 \\ D_1 \\ \vdots \\ D_m \\ \vdots \\ D_{M-1} \\ D_M \end{bmatrix},$$

$$\tag{4.89}$$

where the solution is arranged in terms of the two-vectors Δ_m where

$$\Delta_m = \begin{bmatrix} \Delta\psi_m^{\ell(i)} \\ \Delta\Omega_m^{\ell(i)} \end{bmatrix}, \tag{4.90}$$

for $m = 0, 1, \cdots, M$ and in the above A_m, B_m, C_m, and D_m are the two-by-two matrices and two-vectors

$$A_m = \begin{bmatrix} r \left(b_m \gamma_m^\ell - \theta f_m \lambda_m^\ell \right) & 1 - r \mu_m^\ell \\ 1 & 0 \end{bmatrix}, \tag{4.91}$$

$$B_m = \begin{bmatrix} 3r\nu_m^\ell & -2 - 3r \left(b_m - \theta f_m \right) \beta_m^\ell \\ -2 & -t \end{bmatrix}, \tag{4.92}$$

$$C_m = \begin{bmatrix} -r \left(b_m \gamma_m^\ell - \theta f_m \lambda_m^\ell \right) & 1 + r \mu_m^\ell \\ 1 & 0 \end{bmatrix}, \tag{4.93}$$

$$D_m = \begin{bmatrix} \alpha_m^\ell - r \left(\beta_m^\ell \left(b_m \gamma_m^\ell - \theta f_m \lambda_m^\ell \right) - \mu_m^\ell \nu_m^\ell \right) \\ \rho_m^\ell - t \Omega_m^\ell \end{bmatrix}, \tag{4.94}$$

respectively for $m = 1, 2, \cdots, M - 1$. The remaining entries

$$B_0 = \begin{bmatrix} 1 & 0 \\ -2 & -t \end{bmatrix}, \tag{4.95}$$

$$C_0 = \begin{bmatrix} 0 & 0 \\ 2 & 0 \end{bmatrix}, \tag{4.96}$$

$$D_0 = \begin{bmatrix} \psi_0^\ell \\ 2 \left(\psi_1^\ell - \psi_0^\ell \right) - t \Omega_0^\ell \end{bmatrix}, \tag{4.97}$$

$$A_M = \begin{bmatrix} -2 & 0 \\ 0 & 0 \end{bmatrix}, \tag{4.98}$$

$$B_M = \begin{bmatrix} 2 & t \\ 0 & 1 \end{bmatrix}, \tag{4.99}$$

$$D_M = \begin{bmatrix} 2 \left(\psi_M^\ell - \psi_{M-1}^\ell \right) + t \Omega_M^\ell - 2 \Delta Y \left(|Y_M| + A_{\ell+} \right) \\ \Omega_m^\ell - 1 \end{bmatrix}, \tag{4.100}$$

are derived from the discretised no slip and main deck matching conditions (4.81)-(4.84).

The matrix equation (4.89) is now solved at given ℓ and i for the Δ_m's using a block Thomas algorithm which makes efficient use of the equation's tri-diagonal form. See

Strikwerda (1989). Furthermore the solution algorithm is optimised to take account of the zeroes appearing in the lower right hand corners of the block matrices A_m and C_m. This optimisation improves the efficiency of the algorithm by up to 25%.

The initial guesses $\psi_m^{\ell(0)}$ and $\Omega_m^{\ell(0)}$ are taken to be the solution profiles at the previous streamwise station $\psi_m^{\ell-1}$ and $\Omega_m^{\ell-1}$ respectively. On average these guesses were observed to converge to the true solution profiles, to within a tolerance of 10^{-10}, after four Newton iterations.

Post Processing

After the line marching process is complete and the solutions for ψ_m^ℓ and Ω_m^ℓ have been found for all ℓ and m the streamwise and and transverse components of velocity U_m^ℓ and V_m^ℓ may be found from discretised versions of equations (4.44) and (4.45) respectively. We use 3-point backward and central difference formulae to approximate the X and Y derivatives respectively in these equations. In the example that we are considering for given ℓ we obtain

$$U_m^\ell = \frac{\psi_{m+1}^\ell - \psi_{m-1}^\ell}{2\Delta Y}, \tag{4.101}$$

$$V_m^\ell = -\frac{3\psi_m^\ell - 4\psi_m^{\ell-1} + \psi_m^{\ell-2}}{2\Delta X}, \tag{4.102}$$

for $m = 1, 2, \cdots, M - 1$, the remaining values being given by

$$U_0^\ell = 0, \tag{4.103}$$

$$V_0^\ell = 0, \tag{4.104}$$

$$U_M^\ell = |Y_M| + A_{\ell+}, \tag{4.105}$$

$$V_M^\ell = -\frac{3\psi_M^\ell - 4\psi_M^{\ell-1} + \psi_M^{\ell-2}}{2\Delta X}. \tag{4.106}$$

The viscous pressure gradients $P'_{V\pm}(X)$ are retrieved using discrete versions of either equation (4.54) or (4.55), or an average of the two. In our example we take a straight average of the two, applying 3-point upward differencing for the Y-derivative in

(4.54) to obtain

$$P'_{\ell V+} = -\frac{1}{2}\left(\frac{3\Omega_0^\ell - 4\Omega_1^\ell + \Omega_2^\ell}{2\Delta Y} + A_{\ell+}A'_{\ell+} + V_M^\ell + |Y_M|\,A'_{\ell+}\right). \qquad (4.107)$$

Since we are employing 3-point backward difference formulae to approximate the X-derivatives in the governing equations we cannot use the scheme described above at the first streamwise station $\ell = -L + 1$ as references would be made to quantities outside the solution domain. At this first location we are forced to use a first order accurate scheme, based on the current scheme, with all 3-point backward differences being replaced by the corresponding 2-point ones.

4.5 Further Comments

It was found that the numerical algorithm described in this chapter would only lead to a globally converged solution if the following minor adjustments were made.

To begin with we are forced to hold $A'_-(x)$ fixed, ignoring the relaxation equation (4.58). A converged solution is then found for $A'_+(x)$ using equation (4.57) as normal. Afterward, the roles of $A'_+(x)$ and $A'_-(x)$ are reversed, $A'_+(x)$ being held fixed whilst $A'_-(x)$ is adjusted. We will refer to this process as one 'back-and-forth' iteration cycle. This cycle is repeated and leads, eventually, to a globally converged solution satisfying all the required constraints.

It is also noted that the Wiener-Hopf part of the algorithm, described in section (4.4.2), is only required during the first 'back-and-forth' iteration cycle in order to provide a sufficiently accurate initial approximation to the solution. After this the relaxation equations (4.57) and (4.58) coupled with the boundary layer solver are capable of ensuring pressure continuity in the wake. In fact if the Wiener-Hopf solver is not discarded at this stage it tends to ruin the solution by adversely effecting the relaxation process. Converged solutions for a range of scaled ground clearances, $\bar{\alpha} = \bar{\beta}/2$, are presented in the next section.

4.6 Flow Properties

The Figures 4.3, 4.4, 4.5, and 4.6 show the converged solutions for $P_\pm(X)$, $A'_\pm(X)$, $A_\pm(X)$, and $\Omega_\pm(X,0)$ respectively for a wide range of scaled ground clearances $\bar{\alpha}$. The flow in each of the lower, main, and upper decks can be reconstructed from the functions $P_\pm(X)$ and $A_\pm(X)$ and so these functions effectively define the entire triple-deck solution for flows with ground interference. We notice a number of trends in the solutions which are worthy of note.

Firstly, for large $\bar{\alpha}$ the solution approaches the symmetric solution, of Jobe and Burggraf (1974), for the flow past the trailing edge of a flat plate in the absence of the ground, as it should. We can understand precisely why this is so by taking the limit $\bar{\beta} \to +\infty$ in the interaction equations (4.29) and (4.30). If we do this we obtain

$$P'_-(X) = \frac{1}{\pi} \int_{-\infty}^{+\infty} \frac{A''_-(\xi)}{(\xi - X)} d\xi + \cdots, \qquad (4.108)$$

$$A''_-(X) = -\frac{1}{\pi} \int_{-\infty}^{+\infty} \frac{P'_-(\xi)}{(\xi - X)} d\xi + \cdots, \qquad (4.109)$$

to leading order, which are symmetric versions of (4.27) and (4.30), the interaction laws for the pressure and displacement above the plate. As a result the solution to the system of equations (4.11)-(4.26) for $\bar{\beta} \gg 1$ must be small perturbation of the symmetric solution given by Jobe and Burggraf (1974).

As the ground clearance $\bar{\alpha}$ is decreased, we notice more and more asymmetry in the solution. The streamwise length scale on which the pressure, $P_-(X)$, varies from its upstream value beneath the plate scales with $\bar{\alpha}$. The magnitude of the displacement gradient, $A'_-(X)$, also decreases in line with $\bar{\alpha}$, showing that less and less fluid is being drawn into the viscous lower deck from below. A similar wake-flattening effect was seen in the inviscid solutions of Chapters 2 and 3 as α was reduced. The displacement, $A_-(X)$, also shows a corresponding decrease in magnitude and most
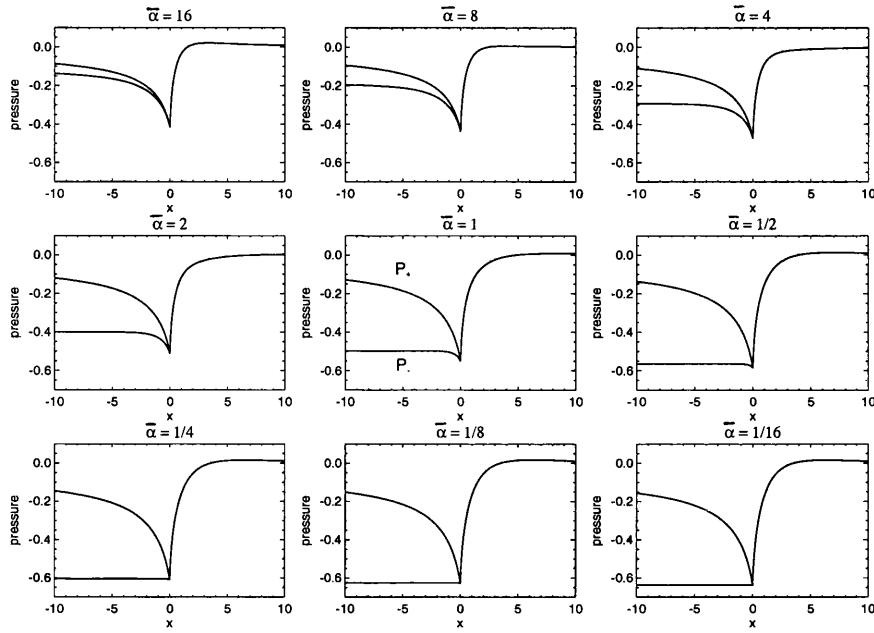
Figure 4.3: The triple deck pressures $P_\pm(X)$ for a flat plate in ground effect for $\bar{\alpha} = 16$ to $\frac{1}{16}$
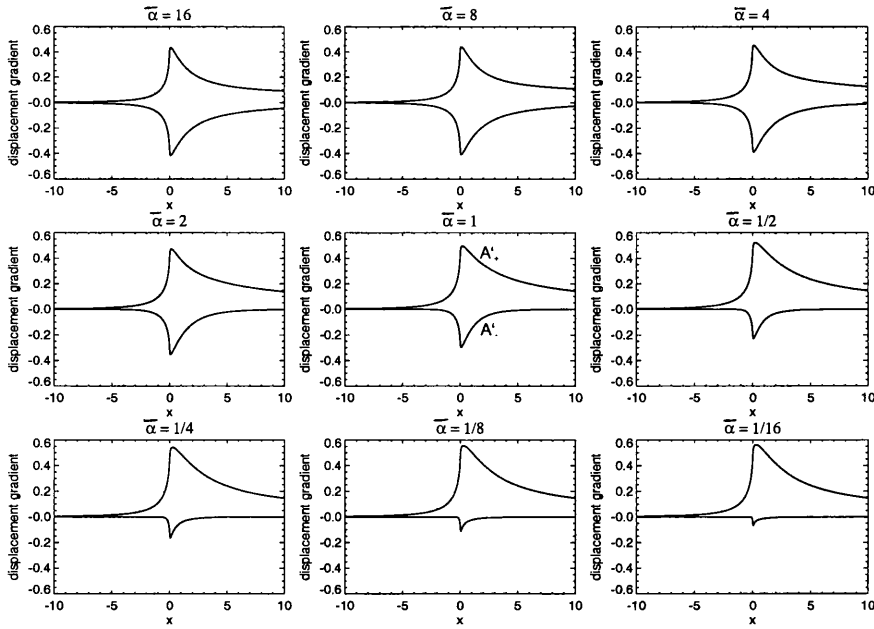
Figure 4.4: The triple deck displacement gradients $A'_\pm(X)$ for a flat plate in ground effect for $\bar{\alpha} = 16$ to $\frac{1}{16}$
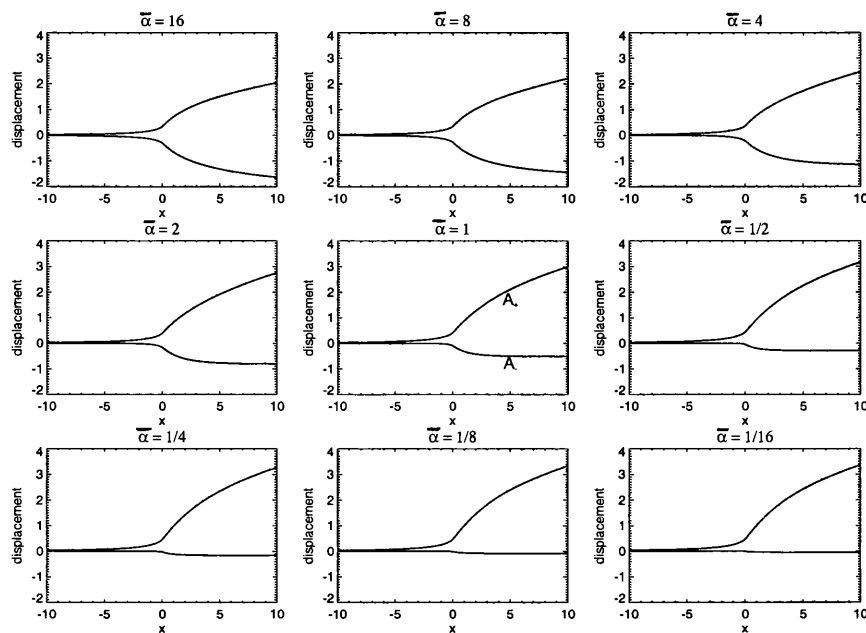
Figure 4.5: The triple deck displacements $A_\pm (X)$ for a flat plate in ground effect for $\bar{\alpha} = 16$ to $\frac{1}{16}$
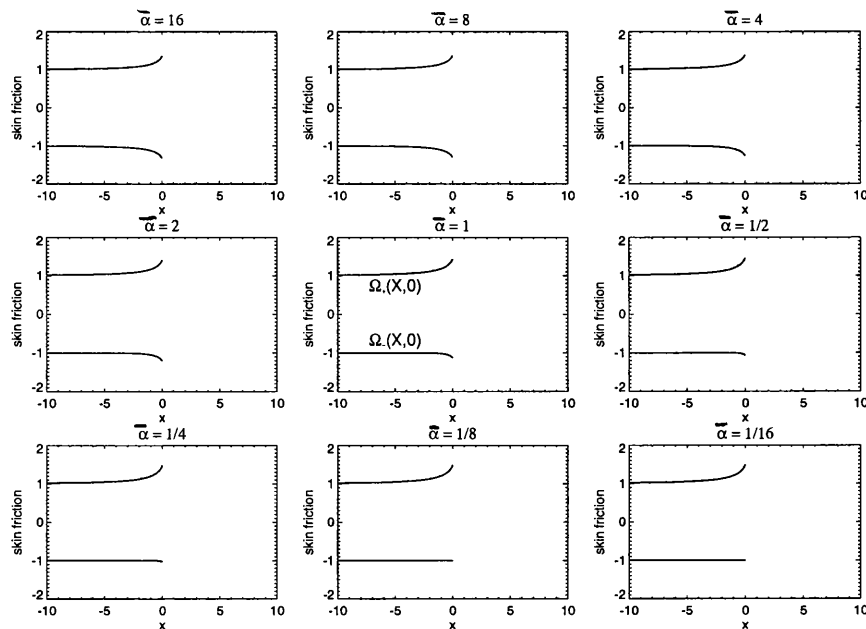
Figure 4.6: The normalised skin frictions $\Omega_\pm (X, 0)$ on the trailing edge of a flat plate in ground effect for $\bar{\alpha} = 16$ to $\frac{1}{16}$

importantly is shown to approach a constant downstream instead of growing like $X^{1/3}$, as in the triple-deck solution of Jobe and Burggraf (1974).

For small $\bar{\alpha}$ it is possible to quantify these trends more precisely by again using the interaction laws (4.29) and (4.30), this time in the limit $\bar{\beta} \to 0$. Examination of equation (4.43), which is effectively the asymptotic expansion of the interaction law (4.29) for small $\bar{\beta}$, shows that the second term on the right hand side of equation (4.43) dominates for small $\bar{\beta}$. This fact used together with equation (4.37), which comes from the Wiener-Hopf analysis of the interaction laws in the form (4.17) and (4.18), leads to the small $\bar{\alpha}$ interaction law

$$P_- (X) = \frac{A_- (+\infty) - A_- (X)}{\bar{\alpha}} + \cdots, \qquad (4.110)$$

to leading order for the pressure and displacement beneath the plate.

The above interaction law explains much. Since no trailing edge pressure eigensolution is permitted, due to the Kutta condition, the pressure, $P_- (X)$, must remain of order unity. As a result, equation (4.110) informs us that to leading order the magnitude of the displacement, $A_- (X)$, must scale with $\bar{\alpha}$. This trend is indeed confirmed by the numerical solutions in Figure 4.5 and in the solutions presented in Appendix C.

For small $\bar{\alpha}$ then, the flow beneath the plate remains largely unchanged from its upstream form, as confirmed by the value of the skin friction in Figure 4.6, until the trailing edge at which point it must adjust itself, on a length scale $\bar{\alpha}$, so as to join with the flow from above the plate. No flow separations were seen in the solutions, as expected.

Chapter 5

Viscous 'Wing-In-Ground' Effect

5.1 Introduction

In this chapter we broaden our view again and consider the flow past a thin aerofoil travelling extremely close to the ground, so close in fact that the moving ground now interferes with the boundary layer flow, on the underside of the aerofoil, directly. The ground is now inside the classical boundary layer and the non-dimensional ground clearance α is consequently of order $Re^{-1/2}$, the classical boundary layer thickness, smaller than in the previous chapters. We again introduce a scaled ground clearance parameter $\hat{\alpha}$, by writing α as $\hat{\alpha}Re^{-1/2}$.

The inviscid small β solution for $p_-(x)$ presented towards the end of Chapter 3 informs us that the leading order term in the pressure solution beneath the aerofoil is of order $Re^{-1/2}\alpha^{-1}$ for small α. Taken to the extreme this <u>inviscid</u> theory suggests that, in the current regime where α is of order $Re^{-1/2}$, the pressure beneath the aerofoil will be of order unity. It is therefore possible to create large overall lifting forces on vehicles which are moving extremely close to the ground, in what is termed <u>extreme</u> wing-in-ground effect.

The driving force behind much of the work presented in this chapter comes from

the world of Formula One racing car design. In this field, instead of using extreme wing-in-ground effect to produce large lifting forces, the large pressures created in the gap between the vehicle and the ground are made negative and therefore create large negative lift or downforce on the vehicle. This downforce presses the racing car onto the ground and leads to better acceleration and faster cornering due to the resulting increased traction.

An underbody shape which has a minimum ground clearance near the front of the car and a gentle divergence of the gap thereafter tends, in practice, to create a beneficial overall downforce. One disadvantage of such an undertray shape is that it creates an adverse pressure gradient towards the trailing edge of the vehicle which can lead to separation of the air flow. One of the aims of this chapter is to develop a theory which can accurately model the important fluid dynamical mechanisms involved in such underbody flows and use this theory to investigate the effects of undertray shape on downforce production.

In reality the flow beneath a racing car is complex, three-dimensional, unsteady, and probably turbulent for the most part ; see computations and experiments described in Dominy (1990, 1992), Wright (1982), Katz (1985a,b), Jacob (1986), Suh and Ostowari (1988), Bearman (1980), and Chawla et al. (1990). On the other hand, little research of a theoretical nature appears to have been done on the fundamental flow mechanisms addressed in this chapter, although significant contributions on various related aspects are by Widnall and Barrows (1970), Newman (1982), Tuck and Bentwich (1983), Szeri (1987), Tichy (1986), Plotkin and Dodbele (1988), Wilson and Duffy (1998), Jensen (1998) and references therein. Accordingly it seems sensible, as a first basic step, to begin by considering only the incompressible range of two-dimensional, steady, laminar flows as we do in this chapter. These flow conditions are most likely to occur in practice over the front wing of a racing car and so it is with this geometry in mind that we begin. See Figures 5.1 and 5.2. Wheels and their influence on underbody flows are not considered here.

Throughout this thesis we have focused on the physical mechanisms underpinning the wing-in-ground effect phenomenon and in this chapter we continue with this approach. The mechanisms encountered here include a viscous-inviscid interaction which fills the entire gap between the vehicle and the ground and is again associated with the requirement of pressure continuity at the trailing edge, the generation of strong upstream influence which forces a localised pressure jump at the leading edge, and substantial flow reversal and separation including certain wake effects. The fact that viscous forces fill the entire gap is important not only because this allows us to treat flow separations in a regular fashion but also because as a result the moving ground condition can be incorporated directly. Both flow separation and the moving ground condition are known to be of fundemental importance from an experimental standpoint.

5.2 Problem Formulation

To begin with, we will consider only thin aerofoil-type bodies of the sort found on the front wing of a racing car. The basic flow geometry and dominant scales are shown in Figure 5.2 . In most places, x is of order unity comparable with the aerofoil's length, y is of order $Re^{-1/2}$, U is of order unity due to the moving ground condition, V is of order $Re^{-1/2}$ from a continuity balance, and P is of order unity from a momentum balance. The above order of magnitude estimates in fact hold upstream, above, below, and in the wake of the aerofoil in regions I, II$_{\pm}$, and III respectively .

There is also a distinct local leading edge region, akin to that encountered in the inviscid small β solutions of Chapter 3, where x is of order $Re^{-1/2}$, comparable with y, and consequently V grows to become of order unity, comparable with U. This leading edge region, region IV, plays an important role. Another less significant region is centred around the trailing edge. It is thought to have a triple-deck-like

Figure 5.1: The front wing or downforce diffuser on the McLaren F1 racing car
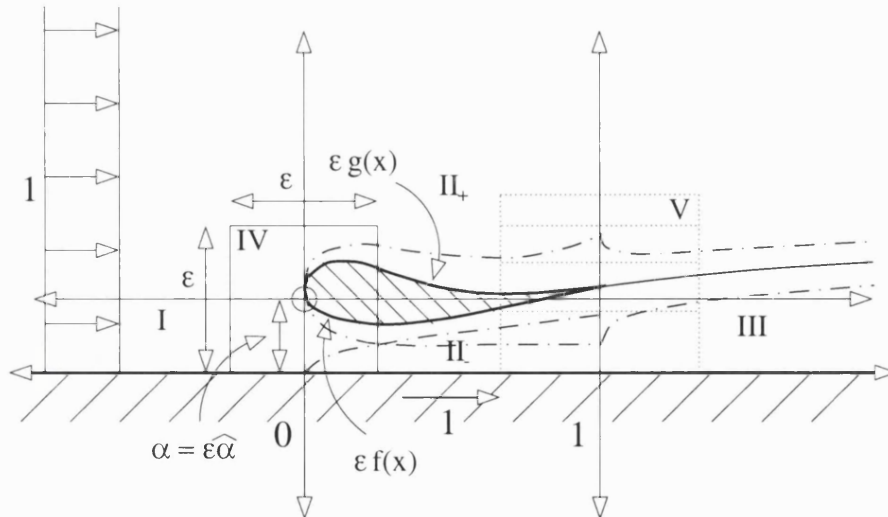
Figure 5.2: Cross-section of a thin aerofoil in extreme ground effect. The boundary layers associated with the aerofoil and the ground merge producing a fully viscous solution beneath the aerofoil.

structure similar to that studied in Chapter 4 for small $\bar{\beta}$. However, the flow in this region, region V, is not considered here.

The comments made above and in the introduction all point towards an application of the viscous boundary layer equations upstream, above, below, and in the wake of the aerofoil and after introducing the scaled transverse co-ordinate $Y = \hat{\alpha} + y/\varepsilon$ we seek a solution of the form

$$U(x,y) = u(x,Y) + \cdots, \tag{5.1}$$

$$V(x,y) = 0 + \varepsilon v(x,Y) + \cdots, \tag{5.2}$$

$$P(x,y) = p(x,Y) + \cdots, \tag{5.3}$$

valid in the above regions, where $\varepsilon = Re^{-1/2}$ is the typical classical boundary layer thickness, aerofoil thickness, and gap thickness. The governing equations, in the gap between the aerofoil and the ground in particular, are the viscous interactive boundary layer equations

$$u\frac{\partial u}{\partial x} + v\frac{\partial u}{\partial Y} = -p'_-(x) + \frac{\partial^2 u}{\partial Y^2}, \tag{5.4}$$

$$\frac{\partial u}{\partial x} + \frac{\partial v}{\partial Y} = 0, \tag{5.5}$$

which must be solved subject to the no slip boundary conditions

$$u(x,0) = 1, \tag{5.6}$$

$$v(x,0) = 0, \tag{5.7}$$

$$u(x,f(x)) = 0, \tag{5.8}$$

$$v(x,f(x)) = 0, \tag{5.9}$$

on the moving ground $Y = 0$ and the underside of the aerofoil $Y = f(x)$ respectively and the other conditions

$$u(0,Y) = u_0 \quad \text{for} \quad 0 < Y < f(0), \tag{5.10}$$

$$p_-(1) = 0, \tag{5.11}$$

which are explained below. Subscripts $+$ and $-$ are used to refer to quantities above and below the aerofoil respectively.

The constraint (5.11) is the, by now familiar, pressure continuity condition. The pressure $p_-(x)$ is unknown making the viscous flow directly beneath the aerofoil interactive in the sense that the displacement is prescribed due to mass flux considerations.

The physical expectation is that overall the pressure $p_-(x)$ will fall from say p_0 at the leading edge to p_1 at the trailing edge. On the other hand the pressures upstream, above, and in the wake of the aerofoil must be identically equal to zero due to the fact that the solution there must match with the free stream $u(x, Y) = 1$, $v(x, Y) = 0$, and $p(x) = 0$ as $Y \to +\infty$. The Kutta condition states that no local eigensolution is permitted at the trailing edge and so p_1 must be equal to zero in order to match with the pressures above and in the wake of the aerofoil. Hence constraint (5.11).

At first sight this argument poses a dilemma since it suggests that a pressure mismatch at the leading edge is unavoidable. However, a leading edge eigensolution, which is able to locally smooth the proposed pressure jump, *is* permitted and so all is well. The details of the leading edge eigensolution are given in Appendix D. However, it is necessary to state here that the flow properties in the leading edge region are essentially inviscid, the governing equations being the Euler equations in the local unknowns $U_0(X, Y)$, $V_0(X, Y)$, and $P_0(X, Y)$ all of which are of order unity. It is also useful to note that the eigensolution takes the simple asymptotic form $U_0(X, Y) = u_0$, $V_0(X, Y) = 0$, and $P_0(X, Y) = p_0$ inside the gap just downstream of the leading edge where the constants u_0 and p_0 are related by the formula

$$p_0 = \frac{1}{2}\left(1 - u_0^2\right), \tag{5.12}$$

since Bernouilli's equation states that $H = P + \frac{1}{2}(U^2 + V^2)$ is preserved at its upstream value of $\frac{1}{2}$ along all streamlines throughout the local leading edge region.

The starting pressure p_0, which determines the value of u_0, is <u>unknown</u> and must be chosen such that integration of the system of equations (5.4)-(5.10) from the leading edge to the trailing edge leads to a trailing edge pressure of zero, satisfying the pressure continuity condition (5.11).

The strong adjustment at the leading edge, implied by equation (5.10), is a non-linear version of the leading edge pressure jump effect studied in Chapter 3 and agrees with similar phenomena found in internal branching flows, Smith and Jones (1999), in non-symmetric blade-wake interactions, Bowles and Smith (1999), and in the problems encountered earlier in this thesis and all in a sense reflect the strength of the Kutta condition at the trailing edge.

The same boundary layer equations (5.4) and (5.5) govern the flow dynamics above, upstream, and in the wake of the aerofoil but with $p(x) = p_+(x) = 0$ respectively as mentioned earlier.

The solution upstream of the aerofoil is simply $u(x, Y) = 1$, $v(x, Y) = 0$, and $p(x) = 0$. The flow above the aerofoil starts with this uniform stream

$$u(0, Y) = 1, \tag{5.13}$$

and must satisfy the no slip conditions

$$u(x, g(x)) = 0, \tag{5.14}$$
$$v(x, g(x)) = 0, \tag{5.15}$$

on the upper surface of the aerofoil $Y = g(x)$ together with the free stream matching condition

$$u(x, +\infty) = 1. \tag{5.16}$$

As a result the solution there is a Prandtl shifted Blasius solution in co-ordinates x and $Y - g(x)$ (see Appendix A). This solution, at the trailing edge, determines the upper part of the starting profile for the wake region, the lower part being provided

by the numerical solution for the flow beneath the aerofoil. The solution in the wake is then obtained numerically by marching the composite starting profile downstream, subject to the no slip conditions (5.6) and (5.7) on the moving ground and the free stream matching condition (5.16) in the far field.

5.3 Mathematical Methods

The central task then is the interactive one of solving (5.4)-(5.11) numerically for the fluid motion directly beneath the aerofoil. Before we address this problem we again remark on the physical mechanisms active here.

They involve a viscous-inviscid coupling over the entire length of the aerofoil, a fixed mass flux in the gap driving a viscous pressure response there, a trailing edge pressure continuity condition, pronounced upstream influence together with an associated pressure jump at the leading edge, and the direct influence of the no slip condition on the moving ground. Moreover, the quasi-fixed displacement in the gap, due to the constant mass flux there, allows us to incorporate flow separations in a regular way. Most importantly, the leading edge pressure jump and the confined nature of the flow geometry work together to allow the creation of the anomalously high or low gap pressures observed in practice.

5.3.1 The Flow Directly Beneath the Aerofoil

In order to find a numerical solution for the flow in the gap we again use a streamfunction vorticity formulation and introduce the streamfunction $\psi(x, Y)$ such that

$$u(x, Y) = \frac{\partial \psi}{\partial Y}, \tag{5.17}$$

$$v(x, Y) = -\frac{\partial \psi}{\partial x}. \tag{5.18}$$

Differentiation of equation (5.4) with respect to Y then eliminates the pressure gradient term, $p'_-(x)$, and together with the introduction of the negative vorticity, $\Omega(x, Y)$, leads to the governing streamfunction-vorticity boundary layer equations

$$\frac{\partial^2 \Omega}{\partial Y^2} = \frac{\partial \psi}{\partial Y} \frac{\partial \Omega}{\partial x} - \frac{\partial \psi}{\partial x} \frac{\partial \Omega}{\partial Y}, \tag{5.19}$$

$$\frac{\partial^2 \psi}{\partial Y^2} = \Omega. \tag{5.20}$$

Before posing the problem in terms of the streamfunction and the vorticity we make a change of variables which, whilst transforming the aerofoil undersurface onto a straight line, also allows us to control the spatial resolution of the numerical solution. The transformation we use is

$$x = k(\xi), \tag{5.21}$$

$$Y = h(\zeta) f(\xi), \tag{5.22}$$

where ξ and ζ are the computational co-ordinates with $k(0) = h(0) = 0$, $k(1) = h(1) = 1$, and $f(\xi) = f(k(\xi))$. It is our intention to discretise the solution domain using an equi-spaced Cartesian grid in computational space and so the functions $k(\xi)$ and $h(\zeta)$ can be used to determine the exact distribution of the data points in physical space. Upon making the above transformation the governing equations, in our computational co-ordinates ξ and ζ, become

$$\frac{\partial^2 \Omega}{\partial \zeta^2} = \frac{h'f}{k'} \left(\frac{\partial \psi}{\partial \zeta} \frac{\partial \Omega}{\partial \xi} - \frac{\partial \psi}{\partial \xi} \frac{\partial \Omega}{\partial \zeta} \right) + \frac{h''}{h'} \frac{\partial \Omega}{\partial \zeta}, \tag{5.23}$$

$$\frac{\partial^2 \psi}{\partial \zeta^2} = (h'f)^2 \Omega + \frac{h''}{h'} \frac{\partial \psi}{\partial \zeta}, \tag{5.24}$$

and must now be solved subject to the simplified no slip boundary conditions

$$\psi(\xi, 0) = 0, \tag{5.25}$$

$$\frac{\partial \psi}{\partial \zeta}(\xi, 0) = h'(0) f(\xi), \tag{5.26}$$

$$\psi(\xi, 1) = u_0 f(0), \tag{5.27}$$

$$\frac{\partial \psi}{\partial \zeta}(\xi, 1) = 0, \tag{5.28}$$

on the moving ground, $\zeta = 0$, and the underbody surface, $\zeta = 1$. We must also impose the upstream boundary conditions

$$\psi\,(0,\zeta) \;=\; u_0, \tag{5.29}$$

$$\Omega\,(0,\zeta) \;=\; 0, \tag{5.30}$$

$$p_-\,(0) \;=\; p_0, \tag{5.31}$$

and the pressure continuity condition (5.11). We note that equations (5.23) and (5.24) remain of a similar form to (5.19) and (5.20) and remind ourselves that the constants p_0 and u_0 are related by equation (5.12).

5.4   Numerical Methods

The computational task of solving the transformed equations (5.23)-(5.31) has to incorporate upstream influence through the unknown starting pressure p_0 and the trailing edge pressure continuity condition (5.11). We achieve this using multi-sweeping in x. An outline of the solution algorithm is given below.

First we make a guess for p_0. Then, we numerically integrate the transformed boundary layer equations (5.23) and (5.24) from the leading edge, where the starting conditions (5.29)-(5.31) apply, to the trailing edge. Thus we obtain a value for $p_-\,(1)$, the pressure at the trailing edge. At this point we check whether the pressure continuity condition (5.11) is satisfied. If it is not then a better approximation for p_0 is obtained automatically, using a secant algorithm, and the steps outlined above are repeated. We continue to update p_0 in this way until condition (5.11) is satisfied to within a specified tolerance.

An alternative approach would be to set p_0 then march the boundary layer solution downstream, just once, until the pressure was zero. It would then be possible to renormalise the lengths and velocities in the problem appropriately so that the pressure zero occurred at the trailing edge. This method was considered but lead

to uncontrolled grid spacings and in any case the first method proved relatively inexpensive computationally.

Close to $x = 0$, for small positive x, the flow solution near each solid surface is Blasius-like, in the sense that the similarity equation

$$q''' (\eta) + \frac{1}{2} q (\eta) \, q'' (\eta) \;\; = \;\; 0, \tag{5.32}$$

holds there for the scaled effective streamfunction $q (\eta)$.

Near the ground $Y = \eta x^{1/2}$ is small, $\psi = x^{1/2} q (\eta)$, and the boundary conditions on $q (\eta)$ are $q (0) = 0$, $q' (0) = 1$, and $q' (+\infty) = u_0$. Whereas near the underbody surface $Y - f (0) = -\eta x^{1/2}$ is small, $\psi - u_0 f (0) = -x^{1/2} q (\eta)$, and $q (\eta)$ must satisfy the conditions $q (0) = 0$, $q' (0) = 0$, and $q' (+\infty) = u_0$.

In between these growing boundary layer regions there is an inviscid core flow which is an order $x^{1/2}$ perturbation of the streamfunction profile $\psi = u_0 Y$. From the mass and momentum balances the induced pressure, $p_- (x) - p_0$, is of order $x^{1/2}$ also.

These irregular starting behaviours provide guidelines on what sort of the fine mesh distribution, controlled by the functions $k (\xi)$ and $h (\zeta)$, is required computationally near $x = 0$.

5.4.1   The Basic Discretisation

We discretise the solution domain using an equi-spaced Cartesian grid in computational space with grid-spacings $\Delta\xi$ and $\Delta\zeta$ in the streamwise and transverse directions respectively. This corresponds to an irregularly spaced grid in physical space which is determined by the exact form of $k (\xi)$ and $h (\zeta)$. The $(\ell, m)^{th}$ grid point has coordinates $(\ell\Delta\xi, m\Delta\zeta)$ in computational space, where the indices ℓ and m run from 0 to L and 0 to M respectively.

At the $(\ell, m)^{th}$ grid point the values of the streamfunction and the vorticity are

denoted ψ_m^ℓ and Ω_m^ℓ respectively. At the ℓth streamwise station the pressure $p_-(x)$ and its first derivative are denoted p_ℓ and p_ℓ' respectively.

5.4.2 The Difference Equations

As in Chapter 4 we use 3-point upwind and backward difference formulae to approximate the ζ-derivatives appearing in the first and second terms of the Jacobian in equation (5.23) respectively. All ζ-derivatives are approximated using 3-point central difference formulae. We also include a FLARE switch, θ, which may be used in the event that flow reversal is encountered at a point in the solution domain where no information is available downstream.

Upon discretisation equations (5.23) and (5.24) become

$$\alpha_m^\ell - r_m^\ell \left(\beta_m^\ell \left(b_m \gamma_m^\ell - \theta f_m \lambda_m^\ell \right) - \mu_m^\ell \nu_m^\ell \right) - s_m \nu_m^\ell = 0, \qquad (5.33)$$

$$\rho_m^\ell - t_m^\ell \Omega_m^\ell - s_m \beta_m^\ell = 0, \qquad (5.34)$$

at the $(\ell, m)^{th}$ grid point, where α_m^ℓ, β_m^ℓ, γ_m^ℓ, λ_m^ℓ, μ_m^ℓ, ν_m^ℓ, ρ_m^ℓ, b_m, and f_m are defined as in equations (4.71)-(4.79). The FLARE switch, θ, takes the value 1 if upwind differencing is to be used and the value 0 if the FLARE approximation is to be used. The coefficients r_m^ℓ and t_m^ℓ, which depend on the grid point indices ℓ and m, are defined as

$$r_m^\ell = \frac{h'(\zeta_m) f(\xi_\ell)}{k'(\xi_\ell)} \frac{\Delta\zeta}{4\Delta\xi} \quad \text{and} \quad t_m^\ell = \left(h'(\zeta_m) f(\xi_\ell) \Delta\zeta \right)^2, \qquad (5.35)$$

respectively. We also introduce the new coefficient s_m, defined below, which depends only on the index m.

$$s_m = \frac{h''(\zeta_m)}{h'(\zeta_m)} \frac{\Delta\zeta}{2}. \qquad (5.36)$$

The no slip boundary conditions (5.25)-(5.28) are discretised using 3-point central differencing in ζ, using equation (5.34) on the boundary to eliminate any references

to quantities outside the computational domain. Hence we obtain the additional equations

$$\psi_0^\ell = 0, \qquad (5.37)$$

$$2\left(\psi_1^\ell - \psi_0^\ell\right) - t_0^\ell \Omega_0^\ell - 2\Delta\zeta\left(1 + s_0\right)h'\left(\zeta_0\right)f\left(\xi_\ell\right) = 0, \qquad (5.38)$$

$$\psi_M^\ell - u_0 f\left(0\right) = 0, \qquad (5.39)$$

$$2\left(\psi_M^\ell - \psi_{M-1}^\ell\right) - t_M^\ell \Omega_M^\ell - 2\Delta\zeta\left(1 - s_M\right)h'\left(\zeta_M\right)f\left(\xi_\ell\right) = 0. \qquad (5.40)$$

5.4.3 The Starting Profiles for ψ and Ω Near $x = 0$

The three-tiered starting behaviour described earlier for small x is incorporated directly using composite starting profiles for ψ and Ω at the first grid point, $\ell = 1$.

The ordinary differential equation (5.32) is numerically integrated, using a fourth order accurate Runge-Kutta shooting algorithm subject to the two sets of boundary conditions stated, in order to provide a numerical approximation to the solution near the ground and the underbody surface. These two boundary layer solutions are then joined using an inviscid core flow solution of the form $\psi = u_0 Y + c$, where c is a constant to be determined. As a result of introducing c a small adjustment must be made to the value of the streamfunction on the underbody surface and hence the mass flux in the gap. This is a weakness of the method.

A composite interpolating function is then constructed and is used to provide the starting values of ψ_m^1 and Ω_m^1 at the computational grid points (ξ_1, ζ_m) for $m = 0, 1, \cdots, M$. The exact form of the grid resolution functions $k\left(\xi\right)$ and $h\left(\zeta\right)$ must be chosen so that the boundary layer features, contained within these composite starting profiles, are properly resolved.

5.4.4 The Solution of the Difference Equations

At a given streamwise station ℓ, equations (5.33) and (5.34) for $m = 1, 2, \cdots, M - 1$, together with the discretised boundary conditions (5.37)-(5.40), constitute $2(M + 1)$ equations in the $2(M + 1)$ unknowns ψ_m^ℓ and Ω_m^ℓ for $m = 0, 1, \cdots, M$. Therefore this system of equations can be solved to find solution profiles for ψ and Ω using a Newton linearisation method as used in Chapter 4. The solution algorithm is exactly the same as that presented in Chapter 4 apart from the fact that the 2x2 block-matrices and 2-vectors A_m, B_m, C_m, and D_m are now defined to be

$$A_m = \begin{bmatrix} r_m^\ell \left(b_m \gamma_m^\ell - \theta f_m \lambda_m^\ell \right) & 1 + s_m - r \mu_m^\ell \\ 1 + s_m & 0 \end{bmatrix}, \tag{5.41}$$

$$B_m = \begin{bmatrix} 3 r_m^\ell \nu_m^\ell & -2 - 3 r_m^\ell \left(b_m - \theta f_m \right) \beta_m^\ell \\ -2 & -t_m^\ell \end{bmatrix}, \tag{5.42}$$

$$C_m = \begin{bmatrix} -r_m^\ell \left(b_m \gamma_m^\ell - \theta f_m \lambda_m^\ell \right) & 1 - s_m + r_m^\ell \mu_m^\ell \\ 1 - s_m & 0 \end{bmatrix}, \tag{5.43}$$

$$D_m = \begin{bmatrix} \alpha_m^\ell - r_m^\ell \left(\beta_m^\ell \left(b_m \gamma_m^\ell - \theta f_m \lambda_m^\ell \right) - \mu_m^\ell \nu_m^\ell \right) - s_m \nu_m^\ell \\ \rho_m^\ell - t_m^\ell \Omega_m^\ell - s_m \beta_m^\ell \end{bmatrix}, \tag{5.44}$$

for $m = 1, 2, \cdots, M - 1$. The remaining entries being

$$B_0 = \begin{bmatrix} 1 & 0 \\ -2 & -t_0^\ell \end{bmatrix}, \tag{5.45}$$

$$C_0 = \begin{bmatrix} 0 & 0 \\ 2 & 0 \end{bmatrix}, \tag{5.46}$$

$$D_0 = \begin{bmatrix} \psi_0^\ell \\ 2 \left(\psi_1^\ell - \psi_0^\ell \right) - t_0^\ell \Omega_0^\ell - 2 \Delta \zeta \left(1 + s_0 \right) h'(\zeta_0) f(\xi_\ell) \end{bmatrix}, \tag{5.47}$$

$$A_M = \begin{bmatrix} 0 & 0 \\ -2 & 0 \end{bmatrix}, \tag{5.48}$$

$$B_M = \begin{bmatrix} 1 & 0 \\ 2 & -t_M^\ell \end{bmatrix}, \tag{5.49}$$

$$D_M = \begin{bmatrix} \psi_M^\ell - u_0 f(0) \\ 2\left(\psi_M^\ell - \psi_{M-1}^\ell\right) - t_M^\ell \Omega_M^\ell - 2\Delta\zeta \left(1 - s_M\right) h'\left(\zeta_M\right) f\left(\xi_\ell\right) \end{bmatrix}. \quad (5.50)$$

The solution is line-marched downstream from the first station, $\ell = 1$, to the trailing edge at which point ψ and Ω are known at all grid points beneath the aerofoil. As in Chapter 4, a first order accurate version of the difference scheme must be used at the first streamwise station due to the fact that at this point information is only available at one upstream location instead of the usual two.

5.4.5   Finding the Pressure $p_-\left(x\right)$

The pressure gradient at the ℓth station can be found by rearranging equation (5.4) for $p_-'\left(x\right)$. The resulting expression is easiest to evaluate either on the moving ground or on the underbody surface due to the no slip condition. As a result, after discretisation we are able to approximate the pressure gradient at the ℓth streamwise station using the averaged, 3-point difference formula

$$p_\ell' = \frac{1}{4\Delta\zeta f\left(\xi_\ell\right)} \left(\frac{\left(3\Omega_M^\ell - 4\Omega_{M-1}^\ell + \Omega_{M-2}^\ell\right)}{h'\left(\zeta_M\right)} - \frac{\left(3\Omega_0^\ell - 4\Omega_1^\ell + \Omega_2^\ell\right)}{h'\left(\zeta_0\right)} \right). \quad (5.51)$$

The pressure at the ℓth station can then be found by numerically integrating the above pressure gradient using the rearranged 3-point backward difference formula

$$p_\ell = \frac{1}{3}\left(4p_{\ell-1} - p_{\ell-2} + 2\Delta\xi g'\left(\xi\right) p_\ell'\right). \quad (5.52)$$

We begin at the leading edge with the starting pressure p_0 and continue downstream to the trailing edge at which point the trailing edge pressure $p_-\left(1\right)$ is determined. If $p_-\left(1\right)$ does not satisfy the pressure continuity condition (5.11) then a better guess for p_0, and hence u_0, is made using a secant algorithm, and the entire process is repeated until condition (5.11) is met to within a given tolerance. Once again a first order accurate version of equation (5.52) must be used at the first grid point. In most cases the solution converged to within a tolerance of 10^{-10} after 4 or 5 streamwise sweeps.

5.5 Flow Properties

In discussion with McLaren Motorsport we investigated the effects of undertray-shape design on downforce production with reference to the front wing, termed front downforce diffuser, on a formula 1 racing car. To start with we decided on a simple piecewise linear design for the undertray-shape described by the function

$$f(x) = \left\{ \begin{array}{ll} \widehat{\alpha} & \text{for} \quad x \in [0, \gamma] \\ \widehat{\alpha} + \frac{(\beta - \widehat{\alpha})}{(1-\gamma)}(x - \gamma) & \text{for} \quad x \in [\gamma, 1] \end{array} \right\}. \tag{5.53}$$

The diffuser has a minimum ground-clearance of $\widehat{\alpha}$, a parallel channel throat of length γ, followed by a linearly expanding region with maximum gap width $\widehat{\alpha} + \beta$ at $x = 1$. See Figure 5.3.

Computational results for the flow in the gap, corresponding to diffusers of the above type, are shown in Figures 5.5 to 5.17. Among other things, these figures present the streamlines of constant $\psi(x, Y)$, the pressures $p_\pm(x)$, and the normalised surface and ground shears $\Omega_-(x)$ and $\Omega_0(x)$ as $\widehat{\alpha}$ the ground clearance parameter, β the expansion parameter, and γ the throat length are varied independently.

Here $\Omega_-(x)$ and $\Omega_0(x)$ are defined as $\partial u / \partial Y$ at $Y = 0$ and $Y = f(x)$ respectively, so the flow is forward, near the underbody, if $\Omega_-(x)$ is negative, but reversed if $\Omega_-(x)$ is positive. Whilst near the ground positive values of $\Omega_0(x)$ correspond to an overshooting velocity profile, in the present moving frame. Some typical examples of velocity profiles, both forward and reversed, are given in Figures 5.5 and 5.6.

In most cases the value of u_0 was found to remain between zero and one, this being associated with fluid slowing down across the leading edge jump relative to the ground. This is in line with the initial pressure, p_0, being positive, leading to an overall drop in pressure along the gap region, despite the areas of negative pressure in the results.

In some cases, particularly those with pronounced expansion of the gap downstream, reversed flow is encountered, always signalled by $\Omega_-(x)$ becoming positive. In the
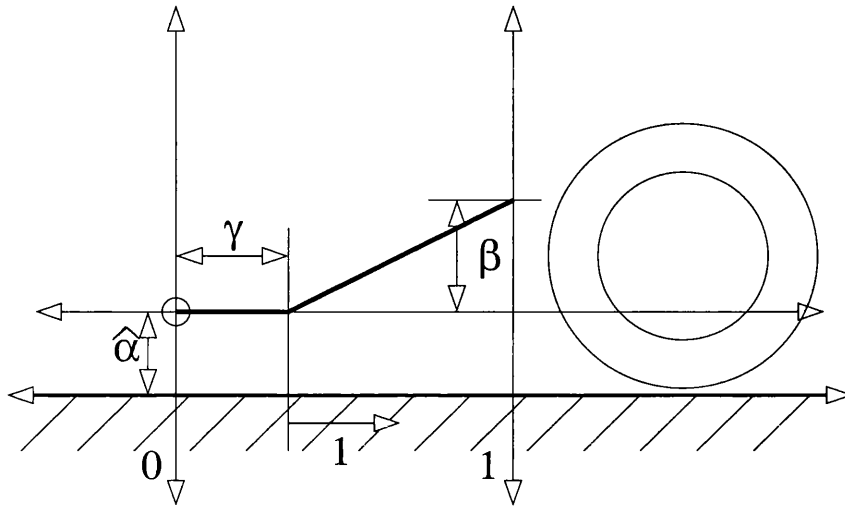
Figure 5.3: The linearly expanding diffuser shape with front wheel (not to scale).
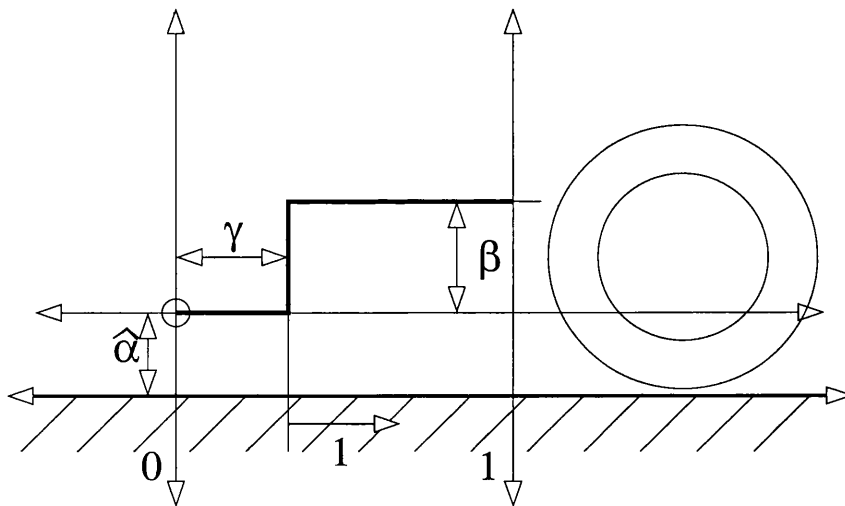
Figure 5.4: The proposed step change in height diffuser shape, which according to lubrication theory produces more downforce than the linearly expanding one.
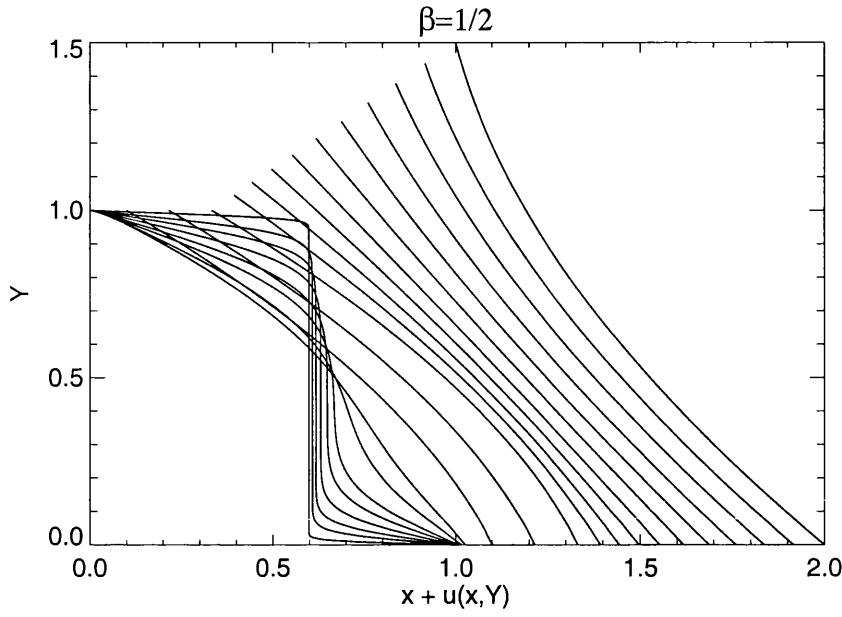
Figure 5.5: Several examples of streamwise velocity profiles $u(x, Y)$, at varying x stations, for forward flow at $\hat{\alpha} = 1$, $\beta = 1/2$, and $\gamma = 1/3$.
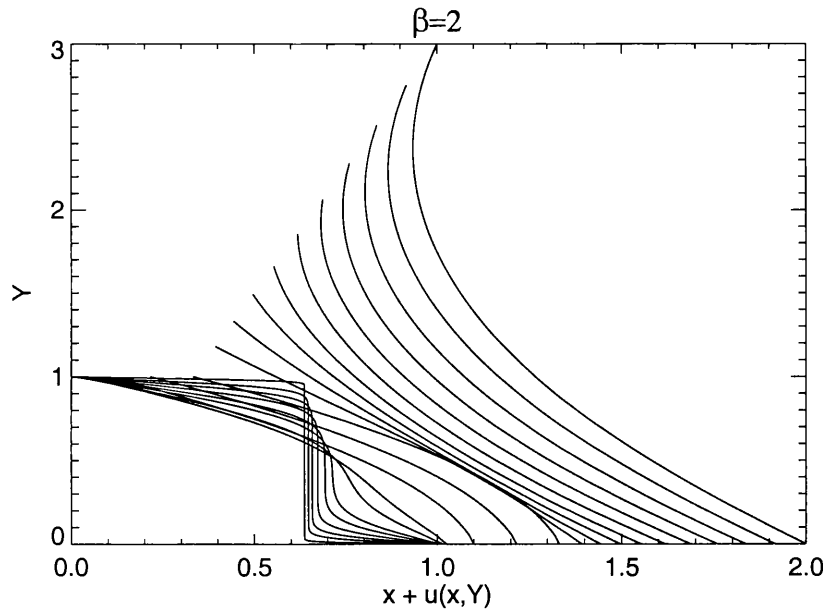
Figure 5.6: Several examples of streamwise velocity profiles $u(x, Y)$, at varying x stations, for a reversed flow case at $\hat{\alpha} = 1$, $\beta = 2$, and $\gamma = 1/3$.

reversed cases the numerical results obtained using windward differencing and the FLARE approximation were usually close. In such flows the pressure reaches a minimum, followed by a region of adverse pressure gradient, eventually leading to separation which occurs with the flow solution remaining regular. If the flow separation is extensive there is generally a relief of pressure gradient, hinting at the approach of a pressure plateau. The motion in the reversed region is comparatively slow, most of the momentum hugging the ground in a jet-like layer akin to that observed in breakaway separation in external aerodynamics.

In Figures 5.7, 5.8, and 5.9 $\hat{\alpha}$ is varied from 16 to 1/16 whilst β and γ are held fixed at 1 and 1/3 respectively. For large ground clearances, $\hat{\alpha} \gg 1$, the solution is largely inviscid as long as there is no flow reversal and so conservation of vorticity implies that $u(x, Y)$ is in fact a function of x alone. Imposing conservation of mass, the momentum balance and the end conditions (5.11) and (5.12) then yields the solution in the form

$$u(x) = \frac{f(1)}{f(x)}, \tag{5.54}$$

$$p_-(x) = \frac{1}{2}\left(1 - u^2(x)\right). \tag{5.55}$$

For near uniform underbody shapes of the form $f(x) = \hat{\alpha} + a(x)$, where $a(x)$ is small compared with $\hat{\alpha}$, the solution becomes

$$u(x) = 1 - \hat{\alpha}^{-1}(a(x) - a(1)) + \cdots, \tag{5.56}$$

$$p_-(x) = \hat{\alpha}^{-1}(a(x) - a(1)) + \cdots. \tag{5.57}$$

Therefore, the pressure is either positive or negative near the leading edge depending on whether the gap beneath the diffuser contracts or expands overall and scales inversely with the ground clearance $\hat{\alpha}$, as noted in Chapters 2 and 3. In the above inviscid solutions the underbody shape $f(x)$ is assumed to include the boundary layer thickness.

For small ground clearances, $\hat{\alpha} \ll 1$, most of the gap flow is governed by the lubrication forces of pressure gradient and viscous diffusion and so $u(x, Y)$ is at most

Figure 5.7: The streamlines of constant $\psi\left(x, Y\right)$ for $\widehat{\alpha} = 16$ to $\frac{1}{16}$, $\beta = 1$, and $\gamma = \frac{1}{3}$ directly beneath the diffuser
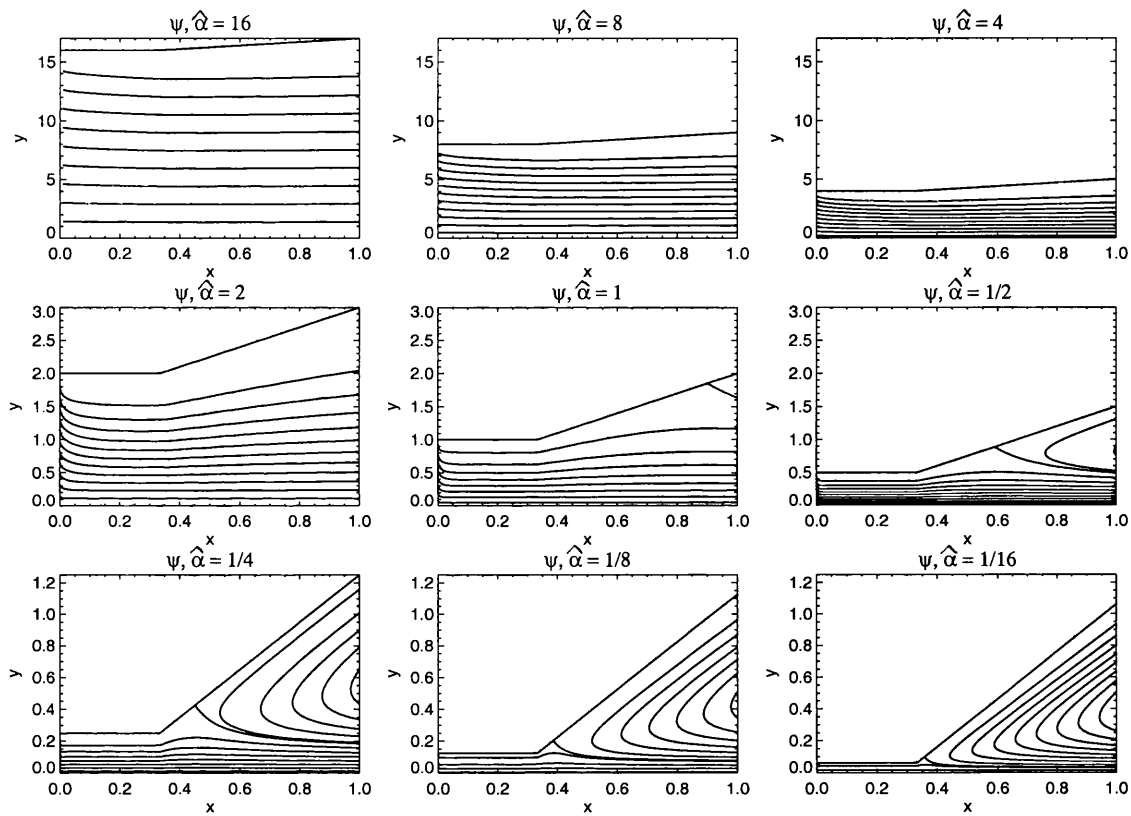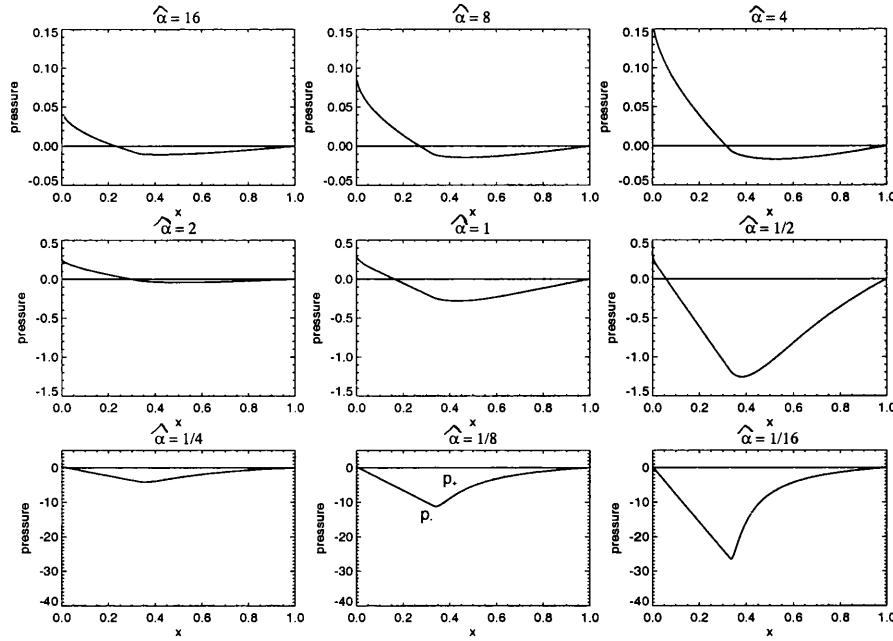
Figure 5.8: The pressures $p_\pm$ (x) for $\hat{\alpha} = 16$ to $\frac{1}{16}$, $\beta = 1$, and $\gamma = \frac{1}{3}$ directly beneath the diffuser. Note the changes of scale between each row of graphs.
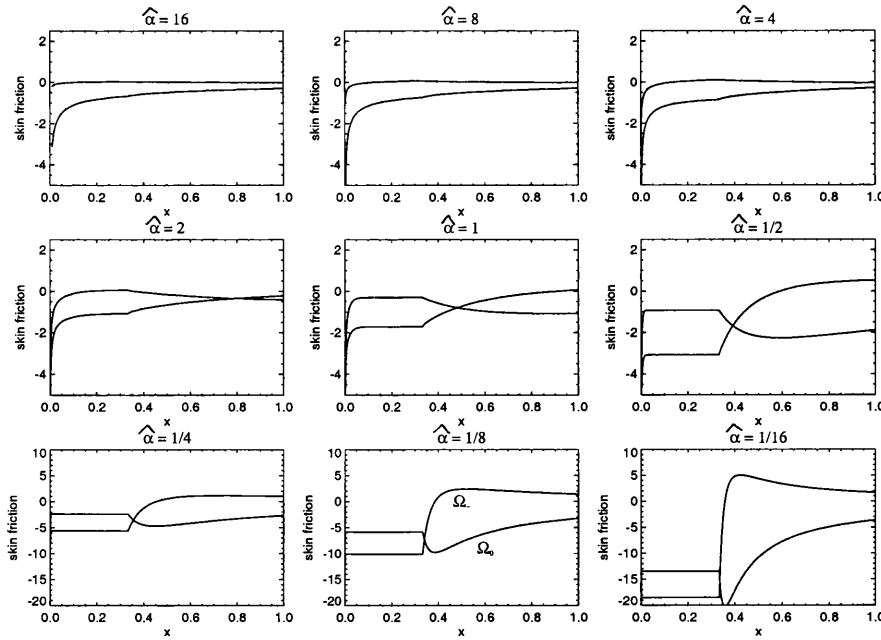

Figure 5.9: The skin frictions Ω_- (x) and Ω_0 (x) for $\hat{\alpha} = 16$ to $\frac{1}{16}$, $\beta = 1$, and $\gamma = \frac{1}{3}$ directly beneath the diffuser

quadratic in Y. Imposition of the boundary conditions (5.6), (5.8), (5.11), and (5.12) then yields the solution in the form

$$u(x, Y) = \frac{1}{2} \, p'_-(x) Y (Y - f(x)) - \frac{Y}{f(x)} + 1,$$

(5.58)

$$p_-(x) = 6 \left\langle f^{-2} \right\rangle \int_0^x \left(\frac{f^{-2}(\xi)}{\langle f^{-2} \rangle} - \frac{f^{-3}(\xi)}{\langle f^{-3} \rangle} \right) d\xi + p_0 \left(1 - \int_0^x \frac{f^{-3}(\xi)}{\langle f^{-3} \rangle} d\xi \right),$$

(5.59)

$$\text{where} \quad \left\langle f^{-2} \right\rangle = \int_0^1 f^{-2}(x) \, dx \quad \text{and} \quad \left\langle f^{-3} \right\rangle = \int_0^1 f^{-3}(x) \, dx.$$

The skin friction on the underbody surface and the ground are then given by

$$\Omega_-(x) = -\frac{1}{f(x)} \left(1 - \frac{1}{2} \, p'_-(x) f^2(x) \right),$$

(5.60)

$$\Omega_0(x) = -\frac{1}{f(x)} \left(1 + \frac{1}{2} \, p'_-(x) f^2(x) \right).$$

(5.61)

We notice that the pressure beneath the diffuser is large, of order $\hat{\alpha}^{-2}$, and that the second term in equation (5.59) is small compared with the first. The smaller term can be discarded, as is usual in lubrication theory, except in the special case where $f(x)$ is a constant in which case the first term vanishes leaving the second term to dominate.

In Figures 5.10, 5.11, and 5.12 β is varied between 16 to 1/16 whilst $\hat{\alpha}$ and γ are held fixed at 1 and 1/3 respectively. The lift is shown to decrease with increasing β until, at some β, separation occurs and as the region of reversed flow becomes large, downforce production is inhibited and the lift begins to increase again. This limiting mechanism leads to the existence of a maximum downforce configuration. Figure 5.11 shows that, in the case considered, the optimal configuration is achieved somewhere between $\beta = 1$ and $\beta = 2$.

In Figures 5.13, 5.14, and 5.15 γ is varied from 0 to 1 whilst $\hat{\alpha}$ and β are both held fixed at 1. As the throat length, γ, is increased from zero the pressure beneath the

Figure 5.10: The streamlines of constant $\psi\left(x, Y\right)$ for $\widehat{\alpha} = 1$, $\beta = 16$ to $\frac{1}{16}$, and $\gamma = \frac{1}{3}$ directly beneath the diffuser
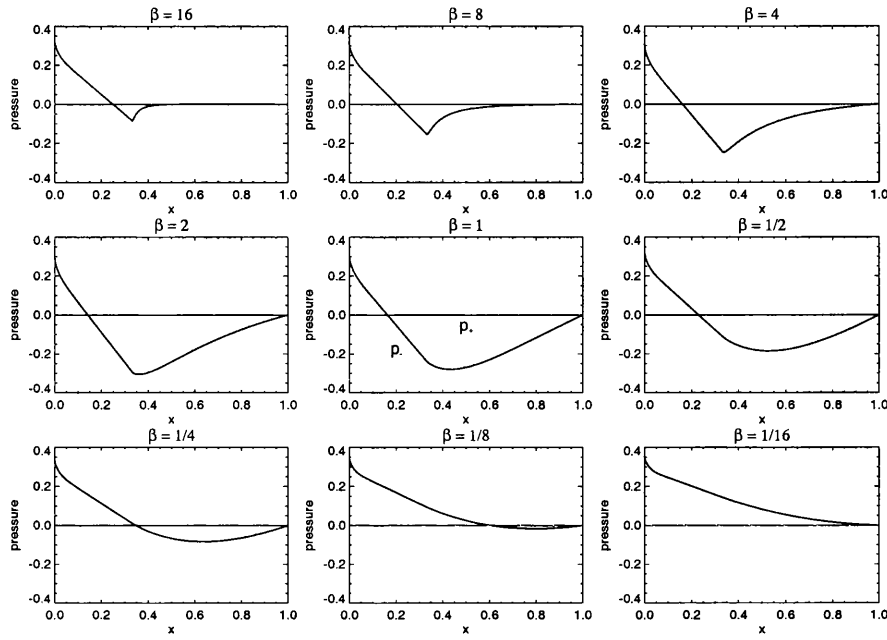
Figure 5.11:   The pressures $p_\pm(x)$ for $\widehat{\alpha} = 1$, $\beta = 16$ to $\frac{1}{16}$, and $\gamma = \frac{1}{3}$ directly beneath the diffuser
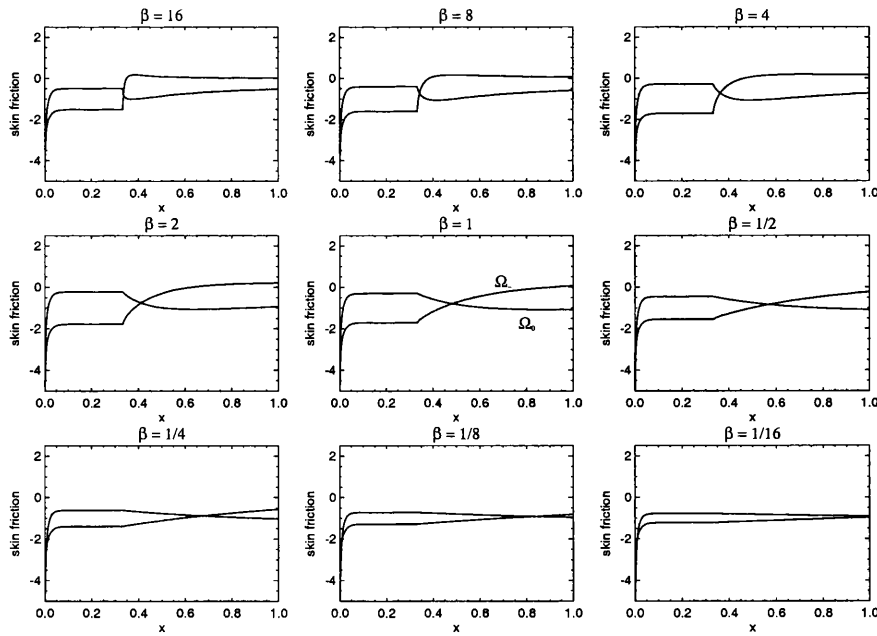
Figure 5.12:   The skin frictions $\Omega_-(x)$ and $\Omega_0(x)$ for $\widehat{\alpha} = 1$, $\beta = 16$ to $\frac{1}{16}$, and $\gamma = \frac{1}{3}$ directly beneath the diffuser

diffuser becomes more negative and so more downforce is produced. However, as γ is increased further, and the expanding part of the diffuser is therefore shortened, a loss of downforce is observed due to the fact that the required recovery of pressure is not possible in the shortened expanding region. This explains the need for both a throat region, in which the initial pressure drop is achieved, and an expanding region, in which the necessary pressure recovery can take place so as to meet the pressure continuity condition at the trailing edge. It is the limiting effect of the relationship between these two diffuser elements which leads, in this case, to a maximum downforce configuration.

In order to identify an overall maximum downforce configuration we must minimise the lift with respect to all three parameters, $\hat{\alpha}$, β, and γ simultaneously. Fortunately, the task is made simpler since Formula One design regulations state that all cars must have a ground clearance greater than a given minimum ride height and therefore we need only minimise the lift with respect to β and γ, nominally setting $\hat{\alpha}$ equal to one. This regulation is sensible, as within our model there is no limiting mechanism on downforce production with regards decreasing $\hat{\alpha}$ and so one must be artificially imposed for safety reasons.

Figure 5.16 shows the lift

$$L = \int_0^1 p_- (x) \, dx, \tag{5.62}$$

plotted as a function of β, γ for $\hat{\alpha} = 1$, calculated as part of many numerical boundary layer solutions. The contour plot clearly identifies a minimum lift configuration with $L = -0.15$, $\beta = 1.55$ and $\gamma = 0.15$. The calculation required around 400 boundary-layer code runs and would become prohibitively expensive if more complicated designs were proposed. Therefore, as a comparison the same calculation was performed using lubrication theory, which gives an analytic expression for the lift on a diffuser of shape $f(x)$, given p_0. Figure 5.17 shows the lift, L, plotted as a function of β, γ for $\hat{\alpha} = 1$, but this time as calculated using lubrication the-
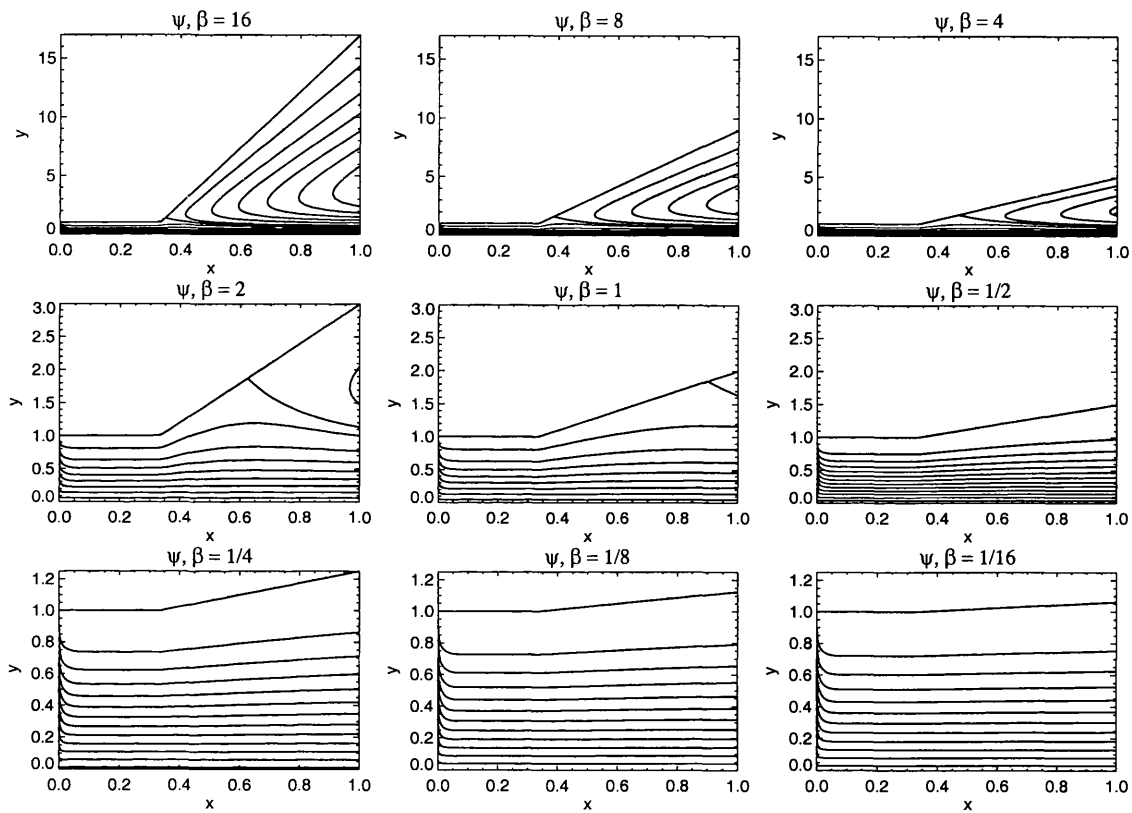
Figure 5.13: The streamlines of constant $\psi(x, Y)$ for $\widehat{\alpha} = 1$, $\beta = 1$, and $\gamma = 0$ to 1 directly beneath the diffuser
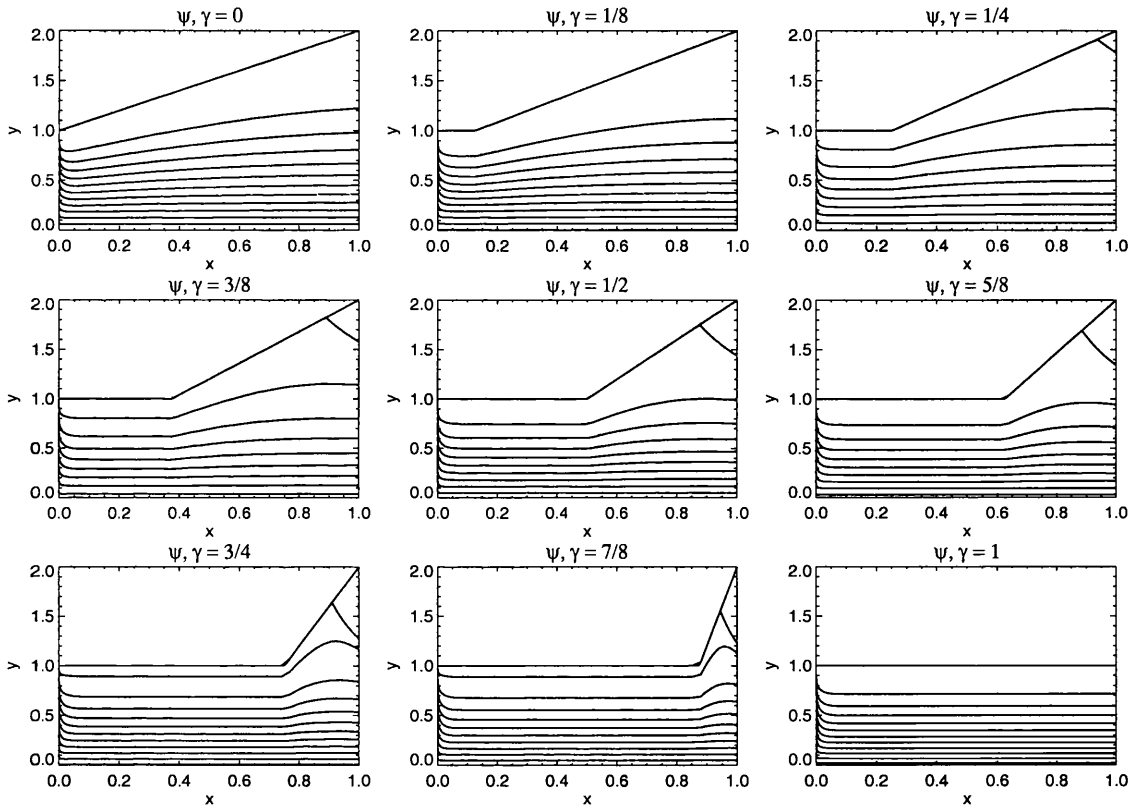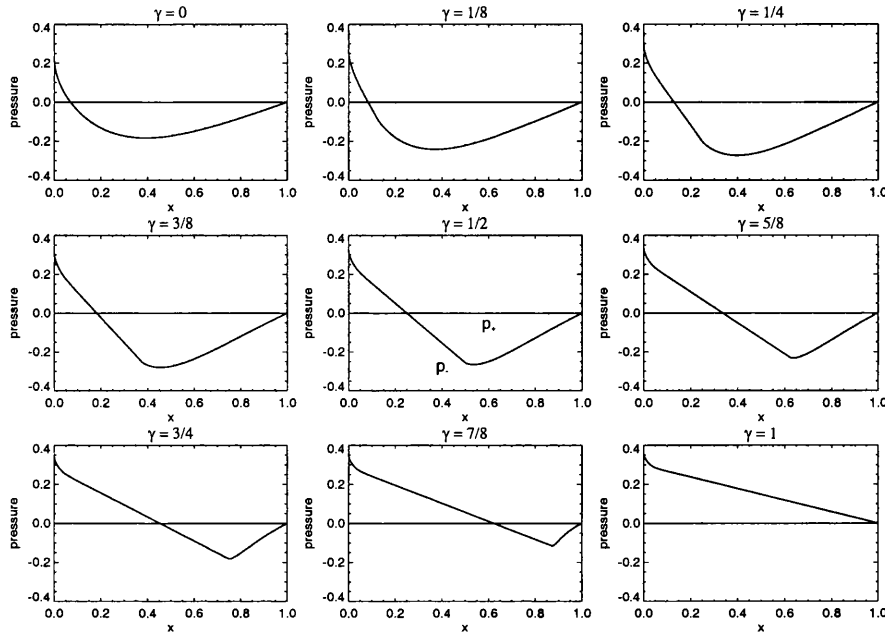
Figure 5.14: The pressures $p_\pm (x)$ for $\hat{\alpha} = 1$, $\beta = 1$, and $\gamma = 0$ to 1 directly beneath the diffuser
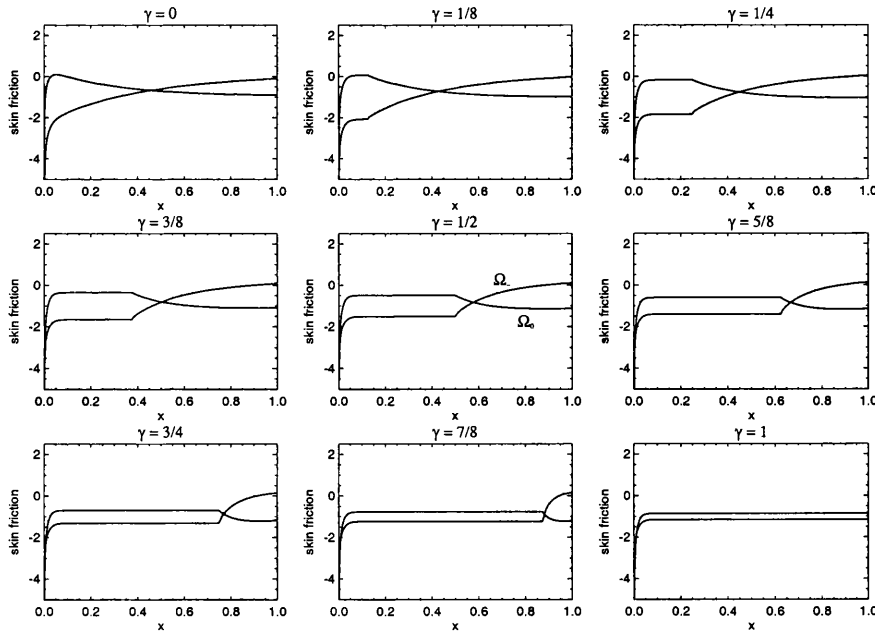
Figure 5.15: The skin frictions $\Omega_- (x)$ and $\Omega_0 (x)$ for $\hat{\alpha} = 1$, $\beta = 1$, and $\gamma = 0$ to 1 directly beneath the diffuser

ory. Again, the contour plot clearly identifies a minimum lift configuration, with $L = -0.1923$, $\beta = 1.242$ and $\gamma = 0.1977$. Comparing this figure to that produced by solving the full non-linear problem shows that lubrication theory can provide a useful tool when considering flows of this type, even for ground clearances as large as $\hat{\alpha} = 1$ where lubrication theory is not strictly valid.

With this in mind it is interesting to note that lubrication theory in fact predicts that a better choice for undertray shape would be a simple step change in height. See Figure 5.4. The function $f_-(x)$ would then take the form

$$f(x) = \begin{cases} \hat{\alpha} & \text{for} \quad x \in [0, \gamma] \\ \hat{\alpha} + \beta & \text{for} \quad x \in [\gamma, 1] \end{cases}.$$

(5.63)

If we repeat the lubrication calculation for the diffuser shape above, with $\hat{\alpha} = 1$, we find a maximum downforce configuration when $\beta = 0.866$ and $\gamma = 0.282$ giving rise to a lift of $L = -0.2063$. This constitutes a 7.3% percent increase in downforce production when compared to the linearly expanding design. This result is of course very interesting with regards Formula One racing car design. We should however point out that on a real diffuser the abrupt step change in height at $x = \gamma$ would have to be smoothed out on some small length scale.

5.5.1   Wake Effects

The flow computations of the previous section were continued beyond the trailing edge into the wake, wherein the pressure, $p(x)$, is identically equal to zero as mentioned earlier. The flow solution in the wake is clearly affected by the velocity profiles entering from regions II$_\pm$. Indeed just beyond the trailing edge, at small $(x - 1)$, a Goldstein-like similarity solution holds near $Y = f(1)$, with the locally scaled effective streamfunction, $q(\eta)$, satisfying the equation

$$q'''(\eta) + \frac{2}{3}q''(\eta)q(\eta) - \frac{1}{3}q'(\eta)^2 = 0,$$

(5.64)

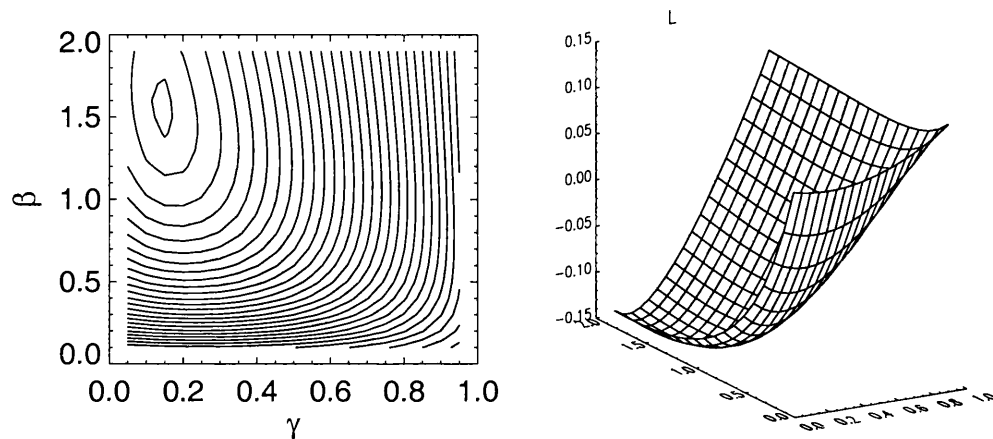Figure 5.16: The non-dimensional lift L as a function of throat length γ and expansion parameter β as calculated as part of many numerical boundary-layer solutions
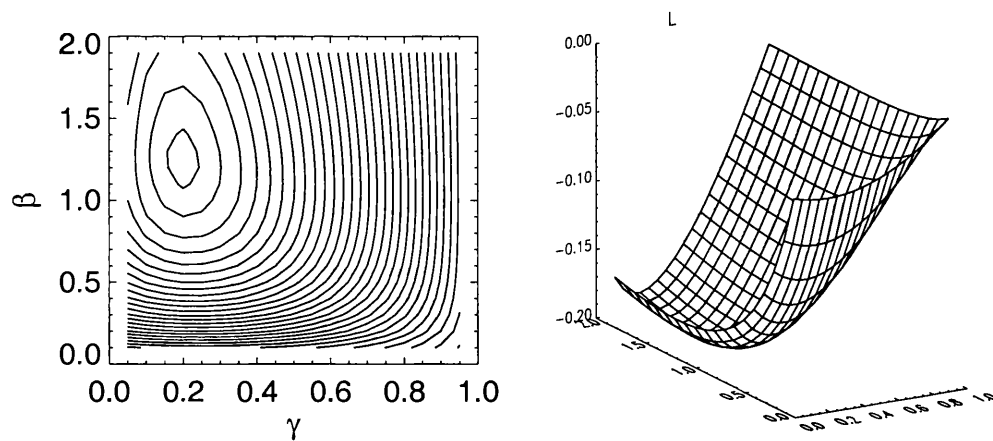

Figure 5.17: The non-dimensional lift L as a function of throat length γ and expansion parameter β as calculated using lubrication theory

where the streamfunction $\psi = (x-1)^{2/3} q(\eta)$ and $Y - f(1) = (x-1)^{1/3} \eta$. The function $q'(\eta)$ must also satisfy the constraints $q'(\eta) \sim \lambda_{\pm}\eta$ as $\eta \to \pm\infty$, where λ_+ is the positive Blasius wall shear and λ_- is the underbody shear from region II$_-$. In general, the solution of (5.64) requires that λ_- be negative and this requirement is entirely consistent with forward flow in the gap. However, if the flow separates from the underbody surface inside the gap, making λ_- positive, then re-attachment must occur prior to the trailing edge in order to make λ_- negative again. Extreme care must be taken in order to capture this effect numerically and even then it is difficult to resolve the relevant scales. Some wake solutions for piecewise linear diffusers are shown in Figure 5.18. In the middle and right hand sets of results extra streamlines have been plotted within the reversed flow region to highlight the details there.

Without flow reversal the wake solution can be marched forward in x relatively easily with $p(x) = 0$. The velocity profiles show gradual diffusion downstream eventually relaxing to the uniform stream $u(x, Y) = 1$. With flow reversal the wake calculations proved far more difficult. The use of windward differencing is now crucial in regions II$_-$ and III, as is the use of extremely refined grids. Most success was achieved by relaxing the condition of zero pressure gradient in the wake and replacing it with a mass flux constraint applied a some finite value $Y = Y_\infty$. In the middle set of results in Figure 5.18 the mass flux constraint $\psi(x, Y_\infty) = c$ has been imposed at $Y_\infty = 32$. In the right hand set of results the mass flux constraint $\psi(x, Y_\infty) = c + 1.5(x-1)^{1/3}$ has been imposed at $Y_\infty = 32$ in an attempt to minimise the pressure gradient in the wake. As $Y_\infty \to +\infty$ we expect the pressure in the wake to tend towards zero, falling in line with the required condition.

Three main features stand out in the reversed flow wake solutions. Firstly, we notice the existence of an extremely small closed eddy close to the trailing edge accompanied by the corresponding intricate streamline pattern. See Figure 5.19. Secondly, we notice that both the small and the large eddy closure appear to occur on an extremely short streamwise length scale, and finally we notice that fluid, from
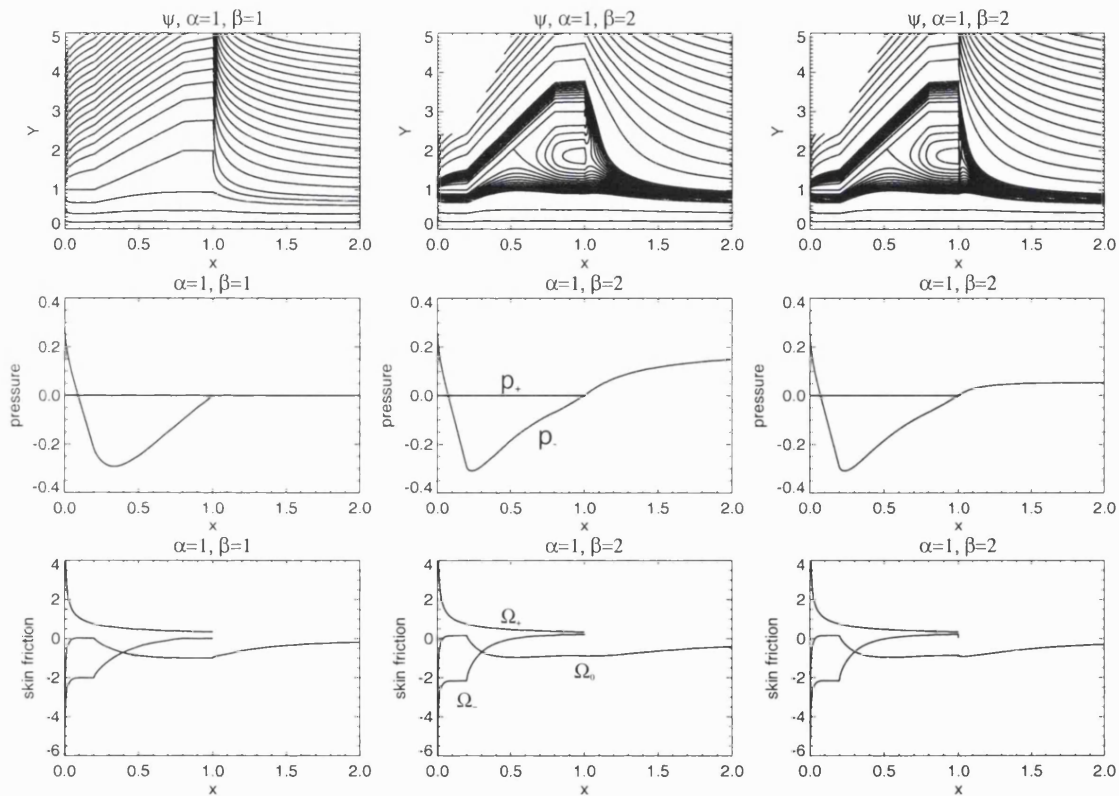
Figure 5.18: Wake results showing streamlines, pressures, and skin frictions for forward and separated flows. Notice the reduced pressure variation in the right hand case.
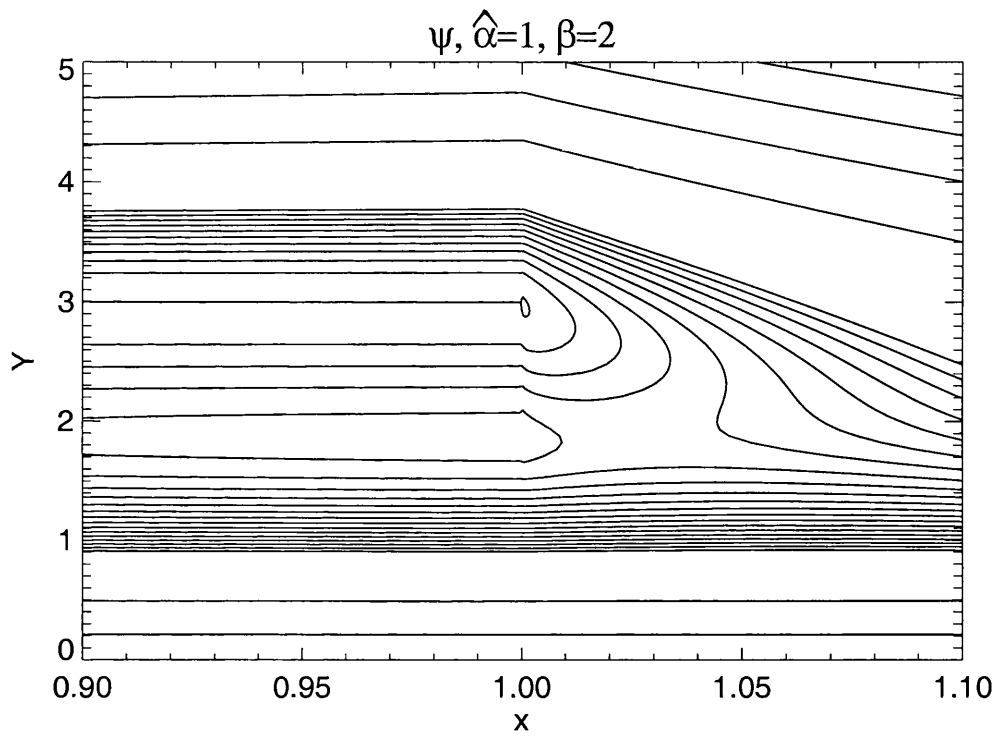
Figure 5.19: Streamlines of constant $\psi\,(x,Y)$ showing the extremely small closed eddy close to the trailing edge.

above the diffuser, is drawn around the trailing edge to entirely fill the region of reversed flow beneath the diffuser. The re-attachment mentioned earlier is in fact made possible by the existence of the small eddy, as is the flow turning associated with fluid being drawn into the separated region from above. Similar flow structures were found, in the context of a non-symmetric trailing edge problem, in Smith (1983).

The observed flow topology near the trailing edge closely resembles that envisaged for vortex shedding behind a circular cylinder and it would be interesting to pursue the separated wake issue further in view of this similarity. See Figures 5.20 and 5.21.
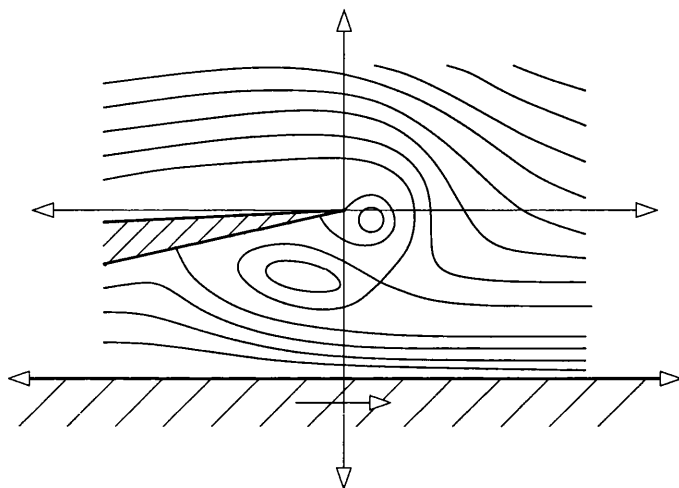
Figure 5.20: The flow topology close to the trailing edge as observed in the numerical wake solutions (not to scale).
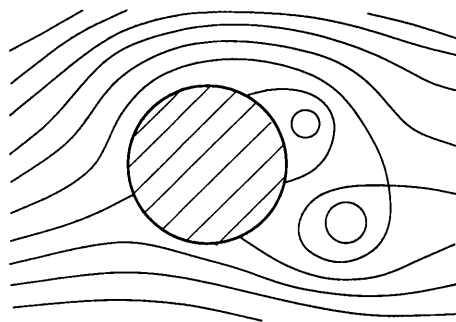
Figure 5.21: A similar flow topology envisaged for vortex shedding behind a circular cylinder.

Chapter 6

Tunnel Effects

Until now we have concerned ourselves with the external non-symmetric problem of studying the flow past a thin aerofoil moving parallel with and at varying distances from the ground. However, by including a ceiling in the problem, it is possible to extend our results to the corresponding internal, non-symmetric problem of the flow past an aerofoil moving through a tunnel.

In this chapter we highlight both the similarities and differences between these two types of flow. As an example we shall consider the inviscid flow past a thin aerofoil moving through a tunnel and compare this flow to that described in Chapter 2. The non-dimensionalised distances between the aerofoil and the tunnel floor and ceiling are denoted α_- and α_+ respectively and the tunnel height is denoted by $\beta = \alpha_+ + \alpha-$. See Figure 6.1.

The fundamental difference in the tunnel problem becomes apparent at the point at which we reinterpret the no penetration conditions, now at the tunnel floor and ceiling, as symmetry conditions. In section 2.3.1 this approach led to the introduction of an image aerofoil beneath the ground. In the tunnel case it has the effect of introducing a doubly-periodic, infinite cascade of image aerofoils. See Figure 6.2.

If we continue to approach the problem as in Chapter 2 we are forced to apply

Cauchy's Integral formula infinitely many times using the contours Γ_{2n+} and Γ_{2n-}, in the relevant limit, and sum the resulting balances over all n. See Figure 6.3.

The resulting infinite sum can be done exactly in Fourier space using results for a geometric progression. By taking real and imaginary parts of this sum we obtain the following integral equations

$$\langle v \rangle (x) = \frac{1}{\pi} \int_{-\infty}^{\infty} l(\xi - x) [v](\xi) d\xi - \frac{1}{\pi} \fint_{-\infty}^{\infty} \left(\frac{\pi}{2\beta} \frac{\left(1 + e^{-\frac{\pi}{\beta}(\xi - x)}\right)}{\left(1 - e^{-\frac{\pi}{\beta}(\xi - x)}\right)} - m(\xi - x) \right) [p](\xi) d\xi,$$

(6.1)

$$\langle p \rangle (x) = \frac{1}{\pi} \fint_{-\infty}^{\infty} \left(\frac{\pi}{2\beta} \frac{\left(1 + e^{-\frac{\pi}{\beta}(\xi - x)}\right)}{\left(1 - e^{-\frac{\pi}{\beta}(\xi - x)}\right)} + m(\xi - x) \right) [v](\xi) d\xi - \frac{1}{\pi} \int_{-\infty}^{\infty} l(\xi - x) [p](\xi) d\xi,$$

(6.2)

which should be compared to equations (2.33) and (2.34) respectively where in the above

$$l(x) = \frac{\pi i}{2\beta} \frac{\left(e^{i\theta_+} - e^{i\theta_-}\right) e^{-\frac{\pi x}{\beta}}}{\left(1 - e^{i\theta_+} e^{-\frac{\pi x}{\beta}}\right)\left(1 - e^{i\theta_-} e^{-\frac{\pi x}{\beta}}\right)},$$

(6.3)

$$m(x) = \frac{\pi}{2\beta} \frac{1 - e^{-\frac{2\pi x}{\beta}}}{\left(1 - e^{i\theta_+} e^{-\frac{\pi x}{\beta}}\right)\left(1 - e^{i\theta_-} e^{-\frac{\pi x}{\beta}}\right)},$$

(6.4)

and $\theta_\pm = 2\pi\beta^{-1}\alpha_\pm$. We note that the two sets of equations are exactly similar in structure and differ only in that the algebraic kernel functions appearing in (2.33) and (2.34) have been replaced with similar exponential ones in equations (6.1) and (6.2). It would seem then that we may extend the results of chapters 2, 3, and 4 to the corresponding tunnel flows by making a simple kernel substitution in all integral equations and then proceed by solving these equations as before. This is indeed the case. As we have seen the integral equations (2.33) and (2.34) are crucial to the understanding of the wing-in-ground effect phenomenon and so equations (6.1) and (6.2) are central to an understanding of tunnel effects.

In our example, the central task becomes one of solving the integral equation (6.1) for the unknown pressure difference across the aerofoil, $[p](x)$, as in Chapter 2. This task must be completed before the boundary conditions and ultimately the flow solution can be found. As in Chapter 2 it is the singular part of the kernel appearing in equation (6.1) which dominates and the dominant equation, corresponding to equation (2.45) in the external case, becomes

$$\frac{1}{\pi} \int_0^1 \frac{\pi}{2\beta} \frac{\left(1 + e^{-\frac{\pi}{\beta}(\xi - x)}\right)}{\left(1 - e^{-\frac{\pi}{\beta}(\xi - x)}\right)} [p](\xi) \, d\xi \;=\; g(x), \qquad (6.5)$$

where

$$g(x) \;=\; \frac{1}{\pi} \int_{-\infty}^{+\infty} l(\xi - x) [v](\xi) \, d\xi - \langle v \rangle (x) + \frac{1}{\pi} \int_{-\infty}^{+\infty} m(\xi - x) [p](\xi) \, d\xi. \qquad (6.6)$$

The desired solution, to the dominant integral equation (6.5), which satisfies the additional constraint of pressure continuity at the trailing edge is

$$[p](x) \;=\; -\frac{1}{\pi} \sqrt{\frac{\sinh \frac{\pi}{2\beta}(1 - x)}{\sinh \frac{\pi}{2\beta} x}} \int_0^1 \frac{\pi}{2\beta} \sqrt{\frac{\sinh \frac{\pi}{2\beta}\xi}{\sinh \frac{\pi}{2\beta}(1 - \xi)}} \frac{\left(1 + e^{-\frac{\pi}{\beta}(\xi - x)}\right)}{\left(1 - e^{-\frac{\pi}{\beta}(\xi - x)}\right)} g(\xi) \, d\xi,$$

$$(6.7)$$

and using this solution it is now possible, as in Chapter 2, to derive a non-singular Fredholm integral equation of the second kind for $[p](x)$ which can be solved. Once this has been done it is a straightforward matter to complete the boundary conditions for $v_+(x)$, $v_-(x)$, $p_+(x)$, and $p_-(x)$ and the full solutions for $v(x, y)$, $p(x, y)$, and $u(x, y)$.

Thus we have shown that the results of Chapter 2, 3, and 4 can, in principle, be extended to include the tunnel flow cases described in this chapter.
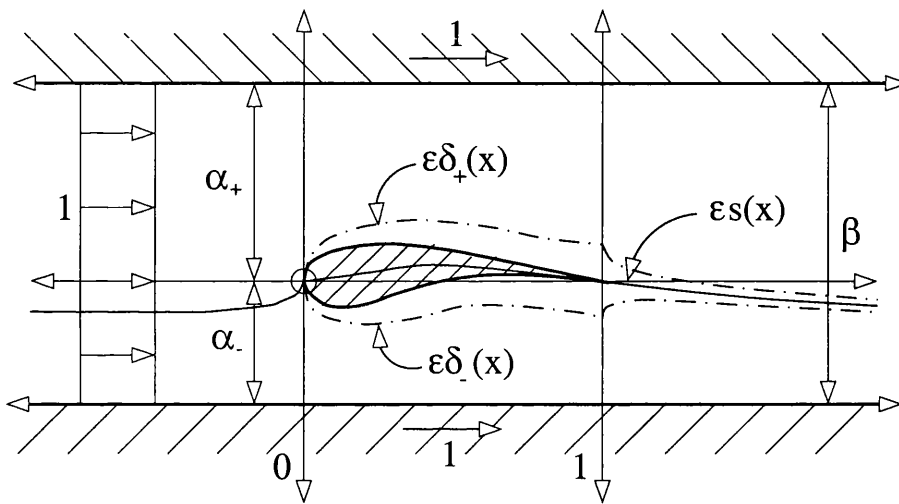
Figure 6.1: Cross-section of a thin aerofoil with boundary layers and a thin viscous wake moving through a tunnel.
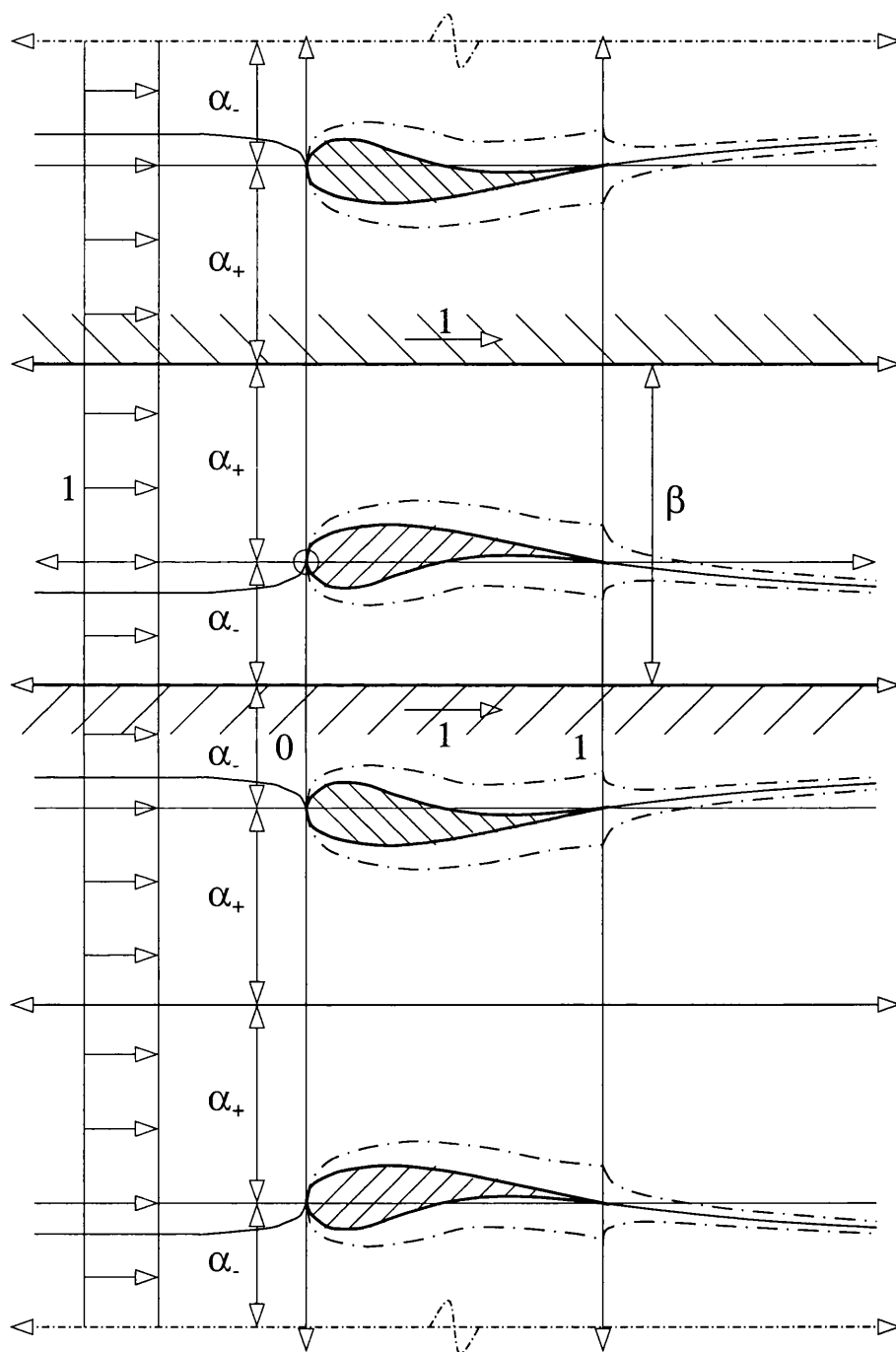
Figure 6.2: The doubly periodic cascade of image aerofoils introduced due to symmetry conditions being applied on the tunnel floor *and* ceiling.
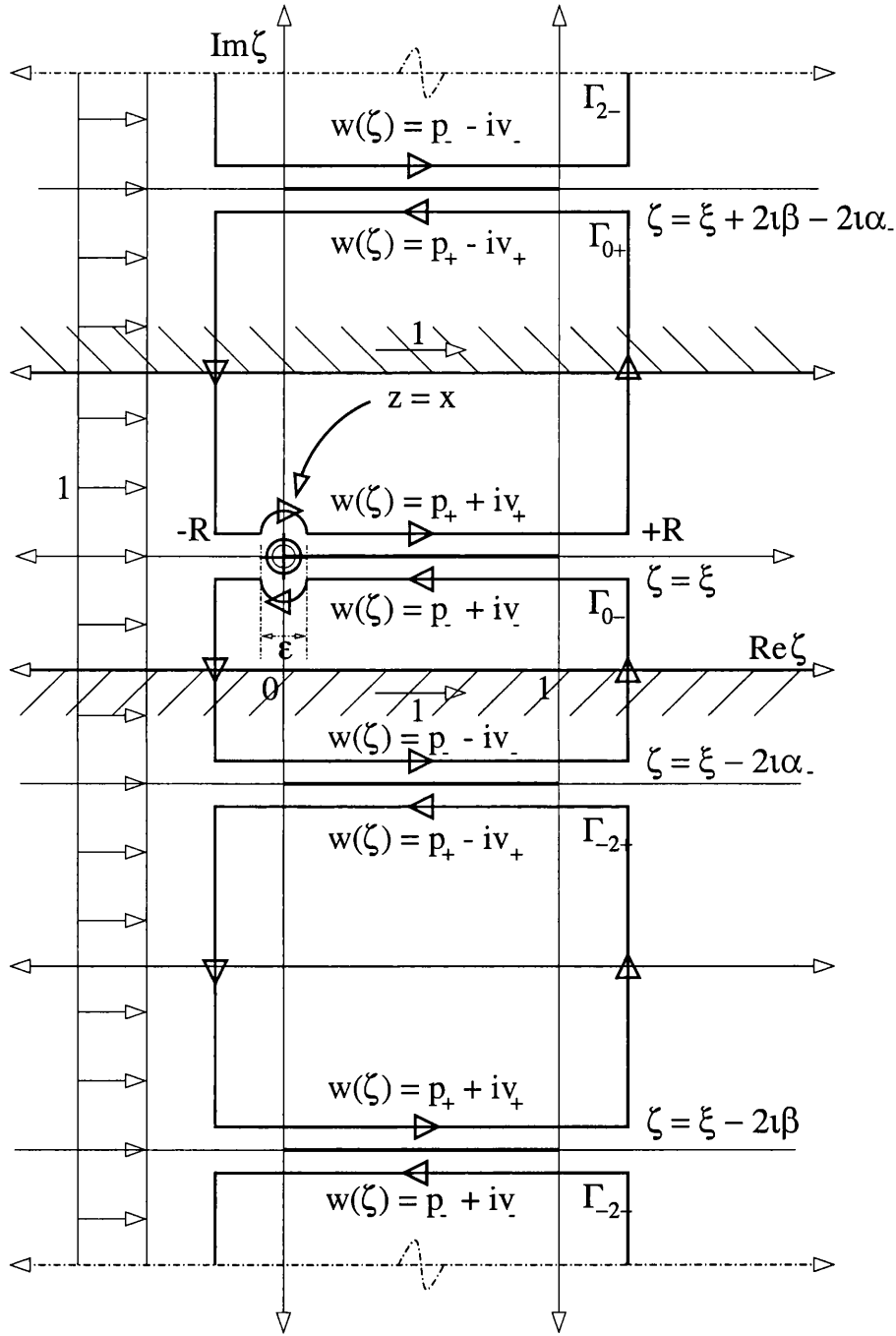
Figure 6.3: Integration contours $\Gamma_{2n\pm}$ in the complex plane corresponding to the doubly periodic cascade of image aerofoils.

Chapter 7

Conclusions and Further Work

7.1 Summary

In Chapter 2 we studied the potential flow past a thin aerofoil travelling parallel with and close to the ground at high Reynolds number. Crucially, we included the effects of viscosity into this otherwise inviscid problem by incorporating the displacement thicknesses of the boundary layers and thin viscous wake, associated with the aerofoil into the boundary conditions for the inviscid problem. Pressure continuity was required upstream, at the trailing edge, and in the wake of the aerofoil and a mechanism was identified which allowed the pressures above and below the aerofoil to interact so as to produce the required continuous pressure field upstream and in the wake. Mathematically this mechanism appeared in the form of the two singular coupled integral equations (2.33) and (2.34). The first of these integral equations had to be solved for the all-important lift distribution on the aerofoil before the rest of the solution could be completed. An analytical solution was found albeit in a form which proved difficult to evaluate.

In Chapter 3 the above ground-interference problem was considered in the limits of large and small ground clearances. Asymptotic solutions to the integral equations

(2.33) and (2.34) were developed using Fourier transform techniques. For large ground clearances the leading order solution was shown to be that of flow past a thin aerofoil in the absence of the ground, as expected; the effect of the ground was to add a virtual angle of attack to the aerofoil at next order. For small ground clearances, α, the pressure solution directly beneath the aerofoil, $p_-(x)$, was shown to take a particularly simple form. This pressure was shown to grow in line with α^{-1} as α was decreased, thus quantifying the large increase in lift associated with wing-in-ground effect flight. The pressure distribution $p_-(x)$ was also shown to exactly reflect the shape of the total lower displacement thickness $\delta_-(x)$ at leading order and was found to within a constant at each higher order. In order to find the unknown constants it was necessary to consider the flow in two local α by α scaled regions around the leading and trailing edges, and then to apply the Kutta condition at the trailing edge. These edge regions allowed the large pressures created beneath the aerofoil to be smoothly joined with the smaller pressures induced in the bulk of the fluid. Two classes of edge flow solution were identified; eigensolutions, permitted only at the leading edge due to the Kutta condition, and non-eigensolutions, permitted at both the leading and trailing edges. A conformal mapping technique and the Wiener-Hopf technique were used to find the general eigen and non-eigen solutions respectively.

In Chapter 4 the local trailing edge flow was shown to take on a 'triple-deck' structure for ground clearances, $\alpha = \bar{\alpha} Re^{-3/8}$, of the order of $Re^{-3/8}$. The ground was then just outside the classical boundary layer and could therefore influence the boundary layer flow, in a viscous sub-layer, through a viscous-inviscid interaction. This effect constituted the first viscous response to the presence of the ground. Ground effects were included explicitly via a new pressure-displacement interaction law, very similar in form to the integral equations encountered in Chapters 2 and 3. The relevant lower deck problem was stated and solved numerically using a novel combination of a discretised Wiener-Hopf solution and finite difference algorithm. For small $\bar{\alpha}$ the interaction law was shown to take a particularly simple form and

the implications for the solution were discussed.

In Chapter 5 we considered the flow past a thin aerofoil moving even nearer the ground, in extreme ground effect, with ground clearances, $\alpha = \hat{\alpha} Re^{-1/2}$, of order $Re^{-1/2}$. In this case the <u>ground was inside the boundary layer</u> and the boundary layer equations were consequently shown to hold throughout the solution domain. Mechanisms encountered in the context of this problem included a viscous-inviscid interaction which filled the entire gap between the ground and the aerofoil; again associated with the condition of pressure continuity at the trailing edge, the generation of strong upstream influence which forced a localised pressure jump at the leading edge, and flow separation including certain wake effects. Flow solutions were found numerically and applications in Formula One racing car design were considered with reference to <u>downforce</u> production. Some wake solutions were computed and intricate streamline patterns were observed very close to the trailing edge in cases where separation occurred beneath the aerofoil, prior to the trailing edge.

Finally, in Chapter 6 tunnel effects were considered by adding a ceiling into the problems posed in Chapters 2, 3, and 4. It was shown that the results presented in Chapters 2, 3, and 4 could be extended to include the corresponding tunnel flows by making a simple kernel substitution in the relevant integral equations. The potential flow problem of Chapter 2 was used to illustrate this point.

7.2 Further Work

There are many directions in which one could continue the work presented in the body of this thesis. In the opinion of the author some of the more interesting extensions would include the following:

To extend the work presented here into the three-dimensional setting. Additional features would then include span-dominated effects, wing-tip vortex roll-up, and in-

flow and out-flow considerations. Some preliminary work is presented in Jones and Smith (1999).

To extend the ideas developed here to flows past bluff bodies in ground effect, such as a circular cylinder for example. Applications of such a theory could be envisaged in all sorts of situations, in the internal aerodynamics of fast moving machinery for example.

Finally, an understanding of the wake effects uncovered towards the end of Chapter 5 is needed. It may be fruitful to consider the internal version of the problem considered in Chapter 5 as a starting point. This would allow us to relax the condition of zero pressure gradient in the wake on physical grounds, replacing it with a mass flux constraint. Numerical solutions would then be relatively easy to compute and would perhaps aid the understanding of the intricate streamline patterns observed close to the trailing edge. Similar calculations are also relevant in internal branching flows as in Smith and Jones (1999). An asymptotic approach would be to begin with a study of the triple-deck like region V, mentioned in the introduction of Chapter 5, for cases where the incoming flow from beneath the aerofoil is both forward and reversed. Perhaps a study on an even shorter length scale is required to properly resolve the small eddy closure.

Appendix A

Thin Layers and the Triple Deck Structure

A.1   Boundary Layers

In the boundary layers adjacent to the upper and lower surfaces of the aerofoil and in a thin wake we reinstate the highest derivatives in the Navier-Stokes equations so as to allow the solution to meet the no slip condition on the aerofoil and adjust to its abrupt absence in the wake. We do this by introducing a local transverse coordinate Y which is measured from the aerofoil surface or wake centreline and is scaled on the classical boundary layer thickness $\varepsilon = Re^{-1/2}$. For example above the aerofoil we have $Y = \varepsilon^{-1}(y - h(x))$, where $h(x)$ describes the shape of the aerofoil's upper surface.

In such a thin layer we seek a solution in the form

$$U(x,Y) = U_0(x,Y) + \varepsilon U_1(x,Y) + \cdots, \tag{A.1}$$

$$V(x,Y) = \varepsilon V_0(x,Y) + \cdots, \tag{A.2}$$

$$P(x,Y) = p_\infty + \varepsilon P_0(x,Y) + \cdots., \tag{A.3}$$

since the streamwise velocity component must change by an order one amount across the layer, to meet the no slip condition for example, and the transverse velocity component must maintain a non-trivial balance in the continuity equation.

Upon substitution of these expansions into the Navier-Stokes equations (2.1)-(2.3) we are left, at leading order, with the boundary layer equations under zero pressure gradient, namely

$$U_0 \frac{\partial U_0}{\partial x} + V_0 \frac{\partial U_0}{\partial Y} - h'(x) U_0 \frac{\partial U_0}{\partial Y} = \frac{\partial^2 U_0}{\partial Y^2}, \tag{A.4}$$

$$\frac{\partial U_0}{\partial x} + \frac{\partial V_0}{\partial Y} - h'(x) \frac{\partial U_0}{\partial Y} = 0. \tag{A.5}$$

We can automatically satisfy the continuity equation (A.5) by introducing a stream-function ψ and we are then faced with the task of solving the third order partial differential equation

$$\frac{\partial \psi}{\partial Y} \frac{\partial^2 \psi}{\partial x \partial Y} - \frac{\partial \psi}{\partial x} \frac{\partial^2 \psi}{\partial Y^2} = \frac{\partial^3 \psi}{\partial Y^3}, \tag{A.6}$$

for $\psi(x, Y)$ where

$$U_0(x, Y) = \frac{\partial \psi}{\partial Y} \quad \text{and} \quad V_0(x, Y) = h'(x) U_0(x, Y) - \frac{\partial \psi}{\partial x}. \tag{A.7}$$

Equation (A.6) admits similarity solutions of the form

$$\psi(x, Y) = (x - c)^n f\left(Y(x - c)^{n-1}\right), \tag{A.8}$$

and as a result our task is reduced to that of solving the *ordinary* differential equation

$$f'''(\eta) + nf(\eta) f''(\eta) - (2n - 1) f'(\eta)^2 = 0, \tag{A.9}$$

for $f(\eta)$ where η, the similarity variable, is equal to $Y(x - c)^{n-1}$. In order to solve this equation we must first decide on the values of c and n and set three appropriate boundary conditions on $f(\eta)$ and its derivatives. These values depend on the kind of layer we are considering.

A.1.1 The Blasius Boundary Layer

We will now consider the boundary layer on the upper surface of the aerofoil as considered by Blasius (1908). Here we require that the solution match with the free stream as Y tends to infinity and satisfy the no slip condition on the aerofoil surface at $Y = 0$. The solution must be aligned with the leading edge and in order to meet these criteria we must have $c = 0$, $n = \frac{1}{2}$, and must consequently solve the equation

$$f''' (\eta) + \frac{1}{2} f (\eta) f'' (\eta) = 0, \tag{A.10}$$

for $f (\eta)$ subject to the boundary conditions $f (0) = 0$, $f' (0) = 0$, and $f' (+\infty) = 1$. We do this numerically by using a fourth order Runge-Kutta shooting algorithm and the solutions for $f (\eta)$, $f' (\eta)$, $f'' (\eta)$, and $(\eta f' (\eta) - f (\eta))$ are shown in Figure A.1.

The profile of $(\eta f' (\eta) - f (\eta))$ is included since it is closely related to $V_0 (x, Y)$ and shows that $V_0 (x, Y)$ tends to a non-zero constant as Y tends to infinity. The transverse velocity in fact takes the asymptotic form

$$V (x, Y) \sim \varepsilon (h' (x) + \delta'_b (x)) + \cdots \quad \text{for large Y}, \tag{A.11}$$

$$\text{where} \quad \delta_b (x) = c_1 x^{1/2} \quad \text{and} \quad c_1 = \lim_{\eta \to +\infty} (\eta f' (\eta) - f (\eta)) = 1.7207.$$

This means that the boundary layer effectively ejects fluid into the free stream, displacing it by an amount $\varepsilon (h (x) + \delta_b (x))$. An important property of the solution is the value of the skin friction at the trailing edge and this is given by $f'' (0) = \lambda = 0.3346$.

Similar arguments apply to the boundary layer flow beneath the aerofoil and from (A.11) we obtain the part of boundary condition (2.16) valid in the interval $x \in [0, 1]$. In equation (2.16) the aerofoil profile $h (x)$ has been split into a camber $c (x)$ and a half-thickness $\frac{1}{2} t (x)$ for convenience.

A.1.2 The Goldstein Near Wake

In the wake things are slightly more complicated as the abrupt change in boundary conditions, caused by the absence of the no slip condition in the wake, occurs within the developing Blasius boundary layer. See Goldstein (1930). As a result we expect the streamfunction ψ to have the similarity form

$$\psi(x, Y) = (x-1)^m g\left(Y(x-1)^{m-1}\right) + \cdots, \tag{A.12}$$

in an inner sub-layer where the similarity variable $\eta = Y(x-1)^{-1/3}$ is of order unity and have the linearised form

$$\psi(x, Y) = \psi_b(Y) + c_2(x-1)^{1/3} U_b(Y) + \cdots, \tag{A.13}$$

in the continuation of the Blasius boundary layer where Y is of order unity. In the above $\psi_b(Y)$ and $U_b(Y)$ are the streamfunction and streamwise velocity profiles of the Blasius solution at $x = 1$ respectively. The forms (A.12) and (A.13) are only valid for $(x-1) \ll 1$ and are required to match asymptotically for large η and small Y. In order to meet this matching criteria we must have $m = \frac{2}{3}$ and must consequently solve the equation

$$g'''(\eta) + \frac{2}{3}g(\eta)g''(\eta) - \frac{1}{3}g'(\eta)^2 = 0 \tag{A.14}$$

for $g(\eta)$ in the sub-layer subject to the boundary conditions $g(0) = 0$, $g''(0) = 0$, and $g''(+\infty) = \lambda$. We again do this numerically and the solutions for $g(\eta)$, $g'(\eta)$, $g''(\eta)$, and $(g'(\eta) - \eta g''(\eta))$ are shown in Figure A.2. The profile of $(g'(\eta) - \eta g''(\eta))$ is important since the value of this function as η tends to infinity sets the unknown constant c_2 in equation (A.13).

The inner similarity layer again causes a <u>displacement</u> effect which is this time transmitted up through the continuation of the Blasius boundary layer into the free stream where it sets an outer boundary condition on the transverse component of
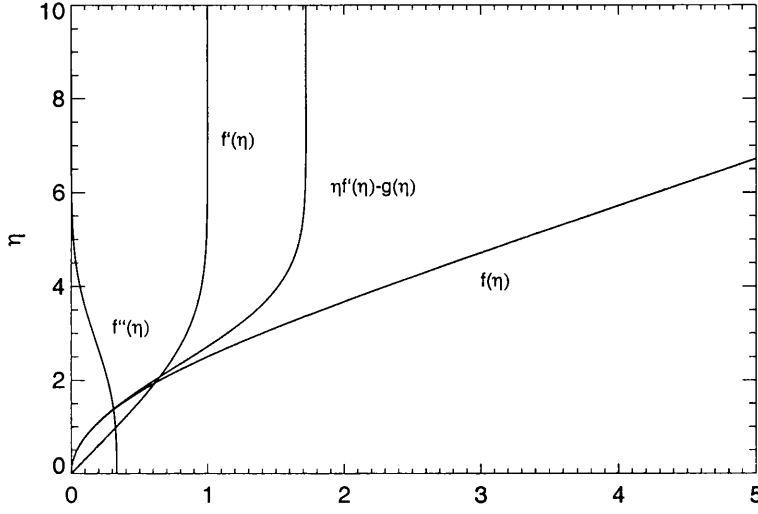
Figure A.1: The solution to the equation $f'''(\eta) + \frac{1}{2}f(\eta)f''(\eta) = 0$ with $f(0) = 0$, $f'(0) = 0$, and $f'(+\infty) = 1$.
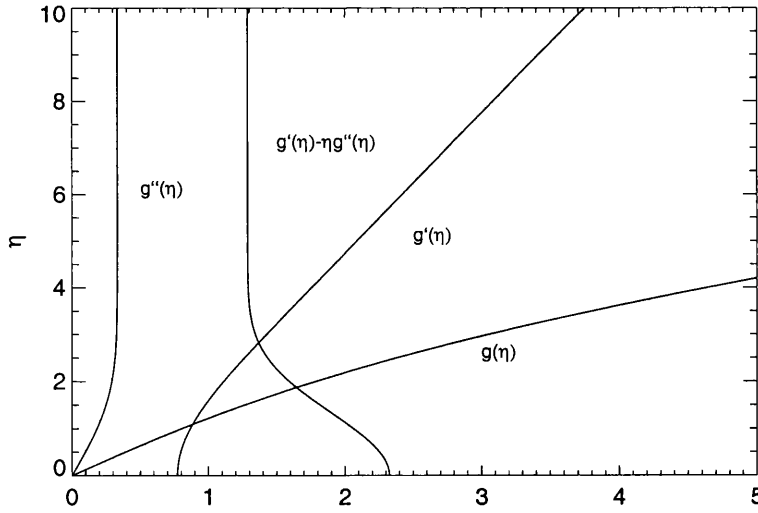

Figure A.2: The solution to the equation $g'''(\eta) + \frac{2}{3}g(\eta)g''(\eta) - \frac{1}{3}g'(\eta)^2 = 0$ with $g(0) = 0$, $g''(0) = 0$, and $g''(+\infty) = \lambda = 0.3346$.

the velocity. The transverse velocity in fact takes the asymptotic form

$$V(x,Y) = \varepsilon \left(h'(x) + \delta_g'(x) \right) + \cdots \quad \text{for large Y,} \tag{A.15}$$

where $\delta_g(x) = c_1 - c_2(x-1)^{1/3}$ and $c_2 = \dfrac{1}{\lambda} \lim_{\eta \to \infty} \left(g'(\eta) - \eta g''(\eta) \right) = 1.2880.$

This shows that fluid from the free stream is effectively drawn into the thin wake allowing the flow there, no longer held back by the no slip condition, to accelerate. Thus from (A.15) we obtain the part of boundary condition (2.16) valid for $x > 1$ where $h(x)$ is replaced by the wake centreline shape $s(x)$.

As mentioned earlier this solution is only valid for $(x-1) \ll 1$ and so in the calculations of Chapter 2 we use a modified form of $\delta_g(x)$ which has the correct behaviour near $x = 1$ but remains finite as x tends to infinity. We in fact take $\delta_g(x)$ to be of the form

$$\delta_g(x) = c_1 - c_2(x-1)^{1/3}(1 + c_3(x-1))^{-1/3}, \tag{A.16}$$

where the additional constant c_3 allows us to set the value of $\delta_g(x)$ as $x \to \infty$.

A.2 The Triple Deck

We have seen that the Goldstein near wake exhibits a two-tiered structure consisting of an inner sub-layer embedded within the continuation of the Blasius boundary layer. However we have also seen that Goldstein's theory predicts that the transverse component of the velocity becomes infinite at the trailing edge since $\delta_g'(x)$ behaves like $(x-1)^{-2/3}$ near $x = 1$. This is physically unacceptable and we now consider a theory, valid in a region where $(x-1)$ is of order $Re^{-3/8}$, which removes this singular behaviour. The flow structure here takes as its inspiration the two-tiered structure of the Goldstein near wake however a larger inviscid region must be added to complete the 'triple-deck' structure of Stewartson (1969) and Messiter (1970). The inner sub-layer is now termed the lower deck, the continuation of the Blasius boundary layer, the main deck, and the larger inviscid region, the upper deck .

The streamwise length scale of the triple-deck is set by ensuring that a viscous-inertial balance, in the lower deck, is driven by an inviscid pressure response originating in the upper deck. Once this all-important length scale has been set it is relatively straight forward to construct a consistent expansion scheme for each of the three decks based around the form of the Blasius boundary layer velocity profile $U_b(Y)$.

In a lower deck of thickness $\epsilon Re^{-1/2}$ the streamwise velocity would be of order ϵ, due to the form of $U_b(Y)$ very near the aerofoil surface, and so by balancing the viscous and inertial terms in the streamwise momentum equation (2.1) we can deduce that streamwise length scale of the triple-deck must be of order ϵ^3. On this length scale an inviscid pressure response to the Goldstein displacement thickness $\delta_g(x)$ would be of order $\epsilon^{-2} Re^{-1/2}$, and to ensure that the remaining pressure gradient term in (2.1) is of the correct order we must have

$$\epsilon = Re^{-1/8}. \tag{A.17}$$

At this stage we adopt ϵ as our small parameter of choice and note that the lower deck, main deck and upper deck are of thickness ϵ^5, ϵ^4, and ϵ^3 respectively.

We introduce a local streamwise coordinate X scaled on the triple deck length scale ϵ^3 and in the lower deck, where $y = \epsilon^5 \underline{Y}$, look for a solution of the form

$$U(X,\underline{Y}) = \epsilon \underline{U}(X,\underline{Y}) + \cdots, \tag{A.18}$$

$$V(X,\underline{Y}) = \epsilon^3 \underline{V}(X,\underline{Y}) + \cdots, \tag{A.19}$$

$$P(X,\underline{Y}) = \epsilon^2 P(X) + \cdots. \tag{A.20}$$

In the main deck, where $y = \epsilon^4 Y$, the solution takes the linearised form

$$U(X,Y) = U_b(Y) + \epsilon A(X) U_b'(Y) + \cdots, \tag{A.21}$$

$$V(X,Y) = -\epsilon^2 A'(X) U_b(Y) + \cdots, \tag{A.22}$$

$$P(X,Y) = \epsilon^2 P(X) + \cdots, \tag{A.23}$$

where $A\left(X\right)$ is an arbitrary function of X. Finally in the upper deck, where $y = \epsilon^3 \overline{Y}$, we have

$$U\left(X,\overline{Y}\right) = 1 + \epsilon^2 \overline{U}\left(X,\overline{Y}\right) + \cdots, \qquad (A.24)$$

$$V\left(X,\overline{Y}\right) = \epsilon^2 \overline{V}\left(X,\overline{Y}\right) + \cdots, \qquad (A.25)$$

$$P\left(X,\overline{Y}\right) = \epsilon^2 \overline{P}\left(X,\overline{Y}\right) + \cdots, \qquad (A.26)$$

to ensure the governing equations are those of linearised potential flow.

In the expansions above we notice that the pressure is the same order in each of the decks and is transmitted down from the upper deck through the main deck to the lower deck without change since $P\left(X\right)$ has no dependence on y. In the lower deck the gradient of this pressure $P'\left(X\right)$ then drives a viscous boundary layer flow with an associated displacement thickness of $-\epsilon^2 A\left(x\right)$. The effects of this displacement thickness are then transmitted back up through the main deck, on the back of the Blasius boundary layer profile $U_b\left(Y\right)$, to provide a boundary condition on the transverse velocity in the upper deck, namely $\overline{V}\left(x,0\right) = -A'\left(X\right)$. In turn this boundary condition produces an inviscid pressure response in the upper deck which is then transmitted down to the lower deck and so on.

This process defines a viscous-inviscid interaction between the upper and lower decks, mediated via the main deck, which is the defining characteristic of triple-deck theory. Of course, since we are considering only steady solutions, there are no signals actually propagating between the upper and lower decks. However it is useful to picture the interaction mechanism as described above.

The unknown pressure $P\left(x\right)$ and displacement $A\left(X\right)$ are related by the pressure displacement interaction law, which in standard triple-deck theory takes the form of the Cauchy-Hilbert integral pair

$$P\left(X\right) = -\frac{1}{\pi} \int_{-\infty}^{+\infty} \frac{A'\left(\xi\right)}{\left(\xi - x\right)} d\xi, \qquad (A.27)$$

$$A'(X) = \frac{1}{\pi} \int_{-\infty}^{+\infty} \frac{P(\xi)}{(\xi - x)} d\xi, \tag{A.28}$$

due to the fact that the complex function $\overline{P}\left(X, \overline{Y}\right) + i\overline{V}\left(X, \overline{Y}\right)$ is an analytic function of $\overline{Z} = X + i\overline{Y}$ in the upper deck.

Once $P(X)$ and $A(X)$ have been found the upper deck pressure $\overline{P}\left(X, \overline{Y}\right)$ and transverse velocity $\overline{V}\left(X, \overline{Y}\right)$ can be obtained in the form

$$\overline{P}\left(X, \overline{Y}\right) = \frac{1}{2\pi} \int_{-\infty}^{+\infty} \frac{\overline{Y}P(\xi)}{(\xi - x)^2 + \overline{Y}^2} d\xi - \frac{1}{2\pi} \int_{-\infty}^{+\infty} \frac{(\xi - x)A'(\xi)}{(\xi - x)^2 + \overline{Y}^2} d\xi, \tag{A.29}$$

$$\overline{V}\left(X, \overline{Y}\right) = -\frac{1}{2\pi} \int_{-\infty}^{+\infty} \frac{(\xi - x)P(\xi)}{(\xi - x)^2 + \overline{Y}^2} d\xi - \frac{1}{2\pi} \int_{-\infty}^{+\infty} \frac{\overline{Y}A'(\xi)}{(\xi - x)^2 + \overline{Y}^2} d\xi, \tag{A.30}$$

by applying Cauchy's integral formula, and the streamwise velocity $\overline{U}\left(X, \overline{Y}\right)$ can then be found from the simple relation

$$\overline{U}\left(X, \overline{Y}\right) = -\overline{P}\left(X, \overline{Y}\right). \tag{A.31}$$

So to complete the triple-deck solution it only remains to solve the lower deck problem and in doing so find the unknown pressure $P(X)$ and displacement $A(X)$. In the lower deck the boundary layer equations

$$\underline{U}\frac{\partial \underline{U}}{\partial X} + \underline{V}\frac{\partial \underline{U}}{\partial \underline{Y}} = -P'(X) + \frac{\partial^2 \underline{U}}{\partial \underline{Y}^2}, \tag{A.32}$$

$$\frac{\partial \underline{U}}{\partial X} + \frac{\partial \underline{V}}{\partial \underline{Y}} = 0, \tag{A.33}$$

hold , by construction, and must be solved subject to the no slip condition on the aerofoil, a symmetry condition on the wake centreline, a main deck matching condition, and an upstream matching condition. No boundary condition can be imposed downstream, due to the parabolic nature of the governing equations, however we expect the solution to match with that of the Goldstein near wake. We must also impose an additional constraint in the form of the pressure displacement law (A.27).

The problem stated above was solved numerically by Jobe and Burggraf (1974) using a method which makes a guess for the unknown displacement $A(X)$ and updates this guess by comparing the pressures obtained first by imposing the pressure displacement law (A.27) and second by integrating the boundary layer equations (A.32) and (A.33) with specified displacement. This process is repeated until these two pressures are equal to within a given tolerance at which point the solution satisfies all the constraints and is complete giving $P(X)$ and $A(X)$.

A.3 Diffusion Layers

In the ground layer we again need to reinstate the highest order derivatives in the Navier-Stokes equations in order to satisfy the no slip condition on the ground. We can do this by introducing the local transverse coordinate $Y = \varepsilon^{-1}(y + \alpha)$. Since the ground is moving at speed one, relative to the aerofoil, it is only necessary to adjust the streamwise velocity component by an order ε amount in order to satisfy the no slip condition and as a result we seek a solution of the form

$$U(x,Y) = 1 + \varepsilon U_0(x,Y) + \cdots, \tag{A.34}$$

$$V(x,Y) = 0 + 0 + \varepsilon^2 V_0(x,Y) + \cdots, \tag{A.35}$$

$$P(x,Y) = p_\infty + \varepsilon P_0(x,Y) + \cdots. \tag{A.36}$$

Notice that the ground layer produces no displacement effect at order ε in contrast with the Blasius boundary layer and Goldstein wake considered earlier.

Introducing the local coordinate Y and the above expansions into the Navier-Stokes equations yields at leading order the equations

$$\frac{\partial U_0}{\partial x} = -P'_=(x) + \frac{\partial^2 U_0}{\partial Y^2}, \tag{A.37}$$

$$\frac{\partial U_0}{\partial x} + \frac{\partial V_0}{\partial Y} = 0, \tag{A.38}$$

which are <u>linear</u>. The pressure $P_=(x)$ is prescribed by the flow solution outside the layer, as described in Chapter 2, and the ground layer is therefore passive in the sense that the flow inside the layer does not influence the flow outside at leading order and indeed can only be determined once the outer flow solution is complete.

We can find a solution to equations (A.37) and (A.38) by writing the first of these equations as the one dimensional diffusion equation

$$\frac{\partial \theta}{\partial x} = \frac{\partial^2 \theta}{\partial Y^2}, \tag{A.39}$$

for $\theta(x, Y) = U_0(x, Y) + P_=(x)$ and solving it subject to the boundary conditions $\theta(x, 0) = P_=(x)$, $\theta(x, +\infty) = 0$, and $\theta(-\infty, Y) = 0$. We choose to solve this problem by using a half range Fourier sine transform in Y and we define the sine transform of $\theta(x, Y)$ to be

$$\theta_s(x, \eta) = \sqrt{\frac{2}{\pi}} \int_0^{+\infty} \theta(x, Y) \sin \eta Y \, dY. \tag{A.40}$$

We note that the inversion formula for the sine transform is exactly the same, meaning that $\theta(x, \eta)$ is the sine transform of $\theta_s(x, Y)$. Applying this transform to the diffusion equation (A.39) yields, after a minor rearrangement, the first order differential equation for $\theta_s(x, \eta)$

$$\frac{\partial \theta_s}{\partial x} + \eta^2 \theta_s = \sqrt{\frac{2}{\pi}} \eta P_0(x), \tag{A.41}$$

where we have used the result below when performing the transform and have also imposed the boundary condition $\theta(x, 0) = P_=(x)$.

$$\int_0^{+\infty} \frac{\partial^2 \theta}{\partial Y^2} \sin \eta Y \, dY = \eta \theta(x, 0) - \eta^2 \int_0^{+\infty} \theta(x, Y) \sin \eta Y \, dY. \tag{A.42}$$

A solution to equation (A.41) which satisfies the other boundary conditions is

$$\theta_s(x, \eta) = \sqrt{\frac{2}{\pi}} \int_{-\infty}^x P_=(\xi) \eta e^{-(x-\xi)\eta^2} \, d\xi, \tag{A.43}$$

and having determined $\theta_s(x, \eta)$ we now inverse sine transform this expression to give $\theta(x, Y)$ and hence the solution for $U_0(x, Y)$, namely

$$U_0(x, Y) = \frac{1}{\sqrt{4\pi}} \int_{-\infty}^{x} \frac{P_=(\xi) Y e^{\frac{-Y^2}{4(x-\xi)}}}{(x-\xi)^{3/2}} d\xi - P_=(x) \tag{A.44}$$

where we have used the integral identity below to perform the inverse transform.

$$\sqrt{\frac{2}{\pi}} \int_{0}^{+\infty} \eta e^{-(x-\xi)\eta^2} \sin \eta Y d\eta = \frac{1}{2\sqrt{2}} \frac{Y e^{\frac{-Y^2}{4(x-\xi)}}}{(x-\xi)^{3/2}} \tag{A.45}$$

In order to complete the solution $V_0(x, Y)$ is obtained from $U_0(x, Y)$ by integrating the continuity equation from zero to Y to give

$$V_0(x, Y) = -\int_{0}^{Y} \frac{\partial U_0}{\partial x} dY. \tag{A.46}$$

Appendix B

Wiener-Hopf Calculations

B.1 Introduction

Here we perform the Wiener-Hopf calculations necessary to specify the constants λ, μ, and ν appearing in the solution given in section 3.7. The general solution procedure is outlined in section 3.6.1, but for our purposes it is only necessary to complete part of the calculation. We are only interested in finding the constants in the upstream or downstream pressures, beneath the aerofoil, which are induced by the boundary conditions at the $\beta^{-2/3}$, $\beta^{-1/2}$, and order unity orders, since this allows us to specify the constants λ, μ, and ν respectively and so complete the small β solution given in section 3.7, in readiness for a quantitative comparison with the earlier numerical work.

In section (3.6.1) the upstream pressure in question is shown to be given by

$$P_- (-\infty) = (-i\gamma)^{1/2} \frac{T(0)_-}{R(0)_-}, \tag{B.1}$$

in the context of a trailing edge problem and so our goal is to perform the kernel decomposition procedure up to the point at which we can evaluate $T(0)_-$ and $R(0)_-$. Since the boundary conditions in the example under consideration are singular in

nature, an attempt must be made in each case to carry out the decomposition process analytically as far as possible, any remaining integrals being calculated numerically.

The product decomposition of $R(K)$ is addressed in section B.2 below, followed by the calculation of the constants λ, μ, and ν in sections B.3, B.4, and B.5 in turn.

B.2 Calculating $R(K)_+$ and $R(K)_-$

Since we must solve the same integral equations at each of the three orders under consideration we must perform the product decomposition of

$$R(K) = \frac{\left(1 - e^{-|K|}\right)\left(K^2 + \gamma^2\right)^{1/2}}{|K|}, \tag{B.2}$$

at each of these orders. We will therefore perform this task first. As part of our general solution equations (3.120) and (3.121) inform us that if we are to write $R(K)$ as a product of $+$ and $-$ transforms $R(K)_+ R(K)_-$ then we must have

$$R(K)_+ = R(K)^{1/2} e^{-\frac{i}{2}\theta(K)}, \tag{B.3}$$

$$R(K)_- = R(K)^{1/2} e^{+\frac{i}{2}\theta(K)} \tag{B.4}$$

where in the above

$$\theta(K) = \frac{1}{\pi} \int_{-\infty}^{+\infty} \frac{\ln\left(|\kappa|^{-1}\left(1 - e^{-|\kappa|}\right)\left(\kappa^2 + \gamma^2\right)^{1/2}\right)}{(\kappa - K)} d\kappa. \tag{B.5}$$

The Hilbert integral above cannot be done analytically and so we must be content in the knowledge that the expression can be easily evaluated numerically. We do note however that

$$R(0)_+ = \gamma^{1/2}, \tag{B.6}$$

$$R(0)_- = \gamma^{1/2}, \tag{B.7}$$

as $R(K)$ is an even function of K and $R(0) = \gamma$, and so we have determined one of the unknown quantities in equation (3.139). We now go on to consider the remaining part of the Wiener-Hopf procedure at each of the three orders.

B.3 Calculating the Constant λ

In order to set the unknown constant λ at the $\beta^{-2/3}$ order we must solve the integral equations (3.88) and (3.89) subject to the specific boundary conditions

$$[V](X) = \left\{ \begin{array}{ll} 0 & \text{for } X < 0 \\ -\frac{2}{3}c_2 X^{-2/3} & \text{for } X > 0 \end{array} \right\}, \qquad (B.8)$$

$$\langle V \rangle (X) = \left\{ \begin{array}{ll} 0 & \text{for } X < 0 \\ ? & \text{for } X > 0 \end{array} \right\}, \qquad (B.9)$$

$$[P](X) = \left\{ \begin{array}{ll} ? & \text{for } X < 0 \\ 0 & \text{for } X > 0 \end{array} \right\}, \qquad (B.10)$$

$$\langle P \rangle (X) = \left\{ \begin{array}{ll} ? & \text{for } X < 0 \\ ? & \text{for } X > 0 \end{array} \right\}. \qquad (B.11)$$

To do this we use the Wiener-Hopf method outlined in section 3.6.1. Once $R(K)$ has been decomposed into the product $R(K)_+ R(K)_-$, via equations (3.110) and (3.111), we are next required to decompose the function $N(K)$ into the sum of $+$ and $-$ transforms $N(K)_+ + N(K)_-$. We find, from equation (3.123), that in this case

$$N(K) \equiv -\frac{4\pi c_2}{3\sqrt{3}\Gamma\left(\frac{2}{3}\right)} e^{-|K|} (-iK)^{-1/3}, \qquad (B.12)$$

where we have used the integral identity

$$\frac{1}{2\pi} \int_{-\infty}^{+\infty} (-iK)^m e^{-iKX} dK = \left\{ \begin{array}{ll} 0 & \text{for } X > 0 \\ -\frac{\sin m\pi \Gamma(m+1)}{\pi |X|^{m+1}} & \text{for } X < 0 \end{array} \right\}, \qquad (B.13)$$

with $m = -1/3$ to calculate the Fourier transform of $[V](X)$. In order to find $N(K)_+$ and $N(K)_-$ from equations (3.124) and (3.125) it is necessary to calculate the Hilbert transform of $N(K)$. By using a contour integral method we find that

$$\frac{1}{\pi i} \int_{-\infty}^{+\infty} \frac{N(\kappa)}{(\kappa - K)} d\kappa = -\frac{4\pi c_2}{3\sqrt{3}\Gamma\left(\frac{2}{3}\right)} \left(e^{-|K|} (-iK)^{-1/3} - 2C(K) \right), \qquad (B.14)$$

where in the above

$$C(K) = \frac{1}{\pi} \int_0^{+\infty} \frac{(r - iK)}{(r^2 + K^2)} r^{-1/3} \sin r \, dr, \tag{B.15}$$

is a finite function of K. We can now write down $N(K)_+$ and $N(K)_-$ in the form

$$N(K)_+ = -\frac{4\pi c_2}{3\sqrt{3}\Gamma\left(\frac{2}{3}\right)} \left(e^{-|K|} (-iK)^{-1/3} - C(K)\right), \tag{B.16}$$

$$N(K)_- = -\frac{4\pi c_2}{3\sqrt{3}\Gamma\left(\frac{2}{3}\right)} C(K). \tag{B.17}$$

Having completed the sum decomposition of $N(K)$ we are next required to decompose the function $T(K)$ into the sum $T(K)_+ + T(K)_-$. However, we need not complete this task in order to specify $T(0)_-$ and so determine the value of the upstream pressure beneath the aerofoil from equation (3.139).

Equation (3.127) defines $T(K)$ to be

$$T(K) = -\frac{4\pi c_2}{3\sqrt{3}\Gamma\left(\frac{2}{3}\right)} \frac{(k + i\gamma)_+^{1/2}}{R(K)_+} C(K), \tag{B.18}$$

since the Fourier transform of $\langle V \rangle (X)_-$ is zero. We notice from equation (3.129) that in order to determine $T(0)_-$ we must first evaluate $T(0)$ and second find the value of the Hilbert transform of $T(K)$ at $K = 0$. The former can be determined analytically and we find that

$$T(0) = -(+i)^{1/2} \frac{4\pi c_2}{3\sqrt{3}\Gamma\left(\frac{2}{3}\right)} \frac{\Gamma\left(\frac{1}{3}\right)}{2\sqrt{\pi}\sqrt[3]{2}\Gamma\left(\frac{7}{6}\right)}, \tag{B.19}$$

where we have used the integral identity

$$\frac{1}{\pi} \int_0^{+\infty} r^{-4/3} \sin r \, dr = \frac{\Gamma\left(\frac{1}{3}\right)}{2\sqrt{\pi}\sqrt[3]{2}\Gamma\left(\frac{7}{6}\right)}, \tag{B.20}$$

when evaluating the constant $C(0)$. The latter must be evaluated numerically to give

$$\frac{1}{\pi i} \int_{-\infty}^{+\infty} \frac{T(\kappa)}{\kappa} d\kappa = -(+i)^{1/2} \frac{\sqrt{2}}{\pi} \int_{-\infty}^{+\infty} \frac{Re\left[T(\kappa)\right]}{\kappa} d\kappa \tag{B.21}$$

$$= -(+i)^{1/2} \frac{\sqrt{2}}{\pi} (-5.18416), \tag{B.22}$$

where we have used the fact that $Im\,[T\,(K)] = Re\,[T\,(-K)]$. Substitution of these results into equation (3.129) with $K = 0$ gives $T\,(0)_-$ and subsequent substitution of $R\,(0)_-$ and $T\,(0)_-$ into equation (3.139) gives a value for the upstream pressure beneath the aerofoil of

$$P_-\,(-\infty) = \frac{1}{2}\left[-\frac{4\pi c_2}{3\sqrt{3}\Gamma\left(\frac{2}{3}\right)}\frac{\Gamma\left(\frac{1}{3}\right)}{2\sqrt{\pi}\sqrt[3]{2}\Gamma\left(\frac{7}{6}\right)}+\frac{\sqrt{2}}{\pi}\,(-5.18416)\right]. \quad (B.23)$$

Finally matching this constant upstream pressure to the global pressure solution beneath the aerofoil $p_-\,(x)$, given in section 3.7, sets the constant λ to be

$$\lambda = P_-\,(-\infty) = -1.9105... \quad (B.24)$$

B.4 Calculating the Constant μ

In order to set the unknown constant μ at the $\beta^{-1/2}$ order we must solve the integral equations 3.88 and (3.89) at the <u>leading</u> edge subject to the specific boundary conditions

$$[V]\,(X) = \left\{\begin{array}{ll} 0 & \text{for}\quad X < 0 \\ c_1 X^{-1/2} & \text{for}\quad X > 0 \end{array}\right\}, \quad (B.25)$$

$$\langle V\rangle\,(X) = \left\{\begin{array}{ll} ? & \text{for}\quad X < 0 \\ 0 & \text{for}\quad X > 0 \end{array}\right\}, \quad (B.26)$$

$$[P]\,(X) = \left\{\begin{array}{ll} 0 & \text{for}\quad X < 0 \\ ? & \text{for}\quad X > 0 \end{array}\right\}, \quad (B.27)$$

$$\langle P\rangle\,(X) = \left\{\begin{array}{ll} ? & \text{for}\quad X < 0 \\ ? & \text{for}\quad X > 0 \end{array}\right\}. \quad (B.28)$$

Since this non-eigensolution exists at the leading edge and not at the trailing edge the Wiener-Hopf solution presented in section (3.6.1) must be modified to take account of this fact. Also, the boundary conditions above force the downstream pressure beneath the aerofoil to behave not as a constant, as assumed in the previous section,

but to decrease like $-2c_1 |X|^{1/2}$ plus a constant. As a result we must make a second modification to the Wiener-Hopf solution of section (3.6.1).

We begin by replacing equations (3.112) and (3.113) with the equations

$$[P](X)_+ = [P]^*(X)_+ + [P]_\infty S(X)_+ + 2c_1 |X|_+^{1/2}, \qquad (B.29)$$

$$\langle P \rangle (X) = \langle P \rangle^* (X) + \langle P \rangle_\infty S(X)_+ - 2c_1 |X|_+^{1/2}, \qquad (B.30)$$

where $[P]^*(X)_+$ and $\langle P \rangle^*(X)$ tend to zero as $X \to \pm\infty$, and in doing so allow the pressure solution to exhibit the correct downstream behaviour beneath the aerofoil. We notice that the pressure difference is now a $+$ function rather than a $-$ function due to boundary condition (B.27). We can Fourier transform the above expressions to give

$$\widehat{[P]}(K)_+ = \widehat{[P]}^*(K)_+ + [P]_\infty \left(\pi\delta(K) + \frac{i}{K} \right)_+ + c_1\sqrt{\pi}(-iK)^{-3/2}, \quad (B.31)$$

$$\widehat{\langle P \rangle}(K) = \widehat{\langle P \rangle}^*(K) + \langle P \rangle_\infty \left(\pi\delta(K) + \frac{i}{K} \right)_+ - c_1\sqrt{\pi}(-iK)^{-3/2}, \quad (B.32)$$

and so replace equations (3.114) and (3.115) respectively.

The Wiener-Hopf solution then proceeds much as before and once $R(K)$ has been decomposed into the product $R(K)_+ R(K)_-$ we are required to sum decompose $N(K)$ as before. In this case $N(K)$ turns out to be

$$N(K) \equiv c_1\sqrt{\pi}e^{-|K|}(-iK)^{-1/2}, \qquad (B.33)$$

where we have again used the integral identity (B.13), with $m = -1/2$, to calculate the Fourier transform of $[V](X)$. We find $N(K)_+$ and $N(K)_-$ by using a contour integral method, as in the previous section, and obtain

$$N(K)_+ = c_1\sqrt{\pi}\left(e^{-|K|}(-iK)^{-1/2} - D(K) \right), \qquad (B.34)$$

$$N(K)_- = c_1\sqrt{\pi}D(K), \qquad (B.35)$$

where in the above

$$D(K) = \frac{1}{\pi}\int\limits_0^{+\infty} \frac{(r-iK)}{(r^2+K^2)}r^{-1/2}\sin r\,dr, \qquad (B.36)$$

is finite for all K. A difference now appears in the Wiener-Hopf decomposition procedure. We now collect all $+$ functions onto the right and all $-$ functions onto the left, in the opposite way to before. As a result equation (3.126) is replaced by

$$\frac{(K - i\gamma)_-^{1/2}}{R(K)_-} \left[\widehat{\langle V \rangle}(K)_- - N(K)_- \right] = \frac{(K - i\gamma)_+^{1/2}}{R(K)_-} \left[N(K)_+ - \widehat{\langle V \rangle}(K)_+ \right]$$
$$- \frac{(-iK) R(K)_+}{(K + i\gamma)_+^{1/2}} \widehat{[P]}(K)_+ .$$

(B.37)

We notice from equation (B.34) that $N(K)_+$ has a singular component at $K = 0$ and from equation (B.31) that $(-iK) \widehat{[P]}(K)_+$ has a similar singular component due to the downstream pressure behaviour which we have built into the solution. We group these singular terms together and redefine the function $T(K)$ to be

$$T(K) \equiv \frac{(k - i\gamma)_-^{1/2}}{R(K)_-} \left[N(K)_+ - \widehat{\langle V \rangle}_+(K) \right] - \frac{c_1 \sqrt{\pi} R(K)_+}{(K + i\gamma)_+^{1/2}} (-iK)^{-1/2} ,$$

(B.38)

thus replacing equation (3.127). Since we know $N(K)_+$ and the Fourier transform of $\langle V \rangle (X)_+$ is zero we have specifically.

$$T(K) = c_1 \sqrt{\pi} \left(\frac{(K - i\gamma)_-^{1/2}}{R(K)_-} e^{-|K|} - \frac{R(K)_+}{(K + i\gamma)_+^{1/2}} \right) (-iK)^{-1/2}$$
$$- c_1 \sqrt{\pi} \frac{(K - i\gamma)_-^{1/2}}{R(K)_-} D(K). \quad \text{(B.39)}$$

The solution now proceeds much as before eventually leading to the expression

$$P_-(\infty) = -(+i\gamma)^{1/2} \frac{T(0)_+}{R(0)_+}, \quad \text{(B.40)}$$

for the constant term in the downstream pressure beneath the aerofoil which replaces equation (3.139). Again we need only determine $R(0)_+$ and $T(0)_+$ in order to ultimately determine the unknown constant μ. We notice from equation (3.128) that we need to first evaluate $T(0)$ and second to find the value of the Hilbert transform of $T(K)$ at $K = 0$. The former can be obtained analytically and we find

$$T(0) = -(-i)^{1/2} \sqrt{2} c_1, \quad \text{(B.41)}$$

where we have used the integral identity

$$\frac{1}{\pi} \int\limits_{0}^{+\infty} r^{-3/2} \sin r \, dr = \sqrt{\frac{2}{\pi}}, \tag{B.42}$$

to calculate the value of $D(0)$. The latter must be evaluated numerically to give

$$\frac{1}{\pi i} \int\limits_{-\infty}^{+\infty} \frac{T(\kappa)}{\kappa} d\kappa = (-i)^{1/2} \frac{\sqrt{2}}{\pi} \int\limits_{-\infty}^{+\infty} \frac{Re\,[T(\kappa)]}{\kappa} d\kappa \tag{B.43}$$

$$= (-i)^{1/2} \frac{\sqrt{2}}{\pi} (-0.518765), \tag{B.44}$$

where we have used the fact that $Im\,[T(K)] = -Re\,[T(-K)]$. Substitution of these values into equation (3.128) with $K = 0$ gives $T(0)_+$ and subsequent substitution of $R(0)_+$ and $T(0)_+$ into equation (B.40) leads to a value for the constant in the downstream pressure beneath the aerofoil of

$$P_-(\infty) = \frac{1}{\sqrt{2}} \left[c_1 - \frac{1}{\pi} (-0.518765) \right]. \tag{B.45}$$

This constant in the downstream pressure is cancelled out exactly by adding an eigensolution of strength $-\mu$ to the non-eigensolution derived here. By doing this we can avoid a pressure mismatch between the local leading edge solution and the global solution beneath the aerofoil just downstream of the leading edge. As a result μ does not appear in the global pressure solution beneath the aerofoil, $p_-(x)$, given in section (3.7) but does appear in the strength of the eigensolution and takes the value

$$\mu = P_-(\infty) = 1.33348... \tag{B.46}$$

B.5 Calculating the Constant ν

In order to find the constant ν at order unity we adopt a different approach. Due to the simple form of the boundary conditions

$$[V](X) = \left\{ \begin{array}{ll} c_1 & \text{for} \quad X < 0 \\ 0 & \text{for} \quad X > 0 \end{array} \right\}, \tag{B.47}$$

$$\langle V \rangle (X) = \begin{cases} 0 & \text{for} \quad X < 0 \\ ? & \text{for} \quad X > 0 \end{cases}, \tag{B.48}$$

$$[P](X) = \begin{cases} ? & \text{for} \quad X < 0 \\ 0 & \text{for} \quad X > 0 \end{cases}, \tag{B.49}$$

$$\langle P \rangle (X) = \begin{cases} ? & \text{for} \quad X < 0 \\ ? & \text{for} \quad X > 0 \end{cases}, \tag{B.50}$$

at this order and the fact that both $[V](X)$ and $[P](X)$ are zero for $X > 0$ we are able to do away with the integral equations (3.88) and (3.89) and find this trailing edge non-eigensolution using a conformal mapping technique. In a similar way to section (3.6.2) we can show that the functions $P(X,Y)$ and $V(X,Y)$ satisfy the Cauchy-Riemann equations in the entire trailing edge region. We are therefore faced with the task of finding a complex function, $W(X + iY) = P(X,Y) + iV(X,Y)$, which is analytic throughout the local trailing edge region and satisfies the boundary conditions

$$W(X + 0i) = P_=(X) + 0i, \tag{B.51}$$

$$W(X + i/2 - 0i) = P_-(X) - i(c_1/2) \quad \text{for} \quad X < 0, \tag{B.52}$$

$$W(X + i/2 + 0i) = P_+(X) + i(c_1/2) \quad \text{for} \quad X < 0, \tag{B.53}$$

where the local trailing edge coordinates $X = (x - 1)/\beta$ and $Y = y/\beta$ have been introduced.

We find such a solution by introducing the complex variables $Z = X + iY$ and $\zeta = \xi + i\eta$ and by using a conformal mapping technique. To obtain the desired non-eigensolution in the Z-plane we map the corresponding solution in the ζ-plane

$$W(\zeta) = \frac{c_1}{\pi} \log\left(1 + e^{2\pi\zeta}\right) - c_1\zeta, \tag{B.54}$$

back onto the trailing edge geometry (Z-plane) using the conformal mapping

$$Z(\zeta) = \zeta + \frac{1}{2\pi}\left(1 + e^{2\pi\zeta}\right). \tag{B.55}$$

This conformal mapping is non-invertible and therefore we may only determine the solution implicitly using ζ. However, for our purposes we do not require a complete solution as in order to specify the constant ν we only need to know the behaviour of the upstream pressure beneath the aerofoil as $X \to -\infty$. The corresponding limit in the ζ-plane is $\xi \to -\infty$ with $\eta = 1/2$ and by examining the real parts of equations (B.54) and (B.55) in this limit we find that the pressure solution takes the simple asymptotic form

$$P_-(\xi) \sim -c_1\xi, \tag{B.56}$$

$$X \sim \xi + \frac{1}{2\pi}. \tag{B.57}$$

Eliminating ξ from these two expressions shows that beneath the aerofoil the pressure grows like $-c_1X + \frac{c_1}{2\pi}$. Matching this upstream behaviour to the global pressure solution beneath the aerofoil $p_-(x)$, given in section 3.7, sets the unknown constant ν to be

$$\nu = \frac{c_1}{2\pi} = 0.27386... \tag{B.58}$$

Appendix C

Triple-Deck Study Problems

C.1 Introduction

The external, non-symmetric, triple-deck calculation presented in Chapter 4 is the culmination of many hours of work on simpler study problems. It would not be practical to mention them all here however, we do consider two such problems noteworthy. They are the flow past an isolated surface roughness on an otherwise flat plate in ground effect and the symmetric flow past the trailing edge of a flat plate in tunnel effect. These two flow solutions are presented here so as not to disrupt the overall flow of the thesis. The flow geometries and important scales are detailed in Figures C.1 and C.2.

In each case the surface clearance, α is of order ε^3 where

$$\varepsilon \; = \; Re^{-1/8}, \tag{C.1}$$

as in Chapter 4, and therefore the moving surface can interfere with the boundary layer flow near the bump/trailing edge through a viscous-inviscid interaction, supported by a triple-deck flow structure. We introduce a scaled surface clearance parameter, of order unity here, by writing α as $\bar{\alpha}\epsilon^3$. The primary difference in these
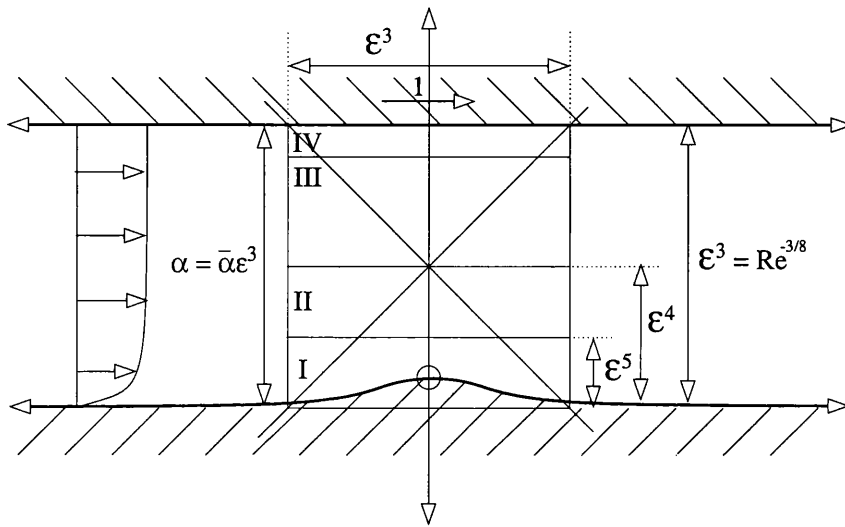
Figure C.1: The triple-deck flow structure around a bump on an otherwise flat surface, which is moving past another surface.
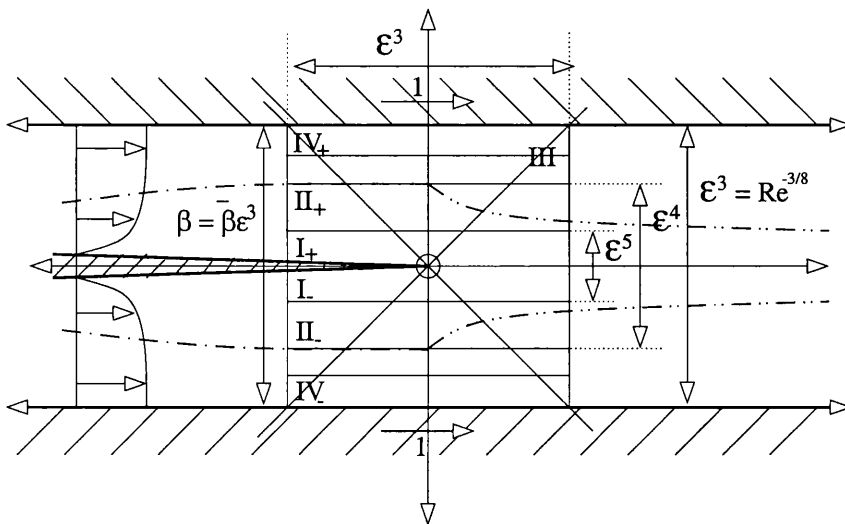

Figure C.2: The triple-deck flow structure near the trailing edge of a thin aerofoil in symmetric tunnel effect.

flows as compared to those of standard triple deck theory is that the Hilbert integral interaction law from the standard theory is replaced by a similar integral relation for flows with ground interference and it is by making this simple change that surface effects are included. This new interaction law takes a simple form for small surface clearances, as shown in Chapter 4, and the implications for the flow solution are noted.

C.2 Flow Past a Bump on a Flat Plate in Surface Effect

In this section we consider the two-dimensional, steady, incompressible flow over an isolated surface roughness situated on an otherwise flat plate placed close to a moving boundary. The roughness has typical dimensions ε^3 and ε^5 in the streamwise and transverse directions respectively and as such sits within the lower deck of the triple deck structure induced by the bump's presence. The flow is confined above by a plane surface, at a distance $\bar{\alpha}\varepsilon^3$ from the plate, moving parallel with the plate at the free stream velocity. The Reynolds number for the flow is based on the free stream speed and the distance of the bump from the leading edge of the plate and we will consider the case where this Reynolds number is large.

C.2.1 Problem Formulation

On the local length scale of the bump the flow takes on a triple-deck structure (see Appendix A) and we seek a solution of the form (A.18)-(A.26) in each of three decks of thicknesses ε^5, ε^4, and ε^3 respectively. The bump profile is given by $\underline{Y} = hG(X)$ where X and $\underline{Y}$ are the local lower deck co-ordinates. As in standard triple deck theory the central task becomes, after renormalising $(\underline{U}, \underline{V}, P, A, X, Y, G, \bar{\alpha})$ on $(\lambda^m, \lambda^{3m}, \lambda^{2m}, \lambda^{-3m}, \lambda^{-5m}, \lambda^{-3m}, \lambda^{-3m}, \lambda^{-5m})$ where $m = 1/4$ and making a Prandtl

shift transformation, one of solving the boundary layer equations

$$U\frac{\partial \underline{U}}{\partial X} + \underline{V}\frac{\partial \underline{U}}{\partial \underline{Y}} = -P'(X) + \frac{\partial^2 \underline{U}}{\partial \underline{Y}^2}, \tag{C.2}$$

$$\frac{\partial \underline{U}}{\partial X} + \frac{\partial \underline{V}}{\partial \underline{Y}} = 0, \tag{C.3}$$

in the lower deck subject to the no slip boundary conditions

$$\underline{U}(X,0) = 0, \tag{C.4}$$

$$\underline{V}(X,0) = 0, \tag{C.5}$$

valid for all X on the bump surface, now $\underline{Y} = 0$ due to the Prandlt shift, the main deck matching condition

$$\underline{U}(X,\underline{Y}) \sim \underline{Y} + hG(X) + A(X), \tag{C.6}$$

valid for all X in the limit $\underline{Y} \to +\infty$, and the upstream matching condition

$$\underline{U}(X,\underline{Y}) \sim \underline{Y}, \tag{C.7}$$

valid for all $\underline{Y}$ as $X \to -\infty$. An additional constraint, in the form of an interaction law, is required to close the problem and for flows with ground interference we have

$$P'(X) = -\frac{1}{\bar{\beta}} \int_{-\infty}^{+\infty} \frac{A''(\xi)}{\tanh \frac{\pi}{\bar{\beta}}(\xi - X)} d\xi, \tag{C.8}$$

$$A''(X) = \frac{1}{\bar{\beta}} \int_{-\infty}^{+\infty} \frac{P'(\xi)}{\sinh \frac{\pi}{\bar{\beta}}(\xi - X)} d\xi, \tag{C.9}$$

where $\bar{\beta} = 2\bar{\alpha}$.

If the bump size parameter, h, is small compared with unity then progress can be made analytically, if not then equations (C.2)-(C.9) must be solved numerically. We consider each of these cases in turn.

C.2.2 Small Bumps ($h \ll 1$)

In the case where the bump is small we take h as our small parameter and following Smith (1973) seek a solution in the form of the perturbed shear flow

$$\underline{U}(X, \underline{Y}) = \underline{Y} + hU_0(X, \underline{Y}) + \cdots, \tag{C.10}$$

$$\underline{V}(X, \underline{Y}) = 0 + hV_0(X, \underline{Y}) + \cdots, \tag{C.11}$$

$$P(X) = 0 + hP_0(X) + \cdots, \tag{C.12}$$

$$A(X) = 0 + hA_0(X) + \cdots. \tag{C.13}$$

The governing boundary layer equations are then linearised to become

$$\underline{Y}\frac{\partial U_0}{\partial X} + V_0 = -P_0' + \frac{\partial^2 U_0}{\partial \underline{Y}^2}, \tag{C.14}$$

$$\frac{\partial U_0}{\partial X} + \frac{\partial U_0}{\partial X} = 0, \tag{C.15}$$

which must be solved subject to the new no slip boundary conditions

$$U_0(X, 0) = 0, \tag{C.16}$$

$$V_0(X, 0) = 0, \tag{C.17}$$

valid for all X, the main deck matching condition

$$U_0(X, \underline{Y}) \sim G(X) + A_0(X), \tag{C.18}$$

valid for all X in the limit $\underline{Y} \to +\infty$, and the upstream matching condition

$$U_0(X, \underline{Y}) = 0, \tag{C.19}$$

valid for all $\underline{Y}$ as $X \to -\infty$. The pressure displacement law becomes

$$P_0'(X) = -\frac{1}{\bar{\beta}} \int_{-\infty}^{+\infty} \frac{A_0''(\xi)}{\tanh \frac{\pi}{\bar{\beta}}(\xi - X)} d\xi, \tag{C.20}$$

$$A_0''(X) = \frac{1}{\bar{\beta}} \int_{-\infty}^{+\infty} \frac{P_0'(\xi)}{\sinh \frac{\pi}{\bar{\beta}}(\xi - X)} d\xi. \tag{C.21}$$

We begin solving the above system of equations by first differentiating equation (C.14) with respect to $\underline{Y}$, eliminating the pressure gradient term, eliminating V_0 using equation (C.15), and introducing the shear stress $\Omega_0 = \partial U_0 / \partial \underline{Y}$. A Fourier transform in X then leads, after some manipulation, to the equation

$$\frac{\partial^2 \widehat{\Omega}_0}{\partial \underline{Y}^2} - (-iK)\, \underline{Y} \widehat{\Omega}_0 \;=\; 0, \tag{C.22}$$

where K is a scaled wavenumber, for the Fourier transform of the shear stress Ω_0. This equation admits solutions of the form

$$\widehat{\Omega}_0\left(K, \underline{Y}\right) \;=\; M\left(K\right) Ai\left(\left(-iK\right)\underline{Y}\right). \tag{C.23}$$

In the expression immediately above $M\left(K\right)$ is an unknown function and $Ai\left(\eta\right)$ is the finite Airy function satisfying the ordinary differential equation $f''\left(\eta\right) - \eta f\left(\eta\right) = 0$. Our aim is to find $M\left(K\right)$ and to subsequently determine all other flow properties of interest. Evaluation of equation (C.14) at $\underline{Y} = 0$, using the no slip conditions (C.16) and (C.17), leads to the relation

$$\widehat{P_0'}\left(K\right) \;=\; Ai'\left(0\right) M\left(K\right) \left(-iK\right)^{1/3}, \tag{C.24}$$

in wavenumber space, the main deck matching condition (C.18) can be written as

$$\widehat{A_0''}\left(K\right) \;=\; \left(-iK\right)^2 \left(\frac{M\left(K\right)}{3\left(-iK\right)^{1/3}} - \widehat{G}\left(K\right)\right), \tag{C.25}$$

in wavenumber space, and the Fourier transforms of the pressure displacement interaction laws (C.20) and (C.21) are

$$\widehat{P_0'}\left(K\right) \;=\; -i\coth \overline{\alpha} K \widehat{A_0''}\left(K\right), \tag{C.26}$$

$$\widehat{A_0''}\left(K\right) \;=\; i\tanh \overline{\alpha} K \widehat{P_0'}\left(K\right). \tag{C.27}$$

Equations (C.24)-(C.27) constitute three independent equations in the three unknowns $M\left(K\right)$, $\widehat{P_0'}\left(K\right)$, and $\widehat{A_0''}\left(K\right)$. We may therefore solve these equations for the three unknowns in terms of $\widehat{G}\left(K\right)$, the Fourier transform of the bump profile. We obtain

$$M\left(K\right) \;=\; 3\left(-iK\right)^{2/3} \frac{\widehat{G}\left(K\right)}{D\left(K\right)}, \tag{C.28}$$

and the Fourier transformed solutions

$$\widehat{P_0}(K) = 3Ai'(0)\frac{\widehat{G}(K)}{D(K)}, \tag{C.29}$$

$$\widehat{A_0}(K) = -3Ai'(0)\frac{\tanh\overline{\alpha}|K|}{|K|}\frac{\widehat{G}(K)}{D(K)}, \tag{C.30}$$

$$\widehat{\Omega_0}(K,0) = 3Ai(0)(-iK)^{2/3}\frac{\widehat{G}(K)}{D(K)}, \tag{C.31}$$

for the pressure, displacement, and skin friction perturbations respectively where in the above

$$D(K) = (-iK)^{1/3} + 3Ai'(0)\frac{\tanh\overline{\alpha}|K|}{|K|}. \tag{C.32}$$

These solutions may be inverse Fourier transformed, taking care to circumnavigate the branch cut in the complex function $(-iK)^{n/3}$, to obtain the corresponding solutions in physical space. Solutions, in the case where $h = 0.01$ and $G(X) = e^{-4x^2}$ for the pressure, $P(X)$, and the displacement, $A(X)$, are given in Figures C.3 and C.4 respectively for a range of surface clearances $\overline{\alpha}$.

C.2.3 Larger Bumps

As mentioned earlier, the flow over larger bumps must be considered numerically and solutions can be found using similar methods to those used in Chapter 4. Solutions for the pressure $P(X)$ and the displacement $A(X)$ are given in Figures C.5 and C.6 respectively for the case where $h = 1$ and

$$G(X) = \begin{cases} (1 - X^2)^2 & \text{for} \quad |X| < 1 \\ 0 & \text{for} \quad |X| \geq 1 \end{cases}, \tag{C.33}$$

again for a range of surface clearances $\overline{\alpha}$.

We can see by comparing the results for large and small bumps that the linear theory does quite well for $h < 1$. Of course, as h is increased further flow separation will occur and the linear solutions will no longer resemble the true solution. As in Chapter 4 we notice that for small $\overline{\alpha}$ the magnitude of the displacement scales with $\overline{\alpha}$, as does the streamwise extent of the upstream influence in the pressure.
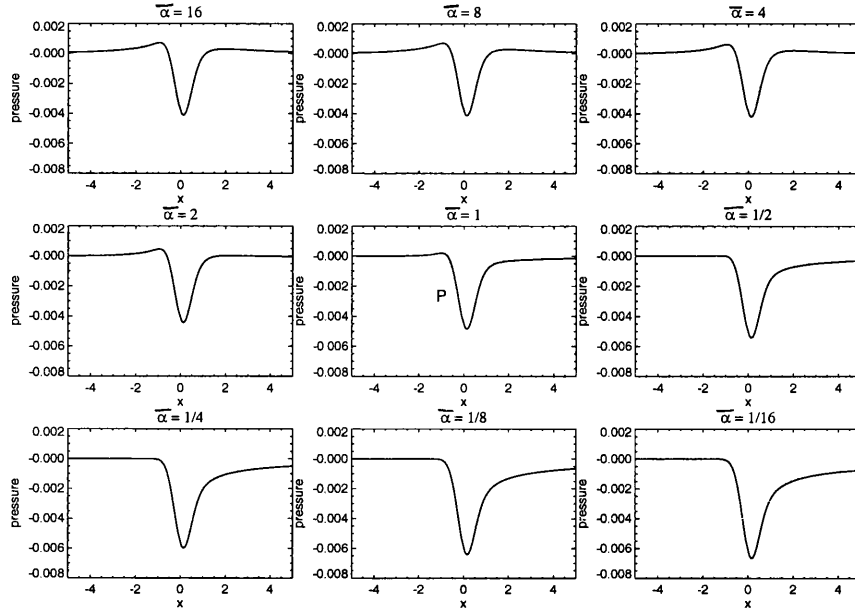
Figure C.3: The pressure distribution $P(X)$ on a small bump in surface effect, for a range of surface clearances $\bar{\alpha}$. $h = 0.01$. $G(X) = e^{-4x^2}$.
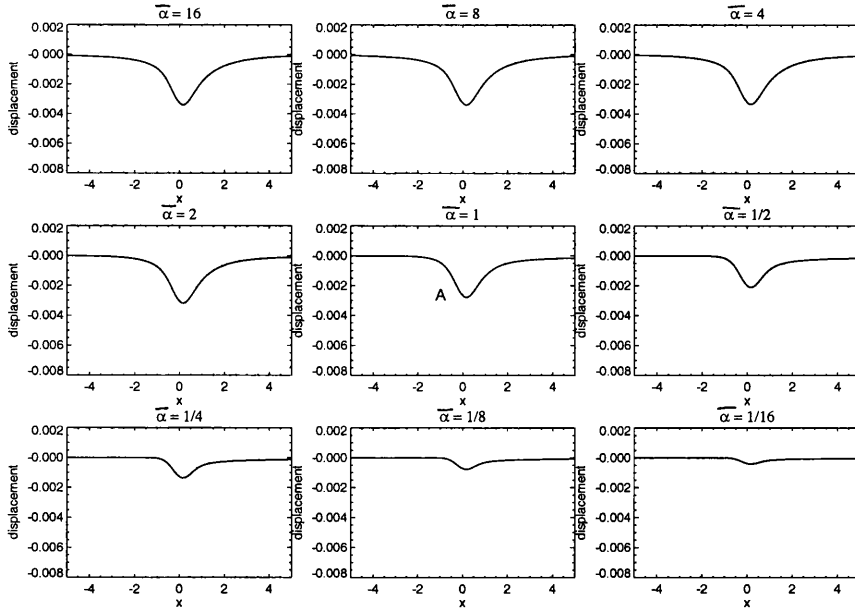

Figure C.4: The displacement $A(X)$ on a small bump in surface effect, for a range of surface clearances $\bar{\alpha}$. $h = 0.01$. $G(X) = e^{-4x^2}$.
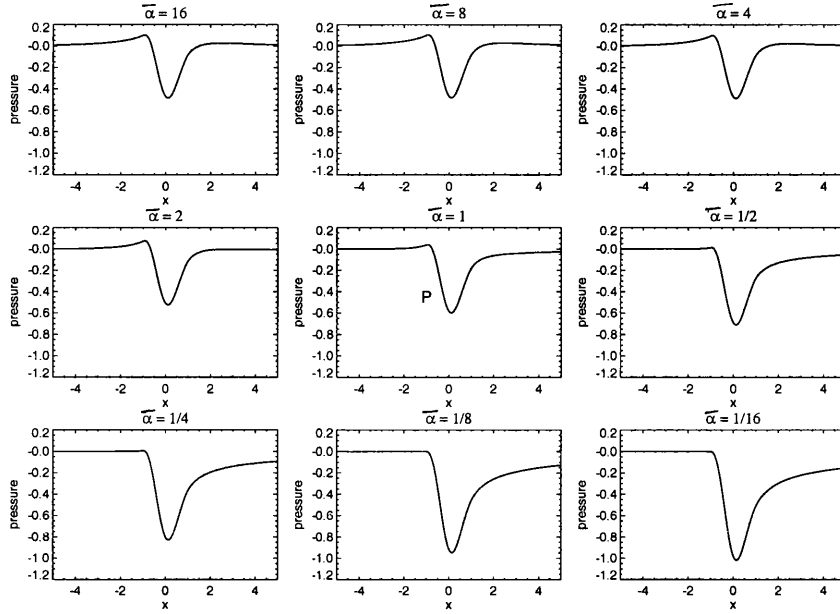
Figure C.5: The pressure distribution $P(X)$ on a larger bump in surface effect, for a range of surface clearances $\bar{\alpha}$. $h = 1$. $G(X) = (1 - X^2)^2$ for $|X| < 1$ and 0 otherwise.
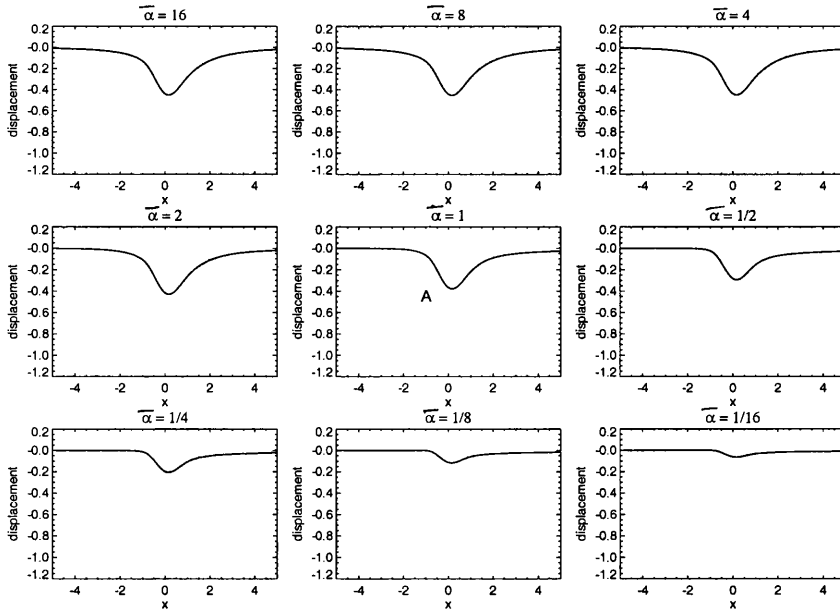

Figure C.6: The displacement $A(X)$ on a larger bump in surface effect, for a range of surface clearances $\bar{\alpha}$. $h = 1$. $G(X) = (1 - X^2)^2$ for $|X| < 1$ and 0 otherwise.

C.3   Flow Past the Trailing Edge of a Flat Plate in Symmetric Tunnel Effect

The second of our study examples is that of the symmetric flow past the trailing edge of a flat plate in tunnel effect, as described in Figure C.2. The resulting triple deck problem is essentially the same as that stated in section C.2.1 except that boundary condition (C.4) is partially replaced by the symmetry condition $\frac{\partial U}{\partial Y} = 0$ for $X > 0$, in the wake, and $hG(X)$ is set to zero in condition (C.6). The corresponding solutions for $P(X)$ and $A(X)$ are given in Figures C.7 and C.8 respectively for a range of tunnel clearances $\bar{\alpha}$.

We again notice that for large $\bar{\alpha}$ the solution approaches that of Jobe and Burggraf (1974) for flow past the trailing edge of a flat plate in the absence of boundaries, as it should. For small $\bar{\alpha}$ we again observe that the magnitude of the displacement $A(X)$ decreases in line with $\bar{\alpha}$, as does the streamwise extent of the upstream influence.

However, in the case considered here one difference stands out. The pressure is no longer forced to fall back to zero as $X \to +\infty$ as there are now boundaries above and below which can support the growing pressure observed in the numerical solutions. Equation (4.110) suggests that the pressure in fact grows like $X^{1/3}$ in line with the displacement.
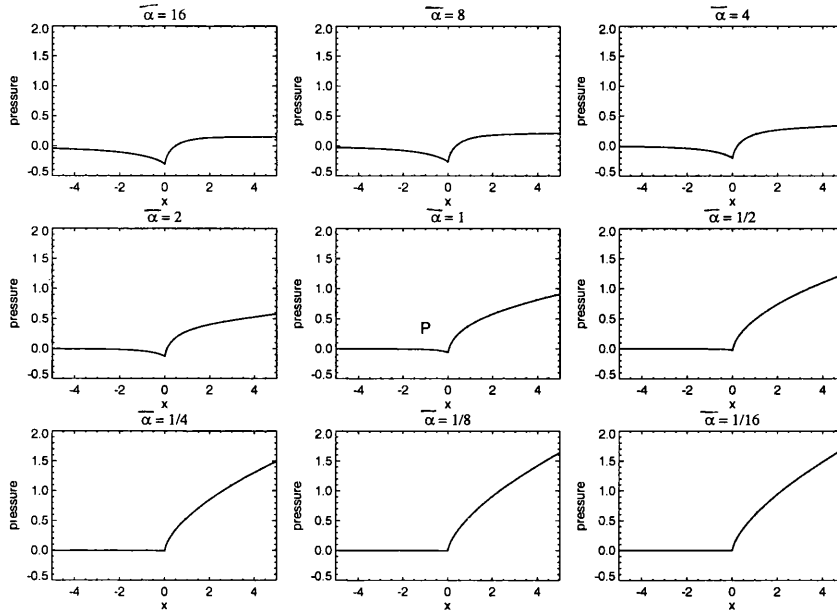
Figure C.7: The pressure $P(X)$ over the trailing edge of a flat plate in symmetric tunnel effect, for a range of surface clearances $\bar{\alpha}$.
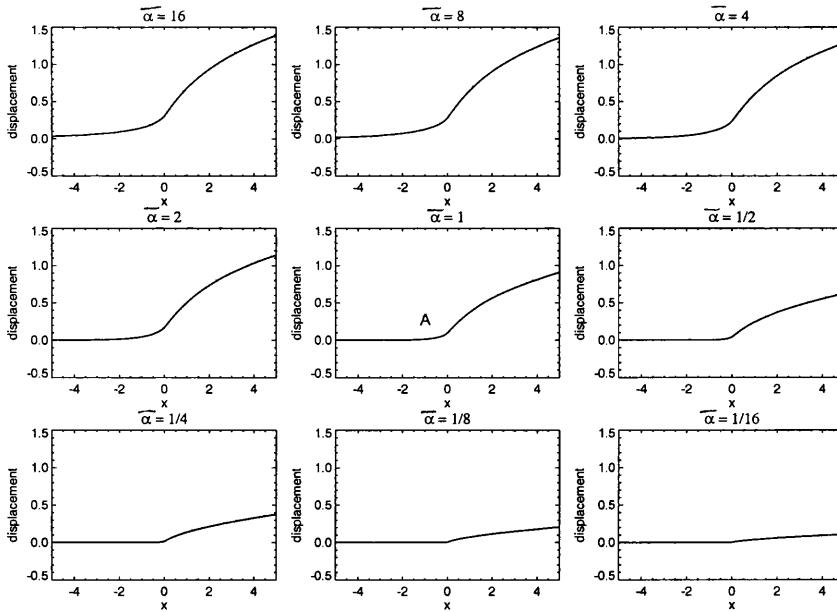
Figure C.8: The displacement $A(X)$ over the trailing edge of a flat plate in symmetric tunnel effect, for a range of surface clearances $\bar{\alpha}$.

Appendix D

Local Leading Edge Solution

The flow properties of Region IV (see Figure 5.2), in which we introduce the local co-ordinates $X = x/\varepsilon$, $Y = \widehat{\alpha} + y/\epsilon$, and the asymptotic expansions

$$U(x,y) = U_0(X,Y) + \cdots, \qquad (\text{D.1})$$

$$V(x,y) = V_0(X,Y) + \cdots, \qquad (\text{D.2})$$

$$P(x,y) = P_0(X,Y) + \cdots, \qquad (\text{D.3})$$

are essentially inviscid with the Euler equations applying to $U_0(X,Y)$, $V_0(X,Y)$, and $P_0(X,Y)$. The vorticity is identically equal to zero however, as the incident flow upstream is a uniform stream and so the local streamfunction $\Psi(X,Y)$, defined by $U_0 = \partial\Psi/\partial Y$ and $V_0 = -\partial\Psi/\partial X$, satisfies Laplace's equation. The boundary conditions holding on Ψ require Ψ to be zero on $Y = 0$, for tangential flow along the ground, Ψ to tend to Y in the farfield outside of the gap, and Ψ to be a constant, say Ψ_0, along the body shape at the leading edge. The body shape is assumed locally flat at the leading edge so that the last boundary condition is effectively applied at $Y = \widehat{\alpha}$ for $X \geq 0$.

In order to find $\Psi(X,Y)$ we write it in the form

$$\Psi(X,Y) = Y + \psi(X,Y), \qquad (\text{D.4})$$

where $\psi(X, Y)$ also satisfies Laplace's equation and the boundary conditions

$$\psi(X, 0) = 0, \tag{D.5}$$

$$\psi(X, \widehat{\alpha}) = \Psi_0 - \widehat{\alpha} \quad \text{for} \quad X \geq 0, \tag{D.6}$$

and $\psi(X, Y)$ approaches zero in the farfield outside the gap.

We find $\psi(X, Y)$ by introducing the complex variables $Z = X + iY$ and $\zeta = \xi + i\eta$ and using a conformal mapping technique. To obtain the desired solution in the Z-plane we map the relevant uniform channel flow in the ζ-plane, for which the streamfunction is given by $\psi = (\Psi_0 - \widehat{\alpha})\eta$, back onto the leading edge geometry (Z-plane) using the conformal mapping

$$Z(\zeta) = \widehat{\alpha}\left(\zeta - \frac{1}{\pi}\left(1 + e^{-\pi\zeta}\right)\right). \tag{D.7}$$

This conformal mapping is non-invertible and therefore we may only define $\psi(X, Y)$, and hence the full solution $\Psi(X, Y)$, implicitly using ξ and η.

For a given ξ, η we have

$$\Psi = Y + (\Psi_0 - \widehat{\alpha})\eta, \tag{D.8}$$

$$X = \widehat{\alpha}\left(\xi - \frac{1}{\pi}\left(1 + e^{-\pi\xi}\cos\pi\eta\right)\right), \tag{D.9}$$

$$Y = \widehat{\alpha}\left(\eta + \frac{1}{\pi}e^{-\pi\xi}\sin\pi\eta\right). \tag{D.10}$$

The complex velocity is given by

$$U_0 - iV_0 = 1 + \frac{(\Psi_0 - \widehat{\alpha})}{\widehat{\alpha}\left(1 + e^{-\pi(\xi+i\eta)}\right)}. \tag{D.11}$$

As we move into the gap, $\xi \to +\infty$, $U_0 \to \Psi_0/\widehat{\alpha}$, $V_0 \to 0$, whereas in the farfield outside the gap $\xi \to -\infty$, $U_0 \to 1$, $V_0 \to 0$ as required. Therefore by Bernoulli's theorem the pressure must jump from zero upstream of the leading edge region to $\frac{1}{2}\left(1 - \left(\frac{\Psi_0}{\alpha}\right)^2\right)$ just downstream of the leading edge region inside the gap.

Bibliography

W. H. Ailor and W. R. Eberle. Configuration effects on the lift of a body in close ground proximity. *J. Aircraft*, 13:584–589, 1976.

M. Ambramowitz and I. A. Stegun. *Handbook of Mathematical Functions*. Dover, 1972.

K. Atkinson. The numerical solution of integral equations on the half-line. *SIAM J. Numerical Anal.*, 6:315–337, 1969.

T. M. Barrows and S. E. Widnall. Optimum lift-drag ratio for a ram wing tube vehicle. *AIAA Journal*, 8:491–497, 1970.

G. K. Batchelor. *Introduction to Fluid Dynamics*. Cam. Univ. Press, 1967.

P. W. Bearman. Bluff body flows applicable to vehicle aerodynamics. *Aeordynamics of Transportation*, 1980. (ed. T. Morel and C. Dalton, pub. A.S.M.E. New York).

H. Blasius. *Z. Math. Phys.*, 56:1, 1908.

R. G. A. Bowles and F. T. Smith. Non-symmetric flow with interaction past a multi-bladed configuration. *In preparation*, 1999.

G. F. Carrier, M. Krook, and C. E. Pearson. *Functions of a Complex Variable*. McGraw-Hill Book Company, 1966.

J. E. Carter. A new boundary layer inviscid iteration technique for separated flows. *AIAA Paper No. 79-1450*, 1979.

200

M. D. Chawla, L. C. Edwards, and M. E. Franke. Wind-tunnel investigation of wing-in-ground effects. *J. Aircraft*, 27:289–293, 1990.

R. V. Churchill and J. Ward Brown. *Complex Variables and Applications*. McGraw-Hill Publishing Company, 1990.

R. G. Dominy. The influence of slipstreaming on the performance of a grand prix racing car. *J. Automobile Eng. (Proc. I. Mech. Eng.)*, 204:35–40, 1990.

R. G. Dominy. Aerodynamics of grand prix cars. *J. Automobile Eng. (Proc. I. Mech. Eng.)*, 206:267–274, 1992.

J. W. Elliott and F. T. Smith. Separated supersonic flow past a trailing edge at incidence. *Computers and Fluids*, 14:109–116, 1986.

H. Fischer. Airfoil technique explained on x-113 and x-114. *International High Performance Vehicle Conference*, November:1–19, 1988.

H. Fischer. Rfb research and development in wig vehicles. *AIAA 89-1495*, 1989.

H. Fischer and K. Matjasic. Some thoughts about the use of lift-off-aids as one condition for the economical operation of wig ships. *Workshop Proceeding of Ekranoplan and Very Fast Craft, University if New South Wales*, May:60–77, 1996.

H. Fischer and K. Matjasic. The hoverwing technology, bridge between wig and acv. *RINA Intenational Conference on WIGs, 4 and 5*, December, 1997.

S. Goldstein. Concerning some solutions of the boundary layer equations in hydro-dynamics. *Proc. Cambridge Philos. Soc.*, 26:1–30, 1930.

G. H. Golub and C. F. Van Loan. *Matrix Computations*. Johns Hopkins, 1996.

K. Jacob. Advanced method for computing flow around wings with rear separation and ground effect. *J. Aircraft*, 24:126–128, 1986.

S. K. Jensen. The stress singularity in surfactant driven thin-film flows. part 2 inertial effects. *J. Fluid Mech.*, 372:301–322, 1998.

C. E. Jobe and O. R. Burggraf. The numerical solution of the asymptotic equations of trailing edge flow. *Proc. R. Soc. Lond.*, 340:91–111, 1974.

M. A. Jones and F. T. Smith. Mechanisms in car undertray-shape and ground effects. *Phil. Trans. Roy. Soc.*, A theme issue accepted for publication:accepted for publication, 1999.

G. W. Jorg. History and development of the aerodynamic ground effect craft (agec) with tandem wings. *The Royal Aeronautical Society Symposium Proceedings*, May: 87–108, 1987.

G. W. Jorg. Tandem airfoil flairboats (taf). *RINA International Conference Proceedings on WIGs 4 and 5*, December, 1997.

T. J.. Kaario. The principles of ground effect vehicles. *Symposium on ground effect phenomena, Princeton University*, 1959a.

T. J. Kaario. Translation from finnish of two patents and one paper describing t.j. kaarios early work on air cushion vehicles (1932-1949). *Aerophysics Co. Washinton D.C.*, Report AR-595, 1959b.

J. Katz. Investigation of negative lifting surfaces attached to an open-wheel racing car configuration. *Int. Congr. and Exposition, Detroit, Michigan, Feb 25 - Mar 1*, 3:383–396, 1985a. SAE tech. ppr. 850283.

J. Katz. Calculation of the aerodynamic forces on automobile lifting surfaces. *J. Fluids Eng., Trans. A.S.M.E.*, 107:438–443, 1985b.

T. Kida and Y. Miyai. Jet-flapped wings in very close proximity to the ground. *AIAA Journal*, 10:611–616, 1973.

J. Kondo. *Integral Equations*. Kodansha-Oxford, 1991.

H. Kopka and P. W. Daly. *A Guide to LaTeX 2_ε*. Addison-Wesley, 1998.

M. G. Krein. Integral equations on a half-line with kernel depending upon the difference of the arguments. *Amer. Math. Soc. Trans*, 22:163–288, 1963.

M. J. Lighthill. *Fourier Analysis and Generalised Functions*. Cambridge University Press, 1960.

A. M. Lippisch. Der aerodynamischen bodeneffeckt und die entwicklung des flugflachen(aerofoil) bootes. *Luftfahrttechnik-Raumfahrttechnik 10*, October:261–269, 1964.

A. F. Messiter. Boundary-layer flow near the trailing edge of a flat plate. *SIAM J. Appl. Math.*, 18:241–257, 1970.

N. I. Muskhelishvili. *Singular Integral Equations*. Noordhoff-Groningen-Holland, 2nd edition, 1946.

J. N. Newman. Analysis of small-aspect-ratio lifting surfaces in ground effect. *J. Fluid Mech.*, 117:305–314, 1982.

B. Noble. *The Wiener-Hopf Technique*. Permagon Press, 1958.

B. P. O'Rourke. The uses of composite materials in the design and manufacture of formula 1 racing cars. *J. Automobile Eng. Part D*, 204:41–48, 1990.

A. Plotkin and S. S. Dodbele. Slender wing in ground effect. *A.I.A.A. J. Tech. Note*, 26:493–494, 1988.

A. Plotkin and C. G. Kennell. Thickness-induced lift on a thin airfoil in ground effect. *AIAA Journal*, 19:1484–1486, 1981.

W. Press, S.A. Teukolsky, W.T. Vetterling, and B.P. Flannery. *Numerical Recipes in C:The art of Scientific Computing*. Cambridge University Press, 1995.

O. Reynolds. *Phil. Trans. Roy. Soc.*, 177, Part 1:157–234, 1886.

N. Rott and R. J. Hakkinen. Similar solutions for merging shear flows. *J. Aerospace Sciences*, 29:1134–1135, 1962.

N. Rott and R. J. Hakkinen. Similar solutions for merging shear flows ii. *AIAA*, 3: 1553–1554, 1965.

L. I. Sedov. *Two-Dimensional Problems in Hydrodynamics and Aerodynamics*. Interscience, 1965.

M. Shinbrot. The solution of some integral equations of wiener-hopf type. *Unknown*, XXVIII:15–36, 1970.

D. N. Sinitsyn. Summary of the construction of the first commercial ekranoplan, amphistar. *Workshop Proceedings of Ekranoplans and Very Fast Craft, University of New South Wales*, December:146–151, 1996.

D. N. Sinitsyn and A. Maskalik. The ekranoplan is a new type of high speed water transport which can be used in all seasons. *Workshop Proceedings of Ekranoplans and Very Fast Craft, University of New South Wales*, December:152–162, 1996.

F. T. Smith. Laminar flow over a small hump on a flat plate. *J. Fluid Mech.*, 57: 803–824, 1973.

F. T. Smith. Flow through constricted or dilated pipes and channels : Part 1. *Q. J. Mech. Appl. Math.*, XXIX:343–364, 1976a.

F. T. Smith. On entry-flow effects in bifurcating, blocked or constricted channels. *J. Fluid Mech.*, 78:709–736, 1976b.

F. T. Smith. Planar incompressible flow over an aerofoil and its wake. *ARC C.P. No. 1352*, 1976c.

F. T. Smith. Interacting flow theory and trailing edge separation - no stall. *J. Fluid Mech.*, 131:219–249, 1983.

F. T. Smith and M. A. Jones. One-to-few and one-to-many branching tube flows. *submitted to J. Fluid Mech.*, 1999.

F. T. Smith and S. N. Timoshin. Blade-wake interactions and rotary boundary layers. *Proc. R. Soc. Lond.*, 452:1301–1329, 1996a.

F. T. Smith and S. N. Timoshin. Planar flows past thin multi-blade configurations. *J. Fluid Mech.*, 324:355–377, 1996b.

I. H. Sneddon. *The Use of Integral Transforms.* McGraw-Hill Book Company, 1972.

J. A. Sparenberg. Application of the theory of sectionally holomorphic functions to wiener-hopf type integral equations. *Koninkl. Ned. Akad. Wetenschap.*, A59: 29–34, 1956.

J. A. Sparenberg. The homogeneous first order integro-differential equation of the wiener-hopf type. *Technische Hogenschool,* Rep. No. 13, 1958.

K. Stewartson. On the flow near the trailing edge of a flat plate. ii. *Mathematika,* 16:106–121, 1969.

K. Stewartson. On laminar boundary layers near corners. *Q. J. Mech. Appl. Math.,* XXIII Part 2:137–152, 1970.

J. C. Strikwerda. *Finite Difference Schemes and Partial Differential Equations.* Chapman and Hall, 1989.

Y. B. Suh and C. Ostowari. Drag reduction factor due to ground effect. *J. Aircraft,* 25:1071–1072, 1988.

A. Z. Szeri. Some extensions of the lubrication theory of osborne reynolds. *J. Tribology, Trans. A.S.M.E.,* 109:21–36, 1987.

C. H. Tan and A. Plotkin. Lifting-line solution for a symmetrical thin wing in ground effect. *AIAA Journal,* 24:1193–1196, 1986.

J. A. Tichy. Entry flow in a narrow channel of varying gap with one sliding surface. *J. Tribology, Trans. A.S.M.E.*, 108:288–293, 1986.

J. A. Tichy and S. H. Chen. Plane slider bearing load due to fluid inertia - experiment and theory. *J. of Tribology*, 107:32–38, 1985.

E. O. Tuck. Irrotational flow past bodies close to a plane surface. *J. Fluid Mech.*, 50:481–491, 1971.

E. O. Tuck. A nonlinear unsteady one-dimensional theory for wings in extreme ground effect. *J. Fluid Mech.*, 98:33–47, 1980.

E. O. Tuck and M. Bentwich. Sliding sheets : Lubrication with comparable viscous and inertia forces. *J. Fluid Mech.*, 135:51–69, 1983.

M. Van Dyke. Entry flow in a channel. *J. Fluid Mech.*, 44:813–823, 1970.

M. Vernacchia. Medium class vehicles with aerodynamic efficiency. *FISITA Conferance*, Paper No. 950127:63, 1990.

S. E. Widnall and T. M. Barrows. An analytical solution for two and three dimensional wings in ground effect. *J. Fluid Mech.*, 41:769–792, 1970.

N. Wiener and E. Hopf. Uber eine klasse singularer integralgleichungen. *S. B. Preuss. Akad. Wiss. Berlin. Phys. Math.*, 30/32:696–706, 1931.

C. Wieselsberger. Wing resistance near the ground. *NACA TM-77*, 1922.

S. K. Wilson and B. R. Duffy. Lubrication with viscous and inertia forces. *Quart. J. Mech. Appl. Math.*, 51:105–124, 1998.

S. Wolfram. *Mathematica - A System for Doing Mathematics by Computer*. Addison-Wesley Publishing Company, 1993.

P. G. Wright. The influence of aerodynamics on the design of formula one racing cars. *Int. J. Vehicle Design*, 3:383–396, 1982.

M. Young. *The Technical Writers Handbook.* University Science Books, 1989.